CERN-THESIS-2006-148

IEKP-KA/2005-1

Qualitätskontrolle und Bestrahlungsstudien an CMS Siliziumstreifensensoren

Alexander Furgeri

Zur Erlangung des akademischen Grades eines
DOKTORS DER NATURWISSENSCHAFTEN
der Fakultät für Physik der
Universität Karlsruhe (TH)

genehmigte

DISSERTATION

von

Dipl. Physiker Alexander Furgeri

aus Mannheim

Karlsruhe, 7. Juli 2006

Tag der mündlichen Prüfung: 7.Juli 2006
Referent: Prof. Dr. W. de Boer
Korreferent: Prof. Dr. Th. Müller

IEKP-KA/2005-1

Quality Assurance and Irradiation studies

on CMS silicon strip sensors

Zur Erlangung des akademischen Grades eines
DOKTORS DER NATURWISSENSCHAFTEN
der Fakultät für Physik der
Universität Karlsruhe (TH)

genehmigte

DISSERTATION

von

Dipl. Physiker Alexander Furgeri

aus Mannheim

Karlsruhe, 7. Juli 2006

Tag der mündlichen Prüfung: 7. Juli 2006
Referent: Prof. Dr. W. de Boer
Korreferent: Prof. Dr. Th. Müller

Contents

German Abstract / Deutsche Zusammenfassung v
Introduction xi

1 The Compact Muon Solenoid Detector (CMS) at the Large Hadron Collider (LHC) 1
1.1 Large Hadron Collider at CERN 1
1.2 Physics at LHC 2
1.2.1 Higgs Physics 2
1.2.2 Supersymmetry Physics 4
1.2.3 Heavy Ion Physics 4
1.3 CMS Detector 5
1.4 CMS Silicon Tracker 7
1.4.1 The Silicon Pixel Detector 7
1.4.2 Silicon Strip Tracker Layout 7
1.4.3 Radiation Environment in the CMS Tracker 8

2 Principles of Silicon Detectors 13
2.1 Properties of Silicon 13
2.2 Doping of Silicon 16
2.3 Generation and Recombination of free Charge Carriers 17
2.3.1 Thermal Generation 19
2.3.2 Generation by Electromagnetic Radiation 19
2.3.3 Generation by Charged Particle Radiation 21
2.3.4 Recombination 22
2.4 p-n-Junctions in Silicon 22
2.4.1 Full Depletion Voltage of a p-n-Junction 24
2.4.2 Capacitance Characteristics of a p-n-Junction 24
2.4.3 Current Characteristics of a p-n-Junction 25
2.5 Schottky Contacts in Silicon-Metal Junctions 26
2.6 MOS Structure and Flatband Voltage 26
2.7 Poly Crystalline Silicon Resistors 30
2.8 Design and Working Principles of a Silicon Sensor 30
2.9 Signal Readout on Sensor Level 31
2.10 Noise Sources in a Sensor 32

3 Radiation Damage in Silicon and Silicon Dioxide 35
3.1 Radiation Damage in Silicon and the NIEL-hypothesis 35
3.2 Changes of Macroscopic Properties by Radiation 39

3.3 Current Annealing of Irradiated Silicon . . . 41
3.4 Full Depletion Voltage Annealing of Irradiated Silicon . . . 44

4 The Radiation Hard Silicon Strip Sensors of CMS 49
4.1 Basic Design of CMS Strip Sensors . . . 49
4.2 Thickness and Resistivity . . . 51
4.3 Metal Overhang Design . . . 53
4.4 The Reason for Using $< 100 >$ Orientated Silicon . . . 54
4.5 Signal Readout on Detector Level . . . 55
4.6 Design of CMS Test Structures . . . 56
4.7 Summary of CMS Sensor Parameters . . . 57

5 Sensor Quality Assurance in CMS 59
5.1 Standard Quality Assurance in CMS . . . 59
5.2 Measurements performed in the Quality Test Centers and in the Irradiation Qualification Centers . . . 59
5.3 Measurement Setups in Karlsruhe - The Probe Stations . . . 61
5.3.1 Total Leakage Current Measurement (IV) . . . 63
5.3.2 Total Capacitance Measurement (CV) . . . 63
5.3.3 Single Strip Leakage Current Measurement (ILeak) . . . 64
5.3.4 Bias Resistor Measurement (Rbias) . . . 65
5.3.5 Coupling Capacitance Measurement (CC) . . . 66
5.3.6 Short Measurement (Pinhole) . . . 67
5.3.7 Interstrip Capacitance Measurement (Cint) . . . 67
5.3.8 Interstrip Resistor Measurement (Rint) . . . 68
5.3.9 ILeak with Potential on the AC Pad . . . 69
5.3.10 Summary of Measurement Methods . . . 69
5.4 Setup for Measurements during Irradiation . . . 71
5.5 Initial Quality of Supplied CMS Sensors - QTC Results . . . 73
5.6 Long-term Stability and Chemical Reactions of STM Sensors . . . 75
5.6.1 Visual Inspection of Stains . . . 76
5.6.2 Chemical Analysis of Stains with Electron Microscopes . . . 78
5.6.3 Relationship of Sensor Operation and Stain Formation . . . 83
5.6.4 Conclusions from Stain Analysis . . . 84
5.7 Stress Dependencies of STM Sensors . . . 84
5.7.1 Observation of Kinks in IV and ILeak . . . 84
5.7.2 Summary of Stress Dependence in QTC . . . 86

6 Irradiations for CMS 87
6.1 Scaling of Fluences with NIEL . . . 88
6.2 The Kompakt Zyklotron at Karlsruhe . . . 88
6.2.1 Calculation of Proton Fluence . . . 90
6.2.2 Measurement of Proton Fluence . . . 91
6.3 The Neutron Facility at Louvain-la-Neuve . . . 93
6.4 Standard Irradiation and Annealing Procedure . . . 95
6.5 Results of Full Depletion Voltage Measurements . . . 95
6.5.1 Full Depletion Voltage after Service Life at LHC . . . 95

6.5.2 Annealing of Full Depletion Voltage . . . 96
6.5.3 Full Depletion Voltages of Final STM Pre-series Sensors . . . 98
6.5.4 Parametrization for High Resistivity Sensors from HPK . . . 100
6.5.5 Summary of Full Depletion Voltage Measurements . . . 105
6.6 Full Depletion Voltage Scenarios for CMS Sensors at LHC . . . 106
6.7 Results of Leakage Current Measurements . . . 108
6.7.1 Total Leakage Current after Service Life at LHC . . . 108
6.7.2 Annealing of Total Leakage Current . . . 110
6.7.3 Characterization of Single Strip Leakage Currents . . . 112
6.7.4 Evaluation of Final STM Pre-series Sensors . . . 112
6.7.5 Leakage Current Measurements on STM Sensors during Irradiation . . . 114
6.7.6 Summary of Leakage Current Measurements . . . 120
6.8 Results of Bias Resistor Measurements . . . 121
6.8.1 Bias resistors after Service Life at LHC . . . 121
6.8.2 Annealing of Poly Crystalline Silicon Resistors . . . 123
6.8.3 Bias Resistors after Service Life at SLHC . . . 124
6.8.4 Summary of Bias Resistor Measurements . . . 126
6.9 Results of Coupling Capacitance Measurements . . . 127
6.9.1 Coupling Capacitances after Service Life at LHC . . . 127
6.9.2 Annealing of Coupling Capacitances . . . 128
6.9.3 Summary of Coupling Capacitance Measurements . . . 129
6.10 Results of Interstrip Capacitance and Interstrip Resistance Measurements . . . 129
6.10.1 Interstrip Capacitances after Service Life at LHC . . . 130
6.10.2 Interstrip Capacitance versus Flat Band Voltage . . . 130
6.10.3 Undetectable Parameters - Evaluation of Final STM Pre-series . . . 133
6.10.4 Annealing of Interstrip Capacitance . . . 134
6.10.5 Summary of Interstrip Capacitance Measurements . . . 134
6.11 Results of Signal-to-Noise-Ratio Measurements . . . 135
6.11.1 Signal-to-Noise-Ratio after Service Life at LHC . . . 135
6.11.2 Evaluation of Final STM Pre-series Sensors on Detector module Level . . . 137
6.11.3 Summary of Signal-to-Noise Measurements . . . 140
6.12 Summary of all Measurements after Irradiation . . . 141

Summary **143**

A Relay Schematics of the Karlsruhe Probe Station **145**

B The ISOBOX **147**

C Full Depletion Voltage Scenarios **149**

D Source Code for Full Depletion Voltage Scenario Calculation **155**

List of Figures **161**

List of Tables **165**

Deutsche Zusammenfassung

Zur Erzeugung des Higgs-Bosons oder supersymmetrischer Teilchen braucht man Teilchenbeschleuniger mit sehr hohen Energien. Mit der höheren Energie sinkt aber der Wechselwirkungsquerschnitt der beschleunigten Teilchen und deswegen werden sehr hohe Luminositäten benötigt. Der Large Hadron Collider (LHC) am CERN[1] verwendet als Teilchenbeschleuniger der neuen Generation zwei entgegengerichtete Protonenstrahlen mit einer Energie von je $7\,TeV$. Aufgrund der Magnetfeldanordnung im LHC können die beiden Protonenstrahlen im selben Ring beschleunigt werden und es werden keine Antiprotonen benötigt. Auf diese Weise will man eine sehr hohe Luminosität von $10^{34}\,cm^{-2}s^{-1}$ erreichen. Aufgrund dieser hohen Luminosität steigen aber auch die Strahlenschäden an den Detektoren. Einer der Detektoren am LHC ist das Compact-Muon-Solenoid-Experiment (CMS). Der innerste Teil des CMS-Detektors ist der sogenannte Spurdetektor. Die ca. 10.000.000 Auslesestreifen der ca. 15.000 Detektormodule des Spurdetektors bestehen aus 24328 Siliziumstreifensensoren mit einer Gesamtfläche von 206 m^2. Die innersten Lagen des Spurdetektors werden voraussichtlich in der Laufzeit von zehn Jahren am LHC mit einer äquivalenten Neutronenfluenz von $1,6 \cdot 10^{14}\ n_{1MeV}/cm^2$ belastet.

Durch die Strahlung entstehen Störstellen im Siliziumgitter der Sensoren. Diese sind vorwiegend akzeptorartiger Natur. Bei den n-dotierten Sensoren des CMS-Spurdetektors sinkt deshalb anfangs die effektive Ladungsträgerkonzentration und damit die zu ihr proportionale Depletionsspannung. Wenn die Anzahl der Donatoren und Akzeptoren gleich groß ist, beträgt die Depletionsspannung 0 Volt. Man spricht von der sogenannten "Typinversion". Durch weitere Strahlenschädigung steigt die Anzahl an Akzeptoren und damit die Depletionsspannung wieder an. Viele dieser akzeptorartigen Störstellen heilen bei Temperaturen über $0°C$ wieder aus und wirken dadurch der Änderung der Depletionsspannung teilweise entgegen. Bei längeren Ausheilzeiten erhöht sich die Akzeptorkonzentration wieder und verstärkt die durch Bestrahlung verursachte Veränderung. Für den Leckstrom wird ein Anstieg mit der Störstellenkonzentration durch Bestrahlung beobachtet. Der Strom zeigt bei Temperaturen über $-20°C$, analog zu den Änderungen der Depletionsspannung, ein Absinken mit der Zeit, jedoch im Gegensatz zur Depletionsspannung kein Ansteigen bei langen Ausheilzeiten. Sowohl für den Leckstrom wie auch für die Depletionsspannung gilt, daß die Ausheileffekte mit zunehmender Temperatur beschleunigt werden. Die Ladungssammlungseffizienz der Sensoren wird nach Bestrahlung durch sogenannte Trappingzentren[2] reduziert, die kein Ausheilverhalten zeigen.

Die CMS-Sensoren sind mit einer Durchbruchspannung von über $500\,V$ für hohe Spannungen ausgelegt. Messungen haben gezeigt, daß die meisten Sensoren sogar eine Durchbruchspannung, die deutlich über $1000\,V$ liegt, haben. Dies garantiert, dass auch nach einer Strahlungsbelastung von 10 Jahren am LHC die Sensoren bei der erhöhten Depletionsspannung noch depletiert werden können. Die Sensoren haben niedrige Resistivitäten und damit eine hohe Anzahl an Donatoren, um den Zeit-

[1] **C***ounseil* **E***uropéenn pour la* **R***echerche* **N***ucléaire*

[2] *to trap, dt. einfangen*

punkt der Typinversion auf höhere Fluenzen zu verschieben. Um den Anstieg der Depletionsspannung nach der Typinversion so gering wie möglich zu halten, werden die Sensoren bei in dieser Arbeit bestimmten Temperaturen und Zeiträumen gezielt ausgeheilt. Zur Reduzierung der Oberflächenströme der Sensoren wird Silizium in der $\langle 100 \rangle$-Orientierung verwendet. Die Kontaktstellen zwischen der Siliziumdioxidschicht und dem $\langle 100 \rangle$-Silizium haben weniger ungebundene Valenzelektronen als bei demselben Aufbau mit $\langle 111 \rangle$-Silizium und deswegen geringere Oberflächenströme.

Die Sensoren werden nach Lieferung an das CERN zu vier Qualitätstestzentren (QTC[3]) verschickt, in denen die Funktionalität der Sensoren vor Bestrahlung getestet wird. Danach werden 5% von mitgelieferten Teststrukturen und 1% der Sensoren an den Bestrahlungszentren (IQC[4]) bestrahlt und die Funktionalität anschließend überprüft. Weitere 5% der Teststrukturen werden an die Prozesskontrollzentren (PQC[5]) geschickt um die Qualität verschiedener Prozessparameter zu kontrollieren. Wenn die Qualität der Sensoren von allen Kontrollzentren als gut eingestuft wurden, werden die Sensoren zum Bau von Detektormodulen freigegeben.

Das Institut für Experimentelle Kernphysik an der Universität Karlsruhe (TH), ist als einziges Institut in der CMS-Kollaboration maßgeblich an der Kontrolle der Sensoren sowohl vor als auch nach Bestrahlung beteiligt. Mit dem Kompaktzyklotron am Forschungszentrum in Karlsruhe werden die Sensoren mit niederenergetischen Protonen ($26 MeV$) bestrahlt und auf ihre Strahlenhärte überprüft. Dabei müssen die Flüsse der niederenergetischen Protonen des Kompaktzyklotrons anhand der NIEL[6]-Hypothese skaliert werden, um die beobachteten Schädigungen auf die LHC Bedingungen übertragen zu können. Das Ziel ist die Strahlenbelastung des LHC mit dem Kompaktzyklotron zu simulieren und zu zeigen, dass die Sensoren nach zehn Jahren Betrieb von CMS noch immer funktionsfähig sind. Im Rahmen dieser Qualitätskontrolle wurden die typischen Veränderungen der Sensorparameter bestimmt.

Für die Produktion der Sensoren wurden die Firmen ST-Microelectronics (STM) in Catania (Sizilien) und die Hamamatsu-Photonics-Company (HPK) in Hamamatsu-City (Japan) von der CMS-Kollaboration anerkannt. STM ist als großer Halbleiterelektronikhersteller neu in die Produktion von hochspannungsfesten und vergleichsweise niedrigresistiven Sensoren eingestiegen, während bei HPK ein eigener Geschäftszweig sich auf die Produktion von Halbleitersensoren spezialisiert und schon bei früheren Hochenergiephysikexperimenten Erfahrungen gesammelt hat. Ursprünglich war es vorgesehen, alle Sensoren des inneren Spurdetektorbereichs (20% aller Sensoren) bei HPK zu bestellen und alle Sensoren des äußeren Spurdetektorbereichs bei STM.

Aufgrund vieler unerwarteter Probleme während der Sensorproduktion, hauptsächlich bei STM, sind viele zum Teil aufwendige Detailstudien verschiedener Sensorparameter notwendig geworden.

Einige Sensoren der Firma STM zeigten eine hohe Flachbandspannung vor Bestrahlung. Die Flachbandspannung ist ein Maß für die Ladungsträgerkonzentration im Siliziumdioxid der Sensoren, welches als Dielektrikum dient. Bei zu hohen Flachbandspannungen erwartet man, daß der Vorteil des $< 100 >$-Siliziums nicht zum Tragen kommt. Es konnte durch eine Bestrahlungsstudie gezeigt werden, daß eine maximale Flachbandspannung von $10 V$ eingehalten werden muss, um ein zu großes Ansteigen der Zwischenstreifenkapazität zu verhindern, die den größten Beitrag zum Rauschen der Sensoren liefert.

HPK lieferte einige Sensoren mit zu hohen Resistivitäten, welche außerhalb der im Vertrag mit der CMS-Kollaboration festgelegt Spezifikationen waren. Bei den bis doppelt so hohen Resistivitäten

[3] **Q***uality* **T***est* **C***enter, dt. Qualitätstestzentrum*

[4] **I***rradiation* **Q***ualification test* **C***enter, dt. Bestrahlungsqualitätstestzentrum*

[5] **P***rocess* **Q***ualification test* **C***enter, dt. Prozesskontrollzentrum*

[6] **N***on* **I***onizing* **E***nergy* **L***oss, dt. nicht ionisierender Energieverlust*

erwartet man eine zu hohe Depletionsspannung nach der Laufzeit von 10 Jahren am LHC. Um den engen Produktionszeitplan von CMS einzuhalten, wurden die Parameter für die Änderung der Depletionsspannungen mit einer Neutronenbestrahlung in Louvain-la-Neuve bestimmt. Die Änderung der Depletionsspannung erwies sich dabei um 25% niedriger als erwartet. Aufgrund diese Erkenntnis und verschiedenen Betriebsszenarioberechnungen hinsichtlich der benötigten Depletionsspannungen dieser Sensoren, die ein Teil dieser Arbeit sind, wurde entschieden, einen großen Teil dieser Sensoren im Spurdetektor zu verwenden. Eine DLTS[7]-Messung zeigt, dass ein unbekanntes Donatorniveau in diesen Sensoren für die höhere Strahlenhärte verantwortlich ist. Dieses Donatorniveau zeigt kein Ausheilverhalten.

Im Rahmen einer speziellen Studie an zwei HPK-Sensoren wurde das Ausheilverhalten aller wichtigen Sensorparameter nach Bestrahlung bestimmt. Dabei zeigen die Depletionsspannungen und die Ströme der Sensoren das erwartete Verhalten. Die Kopplungskapazitäten für die AC-Kopplung der Auslesestreifen an die Ausleseelektronik der Sensoren sinken mit Bestrahlung, zeigen aber kein Ausheilverhalten. Die Biaswiderstände aus polykristallinem Silizium, zum Anlegen eines Potentials an die Auslesestreifen, zeigen deutliche Änderungen mit der Bestrahlung und auch durch Ausheilen. Die Zwischenstreifenwiderstände waren in den meisten Fällen auch nach Bestrahlung zu hoch, um bestimmt zu werden, und die Zwischenstreifenkapazitäten zeigten weder eine Änderung mit Bestrahlung noch ein Ausheilverhalten.

Nach plötzlichen Stromdurchbrüchen von STM-Sensoren im Langzeittest wurde eine Fleckenbildung auf den Aluminiumstrukturen dieser Sensoren gefunden. Diese Flecken wachsen mit der Betriebszeit an und zeigen keinen Sättigungseffekt. Materialanalysen, die mit Hilfe des Fraunhofer-Institutes in Berghausen (bei Karlsruhe) und des Instituts für Technische Chemie (Bereich Wasser- und Geotechnologie) am Forschungszentrum in Karlsruhe gemacht wurden, zeigen in den Regionen die Flecken bilden Kaliumverunreinigungen an der Oberfläche. Diese Verunreinigungen kommen mit großer Wahrscheinlichkeit von Kaliumhydroxid, das für die Sensorproduktion verwendet wird. Es ist anhand einer chemischen Elementanalyse nachgewiesen worden, daß das Kalium beim Betrieb der Sensoren die Aluminiumstrukturen der Sensoren oxidieren läßt. Eine hohe relative Luftfeuchte kann diesen Prozess wesentlich beschleunigen.

Ein weiteres Problem der STM-Sensoren ist die Sensibilität auf mechanische Spannungen, die bei den Sensoren von HPK nicht beobachtet wird. Geringe mechanische Belastungen, wie z.B. das Vakuum in den Teststationen zum Fixieren der Sensoren, erzeugen deutliche Durchbrüche einzelner Streifenleckströme. Um das Verhalten dieser Sensoren zu studieren, wurden während einer Neutronenbestrahlung in Louvain-la-Neuve die Streifenleckströme und der Gesamtleckstrom von zwei dieser Sensoren gemessen. Während der Bestrahlung zeigten mehrere Streifen, die unter mechanischer Belastung vor Bestrahlung Durchbrüche aufwiesen, auch ohne mechanische Belastung Durchbrüche. Dabei erweisen sich die Durchbrüche auch als zeitlich instabil, was sich im unkrontollierten Ansteigen und Absinken einzelner Streifenleckströme bemerkbar machte. Die Ursache für diese Durchbrüche konnte letztendlich nicht auf einen einzelnen Effekt zurückgeführt werden, sondern scheint mit den anderen Problemen gekoppelt zu sein. Geringe mechanische Belastungen, die die Sensoren im μm-Bereich verbiegen und dabei die elektrischen Feldkonfigurationen ändern können, sind eine mögliche Erklärung. Ebenso können lokale elektrisch geladene Verunreinigungen des Dielektrikums der Sensoren, die lokale Oberflächenströme erzeugen, dieses Verhalten erklären. Diese Möglichkeit erscheint ebenfalls möglich durch die Beobachtung eines Streifens, dessen Strom auf ein niedrigeres Niveau als erwartet absinkt.

Aufgrund dieser Probleme bei den Sensoren der Firma STM wurde eine neue Probeserie von

[7] **D***eep* **L***evel* **T***ransient* **S***pectroscopy*

Sensoren von STM bestellt, um über den Einsatz der STM-Sensoren in CMS zu entscheiden. Die Untersuchung dieser Sensoren zeigt noch immer in der QTC und in der PQC die bereits erwähnten Probleme der mechanischen Sensibilität und der Fleckenbildung. Durch Bestrahlungstests von acht Sensoren in Karlsruhe traten weitere bisher nicht aufgetauchte Unstimmigkeiten zu Tage. Zwei dieser Sensoren zeigen trotz gleicher Anfangsdepletionsspannung nach Bestrahlung eine große Differenz in der Depletionsspannung. Ein weiteres Problem bezüglich der Depletionsspannung ist der unerwartet hohe Wert, der bei zwei Sensoren nach voller Designfluenz um ca. 100% höher liegt als erwartet. Die Zwischenstreifenkapazitäten zeigen trotz einer geringen Flachbandspannung von unter $2V$ vor Bestrahlung einen deutlich zu hohen Anstieg nach Bestrahlung der nicht parametrisiert werden kann. Desweiteren wurden acht Detektormodule, auf denen weitere Sensoren dieser Probeserie verbaut wurden, bestrahlt. Die Anzahl der im Rauschen auffälliger Streifen dieser Module ändert sich mit Bestrahlung in nicht vorhersagbarer Art und Weise. All diese Probleme treten bei den Sensoren von HPK nicht auf. Daher wurden letztendlich 90% aller Sensoren für den CMS-Spurdetektor bei HPK bestellt.

Diese Arbeit zeigt die Studien hinsichtlich der Strahlungshärte der Sensoren, die im CMS-Spurdetektor zum Einsatz kommen sollen. Kapitel 1, 2 und 3 geben einen Überblick über die Strahlungsbelastungen im CMS-Spurdetektor, die wichtigsten Eigenschaften von Silizium und den Strahlenschäden und ihrer Auswirkungen auf Sensoren. Die Sensoren des CMS-Spurdetektors und ihre Besonderheiten werden ausführlich in Kapitel 4 beschrieben.

Kapitel 5 beschreibt die speziell für Temperaturen unter $0°C$ entwickelte Teststationen, erklärt die verwendeten Meßmethoden und beschreibt die Materialanalyse der Flecken auf den STM-Sensoren. Desweiteren wird der Aufbau einer Teststation beschrieben, mit der es möglich ist Streifen- und Gesamtleckströme von Sensoren während Bestrahlung zu messen. Im Anschluss wird im Abschnitt 5.5 die Qualität der Sensoren vor Bestrahlung verglichen, und anschließend werden die Analysen der Fleckenbildung in Abschnitt 5.6 und der Sensibilität auf mechnische Spannungen in Abschnitt 5.7 diskutiert.

Kapitel 6 erläutert die Bestrahlungsanlagen in Karlsruhe (Protonen) und Louvain-la-Neuve (Neutronen) und die Bestimmung der Fluenzen und ihre Skalierung auf den äquivalenten Neutronenfluß.

Abschnitt 6.5 fasst alle Messergebnisse der Depletionsspannungen, einschließlich der der hochresistiven Sensoren von HPK, zusammen. Unter zur Hilfenahme dieser Ergebnisse wird in Abschnitt 6.6 das optimale Annealingprocedere anhand vielfältiger Szenarioberechnungen berechnet um die Depletionsspannung whärend der Laufzeit am LHC möglichst gering zu halten. Zusätzlich sind Szenarien für die HPK-Sensoren mit hoher Resistivität berechnet worden. Der deutlich höheren Strahlenbelastung für Ring-5 Module als ursprünglich erwartet, kann mit einer geringeren Sensorsdicke von $400\mu m$ anstatt von $500\mu m$ entgegengetreten werden, wie eine eigene Szenarioberechnung hierzu zeigt. In Anhang C befinden sich all diese Szenarioberechnungen für jede Sensorgeometrie.

Darauf folgend wird das Verhalten des Gesamtleckstromes und der Streifenleckströme in Abschnitt 6.7 geschildert. Die Beobachtungen an den Biaswiderständen, an den Kopplungskapazitäten, an den Zwischenstreifenwiderständen und an den Zwischenstreifenkapazitäten werden in den Abschnitten 6.8 bis 6.10 einschließlich der dazugehörigen Studien erklärt. Abschnitt 6.11 zeigt Messergebnisse von Rauschuntersuchungen an Detektormodulen.

Zusammenfassend kann gesagt werden, daß strahlungsharte Sensoren nicht "off-the-shelf"-Dioden sind, sondern Anforderungen an die Resistivität und Durchbruchspannung spezielles "know-how" verlangen. Dieses "know-how" ist bei den Firmen, die sich auf Halbleitersensoren spezialisiert haben, vorhanden. Bei nicht spezialisierten Firmen ist jedoch eine langwierige Lernphase erforderlich, wie die Erfahrung mit STM gezeigt hat. Ein Problem sind vermutlich die elektrisch geladenen Verunreinigungen und die Qualitätsanforderungen, die bei niederohmigen und durchbruchfesten Sensoren

viel strenger sind als bei hochohmigen Schaltungen für die Elektronikchips auf die sich die meisten Halbleiterfirmen spezialisiert haben.

Es wurde gezeigt, daß die Sensoren von HPK alle Spezifikationen bezüglich der Strahlungshärte mehr als zufriedenstellend erfüllen, so daß einem zehnjährigen Betrieb eines $206\,m^2$ "all silicon"-Spurdetektors nichts mehr im Wege steht.

Introduction

The Large Hadron Collider (LHC) at CERN[8] - a next generation particle accelerator - uses two proton beams of opposite directions and with an energy of $7\,TeV$ for each proton. Due to the arrangement of the magnetic field of the LHC, it is possible to accelerate both proton beams in one ring. Therefore no antiprotons are required which enables a high luminosity of $10^{34}\,cm^{-2}s^{-1}$. The high luminosity and the long service life of the detectors at LHC - which is ten years - require radiation hard sensor designs and made the optimization of sensor properties after radiation to a large field of active research.

One of the detectors at the LHC is the Compact Muon Solenoid experiment (CMS). The inner part of the CMS detector - termed tracker - tracks charged particles through the magnetic field of the superconducting solenoid. The approximately 15,000 readout modules of the tracker consist of 24,328 silicon strip sensors with a total number of approximately 10,000,000 readout strips and an active sensor area of approximately 206 m^2. The most inner layer of the tracker will presumably be subjected to an equivalent neutron fluence of $1,6 \cdot 10^{14}\ n_{1MeV}/cm^2$ during the ten year service life of the CMS detector.

The radiation causes damage in the silicon lattice of the sensors which results in changes in full depletion voltage, increase in leakage current and reduction of the charge collection efficiency. The radiation damage and the resulting changes are neither stable with time nor with temperature. The impacts of these effects require a special sensor design in order to obtain a high break through voltage and low noise integrating preamplifiers for the signal readout. The leakage current will be reduced by operation at low temperatures of about $-10°C$. Special annealing periods at higher temperatures are necessary to anneal the changes by radiation damage.

The Institut für Experimentelle Kernphysik at the University of Karlsruhe is involved in the Quality Assurance of the delivered sensors prior to and after irradiation. The irradiation tests are performed at the Kompaktzyklotron at the Forschungszentrum in Karlsruhe. The $26\,MeV$ protons are scaled with the NIEL[9]-hypothesis in order to produce similar radiation damage to the sensor as expected after the service life at LHC.

Due to many unexpected problems that occurred during the production phase of the sensors, numerous detailed studies had to be carried out concerning their chemical stability and their leakage current dependence on mechanical stress. Also numerous irradiation campaigns have been carried out in order to limit the changes of certain parameters like e.g. excessive increases of interstrip capacitances.

The annealing behavior of all important sensor parameters after irradiation has been investigated on two sensors at room temperature and at $60°C$. The parametrization of full depletion voltage of the sensors can be described with the "Hamburg model". A similar model describes the changes of the leakage currents. In addition to the expected changes in full depletion voltage and leakage currents,

[8] **C***entre* **E***uropéenne pour la* **R***echerche* **N***ucléaire*

[9] **N***on* **I***onising* **E***nergy* **L***oss*

significant changes for the coupling capacitances for the AC coupling between the strip implants, and for the bias resistors made of poly crystalline silicon have been observed.

This thesis gives an overview of the radiation environment inside the CMS tracker, the most important properties of silicon, and the radiation damage and its effects on the properties of the CMS sensors, as determined from measurements before and after irradiation with proton and neutron beams. It describes the special probe stations which have been developed to measure structures below $0°C$. Furthermore, a special test station was developed which enables to measure total and single strip leakage currents of sensors during irradiation.

Scenarios of the development of full depletion voltage during the service life of CMS are calculated for each module geometry of the tracker for different annealing periods and annealing temperatures. The outcome of these scenarios is that some of the CMS sensors are near to the limit of operation and the service life of ten years can only be achieved by certain annealing periods at certain annealing temperatures.

Chapter 1

The Compact Muon Solenoid Detector (CMS) at the Large Hadron Collider (LHC)

The Compact Muon Solenoid (CMS) detector is one of the four experimental setups located at the Large Hadron Collider (LHC) at CERN. It is a multipurpose detector and has been designed to observe signatures of new physics such as the Higgs particle or the lightest supersymmetric particles (SUSY). In order to achieve that, the detector has to identify and precisely measure the four momenta of the muons, electrons, photons and charged particles over a large energy range. This chapter will shortly summarize the main characteristics of the accelerator and the physical objectives, and will describe the overall layout of the CMS detector.

1.1 Large Hadron Collider at CERN

The Large Hadron Collider at CERN (Geneva) is a circular accelerator with a circumference of $27\,km$. Within its two beam pipes protons are accelerated to a final energy of $7\,TeV$. This will be the highest particle energy produced with an accelerator. Currently, the highest particle energy is achieved in the Tevatron collider at Fermilab in Chicago with $2\,TeV$ which collides protons and antiprotons. Figure 1.1 shows a schematic of the LHC and the locations where the four experiments are to be carried out. While ATLAS and the CMS experiment are general purpose detectors, the ALICE experiment is specialized on heavy ion physics and the LHCb experiment is specialized on b-physics.

The production cross sections of new particles scale with $1/E^2$. For this reason, a high luminosity L of $10^{34}\,cm^{-2}s^{-1}$ is required. In order to achieve this luminosity, 2835 bunches of 10^{11} protons are accelerated in each of the two particle beams. The superconducting cavities reach a maximum electric field gradient of $5\,MeV/m$. A magnetic field of $8\,T$ is necessary to deflect the path of the protons on their circular track. For protons, the energy loss caused by synchrotron radiation amounts to approximately $0.6\,W/m$. It is not possible to use electrons because their entire energy would be lost by the higher synchrotron radiation. This is due to the fact that the mass of a electron is 2000 times lower than the mass of a proton. The bunch crossing rate will be at $40\,MHz$ and an average of 17 simultaneous interactions (events) is expected for each bunch crossing, which results in approximately 3000 charged and neutral particles in addition to the event of interest [Mue98]. This places high demands on pattern recognition and trigger selectivity. Most of these particles are hadrons with a low transverse momentum p_T and trigger can filter them by a lower energy cut.

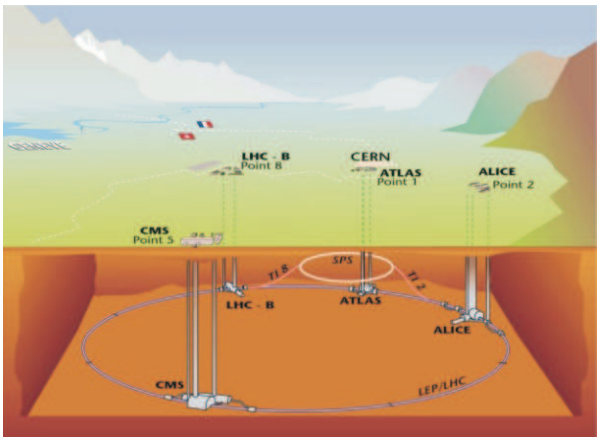

Figure 1.1: **The LHC and experiments at CERN:** *While ATLAS and the CMS experiment are general purpose detectors, the ALICE experiment is specialized on heavy ion physics and the LHCb experiment is specialized on b-physics.*

1.2 Physics at LHC

The standard model is confirmed by all experiments to a high precision. But some open questions point to new physics. One important aspect is the introduction of mass into the standard model via the Higgs mechanism. The running coupling constants of the strong, the weak, and the electromagnetic interactions can unify at a high energy point ($10^{16}\,GeV$) if supersymmetric particles exist. This section gives a short overview about the expected new particles to be observed at LHC.

1.2.1 Higgs Physics

The principle of the Higgs mechanism is spontaneous symmetry breaking of the electroweak scale leading to mass terms which conserve the renormalizability of these theories. In order to prove this theory, a new particle called Higgs boson has to be detected at one of the experiments at LHC.

Figure 1.2 shows possible production mechanisms for the Higgs boson. As the Higgs boson couples to mass, the expected production cross section is highest for the gluon-gluon fusion via quark loops 1.2(a). Due to the large mass of the top quark (around $175\,GeV$) this quark loop is the most probable one. In the standard model one looks forward to a cross section of about $20\,pb$ for that process with a top quark loop and the likely mass of the Higgs boson of $120\,GeV$. The cross sections are much lower for the vector boson fusion in 1.2(b), the associate production with $W^{\pm}$ in 1.2(c) and with $t\bar{t}$ in 1.2(d). Figure 1.3 shows the expected production cross sections in the standard model versus the Higgs bosons mass.

After production the Higgs boson is anticipated to decay on a very short time scale ($< 10^{-20}\,s$). Therefore, the Higgs boson cannot be detected directly but only via its decay products. The decay channels strongly depend on the Higgs mass as shown in Figure 1.4. Due to the fact that the Higgs has not been observed in earlier experiments, a mass below $114\,GeV$ can be excluded. For larger masses of the Higgs boson the following decay channels are important for its discovery:

- For light Higgs bosons ($< 130\,GeV/c^2$) the decays in $b\bar{b}$-quarks or two photons (γ) are important. The huge QCD background at LHC makes the detection of the $b\bar{b}$-channel extremely tedious. The advantage of the rare $\gamma\gamma$-channel is that one gets two clear signatures. This is one reason that the electromagnetic calorimeter of the CMS tracker (explained in Section 1.3) is built for high resolution.

- For intermediate Higgs masses ($130\,GeV/c^2 < m_H < 2m_Z = 2 \cdot 91.2\,GeV/c^2$) the most powerful channels are decays in four leptons $H \rightarrow ZZ^* \rightarrow 4l$ and $H \rightarrow WW^* \rightarrow 2l2\nu$. In order to reduce

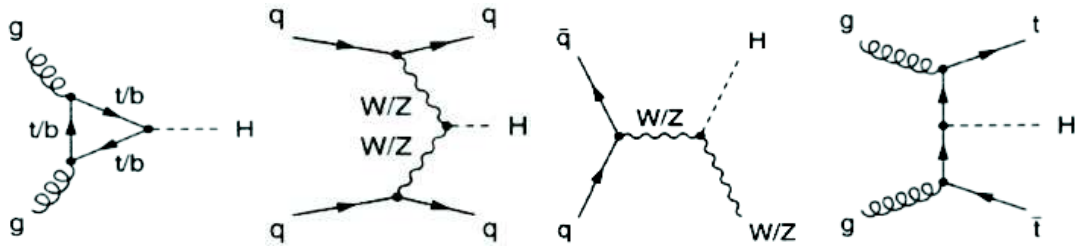

(a) Gluon-Gluon fusion ($\sigma \approx 20\,pb$) (b) Vector boson fusion ($\sigma \approx 2\,pb$) (c) Associate production with W ($\sigma \approx 0.3\,pb$) (d) Associate production with $t\bar{t} - pair$($\sigma \approx 0.05\,pb$)

Figure 1.2: **Higgs production at LHC:** *The most likely channels for the Higgs productions in the standard model are the gluon-gluon fusions in 1.2(a). The vector boson fusion and the associated production mechanisms have much lower cross sections. The cross sections are estimated for an expected Higgs mass of* $120\,GeV$ *and a top mass of* $175\,GeV$.

the background of the first process one has to look for four isolated electrons, apply a mass cut on the lepton pair of the Z mass and require at least $20\,GeV/c^2$ for the other two. The disadvantage of the WW^* channel is that two neutrinos leave the detector without a signature and therefore their energies cannot be reconstructed.

- In case of higher Higgs masses the decay channels into $W^{\pm}$, ZZ^* and $t\bar{t}$ become most important. The advantage of these channels is that $W^{\pm}$ and Z bosons decay partially in heavy leptons which can be used for the trigger. The $t\bar{t}$ channel is problematic since the top quarks decay into four b-jets.

- For a mass of ($2m_Z < m_H < 500\,GeV/c^2$) the Higgs boson will be detected by the golden channel $H \rightarrow ZZ \rightarrow 4l$ with the Z masses on their mass shell. For even higher Higgs masses,

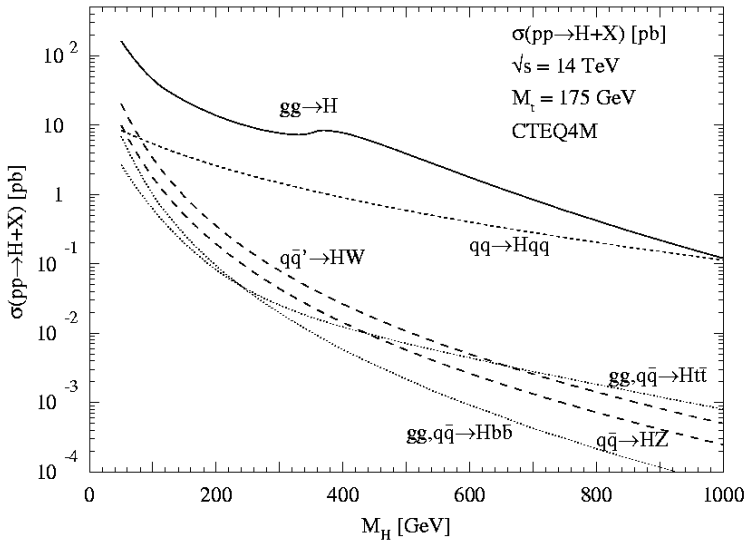

Figure 1.3: **Production cross sections of the Higgs boson in the standard model:** *The most likely channels for the Higgs production are gluon-gluon fusions. All cross sections decrease with increasing mass of the Higgs boson [SSZ00].*

decay modes like $H \rightarrow ZZ \rightarrow l\bar{l}\nu\bar{\nu}$ and $H \rightarrow W^+W^- \rightarrow l\nu jj$ have to be taken into account.

1.2.2 Supersymmetry Physics

Supersymmetry (SUSY) presupposes a symmetry between fermions and bosons. It supplements the standard model with particles of other spin conditions, i.e. for each fermion exists a supersymmetric partner boson and for each standard model boson exists one supersymmetric partner fermion. In addition, there are five Higgs bosons (H, H^+, H^-, A, h) predicted in the minimal supersymmetric standard model (MSSM). Since no SUSY particle has been observed so far, the masses of the super partners are assumed to be high, with masses on the TeV scale or even above. Due to this, this symmetry has to be broken.

Supersymmetry is a necessary condition for the Grand Unifying Theory (GUT) in which the strong, the weak, and the electromagnetic force unify for energies around $10^{16}\,GeV$. SUSY particles can also be a solution for the dark matter problem in the universe. Neutralinos are a hot candidate for forming the Halos of galaxies [SAND04]. Figure 1.5 shows a possible production of SUSY particles at LHC like gauginos, which are expected to be the lightest supersymmetric particles [SAND04]. In $q\bar{q} \rightarrow W^{*\pm} \rightarrow \widetilde{\chi}_1^{\pm}\widetilde{\chi}_2^0 \rightarrow \widetilde{\chi}_1^0 W^{*\pm}\widetilde{\chi}_1^0 Z^{*0} \rightarrow \widetilde{\chi}_1^0 \nu l^{\pm}\widetilde{\chi}_1^0 l^{\pm} l^{\mp}$ the main signature has three leptons and missing energy E_{miss}.

1.2.3 Heavy Ion Physics

In some running periods of the LHC also heavy ions like *Ca* or *Pb* will be accelerated and collided. The collisions produce "little bangs" with temperature 10^5 times higher than the center of our sun and with a density 20 times higher than standard matter. These conditions, called quark-gluon plasma, existed less than $1\,s$ after the Big Bang. CMS is very well suited to study these quark-gluon plasmas through the detection of muons and jets.

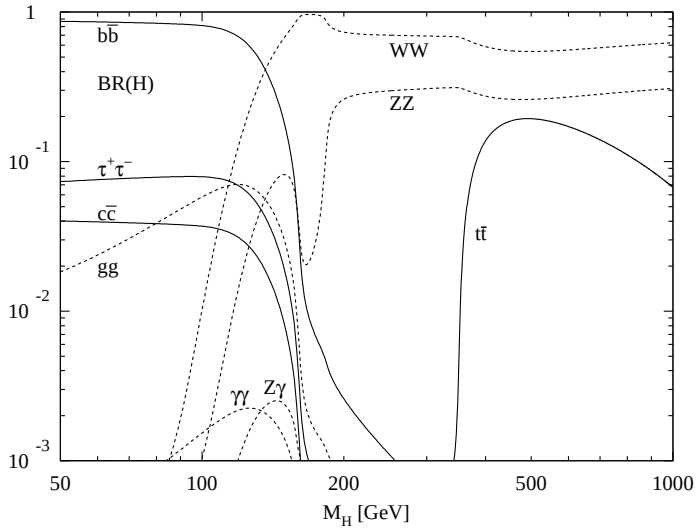

Figure 1.4: **Branching ratio of the Higgs boson versus mass:** *Below a Higgs boson mass of* $130\,GeV/c^2$ *the decays in* $b\bar{b}$ *and* $\gamma\gamma$ *are important. For higher masses decays to* $W^{\pm}$ *and* $t\bar{t}$ *are dominating [DKS97].*

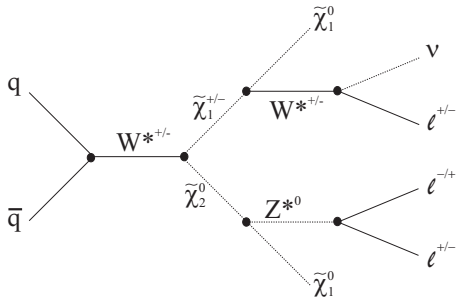

Figure 1.5: **Production of SUSY particles at LHC:** *Two produced gauginos have a signature with three leptons and missing energy E_{miss} [Ves04].*

1.3 CMS Detector

Figure 1.6 presents the CMS detector and its subdetectors. The subdetectors from CMS are from the interaction point to outside [CTDRA00]:

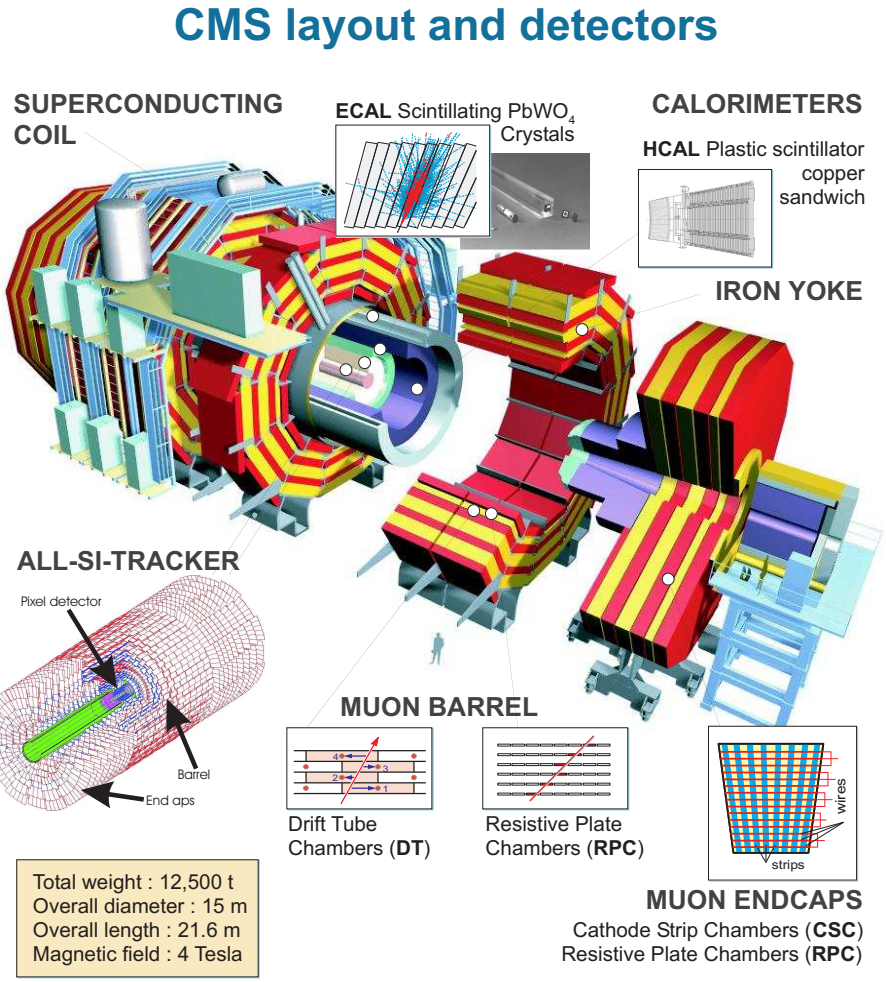

Figure 1.6: **The CMS detector:** *The CMS detector consists of a silicon tracker, a electromagnetic, a hadronic calorimeter, and muon barrels inserted in the iron yoke of the magnet. All subdetectors are subdivided in barrels and endcaps.*

- a silicon tracker consisting of a pixel detector surrounded by a silicon strip tracker
- an electromagnetic calorimeter (ECAL) built of scintillating $PbWO_4$ crystals
- a hadronic calorimeter (HCAL) built of sandwiches of copper and plastic scintillator
- a superconducting coil providing a magnetic field of $4\,T$
- an iron yoke for the return flux of the magnetic field
- muon chambers inserted in the iron yoke

The coverage for all subdetectors is given by the rapidity

$$\eta = -\ln\left(\tan\left(\frac{\theta}{2}\right)\right) \tag{1.1}$$

with the angle θ to the beam line. The advantage of the rapidity is the Lorentz transformation invariance under addition.

The superconducting coil (cooled with liquid He) for the solenoid magnetic field is the largest of its kind with a length of $13\,m$ and a diameter of $5.9\,m$. An energy of $2.7\,GJ$ is stored in the magnetic field.

The return iron yoke is instrumented with the muon chambers. These are made of three different subdetectors to assure redundancy and robustness. The barrel region contains drift tubes, whereas in the endcaps cathode strip chambers are used. In both the barrel and the endcaps resistive plate chambers are installed for an independent triggering. The stand alone momentum resolution of the muon system is $8-15\,\%$ for energies around $10\,GeV$ and $20-40\,\%$ for the region around $1TeV$. Including the information of the silicon tracker a resolution of $1-1.5\,\%$ can be achieved.

The hadronic calorimeter consists of sandwiches of copper layers and plastic scintillators. The light is channelled by fibres used for wave length shifting embedded in the scintillator plates. For the forward region ($\eta < 5.0$) steel/quarz fibre calorimeters are used. The Cherenkov light emitted in the fibres is detected by photomultipliers.

The ECAL is a high precision calorimeter built of $PbWO_4$ crystals, 61.200 in the barrel and 16.000 in the endcaps. It enables the investigations of the $H \rightarrow \gamma\gamma$ channel for low Higgs bosons masses. Each crystal in the barrel region contains two silicon avalanche diodes to detect the scintillation light. For the endcap crystals vacuum photo triodes are used. The design energy resolution is parameterized by

$$\left(\frac{\sigma_E}{E}\right)^2 = \left(\frac{a}{\sqrt{E}}\right)^2 \oplus \left(\frac{b}{E}\right)^2 \oplus c \tag{1.2}$$

The contribution of the stochastic term a which considers fluctuation in the shower containment is $2.7\,\%$ for the barrel and $5.0\,\%$ for the endcaps. Term b considers the noise contribution from the readout electronics and pileup energy. It is $150-210\,MeV$ for the barrel and $205-245\,MeV$ for the endcaps as function of Luminosity L. $c = 0.55\,\%$ is a constant and includes contributions from inter calibration errors, crystal uniformities and shower leakage [Hof97]. A pre shower detector is used to distinguish between single photons and π^0 decays into two photons. It is installed between the ECAL and the strip tracker and consists of lead converters and silicon strip sensors with a constant pitch of $1.9\,mm$. A resolution of $300\,\mu m$ is possible at $50\,GeV$ with the charge-weighted-average. In total the expected efficiency for single photon reconstruction is $74.5\,\%$.

1.4 CMS Silicon Tracker

For the CMS experiment the tracks from muons detected in the muon chambers are connected with the tracks inside the silicon tracker. For this and manyfold other reasons (e.g. vertex reconstruction) a tracker with a high resolution is required. The silicon strip tracker is described in more detail in this section.

1.4.1 The Silicon Pixel Detector

The innermost part of the tracker with a distance down to $4.3\,cm$ to the interaction point is a three layer pixel detector. It contains $45,000,000$ pixels with an area of $100\,\mu m \times 150\,\mu m$ each. The expected primary vertex resolution is $50\,\mu m$ [KS01]. Around the pixel detector lays the silicon strip tracker (SST).

1.4.2 Silicon Strip Tracker Layout

The SST has a diameter of $2.4\,m$ and a length of $5.4\,m$. It contains 24328 silicon sensors with a total area of $206\,m^2$. The operation temperature is below $-10°C$. The tracker is structured in three parts, the barrel and the two endcaps. The individual detector modules are assembled on support structures. For the outer part of the barrel the structures are named rod, and for the endcap they are designated petal. The inner part of the barrel is build up of shells.

Depending on the strip numbers of the sensors the detector modules have 4 or 6 radiation hard readout chips (APV25 with 128 channels). The figures 1.7(a) and 1.8(a) and 1.9 show pictures of the support structures and the figures 1.7(b) and 1.8(b) show detector modules with the necessary rectangular or wedge shaped design for the barrel and the endcap detector modules. The tracker is

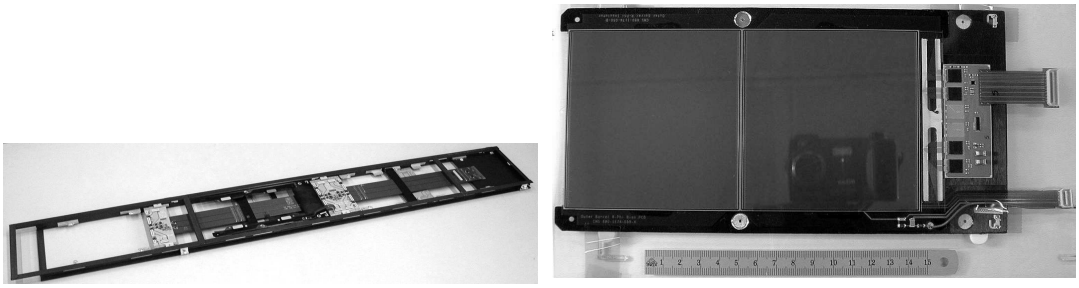

(a) Picture of a CMS rod (b) Picture of a CMS outer barrel detector module

Figure 1.7: **Pictures of a CMS rod and a CMS barrel detector module**

separated in an outer and an inner part. The inner part has detector modules with one sensor of $300\,\mu m$ thickness and the outer part with two sensors of $500\,\mu m$ thickness. The reasons and design features are explained in Chapter 4 after an overview of important silicon properties. Figure 1.10 gives the schematics of the silicon strip tracker. The barrel has four inner layers within a radial distance from $22\,cm$ to $50\,cm$ and six outer barrel layers within $60\,cm$ to $110\,cm$. The endcaps consists of nine discs with up to seven rings of detector modules on them. The tracker outer barrel (TOB) has two different sensor geometries, OB1 and OB2. The tracker endcap (TEC) has sensor geometries W1TEC, W2, W3, W4, W5A+W5B, W6A+W6B and W7A+W7B. The tracker inner barrel (TIB) has the geometries IB1 and IB2 and the tracker inner disc (TID) W1TID, W2 and W3. All sensors are made of silicon

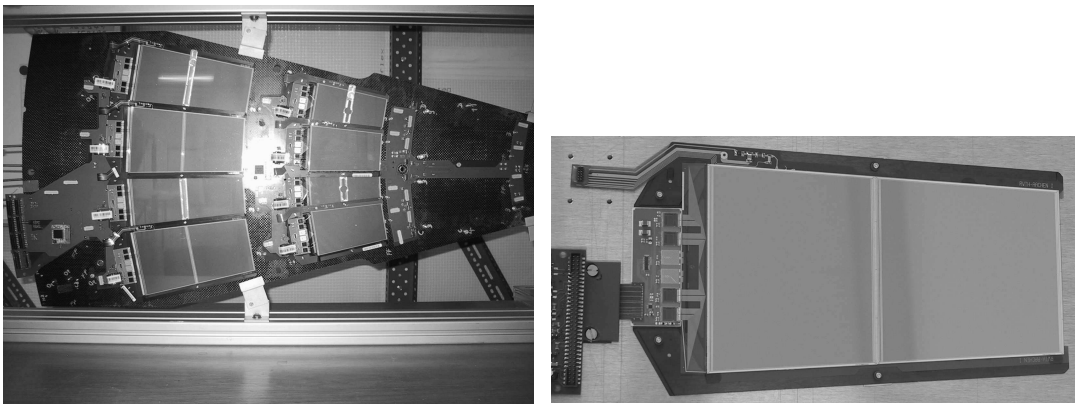

(a) Picture of a CMS endcap petal

(b) Picture of a CMS petal detector module

Figure 1.8: **Pictures of a CMS petal and a CMS wedge shaped detector module**

Figure 1.9: **Picture of a CMS inner barrel shell**

due to the comparatively cheap and in large scale available technology. Table 1.1 and 1.2 give the dimensions of the different sensor geometries and their number in the tracker. The detector modules with a radial distance from 22 cm to 44 cm and 60 cm to 75 cm contain two detector modules back to back with a contortion of 100 $mrad$ to each other. This gives a two dimensional information of the particle transversion.

1.4.3 Radiation Environment in the CMS Tracker

The CMS tracker is operated in an harsh irradiation environment which is not constant for all irradiation periods. Per year three irradiation runs of 60 $days$ are performed. In the first three years a low luminosity phase is planed followed by the high luminosity phase of $L = 10^{34}\,cm^{-2}s^{-1}$. Table 1.3

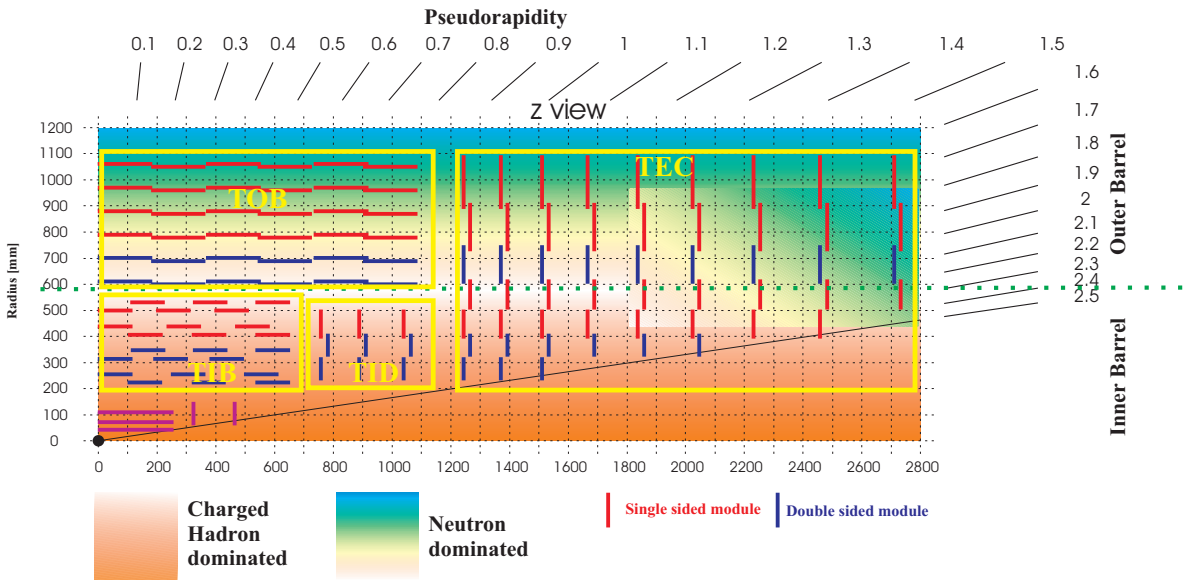

Figure 1.10: **The schematics of the CMS tracker:** *The tracker has the substructures tracker outer barrel (TOB), tracker inner barrel (TIB), tracker inner disc (TID) and the tracker endcap (TEC). The detector modules with a distance from* 22 *cm to* 44 *cm and* 60 *cm to* 75 *cm contain two detector modules back to back with a contortion of* 100 *mrad to each other.*

shows the luminosity and the fluence distribution with time. The expected fluences to be endured by the inner barrel part of the tracker are shown in Figure 1.11. In Chapter 2 the irradiation effects on silicon irradiated will be discussed. For the quality assurance done by the CMS collaboration it is important to irradiate sensors with the fluences given by Table 1.4 and to check their functionality during the operation at LHC. In Karlsruhe (Germany) and in Louvain-la-Neuve (Belgium) sensors are irradiated with protons and neutrons, respectively. The irradiation results are explained in detail

Type	L1 in *mm*	L2 in *mm*	Height in *mm*	Volume in cm^3	Pitch in μm	Thickness in μm	Strips	Multiplicity of sensors
W1TEC	63.1	85.8	85.2	2.03	81-112	320	768	288
W1TID	62.1	91.7	110.9	2.73	80.5-119	320	768	288
W2	86.6	110.1	88.2	2.78	113-143	320	768	864
W3	63.3	81.1	110.7	2.55	123-158	320	512	880
W4	58.1	71.3	115.2	2.39	113-139	320	512	1008
W5A	96.5	109.5	81.2	4.19	126-142	500	768	1440
W5B	110.0	120.1	63.2	3.64	143-156	500	768	1440
W6A	83.6	94.6	96.1	4.28	163-185	500	512	1008
W6B	94.5	104.7	84.9	4.23	185-205	500	512	1008
W7A	71.5	80.1	106.9	4.05	140-156	500	512	1440
W7B	80.4	88.0	94.9	4.00	156-172	500	512	1440

Table 1.1: **Specifications of wedge shaped CMS sensors:** W1,W2 and W5 will be assembled in double sided detector modules, the other geometries in single sided detector modules. All distances are values for the sensors' active area.

Type	Length in *mm*	Height in *mm*	Volume in cm^3	Pitch in μm	Thickness in μm	Strips	Multiplicity of sensors
IB1	61.5	116.9	2.03	80	320	768	1536
IB2	61.5	116.9	2.03	120	320	512	1188
OB1	93.9	91.6	4.30	122	500	768	3360
OB2	93.9	91.6	4.30	183	500	512	7056

Table 1.2: **Specifications of rectangular CMS sensors:** All distances are values of the sensors active area.

Year	% of maximum L	Part of total fluence per year
1	10%	1.23%
2	33%	4.07%
3	66%	8.27%
$4-10$	100%	12.34%

Table 1.3: **LHC luminosity and CMS fluence distribution with time in percent.**

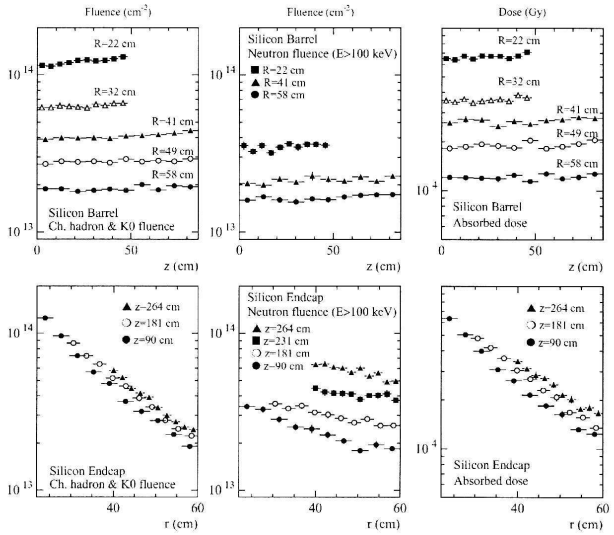

Figure 1.11: **Fluences and doses in the CMS tracker:** *The maximum expected fluence for inner barrel sensors is* $1.6 \cdot 10^{14} n_{1MeV}/cm^2$ *and the maximum expected dose is* $67\,kGy$ *[Pro98].*

in Chapter 6. Table 1.4 shows an estimation of the fluence for the different sensor geometries in the inner and outer barrel. The uncertainties given to the fluences in this table are 30 % for charged particles and 100 % for the neutrons. The values of the fluences are taken from a graph in [Mig01]. An additional factor comes from the expected service life of ten years at the LHC. The integrated goal luminosity is reached after eight years and one of three irradiation intervals. Therefore, the design luminosity which is performed for $500\,fb^{-1}$ has to be multiplied with 1.26. The design parameters of the sensors are discussed in more detail in Chapter 4. Recent simulations indicate a higher fluence (shown in Table 1.4) for ring 5 sensors of disc nine (the outer endcap disc in the tracker). A possible new design of these sensors is discussed in appendix C.

Sensor type	Charged hadron fluence in $10^{14}\,\frac{n_{1MeV}}{cm^2}$	Neutron fluence in $10^{14}\,\frac{n_{1MeV}}{cm^2}$
W1TID	1.02	0.35
W1TEC	1.02	0.35
W2	0.65	0.64
W3	$0.4-0.22$	0.6
W4	$0.3-0.2$	$0.32-0.6$
W5A, W5B disc 7	0.2	0.3
W5A, W5B disc 9	0.4	0.4
W6A, W6B	0.15	0.3
W7A, W7B	0.07	0.3
IB1 inner layer	1.26	0.33
IB1 outer layer	0.67	0.32
IB2	0.4	0.3
OB1	0.1	0.2
OB2	0.05	0.2

Table 1.4: **Maximum fluences expected in the CMS tracker:** *The highest fluences for all sensor geometries achieved at the goal luminosity of* $500\,fb^{-1}$ *are shown. In order to compare the different fluences, the fluences are scaled to neutron equivalent fluences (explained in detail in Section 3.1). The middle column is the sum of the charged hadrons energy spectrum. The right column is the sum of the neutrons spectrum with energies above* $100\,keV$ *which are backscattered from the Electromagnetic Calorimeter. All fluences are taken from a graph in [Mig01]. The uncertainties are* $30\,\%$ *for charged hadrons and* $100\,\%$ *for neutrons. For the design fluence of the sensors these uncertainties have to be added to the fluences given in this table. The fluences for IB1 sensors in the second layer are much smaller in comparison to the sensors in the first layer (important for Section 6.5.4). The fluences for disc 7 and 9 are shown for W5A and W5B sensors. Ring 7 is within the origin outer barrel design fluence of* $0.5 \cdot 10^{14}\,cm^{-2}$*, whereas Ring 9 will be much higher irradiated (in detail discussed in appendix C).*

Chapter 2

Principles of Silicon Detectors

Particle detectors in high energy experiments should provide a high particle track resolution to cope with the enormous particle flux of multi-jet and other events. Because one would like to be as sensitive as possible to the electromagnetic decay channels of the Higgs boson (see Chapter 1) in the CMS experiment, the whole tracker has to be designed and built as light as possible to keep the radiation length low and due to this to minimize the number of conversions. The use of a detector type with excellent spatial resolution such as semiconductor strip or pixel detectors makes an easy and compact tracker design possible. Moreover, the well known technique together with a reasonable financial effort makes the choice of an all silicon strip tracker attractive for the CMS collaboration. Properties and principles of semiconductor sensors important for this work are explained in this chapter.

2.1 Properties of Silicon

Silicon is an element of the fourth main group of the periodic system of elements. It has therefore four covalently bound electrons and forms a lattice in diamond form. The form of a silicon elementary cell is shown in Figure 2.1 [IL95]. With less distance in the lattice the silicon atoms form energy band structures as shown in Figure 2.2. The highest energy band filled with electrons is called valence band with its upper energy border termed E_V. The lowest non filled energy band is called conduction band with its lower energy border termed E_C. The non occupied region between the valence band and the conduction band is named band gap. In order to excite electrons from the valence band to the conduction band the energy E_g is necessary since there are no allowed states for occupation within the band gap.

The band model for metals, semiconductors and insulators is shown in Figure 2.3. For metals the highest filled electron states are inside an energy band and do not fill the whole conduction band. Therefore the excitation of electrons to higher energy level requires only very small energies. If the valence band is completely filled with electrons and the next allowed electron state is above the band gap the material is either a semiconductor or an insulator. The distinction is the magnitude of E_g. The limit values to separate semiconductors from insulators are varying in literature. For intrinsic silicon E_g is $1.12\,eV$. The main properties of silicon are summarized in Table 2.1 [Lut99].

At finite temperatures the covalently bound electrons can transit due to phonons from the valence band into the conduction band. The phonons are quasi-particles with wave vector $\overrightarrow{k}$ describing lattice

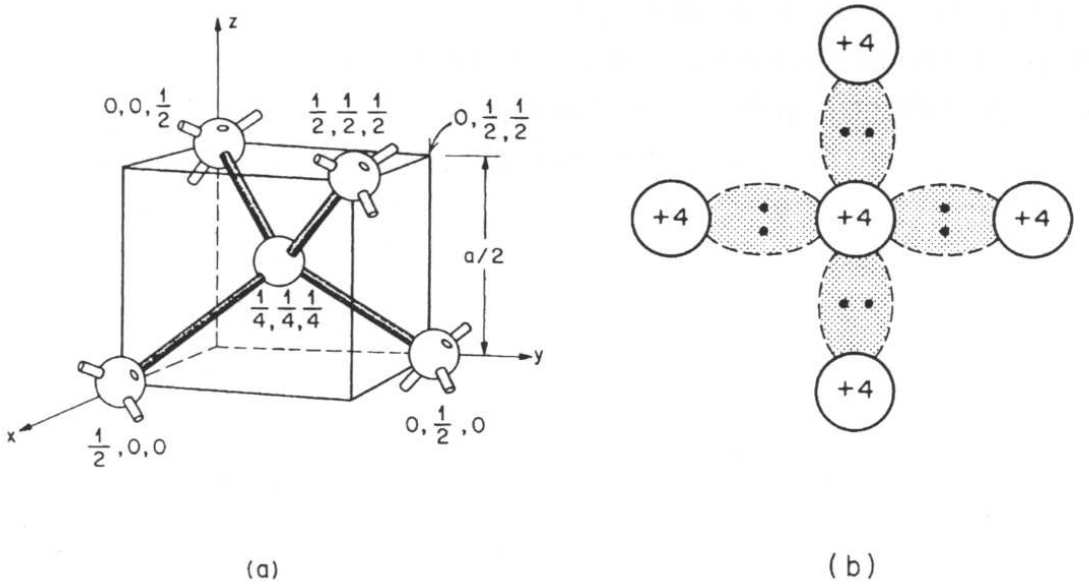

Figure 2.1: **The element silicon:** *Silicon atoms have four covalent electrons and form a lattice with diamond configuration [IL95].*

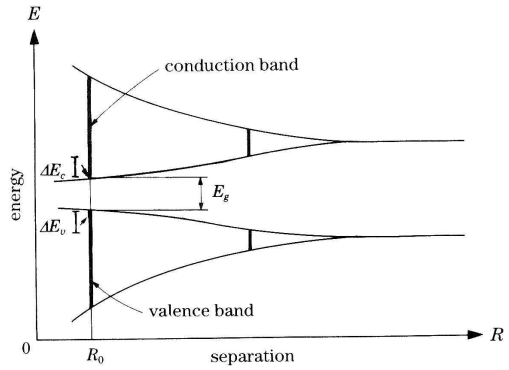

Figure 2.2: **Energy bands in silicon lattice:** *The covalently bound neighbors in the silicon lattice form below a certain separation of the silicon atoms energy bands of allowed electron states [SH95]. The equilibrium separation distance in the silicon lattice is* 5.43Å *[IL95].*

vibrations. The probability for the transition process is given by the Fermi-Dirac-statistics:

$$F(E) = \frac{1}{1+\exp\left(\frac{E-E_F}{k_BT}\right)} \tag{2.1}$$

with the Fermi energy level E_F at which the occupation probability is one half, the Boltzmann constant k_B and the temperature T. For $|E-E_F| > 3k_BT$ the Fermi-Dirac-statistics for electron F_e and holes F_h can be approximated by:

$$F_e(E) \approx \exp\left(-\frac{E-E_F}{k_BT}\right), \quad F_h(E) = 1-F_e(E) \approx \exp\left(-\frac{E_F-E}{k_BT}\right) \tag{2.2}$$

with $F_e + F_h = 1$. The state density for electrons near the bottom of the conduction band is given by:

$$N(E) = \frac{(2m_D^*)^{3/2}}{2\pi^2\hbar^3\sqrt{E-E_C}} \tag{2.3}$$

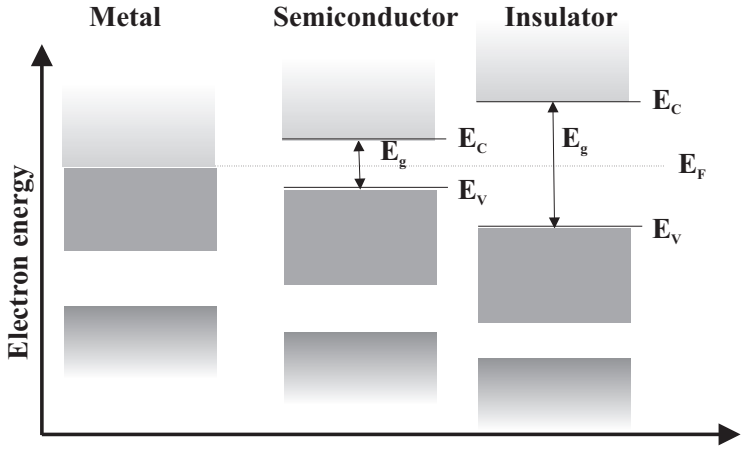

Figure 2.3: **Simplified band model of metal, semiconductor and insulator:** *In metals the Fermi Level is in the conduction band. In semiconductors and insulators the Fermi Level lies between the conduction and the valence band. The difference between semiconductors and insulators is only given by the size of the band gap energy E_g which varies with literature.*

Property	Value
Atomic number	14
Atomic weight $[u]$	28.09
Density $[g/cm^3]$	2.329
Relative permittivity	11.9
Lattice structure	Diamond
lattice spacing $[\dot{A}]$	5.431
Band gap E_g $[eV]$	1.12
Intrinsic charge carrier concentration $[cm^{-3}]$	$1.02 \cdot 10^{10}$
Energy for creation of e-h pair $[eV]$	3.63
Mobility $[cm^2/Vs]$	
Electrons	1450
Holes	450
Intrinsic resistivity $[k\Omega cm]$	2,3

Table 2.1: **Properties of silicon [Lut99]**

with the effective electron mass $m_D^* = 0.32m_e$ which depends on the orientation of the silicon lattice [Kit02]. The free electrons density n is a convolution of the state density $N(E)$ and the corresponding occupation probability $F_e(E)$:

$$n = \int_{E_C}^{\infty} N(E) \cdot F(E) dE = \frac{2}{\hbar^3} (2\pi m_D^* k_B T)^{3/2} \exp\left(-\frac{E_C - E}{k_B T}\right) = N_C \exp\left(-\frac{E_C - E_F}{k_B T}\right) \tag{2.4}$$

Respectively for free holes the density is given by:

$$p = N_V \exp\left(-\frac{E_F - E_V}{k_B T}\right) \tag{2.5}$$

Figure 2.5(a) shows the state density $N(E)$, the Fermi-Dirac-Statistic $F(E)$ and the free electron den-

sity n and free hole density p for the intrinsic case, where the intrinsic free charge density is given by:

$$n_i = \sqrt{N_C N_V} \exp\left(-\frac{E_g}{2k_B T}\right) \tag{2.6}$$

resulting in $n_i = n = p \approx 1.45 \cdot 10^{10}/cm^3$ at $300\,K$. The Fermi energy level of intrinsic silicon can be calculated to:

$$E_i = \frac{E_C + E_V}{2} + \frac{3k_B T}{4} \ln\left(\frac{m_p}{m_n}\right) \tag{2.7}$$

2.2 Doping of Silicon

For room temperature, where $k_B T = 26\,meV$, the density of free charges in intrinsic silicon is quite low. Intrinsic silicon is doped with low amounts of foreign atoms to increase the charge carrier density, e.g. for a higher free electron density phosphorus can be inserted in the silicon lattice. The fifth covalent electron of the phosphorous has no possibility to bond to neighbored atoms. An energy of $E_D = 0.44\,eV$ is necessary to excite it into the conduction band of the silicon lattice. Phosphorus and other impurity atoms exciting electrons are therefore named donors with their concentration N_D and the silicon is termed n-type. A higher free hole density can be obtained by impurity atoms with three covalent bound electrons, e.g. boron. Where the three covalently electrons are bond to the neighbored silicon atoms, a further electron can be captured resulting in a free hole in the silicon lattice valence band. For this process an energy of $E_A = 0.45\,eV$ is necessary. The name for the electron capturing foreign atom is acceptor and the silicon is named p-type. The acceptor concentration is N_A. Figure 2.4 shows the crystal lattices for n- and p-doped silicon and the energy levels of donors and acceptors . With Equation 2.4 and the approximation $n = N_D$ for n-type silicon and $p = N_A$ for p-type material the Fermi Levels read:

$$E_C - E_F = k_B T \ln\left(\frac{N_C}{N_D}\right) \qquad E_F - E_C = k_B T \ln\left(\frac{N_V}{N_A}\right) \tag{2.8}$$

The Fermi Level defines the free electron and hole densities:

$$n = n_i \exp\left(-\frac{E_F - E_i}{k_B T}\right) \qquad p = n_i \exp\left(\frac{E_i - E_F}{k_B T}\right) \tag{2.9}$$

The mass-action law from the definitions above is given by:

$$n \cdot p = n_i^2 \tag{2.10}$$

An important fact of this law is that if one type of charge carriers is increased the other one is reduced. Figure 2.5(b),(c) show the state density $N(E)$, the Fermi-Dirac-Statistic $F(E)$ and the density of free electrons n and free holes p for n-type and p-type silicon. For low temperatures the donors and acceptors are partially ionized following the Fermi-Dirac statistic:

$$N_D^+ = N_D \left[1 - \frac{1}{1 + \frac{1}{2}\exp\left(\frac{E_D - E_F}{k_B T}\right)}\right] \qquad N_A^+ = N_A \frac{1}{1 + 4\exp\left(\frac{E_A - E_F}{k_B T}\right)} \tag{2.11}$$

The Fermi energy can be calculated by using the neutrality condition $n = N_D^+ + p$ leading to

$$n \approx \sqrt{\frac{N_D N_C}{2}} \exp\left(\frac{E_C - E_D}{2k_B T}\right) \tag{2.12}$$

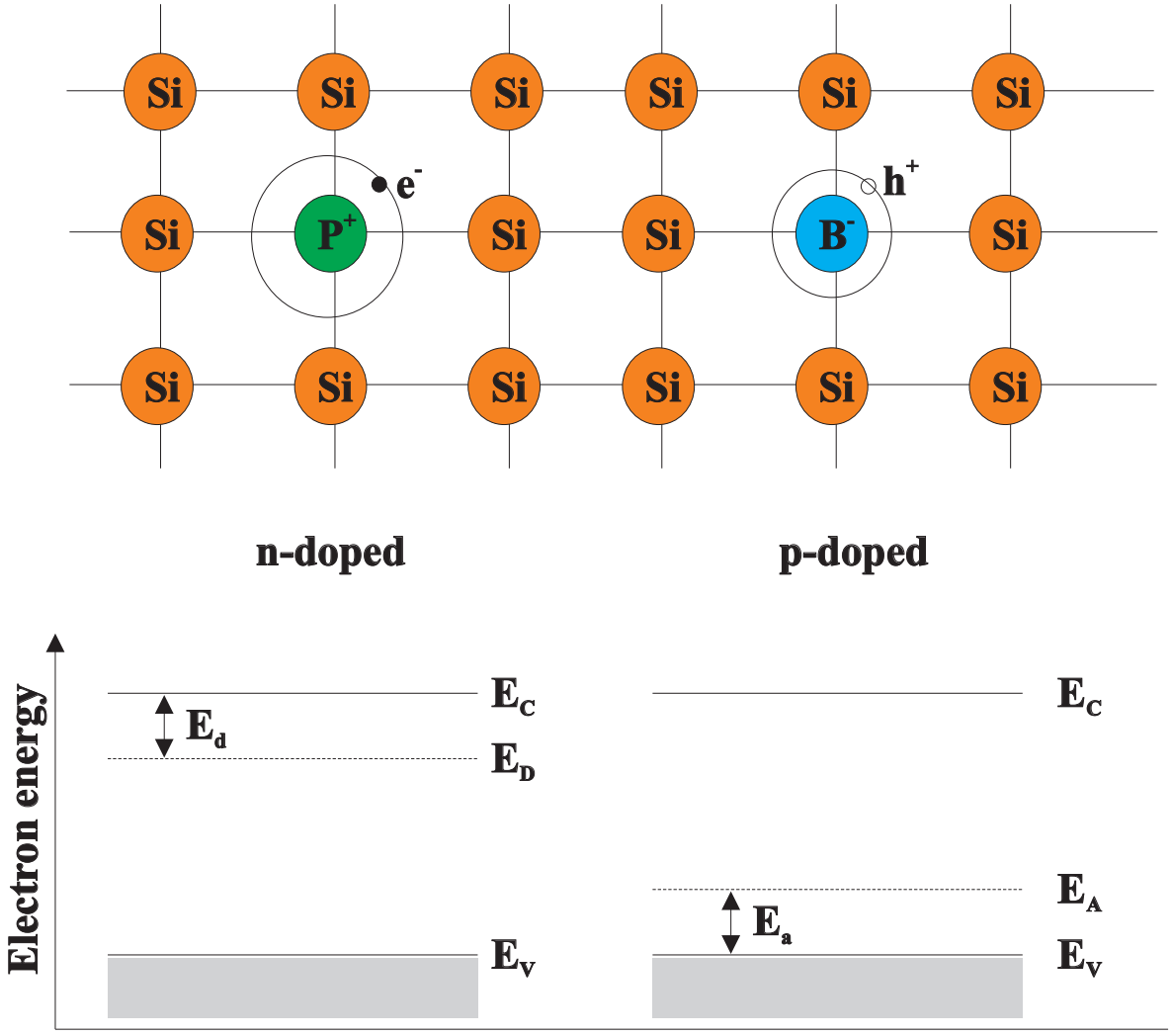

Figure 2.4: **Energy levels of p- and n-doped silicon:** *For n-doping of silicon in most cases phosphorous is used and for p-doping boron, respectively. The fifth covalent electron of the phosphorous atom is an additional negative free charge. Boron has instead only three covalent electrons. The missing covalent electron to the corresponding silicon neighbor is a trap for a negative charge. The missing negative charge acts as a free positive charge in the silicon lattice. The concentrations of the doping atoms is in the order of impurities in the silicon crystal.*

with $E_d = E_C - E_D$ and $N_D \gg \frac{1}{2} N_C \exp\left(\frac{E_d}{k_B T}\right) \gg N_A$. For the temperature range from $100\,K$ to $500\,K$ all donors and acceptors are ionized.

2.3 Generation and Recombination of free Charge Carriers

In Section 2.1 and 2.2 the densities for free charge carriers were calculated for thermal equilibrium. The ionization of shallow dopants is easy at room temperature and leads to a constantly high number of free charge carriers. In reality the silicon lattice has imperfections and there are also foreign atoms in the silicon lattice. These imperfections and foreign atoms have similar to the wanted doping atoms

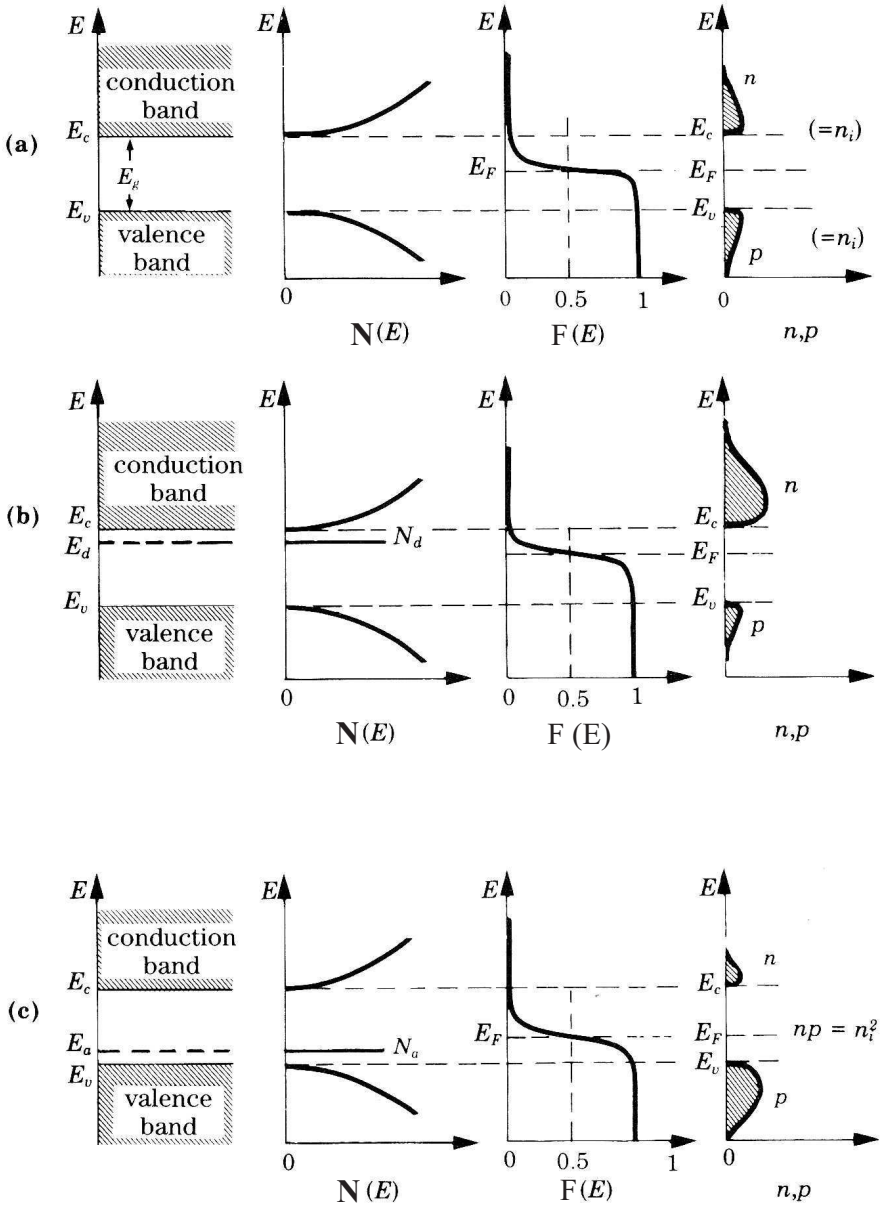

Figure 2.5: **Fermi Levels, state density, and free charge density in silicon:** *The density of states $N(E)$ is the same for intrinsic (a) and doped silicon (b,c), whereas the Fermi Levels for n-type (b) and p-type silicon (c) and the final free charge densities change [SH95].*

excitation energy levels in the band gap of the silicon lattice. Most levels are near the middle of the band gap, which increase the generation and recombination probability of electrons and holes significantly, because the level occupancy probability follows the Boltzman statistic. In the following the main generation processes by thermal generation, interaction of electromagnetic radiation and charged particles with matter are explained followed by the recombination processes.

2.3.1 Thermal Generation

If all free charge carriers are removed (e.g. with an applied electric field), the system tries to come back to thermal equilibrium via thermal generation. The time to reach thermal equilibrium is given by:

$$\tau_g = \frac{n_i}{G_{th}} = \frac{1}{N_t}\left[\frac{1}{v_{th,p}\sigma_p}\exp\left(\frac{E_t - E_i}{k_B T}\right) + \frac{1}{v_{th,n}\sigma_n}\exp\left(\frac{E_i - E_t}{k_B T}\right)\right] \tag{2.13}$$

with the generation rate G_{th}, the intermediate trapping state energy level E_t with its cross sections $\sigma_{n(p)}$, the thermal velocities $v_{th,n(p)}$ for electrons (holes) and the trapping center density N_t. With $\sigma_n v_{th,n} = \sigma_p v_{th,p}$ Equation 2.13 reduces to:

$$\tau_g = 2\cosh\left(\frac{E_t - E_i}{k_B T}\right) \tag{2.14}$$

The magnitude of the relaxation time τ_g is in the order of $\sim 1\,ms$. In depleted silicon, i.e. all free charge carriers flow due to an applied electric field out of the silicon, the current density for trap assisted thermal generation is given by:

$$j = \sum_{traps} qG_{th} \approx \frac{n_i}{\tau_g} = \frac{N_t \sigma v_{th} n_i}{2\cosh\left(\frac{E_t - E_i}{k_B T}\right)} \sim T^2 \frac{\exp\left(\frac{E_g}{2k_B T}\right)}{\cosh\left(\frac{E_t - E_i}{k_B T}\right)} \tag{2.15}$$

with the charge carriers charge q. The temperature results from $v_{th,n(p)} \sim \sqrt{T}$ and $n_i \sim T^{3/2}\exp\left(-\frac{E_g}{2k_B T}\right)$ given in Equation 2.6, whereas N_t and $\sigma_{n(p)}$ are constant.

2.3.2 Generation by Electromagnetic Radiation

Photons can interact with electrons in the silicon lattice and excite them to higher energy states if the excited state is an allowed one. Figure 2.6 shows the band structure of silicon in the first Brillouin zone [Kit02]. For silicon the minimum of the conduction band is not located directly above the maximum of the valence band at $\overrightarrow{k} = \overrightarrow{0}$. Material with such band structures have so named indirect band gaps. In silicon an energy of $3.6\,eV$ is necessary for a direct production of an electron-hole pair.

The excess energy is subsequently transferred to the silicon lattice by phonons until the remaining electron energy is at the lower conduction band border and for holes the upper border of the valence band, respectively. The momentum transfer $q = p_{inital} - p_{final}$ can be neglected for the photon in case of direct transition since $q \approx 4 \cdot 10^4\,cm^{-1} \ll k_{min}$ and therefore the absorption coefficient results in:

$$\alpha \sim (h\nu - E_g(k=0))^{1/2} \tag{2.16}$$

For electrons below $3.6\,eV$ only an indirect second order process transition with phonon absorption and emission is possible. The electron is first excited to a free intermediate state of the energy $E^* \geq E_g(|\overrightarrow{k}| = 0)$ with momentum transfer $q \approx 0$. It scatters in the time $(E_i - h\nu)/\hbar$ with a phonon with $q \approx |k_{min}|$. The additional dependence on $E_i - h\nu$ makes transitions for electrons with $|\overrightarrow{k}| = |\overrightarrow{k_{min}}|$ in the valence band to the minimum in the conduction band improbable. The absorption coefficient for allowed indirect transitions is [Bla68]:

$$\alpha_i = C_i\left[\frac{(h\nu - E_g + \hbar\omega_q)^2}{\exp\left(\frac{\hbar\omega_q}{k_B T}\right) - 1} + \frac{(h\nu - E_g - \hbar\omega_q)^2}{1 - \exp\left(\frac{\hbar\omega_q}{k_B T}\right)}\right] \tag{2.17}$$

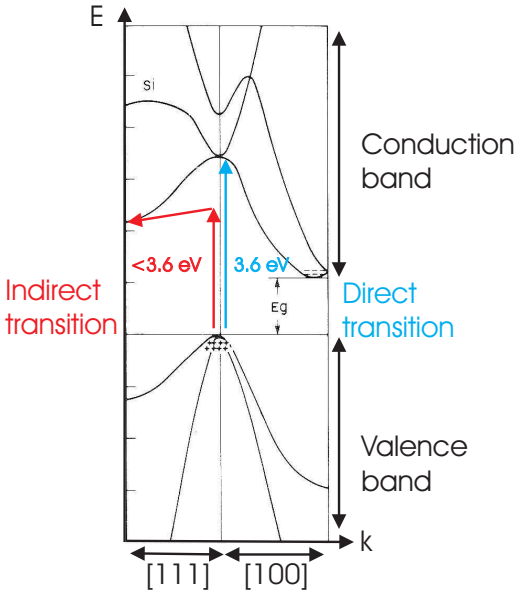

Figure 2.6: **Band structure of silicon:** *The graph shows the first Brillouin zone of* [111] *and* [100] *orientated silicon. The minimum of the conduction band is not above the maximum of the valence band. For transition energies below the direct transition at* $\overrightarrow{k} = \overrightarrow{0}$ $(3.6eV)$ *an interaction with the lattice phonons is required to get the missing momentum for an indirect transition [Sze85].*

The absorption coefficients from silicon, gallium arsenide and germanium are shown in Figure 2.7.

With an applied electric field separating the free charge carriers from each other it is possible to get the free charge carriers out of the silicon before recombination. These basic processes are used in semiconductor photo detectors and solar cells.

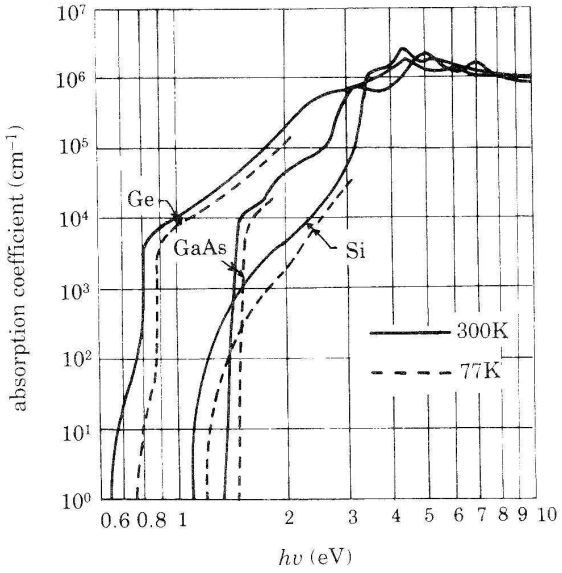

Figure 2.7: **Absorption coefficients of Si, GaAs and Ge [Sze85]**

2.3.3 Generation by Charged Particle Radiation

The electron cloud in the silicon lattice interacts with the Coulomb field of traversing charged particles. The energy loss for charged particles traversing matter is given by the Bethe-Bloch formula [Lut99]:

$$\frac{dE}{dx} = 2\pi N_L r_e^2 m_e c^2 \rho \frac{Zz^2}{A\beta^2}\left[\ln\left(\frac{2m_e\gamma^2 v^2 W_{max}}{I^2}\right) - 2\beta^2 - \delta - 2\frac{C}{Z}\right] \tag{2.18}$$

with

- the path length x in g/cm^2
- the classical electron radius $r_e = \frac{e^2}{4\pi m_e c^2} = 2.817 \cdot 10^{-13} cm$
- the matter density ρ
- the atomic number N_L
- the atomic weight A
- the traversed matters charge Z
- the traversing particles charge z
- the traversing particles velocity v
- $\beta = \frac{v}{c}$ and $\gamma = \frac{1}{\sqrt{1-\beta^2}}$
- the ionization energy I averaged over all electrons
- the density correction δ which flattens the relativistic rise
- the shell correction C for very low velocities of the traversing particle
- the maximum energy transfer W_{max} in a single collision

Figure 2.8 shows the energy loss of electrons versus their kinetic energy according to Equation 2.18. Electrons with an energy of $1.5 MeV$ have the lowest energy loss. In order to detect all charged particles the sensors for particle detection in high energy physics have also to detect these minimum ionizing particles (MIP). For this reason the signal to noise ratio (SNR), the most important parameter describing the detectors performance, is defined as the ratio of the signal of the MIP to the noise. The energy loss calculated by the Bethe-Bloch formula 2.18 describes the mean energy loss per traversed matter and just a fraction of the energy loss creates electron-hole pairs. The fluctuation around this mean value is described by the Landau distribution. The probability $\phi(E)dE$ that a charged particle looses energy between E and $E \pm dE$ is given to:

$$\phi(E)dE = \frac{2\pi N_L e^4 Z}{m_e v^2 A}\frac{1}{E^2} \tag{2.19}$$

The mean energy loss by Bethe-Bloch formula 2.18 and the Landau probability distribution in Equation 2.19 lead to the deviation from the mean value $\lambda = E - E_{mean}$ [Mov55]:

$$\omega(\lambda) = \frac{1}{\pi}\int_0^\infty \exp\left(-u\ln(u) - \lambda u\right)\sin(\pi u)du \approx \frac{1}{\sqrt{2\pi}}\exp\left(-\frac{1}{2}\lambda + e^{-\lambda}\right) \tag{2.20}$$

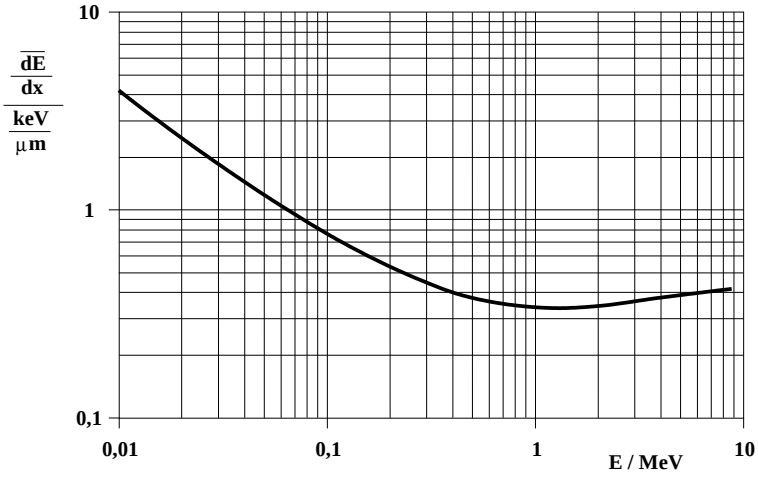

Figure 2.8: **Energy loss of electrons in silicon after Bethe-Bloch formula:** *The minimum energy loss of electrons have electrons with a kinetic energy of* $1.5\,MeV$. *These particles are called minimum ionizing particles (MIP).*

2.3.4 Recombination

Due to the indirect band gap of silicon direct recombination of free charge is suppressed since a large momentum has to be transferred to the silicon lattice. Defects in the band gap can assist local trapping and recombination by changing their charge by emission or capturing of electrons or holes. For n-type semiconductor the recombination time τ_r is given to:

$$\frac{1}{\tau_r} = \beta n_0 = n_0 \frac{N_t v_{th,n} \sigma_n v_{th,p} \sigma_p}{v_{th,n}\sigma_n \left[n + n_i \exp\left(\frac{E_t - E_i}{k_B T}\right)\right] + v_{th,p}\sigma_p \left[p + n_i \exp\left(\frac{E_i - E_t}{k_B T}\right)\right]} \tag{2.21}$$

with the initial doping concentration n_0 and the parameters given by Equation 2.13.

2.4 p-n-Junctions in Silicon

n-doped or p-doped silicon is a comparatively good electrical conductor. An applied electric field moves the charge carriers to the voltage sources electrodes and a certain current is flowing through the silicon device. A combination of n-type and p-type silicon is used in semiconductor sensors.

The voltage, current, and capacitance characteristic of these p-n-junctions depends on the polarity of the applied electric field contrary to the behavior of metals or one-type doped semiconductors. The majority charge carriers in the connection zone of the n-type and the p-type silicon diffuse into the neighbored regions and recombine there. The resulting region of ionized acceptors and donors is named space charge region (SCR). The evolved electric potential is the built-in voltage:

$$U_{bi} = \frac{1}{e}\left(E_i^p - E_i^n\right) = \frac{k_B T}{e} \ln\left(\frac{N_A N_D}{n_i^2}\right) \tag{2.22}$$

Figure 2.9 shows the space charge region with the width $W = d_p + d_n$, the doping concentration which does not change by diffusion, the resulting electric field, the electric potential and finally the energy band structure. The calculation of the width of the SCR is given to [Lut99]:

$$W = d_p + d_n = \sqrt{\frac{2\varepsilon\varepsilon_0 U_{bi}}{e(N_A + N_D)}} \left[\sqrt{\frac{N_A}{N_D}} + \sqrt{\frac{N_D}{N_A}}\right] = \sqrt{\frac{2\varepsilon\varepsilon_0 (N_A + N_D) U_{bi}}{e N_A N_D}} \tag{2.23}$$

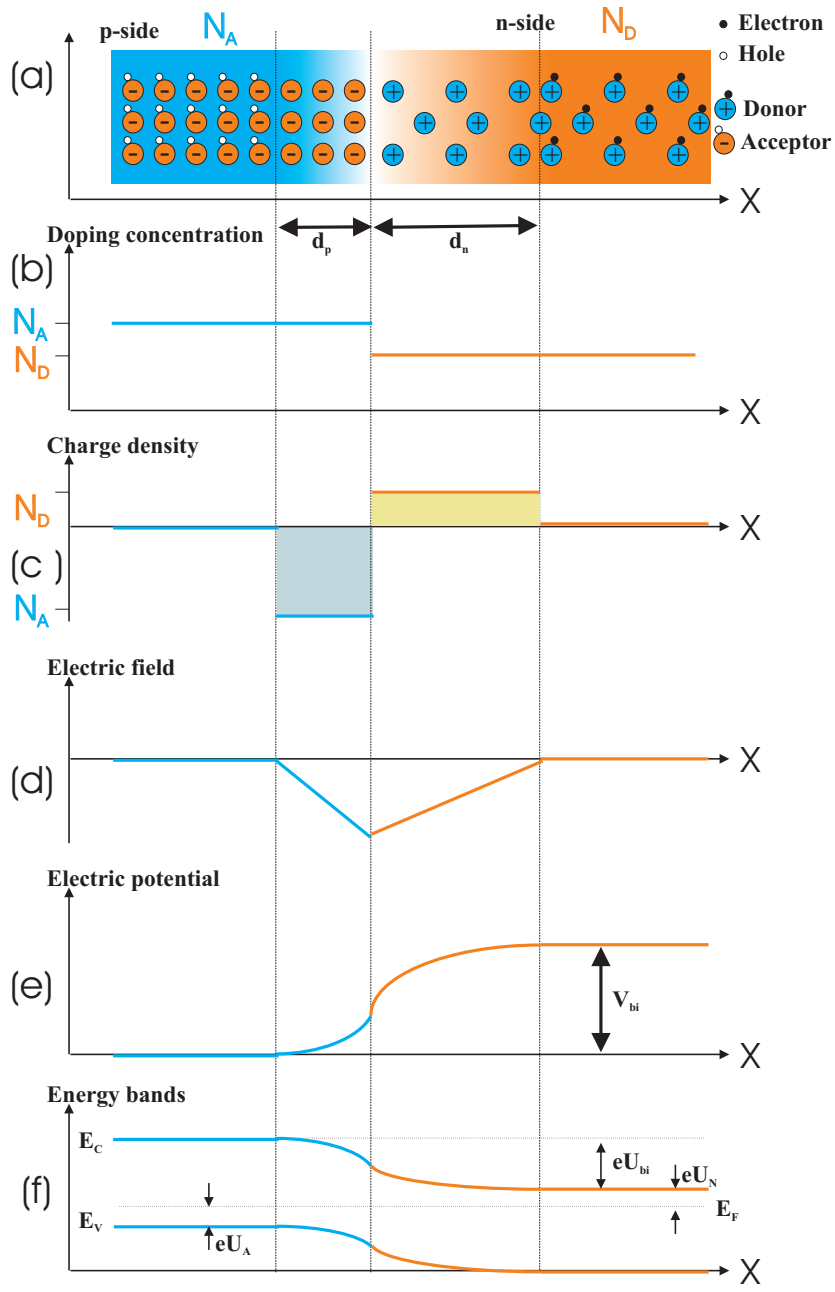

Figure 2.9: **The p-n-junction:** *Diagram (a) presents the donor and acceptor distribution in a partially depleted p-n-junction with their charge states. Diagram (b) shows the different doping concentration and the resulting charge distribution diagram (c) has due to conservation of charge two areas of the same size. Below the resulting electric field (d), the final potential distribution (e) and at bottom (f) the energy band structure are shown.*

The maximum electric field is then calculated to:

$$E_{max} = \frac{e}{\varepsilon\varepsilon_0} N_D x_n = \sqrt{\frac{2e}{\varepsilon\varepsilon_0} \frac{N_A N_D}{N_A + N_D} U_{bi}} \tag{2.24}$$

For practical reasons, one-type doped wafers are used and the p-n-junction is realized by heavily contrary doping of small regions of the wafer, e.g. for CMS sensors the wafers are n-doped with a thickness of $d = 320\,\mu m$ or $d = 500\,\mu m$ and the p-doped strips on these wafers have a thickness of a few μm. For such extreme asymmetric p-n-junctions the thinner implants need higher doping concentrations because of charge conservation. In Figure 2.9(c) the areas of the charge densities of

the n-doped region and the p-doped region have the same size. In this case, the main voltage drop is in the n-doped region of the junction.

2.4.1 Full Depletion Voltage of a p-n-Junction

An applied voltage with positive potential on the p-side and negative potential on the n-side is called forward bias and the contrary polarity reverse bias, respectively. For reverse and forward bias the built-in voltage U_{bi} has to be substituted by $U_{bi} - U_{bias}$. The voltage at which the SCR reaches the borders of the device is called full depletion voltage. It is given by:

$$U_{FD} = \frac{e}{2\varepsilon\varepsilon_0}|N_D - N_A|d^2 \tag{2.25}$$

with the thickness d of the device. $|N_D - N_A|$ is also called effective doping concentration $|N_{eff}|$. The resistivity ρ given by

$$\rho = \frac{1}{e\mu N_{eff}} \tag{2.26}$$

is more important for sensor producers. The reason is that the silicon ingots which are cut to wafers are qualified with this parameter.

In non ideal devices, the p-n-junctions are segmented and therefore the electric field is not linear in the device but contains edge effects and the depletion zone grows not homogeneously. The Poisson equation has to be solved to get the voltage drop in the device . The solution for strip sensors is given by [Bra00]:

$$U_{FD,sensors} = U_{FD,diode}\left[1 + 2\frac{p}{d}f\left(\frac{w}{p}\right)\right] \tag{2.27}$$

The pitch p is the distance from the middle of one strip to middle of the next neighbored strip. w is the width of the implants. The function $f(w/p)$ is a numerical approximation of the solution of the poisson equation and is given by:

$$f(x) = -0.00111x^{-2} + 0.0586x^{-1} + 0.240 - 0.651x + 0.355x^2 \tag{2.28}$$

For CMS, the strip sensors width to pitch ratio is $w/p = 0.25$ for all sensor geometries. Therefore the function 2.28 is constant for all geometries and has a value of $f(w/p) = 0.31608$. Table 2.2 shows the correction factor of Equation 2.27 for all CMS strip sensor geometries. For the wedge shaped sensor geometries the highest pitch from Table 1.1 and Table 1.2 is chosen for the calculation. The highest value can be found on W3 sensors with 31 %.

2.4.2 Capacitance Characteristics of a p-n-Junction

The capacitance versus voltage characteristics of a p-n-junction under reverse bias is depending on the effective doping concentration and therefore on the full depletion voltage given by Equation 2.25. The change of the surface charge on the p^+-implant when increasing the SCR from x to $x + dx$ is $eN_D dx$, the electric field change is $eN_D dx/(\varepsilon_0\varepsilon_S)$, and surface voltage change is $xeN_D dx/(\varepsilon_0\varepsilon_S)$. Integration over the bulk thickness of the p-n-junction results in:

$$Q_p = -\int_0^D eN_D(x)dx \tag{2.29}$$

sensor geometry	pitch μm	correction factor
IB1	80	1.158
IB2	120	1.237
W1TEC	112	1.221
W1TID	119	1.235
W2	143	1.282
W3	158	1.312
W4	139	1.275
OB1	122	1.154
OB2	183	1.231
W5A	142	1.179
W5B	156	1.197
W6A	185	1.234
W6B	205	1.159
W7A	156	1.197
W7B	172	1.217
mini sensor	180	1.25

Table 2.2: **Correction factors for full depletion voltage of CMS sensors:** *With a constant strip width to strip pitch ratio $w/p = 0.25$ the full depletion voltage of a CMS strip sensor is up to 31 % higher than a diode with the same properties like effective doping concentration or thickness of the bulk. Since the rectangular inner (IBx) and outer barrel (OBx) sensor designs have a constant pitch, the pitch values of the wedge shaped sensor designs (Wxx) vary within a wide range. The correction factors for these geometries are calculated for the largest pitch value.*

for the charge Q_p. The potential difference

$$\psi_p = \int_0^D \frac{xeN_D(x)}{\varepsilon_0\varepsilon_S} dx \tag{2.30}$$

must be the same as $U_{Bias} - U_{bi}$. The capacitance of a depleted diode can be derived to:

$$C = \begin{cases} A\sqrt{\frac{e\varepsilon_0\varepsilon_S N_D}{2U_{Bias}}} & ,U_{Bias} \leq U_{FD} \\ A\frac{\varepsilon_0\varepsilon_S}{d} & ,U_{Bias} > U_{FD} \end{cases} \tag{2.31}$$

with the area A of the diode. For the not fully depleted case the doping profile N_D can be derived to:

$$\frac{\partial\left(\frac{1}{C^2}\right)}{\partial U} = \frac{\partial\left(\frac{1}{C^2}\right)\partial D}{\partial U/\partial d} = \frac{2d/(\varepsilon_0\varepsilon_S)^2}{eN_D d/\varepsilon_0\varepsilon_S} = \frac{2}{eN_D\varepsilon_0\varepsilon_S} \tag{2.32}$$

Examples for capacitance versus voltage characteristics can be seen in Figure 5.16(a) on Page 75. The double logarithmic plot accents the kink at full depletion voltage.

2.4.3 Current Characteristics of a p-n-Junction

The current voltage characteristics can be derived from the minority charge carrier concentration at the edge of the neutral region:

$$n_p = n_n \exp\left(-\frac{eU_{bi} - U_{bias}}{k_B T}\right) = n_{p_0} \exp\left(\frac{eU_{bias}}{k_B T}\right) \qquad p_n = p_{n_0} \exp\left(\frac{eU_{bias}}{k_B T}\right) \tag{2.33}$$

Since the minority charge carrier diffusion current is proportional to the deviation from thermal equilibrium, the current is calculated to:

$$J = J_s \left(\exp\left(\frac{eU_{bias}}{k_B T} \right) - 1 \right) \tag{2.34}$$

with the saturation current J_s for reverse bias given by:

$$J_s = e \left(\frac{n_{p_0} D_n}{\sqrt{D_n \tau_{r,n}}} + \frac{p_{n0} D_p}{\sqrt{D_p \tau_{r,p}}} \right) \tag{2.35}$$

$\tau_{r,n(p)}$ is the trapping time and $D_{n(p)}$ is the diffusion length of the electrons and holes, respectively. Equation 2.35 is only valid for the assumption that no charge carriers are generated in the SCR. For $n \cdot p \ll n_i^2$ the thermal generation by Equation 2.15 dominates and the volume generated current is given by:

$$J_V \approx -e \frac{n_i}{\tau_g} W \tag{2.36}$$

with the width W of the p-n-junction.

For high electric field concentrations within the p-n-junction, the current rises up rapidly. This current break trough is caused by avalanche or Zener effects and is most times observed beyond full depletion voltage of the p-n-junction [Sze85].

2.5 Schottky Contacts in Silicon-Metal Junctions

When a metal is brought into intimate contact with a semiconductor the Fermi Levels are balancing. The work function - which is the difference between the vacuum energy level and the Fermi Level - is in most cases different for the metal and the semiconductor. For metals it is quoted as $e\phi_m$ and for semiconductors $e(\chi + U_n)$ with χ the electron affinity of the conduction band to the vacuum level and U_n the distance from the Fermi Level to the conduction band. For n-type silicon electrons coming from the metal to the semiconductors see a barrier with the height

$$e\phi_{Bn} = e(\phi_m - \chi) \tag{2.37}$$

and for p-type

$$e\phi_{Bp} = E_g - e(\phi_m - \chi) \tag{2.38}$$

respectively. With such a kind of contact, a diode like behavior is given (Schottky diode). A Shottky contact can be inhibited by a thin and highly doped layer between the semiconductor material and the metal contact. This small layer has a much higher Fermi Level than the lower doped semiconductor and the barrier between the metal and the semiconductor is very small as shown in Figure 2.10. The electrons can tunnel from the metal into the semiconductor and an ohmic contact is realized.

2.6 MOS Structure and Flatband Voltage

Metal-**O**xide-**S**emiconductor structures can be used to qualify the sensors surface. Therefore the CMS collaboration decided to produce at least two MOS structures on each sensor wafer. In this section the working principles are explained [Lut99].

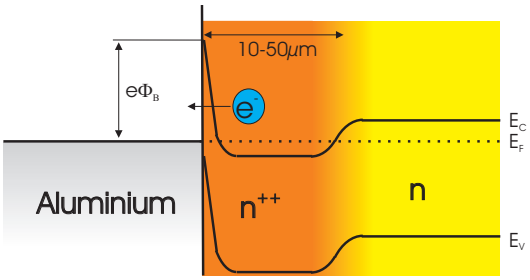

Figure 2.10: **Energy band structure of a Schottky contact:** *The high potential difference between the two vacuum levels forms a barrier for electrons. High doping concentration in a thin layer of the semiconductor makes the barrier very small and allows electrons to tunnel in both directions. This method is mainly used to avoid Schottky contacts and to realize ohmic contacts.*

The MOS structures are made of a semiconductor, a dielectric layer and a metal contact above. The CMS MOS structures have a silicon dioxide layer as dielectric with a thickness of approximately $2\mu m$. An important point is that no current flows from the metal to the semiconductor. Therefore a MOS structure has to be operated below the break through voltage of the insulator.

The work function of the aluminium - silicon dioxide contact is $e\phi_m = 4.1\,eV$ and for the silicon - silicon dioxide contact the work function is $e\phi_S = e\chi + E_C - E_F$. The electron affinity $\chi = 0.56\,eV$ does not depend on the doping concentration. The distance from the resulting Fermi Level to the intrinsic Fermi Level is given by:

$$e\psi_B = E_F - E_i = k_B T \ln\left(\frac{N_D}{n_i}\right) \tag{2.39}$$

An applied electric field influences the Fermi Levels of the metal and the semiconductor. Figure 2.11 shows the effective capacitances and band structures of all operation cases of a MOS structure. In MOS structures the following cases for an applied voltage U can be distinguished:

- **Accumulation** ($U > U_{FB}$)

  A higher voltage than the flat band voltage bends the conduction band level and the valence band level towards the Fermi Level as shown in Figure 2.11(a). Thus the electron concentration is increasing according to the thermal equilibrium condition $n = n_i \exp\left((E_F - E_i)/k_B T\right)$. This results in a very thin layer with surface charge carriers in the semiconductor (below the insulator) with:

$$Q_{accumulation} = -\varepsilon_{oxide}\varepsilon_0 \frac{U - U_{FB}}{d_{oxide}} = -C_{oxide}(U - U_{FB}) \tag{2.40}$$

- **Flatband condition** ($U = U_{FB}$)

  Under this condition, the applied electric field forms a flat conduction and valence band as shown in Figure 2.11(b). In this case the flat band voltage U_{FB} is given by:

$$U_{FB} = \phi_m - \phi_s \tag{2.41}$$

  This equation is only valid without charges in the silicon dioxide. The mobility of electrons in the silicon dioxide is much higher than for holes. By ionization induced charge carriers can be captured in lattice defects in the silicon dioxide layer, but their emission is suppressed by the high band gap of $E_g = 8.8\,eV$. For CMS also Si_3N_4 is used with a band gap of $E_g = 5.0\,eV$. The applied electric field moves the charge carriers in the silicon dioxide to the semiconductor

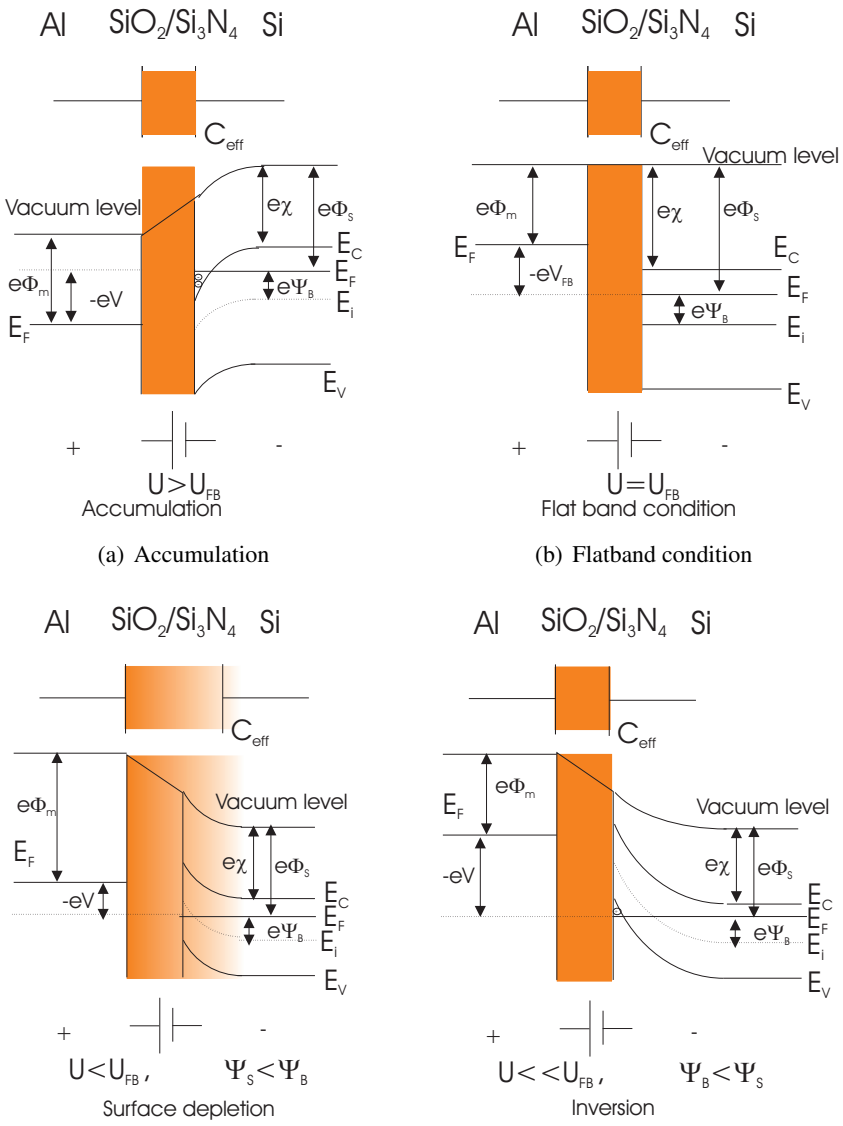

(a) Accumulation

(b) Flatband condition

(c) Surface depletion

(d) Inversion

Figure 2.11: **Energy band structures of a MOS structure:** *Applied voltages above U_{FB} increase the Fermi Level in the semiconductor and bend the energy bands near the surface developing allowed electron states and therefore an accumulation of electrons (2.11(a)). If one reduces the applied voltage to U_{FB} the allowed electron states at the surface disappear (2.11(b)). A further reduction of the applied voltage bends the energy bands near the surface and allowed electron states in the conduction band disappear and one gets a surface depletion which increases the effective capacitance of the device (2.11(c)). At a certain point the Fermi Level is low enough to get allowed hole states in the valence band and one gets a so called inversion (2.11(d)). An experimental method to determine U_{FB} is a capacitance versus applied voltage measurement. U_{FB} is the reflection point of the curve between the case of accumulation and surface depletion. Figure 6.50 on page 131 shows an example of these measurements.*

insulator interface which is in this case also called surface [Sze85]. The different lattice constants of the insulator layer and the semiconductor are adapting at the surface and the positive charge carriers in the insulator layer are accumulated. The charge concentration N_{ox} saturates at $3 \cdot 10^{12}\, cm^{-3}$ [Wue01]. The increase of the flatband voltage with induced charge carriers in the silicon dioxide is given by:

$$\Delta U_{FB} = -\frac{1}{\varepsilon_{oxide}\varepsilon_0}\left(\sigma_{int} d_{oxide} + \int_0^{d_{oxide}} \rho(x) x dx\right) \tag{2.42}$$

with the two dimensional charge carrier density σ_{int} at the surface, the oxide thickness d_{oxide} and the volume charge density in the oxide $\rho(x)$.

- **Surface depletion** ($U < U_{FB},\ \psi_s < \psi_B$)

  A lower voltage than the flat band condition bends the energy bands upwards, respectively (Figure 2.11(c)). The energy band bending between the boundary of the surface and deep inside the semiconductor is expressed by:

$$\psi_S = e\frac{N_D d_s^2}{2\varepsilon_0 \varepsilon_S} \tag{2.43}$$

  The distance from the Fermi Level to the intrinsic Fermi Level is decreasing and the surface is depleted up to a depth of:

$$d_s = \sqrt{\frac{\varepsilon_s \varepsilon_0}{eN_D}(U_{FB} - U) + \left(\frac{\varepsilon_s}{\varepsilon_{oxide}} d_{oxide}\right)^2} - \frac{\varepsilon_s}{\varepsilon_{oxide}} d_{oxide} \tag{2.44}$$

- **Inversion** ($U << U_{FB},\ \psi_s > \psi_B$)

  If the voltage is much lower than the flat band voltage, the Fermi Level cross from a certain point on underneath the intrinsic Fermi Level. In this case the hole concentration is increasing in the depleted zone (Figure 2.11(d)). In comparison to the accumulation described above the inversion charge is described by:

$$Q_{inversion} = \left(U_{FB} - 2\psi_B - \frac{d_{oxide}}{\varepsilon_{oxide}\varepsilon_0}\sqrt{4eN_D\varepsilon_s\varepsilon_0\psi_B} - U\right) C_{oxide} \tag{2.45}$$

The capacitance C from a MOS structure is depending on the silicon dioxide thickness and the depletion width (see Equation 2.44). The total capacitance C is the series of the bulk and the silicon dioxide capacitances:

$$C = \frac{C_{oxide} C_{bulk}}{C_{oxide} + C_{bulk}} \tag{2.46}$$

The flat band voltage is measured by means of a CV curve. Starting from a low bias voltage the capacitance from Equation 2.46 is decreasing while reaching the surface depletion. The flat band voltage is the inflection point of the CV curve. Important is the measurement frequency for the CV curve. It has to be high enough to avoid movements of the minority charge carriers and therefore for CMS MOS structures a measurement frequency of $50\, kHz$ is used.

2.7 Poly Crystalline Silicon Resistors

An ohmic resistor of a CMS sensor is built of poly crystalline silicon. It is fabricated by deposition of a poly crystalline silicon layer of very fine grain size upon an insulator surface, followed by ion implantation of boron (or phosphorous) equal to or slightly in excess of the solubility limit of the poly crystalline silicon. An implant dosage of the dopant is within the range from $5 \cdot 10^{14}$ to $10^{16}\, ions/cm^2$. This ion implantation is normally done using a screen silicon dioxide surface layer. The structure may be annealed at temperatures of between about $800°C$ to $1,100°C$ for 15 to 180 min to control the grain size of the poly crystalline silicon layer, homogenize the distribution of the boron (or phosphorous) ions throughout the entire film thickness and to raise the concentration of the boron (or phosphorous) in the silicon grains to the solid solubility limit [GKS84][Zac95].

Normally, just the value of the resistance is defined and it is the decision of the sensor producer which kind of poly crystalline silicon and doping is used.

2.8 Design and Working Principles of a Silicon Sensor

Figure 2.12 shows schematically the design and the principle of a strip or pixel sensor. The most common way to produce a silicon sensor is to take a slightly doped bulk and to insert comparatively

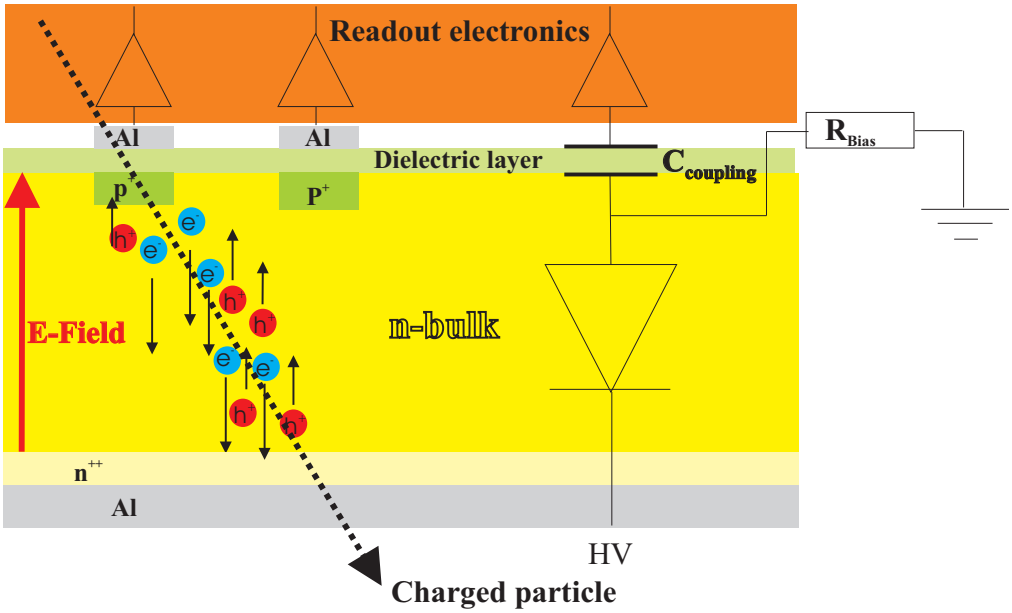

Figure 2.12: **Schematics of a semiconductor sensor:** *The sensor is built of p-n-junctions which are fully depleted by an applied reverse bias voltage. Since charged particles traversing semiconductors produce electron-hole pairs, the applied electric field separates electrons and holes from each other and collects them at the electrodes. In single sided strip or pixel sensors one charge carrier type is collected while the other charge carrier type is drifting to the unstructured contact and gets lost. The dark current of the fully depleted p-n-junction is separated from the readout electronics by capacitances. These are realized by a small non conductive dielectric layer between the implants and the metal segmentations above. Bias resistors are necessary to apply a potential to the implants and to form a certain RC value with the coupling capacitance.*

highly doped structures of opposite doping. The bulk and the structures are biased with a voltage of reverse direction in order to deplete the whole semiconductor and to remove all free charge carriers. Then only a constant thermal generated bulk current flows through the sensor. If charged particles track through the bulk, electron-hole pairs are generated due to the energy transferred after the Bethe-Bloch-formulae. For silicon about 108 electron-hole pairs per μm are created for a minimum ionizing particle (see Section 2.3.3). These charge carriers are drifting to the electrodes of the applied voltage source.

Depending on the application different readout principles for the created free charge carriers are required. These can be either DC or AC readout. For CMS sensors the AC readout is used and therefore these sensors contain coupling capacitances between the strip implants and the readout channels of the preamplifier. These capacitances are realized by an insulating layer between the implanted structures and the aluminium segmentations on top. The reason to produce the capacitance on the sensor and not in the readout chip is the magnitude of the capacitance which should be as high as possible, since a low coupling capacitance is a high resistance for the readout signal and it is in series with the bulk and the preamplifier. For silicon it is in most cases silicon dioxide, but also silicon nitride is used. Both have -in comparison with silicon- similar lattice constants and the connection between these materials has less dangling bonds resulting in low surface currents.

In case of a high bias voltage and a non high voltage stable readout electronic one has to take care of the voltage drop. Either the readout electronic has to be connected to low potential structures of the sensor or the readout electronic has to be connected to a high potential sensor structure and its inner potential has to be floating. In case of the CMS sensors, the readout electronic is connected to the low potential AC coupled aluminium segmentations above the strip implants. With an ohmic resistor, a certain (low) potential is applied to the implants. This is necessary because a fix potential between the readout electronics and the implants (e.g. by a voltage source) would swallow the signals of the electrons and holes. The resistor has to be above a certain value in order to enable the AC readout via the coupling capacitance before the signal flows to the voltage source.

Furthermore, the range of the bias resistors is limited by noise reasons which are explained in Section 2.10 and by the time constant of the bias resistors and the coupling capacitances.

2.9 Signal Readout on Sensor Level

The geometry of the readout electrodes affects the readout signal. The Reciprocity Theorem

$$\sum_{electrodes} Q'_n U_n = \sum_{electrodes} Q_n U'_n \tag{2.47}$$

delivers the induced current in a multi electrode system. By using this equation one can derive the change in potential for a given change in charge. A single pixel can be approximated as a simple plate capacitor with two electrodes. In one state one electrode is on ground $(U_1 = 0, Q_1)$ and the other one at the potential (U_2, Q_2). In the second state the electrode is put on a potential (U'_1, Q_1) which induces charge Q'_2 in the other electrode. This results in:

$$Q'_1 U_1 = Q_2 U'_2 \implies \frac{Q'_1}{U'_2} = \frac{Q_2}{U_1} \implies C_{21} = C_{12} \tag{2.48}$$

The capacitance seems not to depend on the side where the measurement (charge introduction) is performed. For a drift charge Q_{dr} considered as an electrode on potential U_{dr} with all other electrodes

on ground one can select a sensing electrode with induced charge Q_S. As a second state one puts the sensing electrode on potential U'_S and gets the potential U'_{dr} at the charge's position with $Q'_{dr} = 0$:

$$\begin{aligned} Q'_s U_s + Q'_{dr} U_{dr} &= Q_s U'_s + Q_{dr} U'_{dr} \\ 0 + 0 &= Q_s U'_s + Q_{dr} U'_{dr} \end{aligned} \tag{2.49}$$

The induced current at the sensitive electrode is calculated with Ramo's theorem to:

$$I = \frac{dQ_s}{dt} = -Q_{dr}\frac{dU_W}{dt} = -Q_{dr}\frac{dU_W}{d\vec{r}}\frac{d\vec{r}}{dt} = -Q_{dr}\vec{\nabla}U_W\vec{v} \tag{2.50}$$

with the velocity $\vec{v}$ of the drifting charge and the weighted electric field $\vec{E}_W = -\vec{\nabla}U_W$ [Ram39]. For unsegmented extreme asymmetric p-n-junctions the weighted field is approximated by $E_W \propto d^{-1}$ which is proportional to the drift velocity. This approximation is important for the transient current technique (TCT). All charges in a given time interval are collected by a charge sensitive amplifier in the readout electronics which sends the coordinates to the front-end electronics. For charge clouds smaller than the pitch p the measurement precisions variance $\langle \Delta x^2 \rangle$ of the read-out electronics is calculated to:

$$\langle \Delta x^2 \rangle = \frac{1}{p}\int_{-p/2}^{+p/2} x^2 dx = \frac{p^2}{12} \tag{2.51}$$

2.10 Noise Sources in a Sensor

A sensor has different noise sources. Some have their origin in the detector principle, for example the discrete charge scale e, others are additional currents generated in discrete components like the bias resistors. Figure 2.13 shows the schematics of the noise sources in a CMS sensor which has the same principle design as shown in Figure 2.12.

One distinguishes between two different types of noise sources, serial (voltage) and parallel (current) noise. The noise sources are explained in the following [Lut99].

The parallel noise of a p-n-junction, which is called shot noise, of a single strip or pixel is based on the statistic charge carrier fluctuation:

$$\frac{d\langle i^2_{shot}\rangle}{df} = 2eI_{Leakage} \tag{2.52}$$

The bias resistors' resistance leads to a parallel thermal noise through its thermal fluctuations of the electron velocity distribution:

$$\frac{d\overline{i^2_{n,bias}}}{df} = \frac{4k_B T}{R_{Bias}} \tag{2.53}$$

For the same reason the aluminium strip - which acts as a serial resistor within the readout line - gives a thermal noise distribution with a serial noise voltage:

$$\frac{d\overline{u^2_{n,strip}}}{df} = 4k_B T R_{metal} \tag{2.54}$$

A further contribution to the noise of the detector modules comes from the readout electronics which contains noise sources. The main contribution comes from the preamplifier's input transistor. Its serial noise voltage is $u_{n,amp}$. The equivalent noise charge contributions at the proper amplifier are

$$Q_{n,p} = -u_{n,amp}(C_{strip,bulk} + C_{interstrip} + C_f) \tag{2.55}$$

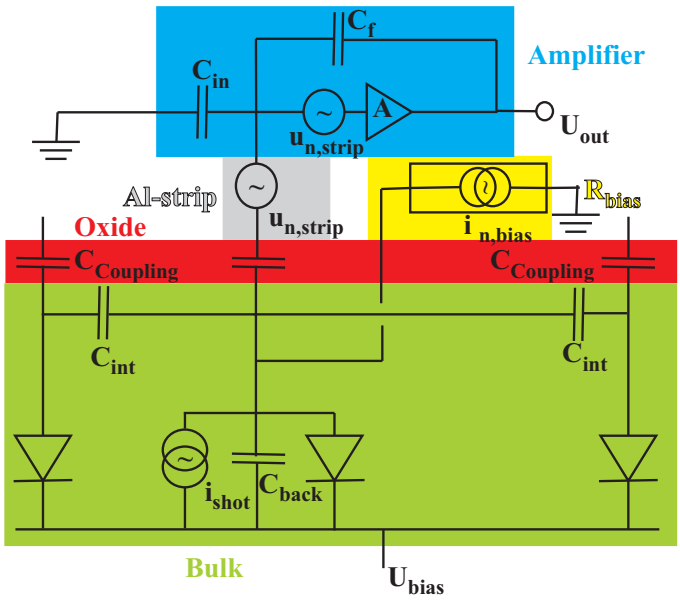

Figure 2.13: **Schematics of noise sources in a CMS detector:** *The preamplifiers effective load capacitance depends on the network of interstrip capacitances between two strips C_{int}, the coupling capacitance $C_{Coupling}$ and the bulk capacitances $C_{strip,bulk}$ of a strip. Depending on sensors dimensions, the bulk capacitance of the neighbored strip can also be important for the load capacitance. The bulk and the bias resistor of a strip can be substituted by current noise sources, the metal strip and the preamplifier can be substituted by voltage noise sources, respectively.*

for parallel noise and

$$Q_{n,s} = u_{n,amp} C_{strip,bulk} \tag{2.56}$$

for serial noise, whereas $C_{strip,bulk}$ is the bulk capacitance of a single strip or pixel and $C_{interstrip}$ is the capacitance between two neighbored strips or pixels. The noise contributions are produced in the capacitive network which is seen by the adjacent preamplifier. The total strip capacitance is given to:

$$C_{strip,tot} = \frac{C_{Coupling}(2C_{interstrip} + C_{strip,bulk})}{C_{Coupling} + (2C_{interstrip} + C_{strip,bulk})} \approx 2C_{interstrip} + C_{strip,bulk} \tag{2.57}$$

whereas $C_{strip,bulk}$ can be approximated by $C_{strip,bulk} \approx C_{total}/N_{strips}$ with the total sensors capacitance C_{total} measured by the CV curve and the sensors strip number N_{strips}. The total noise is the quadratic sum of all noise components:

$$Q^2_{total} = 2eI_{Leakage}T_s F_i + \frac{4k_B T}{R_{Bias}} T_s F_i + C_{strip,tot} 4k_B T R_{metal} \frac{F_u}{T_s} + C^2_{strip,tot} u^2_{n,amp} \frac{F_u}{T_s} + F_{uf} A_f C^2_{tot} \tag{2.58}$$

with the pulse shaping time T_s and the pulse shaping correlated form factors F_u for noise voltages and F_i for noise currents, respectively. F_{uf} and A_f are the correlated form factors and the noise contributions of the preamplifier. F_i and F_u are given by:

$$F_i = \frac{1}{2T_s} \int_{-\infty}^{\infty} W(t)^2 dt, \qquad F_u = \frac{T_s}{2} \int_{-\infty}^{\infty} \left[\frac{dW(t)}{dt} \right]^2 \tag{2.59}$$

Noise source (Type)	$ENC\,(RMS\,e^-)$ (peak mode)	Formula at $T=-10°C$	Deconvolution mode
Reverse bias current (parallel)	$\sqrt{\frac{ei_{n,bias}T_s}{4}}$	$\approx 108\sqrt{i_{n,bias}(\mu A)T_s(ns)}$ $(\simeq 50-1320)$	$\times 0.45$
Bias resistance (parallel)	$\sqrt{\frac{k_BTT_s}{2R_{bias}}}$	$\approx 22.5\sqrt{\frac{T_s(ns)}{R_{bias}(M\Omega)}}(\simeq 170)$	$\times 0.45$
Metal strip resistance (series)	$C_{strip,tot}\sqrt{\frac{k_BTR_{metal}}{6T_s}}$	$\approx 13C_{strip,tot}(pF)\sqrt{\frac{R_{metal}}{T_s(ns)}}(\simeq 390)$	$\times 1.45$
Front-end electronics (series)		$246+36C_{strip,tot}(pF)(\simeq 786)$	$396+59C_{strip,tot}(pF)$ $(\simeq 1281)$
Total		$895-1595$	$1400-1525$

Table 2.3: **Noise currents of the CMS readout system:** *The equivalent noise currents (ENC) in e^- are calculated to the values in brackets for a TOB detector module consisting of two sensors. The deconvolution mode is a feature of the CMS readout electronics and is described in section 4.5 on page 55. The readout chips pulse shaping time is $T_s = 50\,ns$ and the mean value of the bias resistances is $R_{bias} = 1.8\,M\Omega$. The resistance of the metal of the readout strip is assumed to be $R_{metal} = 2\cdot 100\,\Omega$ and a value of $C_{strip} = 2\cdot 7.5\,pf$ is assumed for the strip capacitance. The single strip leakage current changes with fluence and is increasing from $I_{leakage} = 2\,nA$ up to $1500\,nA$ (see Section 3.1) [Pro98][CTDRA00].*

with the pulse response function $W(t)$ [Hag02]. Table 2.3 gives the equivalent noise sources of a TOB detector module with two CMS sensors (explained in detail in Chapter 4). The chosen values are common ones for non irradiated CMS sensors. After irradiation with a fluence comparable to ten years of operation at LHC an increase of C_{int} up to $1.3pF/cm$ is allowed by the CMS sensors noise requirements. This would result in an equivalent noise current (ENC) of $1845\,e^-$ for peak mode operation and $2110\,e^-$ for deconvolution mode operation, which means an increase of 38 % in noise after irradiation. With Equation 2.57 the interstrip capacitance and its increase with fluence is one of the most important parameters of the sensor's noise and therefore a detailed analysis concerning these values is shown in Section 6.10.2.

Chapter 3

Radiation Damage in Silicon and Silicon Dioxide

The main topic of this thesis is the analysis of the changes of macroscopic properties by radiation damage introduced by charged and non charged particle irradiation. The radiation damage causes a change of leakage current, a change of full depletion voltage and a trapping of charge carriers within the sensor. Particularly charged particle irradiation causes charge carriers in dielectric layers which cause changes in surface currents. Many changes are neither stable with temperature nor with time since so called annealing effects take place. All these effects reduce the sensor's performance and it is important to predict the sensor properties during the service life of CMS.

The following sections give an overview on the radiation damage mechanisms, the changes of material properties, and the behavior with respect to temperature after irradiation.

3.1 Radiation Damage in Silicon and the NIEL-hypothesis

Ionization is the most important process of interaction of charged particles with matter. The Coulomb field of the particle interacts with the electron cloud of the irradiated matter and creates electron-hole pairs. This reversible process causes no permanent damage and can be, except for the signal readout, neglected. However, the interaction of charged or neutral particles with the silicon lattice causes irreversible (partially electrically charged) mutations. This damage can cause trapping of charge carriers resulting in a reduction of the readout signal, an increase of leakage current, or in changes of the effective doping concentration. In non conductive layers like SiO_2 or Si_3N_4, where the band gap energy is higher than in silicon, the produced charge carriers (mainly by charged particle irradiation) have longer lifetimes and in case of an applied electric field they move to the borders of the non conductive layer and they are trapped there, due to imperfect connections at the interfaces to other materials. For the interface between the sensor's bulk and its dielectric (for AC coupled readout) or passivation layer (for DC coupled readout) the non-bound valence electrons (dangling bonds) cause surface currents below the dielectric or passivation layer.

Charged particles have a higher cross section for interaction with the crystal lattice atoms than neutral particles with the same energy due to their Coulomb field.

The minimum recoil energy to kick a silicon atom out off its lattice site is $15\,eV$. The energy at which the probability to displace an atom is one half is $E_d = 20\,eV$ [LFL80], since it depends on the recoil direction. Particles with energies below E_d dissipate their energy to phonons and cause no irreversible damage. Particles with energies just above this limit create vacancy interstitial (V-I) pairs,

	Electrons	**Protons**	**Neutrons**	**Si^+**
Scattering mechanism	Coulomb	Coulomb and nuclear	Elastic nuclear	Coulomb
$E_{R,max}/E_{R,av}$ $[keV]$ for $E_{kin} = 1MeV$	0.155/0.046	133.7/0.21	133.9/50	1000/0.265
min. energy for point/ cluster defect $[keV]$	260/4600	0.19/15	0.19/15	0.025/2

Table 3.1: **Characteristics of typical irradiation interactions in silicon:** *$E_{R,max}$ is the maximum recoil energy and $E_{R,av}$ is the average recoil energy of the named particles for a collision with a silicon atom.*

named Frenkel pairs. The maximum recoil energy E_{max} of a particle with mass m and energy E in head-on collision with silicon ($M \approx 28 m_{proton}$) is:

$$E_{max} = \frac{4Mm}{(M+m)^2}E \tag{3.1}$$

In Table 3.1 the maximum $E_{r,max}$ and average $E_{r,av}$ recoil energies are given for electrons, protons, neutrons and silicon atoms. The first silicon atom hit, called primary knock-on atom (**PKA**), is able to move through the crystal lattice and to create further damage along its track. Its range is given by [LFL80]:

$$R \approx 32\frac{nm}{keV}\sqrt{E_R} \quad for \quad E_R < 10keV \tag{3.2}$$

E_R is the recoil energy of the PKA. The rate of energy loss can be derived from the ranges as $\frac{dE_R}{dz} \sim \sqrt{E_R}$. Silicon atoms hit by the PKA (secondary process) might also cause further damage if the remaining recoil energy is high enough for ternary processes. For energies in the range of $1-2\,keV$ only isolated point defects can be created. In case of higher recoil energies ($E_R \geq 10\,keV$) clusters, which are dense accumulations of single point defects, are created in addition to the point defects at the end of the tracking path. Both the energy loss and the mean free path between two interactions decrease with decreasing recoil energy. It is worth to mention that the mean free path reduces faster than $\sqrt{E_R}$. Below $5\,keV$ the mean free path is in the order of $1\,nm$ and the created defects cluster in a very close region. Figure 3.1 shows the most frequent lattice damage in a silicon crystal. Displaced silicon atoms called interstitials or empty places in the silicon lattice named vacancies can form different defects with foreign atoms like oxygen, phosphorus, boron, or carbide. All of the shown defects can also be clustered in larger defect centers.

Figure 3.2 shows simulation results of the vacancy distributions in silicon for different particle types and particle energies. The plots are projections over a cube with $1 \times 1 \times 1\,\mu m^3$ and correspond to a fluence of $10^{14}\,cm^{-2}$. The left plot shows the vacancies produced by $10\,MeV$-protons, the middle one for $24\,GeV$-protons, and the right one for $1\,MeV$-neutrons [huh01]. The ratio of high number of point defects to low number of cluster defects for proton irradiation reflects the low power dissipation of the coulomb interaction.

The displacement damage $D(E)$ can be calculated by:

$$D(E) = \sum_i \sigma_i(E) \int_0^{T_{max}} f_i(E,T)P(T)dT \tag{3.3}$$

with the cross section σ_i of the corresponding interaction and the probability $f_i(E,T)$ to have a collision of a particle with a kinetic energy E, which transfers a recoil energy of T. $P(T)$ is the Lindhardt

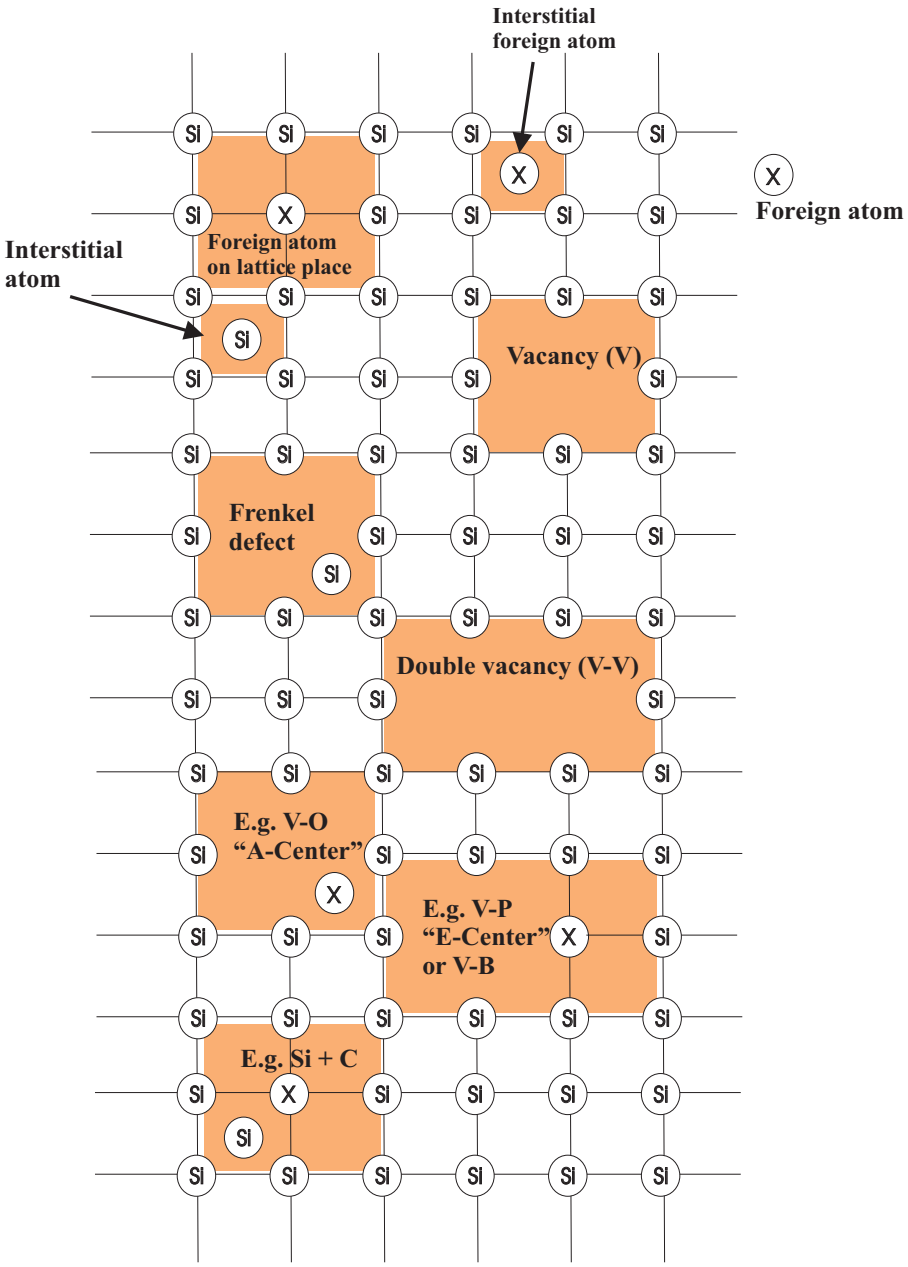

Figure 3.1: **Examples of different lattice damage in silicon:** *The variety of damage in the silicon lattice is large and therefore only a few examples are represented. Important damage caused by radiation are vacancies ”V” and oxygen containing damage structures like the ”A-Center”. All of this damage can also be clustered in large defect centers.*

Partition function [LN62] and gives the fraction of the energy going into displacement of a silicon atom. Table 3.2 shows the values of the Lindhardt partition function for several particles [huh01].

In order to simulate a certain particle fluence the **NIEL** (**N**on-**I**onising-**E**nergy-**L**oss) hypothesis is used to compare damage induced by different particle types and particle energies. The NIEL hypothesis relies on the assumption that the amount of damage scales linearly with fluence. The common

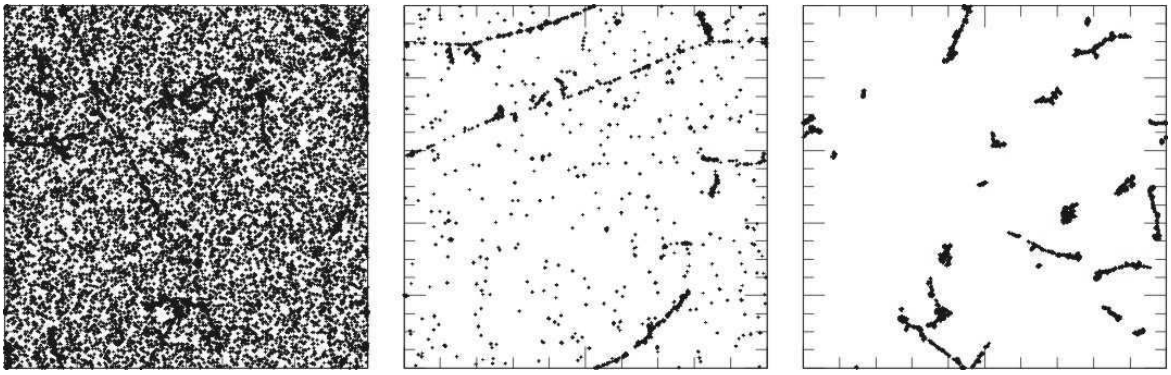

Figure 3.2: **Damage simulation in silicon:** *The plots are projections of a* $1 \times 1 \times 1\,\mu m^3$ *cube and show the projections of the initial distribution of vacancies produced by* $10\,MeV$*-protons (36824 vacancies, left),* $24\,GeV$*-protons (4145 vacancies, middle) and* $1\,MeV$*-neutrons (8870 vacancies, right) for fluences of* $10^{14}\,cm^{-2}$*. The high number of point defects produced by protons corresponds to the high cross section but low power dissipation of the proton's Coulomb field.*

Particle type	$P(T)$ %
p_{10MeV}	50
p_{24GeV}	42
n_{1MeV}	43

Table 3.2: **Lindhardt Partition function values for several particles [huh01]**

way to compare radiation damage is to scale all fluences to an equivalent fluence Φ_{eq}. The reference particles are neutrons with an energy of $1\,MeV$. Their corresponding displacement damage $D(1\,MeV)$ is $95\,MeV \cdot mb$ [LWM86]. The ratio of fluence to equivalent fluence is called hardness factor κ and is given by:

$$\kappa = \frac{\int D(E)\Phi(E)dE}{D(1\,MeV)\int \Phi(E)dE} = \frac{\int D(E)\Phi(E)dE}{95\,MeV mb \cdot \Phi} = \frac{\Phi}{\Phi_{eq}} \tag{3.4}$$

with the fluence $\Phi(E)$.

Unfortunately, many resonances are in this energy region of the neutrons, and the determination of the equivalent displacement damage is difficult. Figure 3.3 shows the summarized displacement damage for protons, electrons, neutrons and pions scaled to $95\,MeV \cdot mb$ from [Gri96][HuA93a][HuA93b] [Kon92][Sum93].

The kind of damage in an irradiated material can be determined by deep level transient spectroscopy (DLTS) or thermally stimulated current (TSC) measurement setups. The principle of TSC is to cool down the p-n-junction under reverse bias and the measured current is related to the steady state generation of defect levels close to the middle of the band gap level. At low temperature the defect level can be filled by illumination or forward bias. When heating up under reverse bias the TSC spectrum is recorded and at each temperature at which a peak is detected a defect level is emptied. This technique is proposed for samples irradiated to high fluences and does not depend on the resistivity [BBB94][Fei97]. For the DLTS measurement the p-n-junction is under reverse bias and the defect levels are filled by rapidly changing the bias voltage or by laser pulsing. The emission processes are observed and depend on the parameter one distinguishes C-DLTS for capacitance DLTS [Bra79], CC-DLTS for constant capacitance DLTS [MLK77], and I-DLTS for current DLTS [MG92]. These

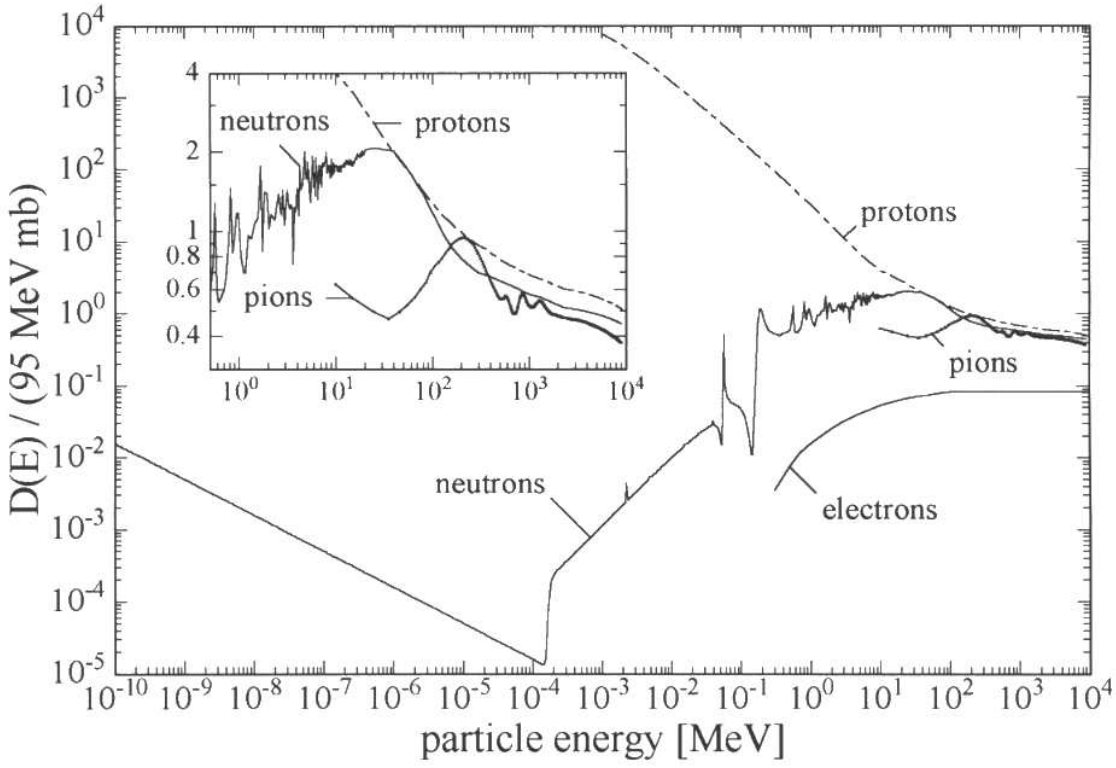

Figure 3.3: **Displacement damage of several particles versus energy:** *The displacement damage $D(E)$ is scaled to a reference of $1\,MeV$-neutrons. In the range from $0.1\,MeV$ to $10\,MeV$ neutrons have resonances, exacerbating the determination of $D(1\,MeV)$ [Gri96][HuA93a][HuA93b][Kon92][Sum93].*

measurements have the disadvantage that the defect concentration must be low in comparison to the effective doping concentration $N_t \ll N_{eff}$. A C-DLTS setup is used for the results in Section 6.5.4 where the defect levels of some sensors delivered from HPK are determined. A detailed description of the used setup and of the analysis method of the measured data can be found in [Mol99]. Since the defect concentration of the irradiated structures is too large (after type inversion, explained in Section 3.4), the characterization can be only be done in a qualitative way instead of a quantitative one.

3.2 Changes of Macroscopic Properties by Radiation

Defects with energy levels in the band gap can act as centers for generation and recombination of electron-hole pairs. Particularly for energy levels in the middle of the band gap, the probability for these processes is high. This results in an increase of the total leakage current with irradiation.

Another possible mechanism caused by the defects is the trapping of free charge carriers. They can be captured and are emitted after a comparatively large time. This process is undesired for the charge collection efficiency (CCE) of a particle detector, since the signal length in a silicon sensor has typically the length of a few *ns* and the time delay by trapping can be in the order of $\mu s - ms$.

Furthermore, the additional charges of the radiation damage affect the charge densities in the space

charge region. Therefore the full depletion voltage changes with irradiation. Table 3.3 shows some defect types in silicon with their possible charge states and their energy levels to the next less charged state. Contrary to the increase of leakage current the change of full depletion voltage depends on the initial doping concentration N_{eff}. Considering thermal equilibrium one gets for the electron and hole capture rates:

$$\begin{aligned} R_n &= \sigma_n v_{th,n} n_i N_d (1 - F(E_d)) \exp\left(\frac{E_F - E_i}{k_B T}\right) \\ R_p &= \sigma_p v_{th,p} n_i N_d (1 - F(E_d)) \exp\left(\frac{E_i - E_F}{k_B T}\right) \end{aligned} \tag{3.5}$$

and the electron generation rate

$$G_n = N_d F(E_d) \varepsilon_n \tag{3.6}$$

with

$$F(E_d) = \frac{1}{1 + \exp\left(\frac{E_d + E_F}{k_B T}\right)} \tag{3.7}$$

The emission probabilities are calculated to

$$\begin{aligned} \varepsilon_n &= \sigma_n v_{th,n} n_i \exp\left(\frac{E_d - E_i}{k_B T}\right) \\ \varepsilon_p &= \sigma_p v_{th,p} n_i \exp\left(\frac{E_i - E_d}{k_B T}\right) \end{aligned} \tag{3.8}$$

for electrons and holes, respectively. For low fluences the ratio of charge states in the space charge

Defect	Charge state	Energy level $[eV]$
Interstitial	I^-	$E_C - 0.39$
	I^0	
	I^+	$E_V + 0.4$
Vacancy	V^{2-}	$E_C - 0.09$
	V^-	$E_C - 0.4$
	V^0	
	V^+	$E_V + 0.05$
	V^{2+}	$E_V + 0.13$
Divacancy	V_2^{2-}	$E_C - 0.23$
	V_2^-	$E_C - 0.39$
	V_2^0	
	V_2^+	$E_V + 0.21$
A-Center	VO^-	$E_C - 0.18$
	VO^0	
E-Center	VP^-	$E_C - 0.18$
	VP^0	
Phosphorous	P^0	
	P^+	$E_C - 0.44$
Boron	B^-	$E_V + 0.45$
	B^0	

Table 3.3: **Energy levels of important defects in silicon:** *The energy levels have the same order of magnitude as the standard doping levels of phosphorus and boron.*

region can be calculated to

$$\frac{f^-}{f^+} = \frac{\varepsilon_n}{\varepsilon_p} = \frac{\sigma_n v_{th,n}}{\sigma_p v_{th,p}} \exp\left(2\frac{E_d - E_i}{k_B T}\right) \tag{3.9}$$

Defects with an energy above the intrinsic Fermi Level E_i have a higher electron emission probability. Energy levels below E_i prevail electron capturing. For heavily irradiated p-n-junctions the leakage current increases to large values and the charge ratio in this case is given by [Lut99]:

$$\frac{f^-}{f^+} = \frac{\varepsilon_n + pc_p}{\varepsilon_p + nc_c} = \frac{c_n n_i \exp\left(\frac{E_d - E_i}{k_B T}\right) + pc_p}{c_p n_i \exp\left(-\frac{E_d - E_i}{k_B T}\right) + nc_n} \tag{3.10}$$

The increase of leakage current is expected to be proportional to the sensor volume and to the equivalent fluence. The proportionality is expressed by the so named current related damage rate α, which is defined as [Wun92]:

$$\alpha = \frac{\Delta I}{V \Phi_{eq}} \tag{3.11}$$

Figure 3.4 shows the increase of leakage current density with fluence. After a heat treatment at $60°C$ for $80\,min$, the current related damage rate is $(3.99 \pm 0.03) \cdot 10^{-17} A/cm$ [Wun92]. The reason for the heat treatment is given in the next section. It has to be pointed out that the initial resistivity has no influence on the increase of leakage current density.

3.3 Current Annealing of Irradiated Silicon

Some of the defects mentioned above show an annealing behavior with time. Single defects can form complexes by migration and complexes can also dissociate. It is also possible e.g. that silicon atoms in Frenkel defects (see Figure 3.1) fall into the vacancies. Due to the large variety of the damage no single defects but their influences on the sensor parameters like leakage current and full depletion voltage are observed. Changes in these parameters (after irradiation) independent of the direction are called annealing. Figure 3.5 shows the change of the current related damage rate α with time and for different temperatures. The higher the temperature, the faster α anneals. Thus the current related damage rate is parameterized by [Chi95]:

$$\alpha(t, T_a) = \alpha_\infty \sum_i \frac{b_i}{b_\infty} \exp\left(-\frac{t}{\tau_i(T_a)}\right) \tag{3.12}$$

with the annealing temperature T_a. The corresponding coefficients are given in Table 3.4 [Mig01]. b_∞ and α_∞ are the stable components of the leakage current produced by irradiation and have to be

	τ_i	b_i
$i = 1$	$1.78 \cdot 10^1$	0.156
$i = 2$	$1.19 \cdot 10^2$	0.116
$i = 3$	$1.09 \cdot 10^3$	0.131
$i = 4$	$1.48 \cdot 10^4$	0.201
$i = 5$	$8.92 \cdot 10^5$	0.093
$i = 6$	∞	0.303

Table 3.4: **Parameters for leakage current annealing at room temperature [Mig01]**

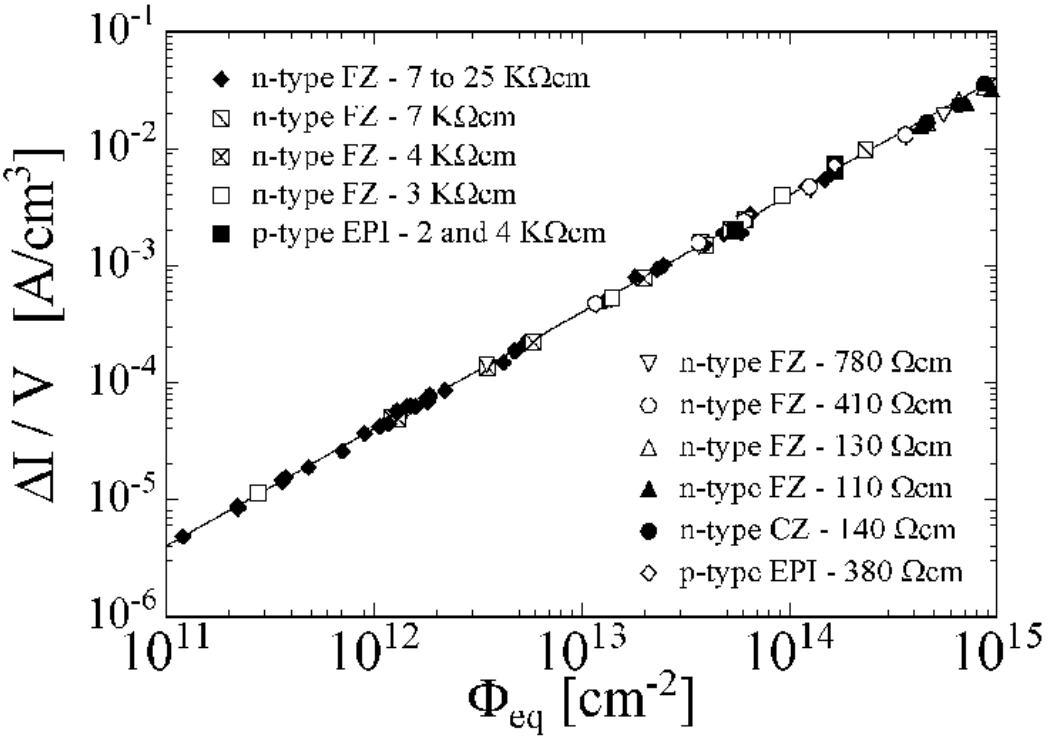

Figure 3.4: **Increase of leakage current density with fluence:** *The leakage current density increases linearly with fluence. The slope is called current related damage rate* α *(see Equation 3.11). After heat treatment at* $60°C$ *for* $80\,min$*, the value of* α *is* $(3.99 \pm 0.03) \cdot 10^{-17} A/cm$*. The resistivity of the silicon has no influence on* α *[Mol99].*

individually determined at each temperature. The different values for b_∞ and α_∞ can be explained with more available energy for annealing processes due to higher temperatures. In this work for not type inverted and for type inverted material (explained in the following section) the parameters given in Table 3.4 have been consistent and no differences have been observed as in [Wun92]. The explanation for this given in [Mol99] is that the active sensor volume for these measurements was not exactly defined (e.g. via a guard ring). The CMS sensors have a large active volume (see Table 1.1 and Table 1.2) and the length of the cut lines of the sensors play a marginal role. In addition, a guard ring surrounds the active volume. It defines the active volume by separating the currents of the cut lines from the inner sensor area.

For long annealing times above one year at room temperature the parametrization given by Equation 3.12 does not work anymore. It is most obviously seen in Figure 3.5, where no saturation for higher temperatures is seen. Therefore the following parametrization has to be used for the long-term annealing [Mol99]:

$$\alpha(t) = \alpha_I \exp\left(-\frac{t}{\tau_I}\right) + \alpha_0 - \beta \ln\left(\frac{t}{t_0}\right) \tag{3.13}$$

with the parameters given in Table 3.5. The time constants τ_I have been measured and determined with a Arrhenius plot to

$$\frac{1}{\tau_I} = k_{0I} \exp\left(-\frac{E_I}{k_B T}\right) \tag{3.14}$$

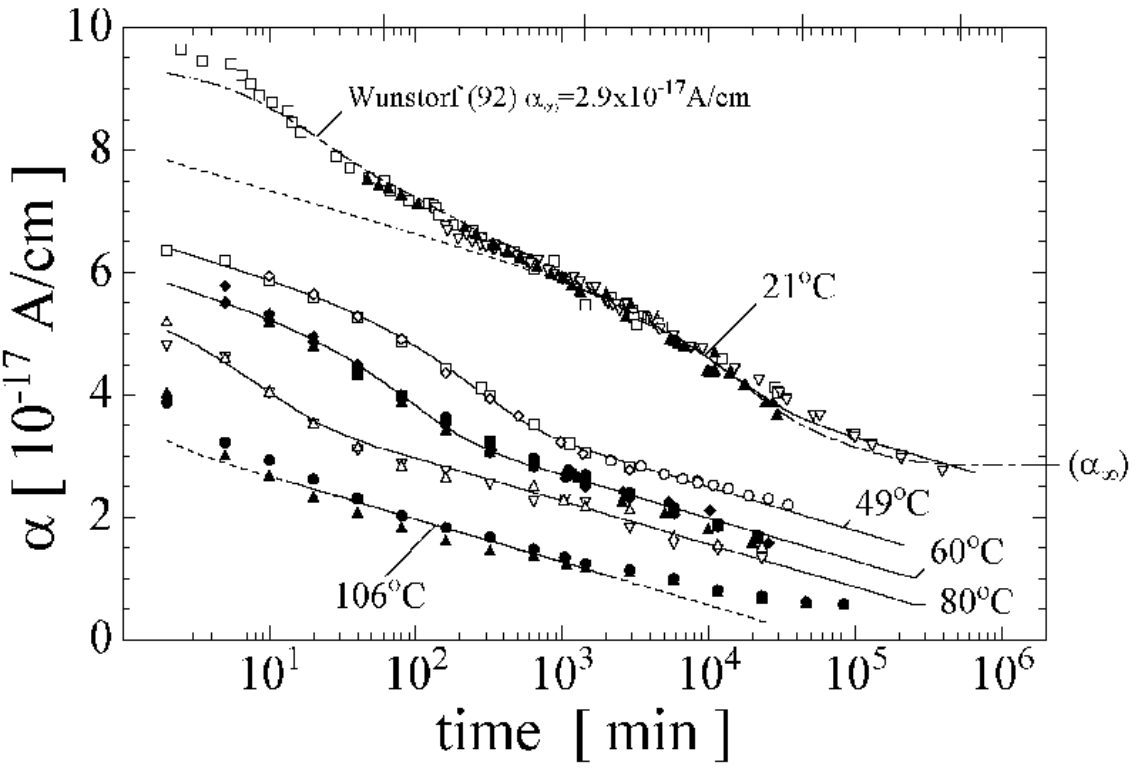

Figure 3.5: **Current annealing of irradiated silicon:** *The current related damage rate anneals with time. The saturation value* $\alpha_\infty = 2.9 \cdot 10^{-17} A/cm$ *is reached for* $21°C$ *after orders of* $10^5 min$*. For higher temperatures* α *can reach even lower values [Mol99].*

$T_{Annealing}$ $[°C]$	21	49	60	80
α_0 $[10^{-17}A/cm]$	7.07	5.36	4.87	4.23
τ_I $[min]$	140,000	260	94	9
α_I $[10^{-17}A/cm]$	1.23	1.28	1.26	1.13
β $[10^{-17}A/cm]$	32.9	31.1	31.6	28.3

Table 3.5: **Time constants for long-term current annealing:** *Below room temperature* τ_I *becomes larger than 100 days and the exponential term in Equation 3.13 vanishes, which means that hardly any annealing of the leakage current takes place any more. The fit parameter* t_0 *of Equation 3.13 is* $1 min$*.*

with $k_{0I} = 1.2^{+5.3}_{-1.0} \cdot 10^{13} s^{-1}$ and $E_I = 1.11 \pm 0.05 eV$. Nevertheless the following parametrization can be given for α_0 from the Arrhenius plot:

$$\alpha_0 = -(8.9 \pm 1.3) \cdot 10^{-17} \frac{A}{cm} + (4.6 \pm 0.4) \cdot 10^{-14} \frac{1}{T_a} \frac{AK}{cm} \tag{3.15}$$

An increase of the leakage current by annealing has never been observed and for a certain annealing step ($80 min$ at $60°C$) the current related damage rate seems to strictly follow the NIEL hypothesis.

3.4 Full Depletion Voltage Annealing of Irradiated Silicon

The full depletion voltage shows a completely different behavior with temperature than the leakage current. The effective doping concentration N_{eff} (see Equation 2.25 on Page 24) is changing with irradiation and time, but not only in one direction as the current related damage rate does. The change in the effective doping concentration can be described by the Hamburg model giving the following parametrization [Mol99]:

$$\Delta N_{eff}(\Phi_{eq},t) = N_C(\Phi_{eq}) + N_A(\Phi_{eq},t) + N_Y(\Phi_{eq},t) \tag{3.16}$$

The component $N_C(\Phi_{eq})$ is named stable damage and is given by the following equation:

$$N_C(\Phi_{eq}) = r_C N_{eff,0}(1-\exp(-c\Phi_{eq})) + g_C\Phi_{eq} \tag{3.17}$$

The first term describes an incomplete donor removal from initial resistivity $N_{eff,0}$ given to $|N_D - N_A|$. The parameter r_C is expected to be 0.65. The second term describes a linear increase of stable acceptors with fluence. The stable acceptor introduction rate g_C is found to be $1.49 \cdot 10^{-2}\,cm^{-1}$. The constant c depends on the initial doping concentration:

$$c = \frac{(10.9 \pm 0.8) \cdot 10^{-2}\,\frac{1}{cm}}{N_{eff,0}} \tag{3.18}$$

The production of acceptors causes a decrease of effective doping concentration for n-type silicon. After reaching the same concentration for acceptors as for donors the effective doping concentration is zero. Further irradiation produces more acceptors and the now higher acceptor than donor concentration results in a p-type like material. Therefore the point where the full depletion voltage is zero is also called point of type inversion. The full depletion voltage of n-type silicon versus fluence is shown in Figure 3.6.

No saturation of acceptor concentration is found for fluences up to $2.4 \cdot 10^{16}\,n_{1MeV}/cm^2$. In addition to the stable damage two further terms in Equation 3.16 describe the annealing behavior of silicon.

The beneficial annealing N_A is a sum of exponential decays of radiation induced damage:

$$N_A(\Phi_{eq},t) = \Phi_{eq}\sum_i g_{a,i}\exp\left(\frac{t}{\tau_{a,i}}\right) \tag{3.19}$$

In most cases these different exponential decays can be summarized to one final exponential damage decay with the time constant τ_a. This time constant can be expressed by a standard Arrhenius relation:

$$\frac{1}{\tau_a} = k_a = k_{0a}\exp\left(-\frac{E_{aa}}{k_B T}\right) \tag{3.20}$$

The value for the activation energy is $E_{aa} = 1.09 \pm 0.03\,eV$ and for the frequency factor it is $k_{a0} = 2.4^{+1.2}_{-0.8} \cdot 10^{13}\,s^{-1}$ [Mol99],[BL83]. The main difference between the beneficial annealing of full depletion voltage and leakage current annealing is the direction of the changes of the observed parameters. The full depletion voltage increases in n-type silicon before type inversion and decreases after type inversion, respectively.

In addition to the beneficial annealing there is a second process, named reverse annealing. Up to now different parameterizations of this process can be found in literature. A first order process means that the reaction rate of this process scales linearly with the defect concentration (observed in

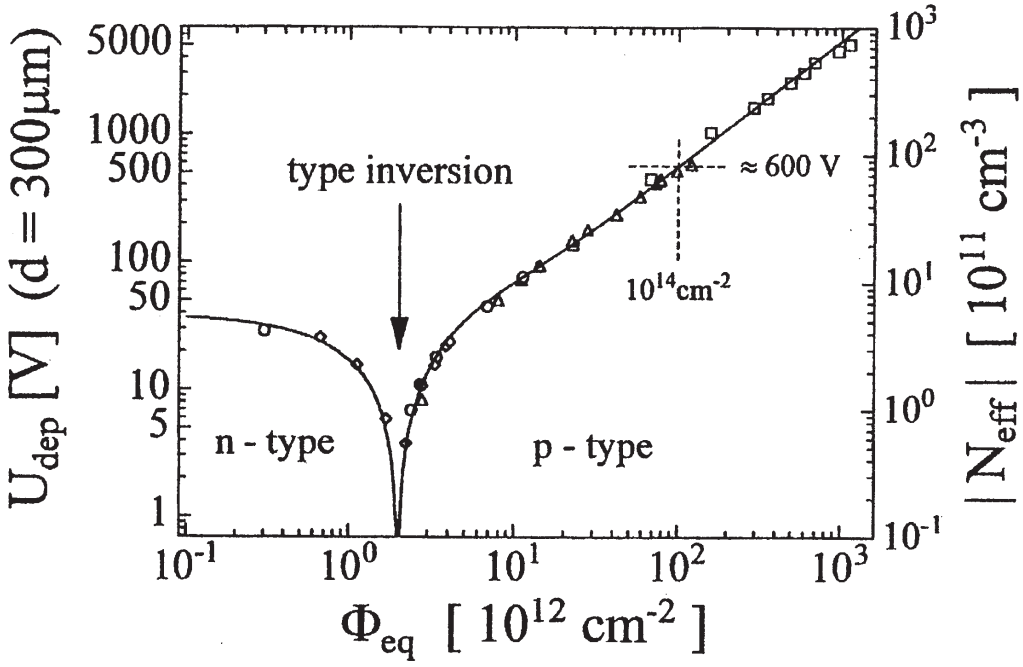

Figure 3.6: **Changes in the effective doping concentration with fluence:** *The effective doping concentration and therefore also the full depletion voltage changes with fluence. n-type silicon gets type inverted at a certain fluence by introduced acceptors and the full depletion voltage is decreasing. With further introduction of acceptors by irradiation the full depletion voltage after type inversion increases [Wun92].*

[ZLi95] and [Zio94]), since in a second order process (observed in [FFG94], [SFF94] and [Sch96]) the reaction rate depends on the square of the concentration of the corresponding defect.

The best fit for this process observed in this thesis is of second order:

$$N_Y(\Phi_{eq},t) = g_Y \Phi_{eq} \left(1 - \frac{1}{1+\frac{t}{\tau_y}}\right) \tag{3.21}$$

with the introduction rate $g_Y = (5.16 \pm 0.09) \cdot 10^{-2}\, cm^{-1}$. The time constant τ_y can be expressed by an Arrhenius plot as done before for the beneficial annealing time constant:

$$\frac{1}{\tau_y} = k_Y = k_{0Y} \exp\left(-\frac{E_Y}{k_B T}\right) \tag{3.22}$$

with $E_Y = 1.33 \pm 0.03\, eV$ and $k_{0Y} = 1.5^{+3.4}_{-1.1} \cdot 10^{15}\, cm^{-1}$.

It is not possible to measure both annealing terms independently since both processes cannot be separated by any temperature or other influences. Table 3.6 gives the annealing time constants of the beneficial and the reverse annealing at different annealing temperatures. It is obvious, that the reverse annealing gets important for longer annealing times whereas the beneficial annealing is dominating directly after the irradiation as shown in Figure 3.7.

$T_{Annealing}[°C]$	-10	0	10	20	40	60	80
beneficial annealing	$306d$	$53d$	$10d$	$55h$	$4h$	$19min$	$2min$
long-term reverse annealing	$516y$	$61y$	$8y$	$475d$	$17d$	$21h$	$92min$

Table 3.6: **Time constants of beneficial and long-term reverse annealing of full depletion voltage [Mol99]**

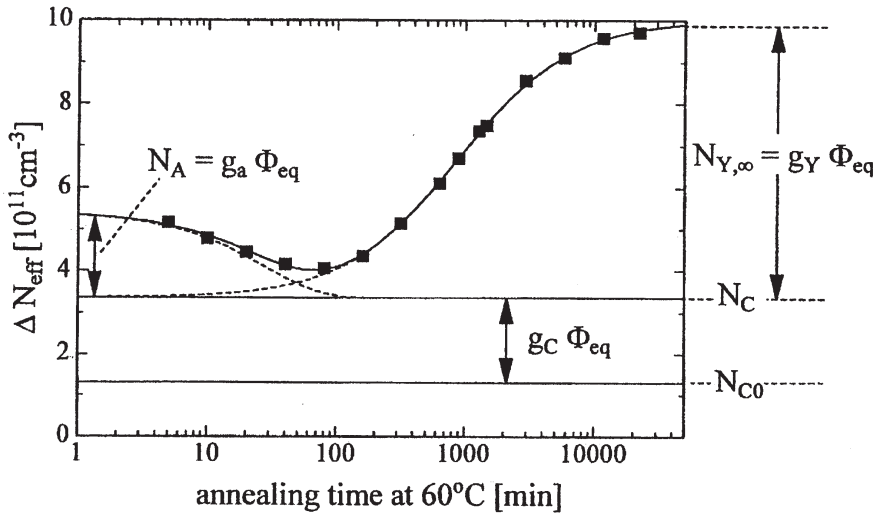

Figure 3.7: **Annealing of the effective doping concentration after irradiation:** *For fluences above type inversion the effective doping concentration is decreasing on a short time scale. The time constants of this beneficial annealing are given in Table 3.6. For much longer times the reverse annealing becomes important, whereas the beneficial annealing vanishes. The constant damage N_C is not changing with time [Mol99].*

The annealing process is not completely understood. Particularly in case of reverse annealing, the errors are quite large depending on material properties which were not mentioned so far. Annealing at higher temperatures causes problems to determine the introduction rate g_Y. It is necessary to keep the irradiated structure at room temperature for around $24h$, otherwise the full depletion voltage is higher than expected. This is caused by changes in the effective doping concentration by the temperature treatment. This fact is one of the reasons why a first order parametrization of the reverse annealing can be found in some literature, e.g. [Mig01]. Figure 3.8 shows the full depletion voltage versus equivalent fluence and annealing time.

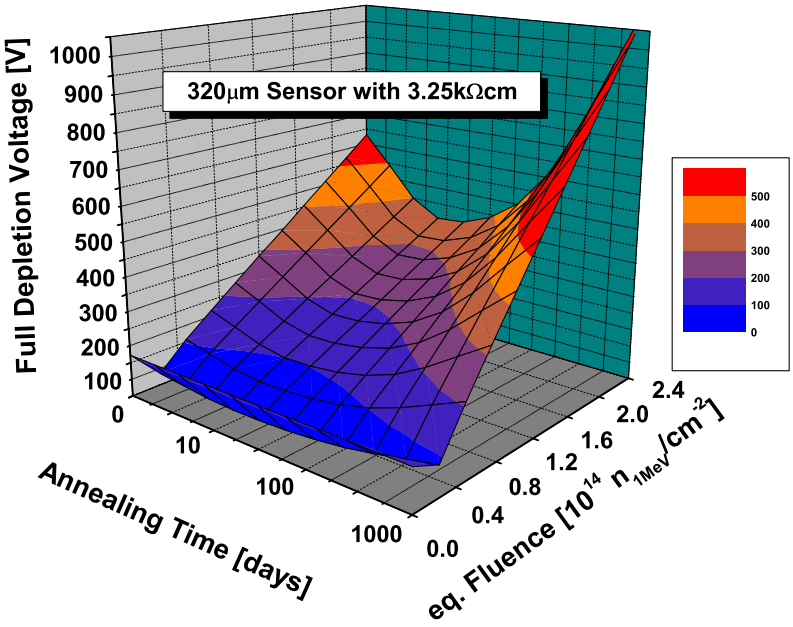

Figure 3.8: **Full depletion voltage versus fluence and annealing time:** *The full depletion voltage of n-doped silicon first decreases with fluence and increases after type inversion. After type inversion the full depletion voltage decreases with annealing time (beneficial annealing) and increases afterwards (long-term reverse annealing).*

Chapter 4

The Radiation Hard Silicon Strip Sensors of CMS

One of the central design issues of the CMS silicon tracker is its long-term survival in the harsh radiation environment of the LHC. A further design issue concerns the complexity of the sensor structures. The large amount of around 30,000 sensors to be purchased requires a low-cost and simple technology. The idea behind this approach is to have a number of suppliers which are able to produce a large number of high-quality sensors within a reasonable period of time because it is expected that the required large quantity of sensors cannot be produced by a single company.

In this chapter all design parameters of the CMS silicon strip sensors are summarized.

4.1 Basic Design of CMS Strip Sensors

The CMS sensors are single-sided sensors with p^+ strip implants on n-bulk, with poly crystalline bias resistors and AC coupling [Kra04][Har02]. The special features of the CMS sensors are: operation beyond the type inversion explained in Section 4.2, metal overhang design explained in Section 4.3, and use of $< 100 >$ orientated silicon explained in Section 4.4. The geometry of the CMS silicon strip tracker and the available wafer size, which was $6''$ at that time, determine the requirements as to sensor lengths, widths and geometries. The thickness of the sensors is either $320\mu m$ or $500\mu m$ (see Section 4.2). The pitch p depends on particle track resolution requirements and the number of 128 channels available at one readout chip, which results in $4 \times 128 = 512$ or $6 \times 128 = 768$ strips per sensor. All these parameters have been summarized in Table 1.1 and 1.2 on Page 10. The components of the CMS silicon strip sensors are explained below [Spe00]. Characteristics of the components are summarized in Table 4.1.

- **Bulk**

  The CMS sensors are produced on $6''$ n-doped silicon wafers. The resistivity, the thickness and the choice of n-type silicon are explained in Section 4.2. It has to be noted that high voltages of a few hundred volts will be necessary to operate the sensors.

- **Bulk Orientation**

  The wafers orientation is $< 100 >$. The advantages of this material are explained in detail in Section 4.4 on page 54.

- **Strip implants**

  strip implants are realized by p^+ doping one side of the wafer whilst the surface of the other side is not textured (see backside contact).

- **Strip width to strip pitch ratio**

  The strip width to strip pitch ratio w/p is 0.25 for all sensor geometries. This results in a uniform capacitance between two adjacent strips because the ”interstrip capacitances” result from the distribution of the electric field.

- **Backside contact - ”backplane”**

  The non-textured side of the sensors, named backplane, has a n^{++} layer with a thickness of a few μm and an aluminium coverage. The function of this n^{++} layer is to provide an ohmic contact between the sensor bulk and the aluminium layer on the backplane to which a high potential can be applied (see Section 2.5 on Page 26). The heavily n-doped layer is not depleted since the voltage in the lower doped bulk region drops. For this reason, the effective readout thickness of the sensors is less than the wafer thickness.

- **Coupling capacitance**

  Layers of SiO_2 and Si_3N_4 cover the whole textured side of the bulk and isolate the p^+ implants from the aluminium strips above. These p^+ strips are then AC coupled to the readout electronics. For this reason, the wider ends of the strips which are used for contacting the aluminium strip via micro bonds to the readout electronics are called AC pads. The resulting capacitance between an aluminium strip and a p^+ implant has to be as large as possible in order to minimize the resistance for the signal. For noise reasons, the magnitude of the coupling capacitance must exceed the sum of the two interstrip capacitances between two adjacent strips and the strip's capacitance between the strip implant and the backplane (see Section 2.10 on Page 32) Since the capacitance has to be large, the thickness of the dielectric has to be as low as possible. For this reason it is not possible to apply a high voltage drop at the coupling capacitances.

- **Bias ring**

  The bias ring is a p^+ implant ring which encloses all strip implants. It is connected with small aluminium connections, termed ”vias”, to an upper aluminium ring which encloses all aluminium strips. The p^+ ring acts as guard ring (described below) and the aluminium ring acts as low potential contact. It is connected to the p^+ strip implants via bias resistors.

- **Bias resistors**

  The connection from the p^+ strip implants to the aluminium bias ring is accomplished with bias resistors. The reason of using bias resistors is to apply a variable potential to the strip implants. These ohmic resistors are made of heavily doped poly crystalline silicon (see Section 2.7 on Page 30). They are applied on top of the isolating layer between the aluminium structures and the implants and they are connected to the strips with aluminium vias. The upper part of the vias is enlarged in order to enable contacting micro bonds or needles and is called DC pad. Within one sensor, the bias resistors should have uniform values as they define the potential on the p^+ implants. The potential should be the same on all strips. The lower resistance limit of the bias resistors is determined by noise considerations (see Equation 2.58 on Page 33). In addition, the complete resistance range results from the requirements of the RC constant of the bias resistors and the coupling capacitances.

- **Guard ring**

  The guard ring encloses the bias ring and like the bias ring it has a p^+ ring implant and an aluminium ring which are connected to each other with vias. Its inner side has to form the electric field around the bias ring. Together, the bias ring and the guard ring form an electric field in order to obtain an electric field for the outer strips in the same way as an electric field is provided for the inner strips by their neighbours. The outer side of the guard ring has to adjust the electric field distribution towards the edges of the sensors. In contrast to the bias ring, the guard ring is operated in floating mode, i.e. it is not connected to a preset potential. Normally, multiple guard ring designs are used to adjust the voltage drop step by step. Thanks to the metal overhang design (see Section 4.3) just one extended guard ring is necessary for smoothly adjusting the potential.

- **Outer n^+ ring**

  A n^{++} ring implant located at a distance to the bias ring of $1140\,\mu m$ ($1500\,\mu m$) longitudinally and $1000\,\mu m$ ($1350\,\mu m$) orthogonally to the strip direction for $320\,\mu m$ ($500\,\mu m$) encloses the sensitive area including the guard ring and the bias ring. It is operated in floating mode like the guard ring and its mission is to avoid the flow of high currents from the outer edges into the active inner area of the sensor. The n^{++} ring implant is connected with vias to an aluminium structure above the isolating layer which contains special marks for alignment and the strip numbers.

- **Passivation layer**

  On top of the sensor a passivation layer protects the sensor surface. It is chemically removed in those areas where electrical contact has to be made by means of micro bonds or probe needles.

Figure 4.1 shows the basic design of a CMS sensor.

The sensors will be operated at a temperature below $-10°C$ in order to keep the leakage current and therefore the power consumption low and to avoid annealing effects. After irradiation at this temperature, a maximum leakage current of approximately $1\,mA$ is expected for a single sensor. With a maximum available voltage of $600\,V$ the power consumption will be approximately $600\,mW$ per sensor. If the power consumption becomes too high, i.e. if the sensor heat cannot be removed by cooling, the leakage current increases. When this happens, the power consumption and the sensor temperature becomes even higher. If the power consumption exceeds the capacity of the power supplies, the voltage becomes unstable and the sensor cannot be operated anymore. This scenario is referred to as "thermal runaway". In this case, the tracker has to be switched off and after cooling down to a lower temperature it can be operated again. The power supply limit of $600\,V$ also limits the full depletion voltage. If the required overdepletion of the detector modules is taken into account ($50\,\%$), the final full depletion voltage has to remain below $400\,V$.

4.2 Thickness and Resistivity

On one hand, the thickness of the CMS sensors should be as high as possible to get a high signal. On the other hand, the tracker mass has to be minimized in order to keep the radiation length in the tracker as low as possible.

The full depletion voltage depends on the square of the sensor thickness and the effective doping concentration (see Equation 2.25 on Page 24). Since the acceptor concentration increases with fluence

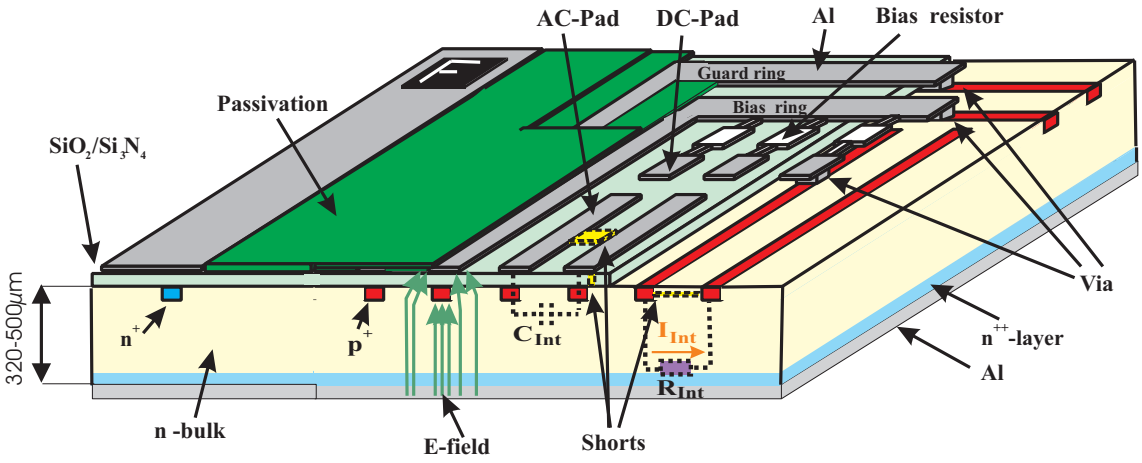

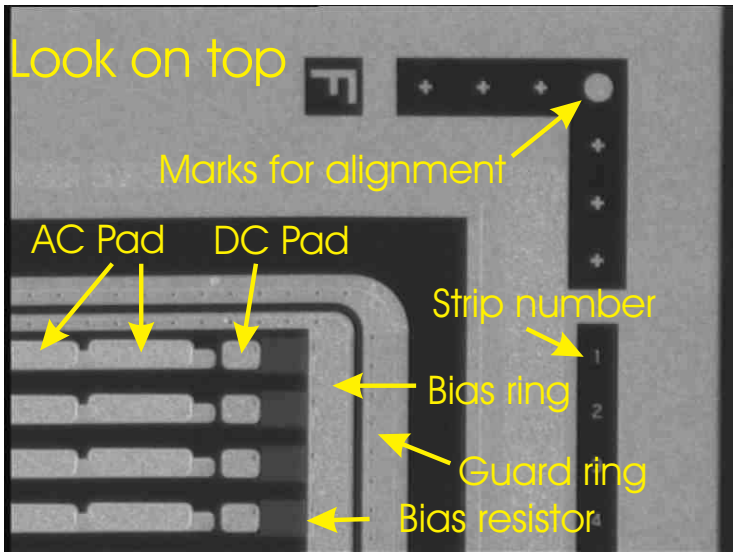

Figure 4.1: **Principle design of a CMS sensor:** *The CMS sensors are single-sided sensors with p^+ strip implants on n-bulk, with poly crystalline bias resistors and AC coupling [Kra04][Har02]. The bias ring and the guard ring enclose the strip implants. Since the bias ring is connected to low potential the guard ring is floating. Both define the active volume of the sensor and they are responsible for the adjusting of the field configuration to the edges. The backside of the wafer has a heavily doped n^+ layer between the bulk and the aluminium layer which avoids a Shottky contact. The outer n^+ ring encloses the guard ring and avoids the flow of edge currents into the active inner area of the sensors. The ends of the aluminium strips are wider than the strip and are called AC pads. The p^+ implants are connected with aluminium vias to the bias resistors connecting the bias ring. The upper enlarged part of the vias which is used for contact is called DC pad. The metal strips have a $4\,\mu m$ larger width than the p^+ implants. This metal overhang shifts the breakthrough mechanism to high voltages (far beyond full depletion voltage) of the p-n junctions by moving the points of highest electric field density into the isolating layer.*

for p-type silicon, the full depletion voltage also increases. For this reason, the CMS sensors are produced from n-bulk. In this material, the full depletion voltage decreases with fluence prior to type inversion and increases afterwards as summarized in Section 3.4. The best full depletion voltage scenario for the defined service life of ten years is that full depletion voltages are the same level before and after irradiation. Together with an acceptable signal to noise ratio (SNR) after irradiation, which should be above ten for minimum ionizing particles in deconvolution mode (see Section 4.5 on Page 55), the following values are required for the resistivity and the thickness of the sensors.

The resistivity range is $1.25\,k\Omega cm$ to $3.25\,k\Omega cm$ for the inner barrel sensors. They have a thickness of $320\,\mu m$. The sensors in the outer barrel have a resistivity of $4\,k\Omega cm$ to $8\,k\Omega cm$ and their thickness is $500\,\mu m$. The reason to use two different thicknesses is the number of sensors on a detector module which is either one for inner barrel detector modules or two for outer barrel detector modules. Therefore, the outer barrel detector modules have a higher interstrip capacitance and therefore a higher noise level which has to be compensated by a greater signal which can be increased with larger thickness of the bulk.

For both combinations of thickness and resistivity, the initial full depletion voltages are between $100\,V$ and $300\,V$ and the final full depletion voltages are expected to be in the same range after ten years of service life at the LHC. Scenario calculations for all CMS sensor geometries can be found in appendix C.

4.3 Metal Overhang Design

The electric field in a p-n junction depends on the full depletion voltage and the overdepletion, i.e. the difference between the applied bias voltage and the full depletion voltage. When the voltage increases while it is still below the full depletion voltage the depletion zone becomes larger until it reaches the borders of the sensors' p-n junction. For voltages above the full depletion voltage, the density of the electric field increases with increasing voltage. High electric field densities lead to a fast drift of charge carriers and reduce the chance of trapping. At a certain voltage level, the charge collection efficiency does not longer increase and higher voltages will not have further advantages. The best signal to noise ratio of CMS sensors is achieved for bias voltages which are 50 % higher than the full depletion voltage [Wei04].

For this reason, the safety margin between the full depletion voltage and the breakthrough voltage has to be as large as possible. In order to achieve a high breakthrough voltage, a design termed "metal overhang design" is used for the CMS sensors. The aluminium strips on top of the p^+ implants are $4\mu m$ wider than the implants below the dielectric layer. Figure 4.2 shows the principle of the metal overhang design. The metal overhang moves the maximum electric field density areas, which are expected to be around the implants, into the dielectric layer. Here a breakthrough mechanism like the avalanche or Zener effect is suppressed since there is only a negligible number of free charge carriers due to the high band gap. The bias ring and the guard ring also have a metal overhang. The outer side of the guard ring has an overlap that is significantly larger than $4\,\mu m$. This equalizes the high potential of the surrounding n^{++} ring continuously to ground potential in the same way as in earlier experiments which used multiple guard ring structures.

Below $1300\,V$ - tested several times -, the lower electric field density prohibits a breakthrough. This makes it possible to heavily overdeplete the sensors and the current full depletion voltage does only influence the charge collection efficiency which is best above 50 % overdepletion.

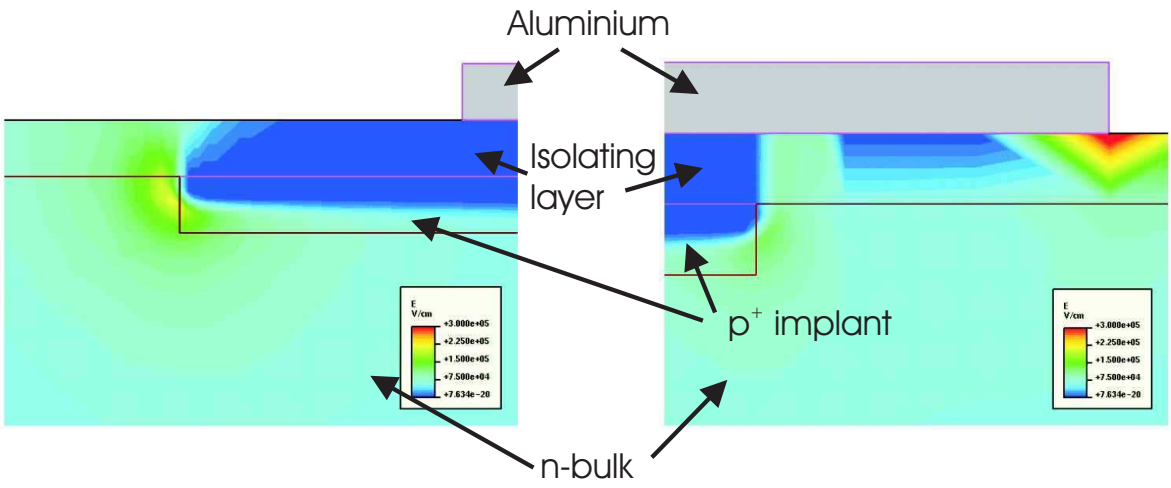

Figure 4.2: **Principle of the metal overhang design:** *The two pictures show results of electric field density calculations done with a simulation software (ISE-TCAD). In both cases the p-n junction is heavily overdepleted. The picture on the left side shows the results for an AC coupled strip without a metal overhang. Here the area of highest electric field density is within the bulk and can cause avalanche or Zener effects. The picture on the right side shows the results for an AC coupled strip with aluminium overhang. The area of highest electric field density is within the isolating layer and owing to the very low number of free charge carriers no breakthrough is caused by the electric field [Die04].*

4.4 The Reason for Using $< 100 >$ Orientated Silicon

Radiation damage affects the interstrip capacitance and the interstrip resistance of a sensor. This influence can be kept low by using silicon with $< 100 >$ orientation instead of $< 111 >$ orientation. Figure 4.3 schematically shows $< 111 >$ and $< 100 >$ orientated silicon. $< 100 >$ silicon has the advantage of less dangling bonds than $< 111 >$ silicon because a smaller number of charge carriers is present in the silicon and silicon dioxide interface. The interface structure of $< 100 >$ silicon allows a lower two-dimensional charge carrier density σ_{int} (see Equation 2.40 on Page 27). The initial quality of the interface can be tested by means of capacitance versus voltage characteristics on MOS structures as described in Section 2.6. Examples of those characteristics can be found in Figure 6.50. A small number of dangling bonds (i.e. charge carriers) results in a low initial flat band voltage (see Equation 2.42 on Page 29).

Radiation increases the number of positive charge carriers in silicon dioxide and silicon nitride whilst the negative charge carriers can move out of the isolating layer owing to their high mobility (see Table 2.1 on Page 15). The positive charge carriers can only move slowly towards the silicon and silicon dioxide interface (in this case also called surface [Sze85]) due to their low mobility, where they are trapped. The electric field of the trapped charge carriers near the surface influences the electric field below the dielectric layer (Equation 2.40) and causes an increase in surface currents and interstrip capacitances. Then strong electric fields are necessary to reduce the influence on the charge carriers' electric field. It has to be taken into account that the charge concentration at the interface levels off at doses of approximately $50\,kGy$ [Wue01]. It is pointed out here, that the advantage of the $< 100 >$ silicon is only exploitable with a perfectly grown silicon dioxide with a very low amount of impurities.

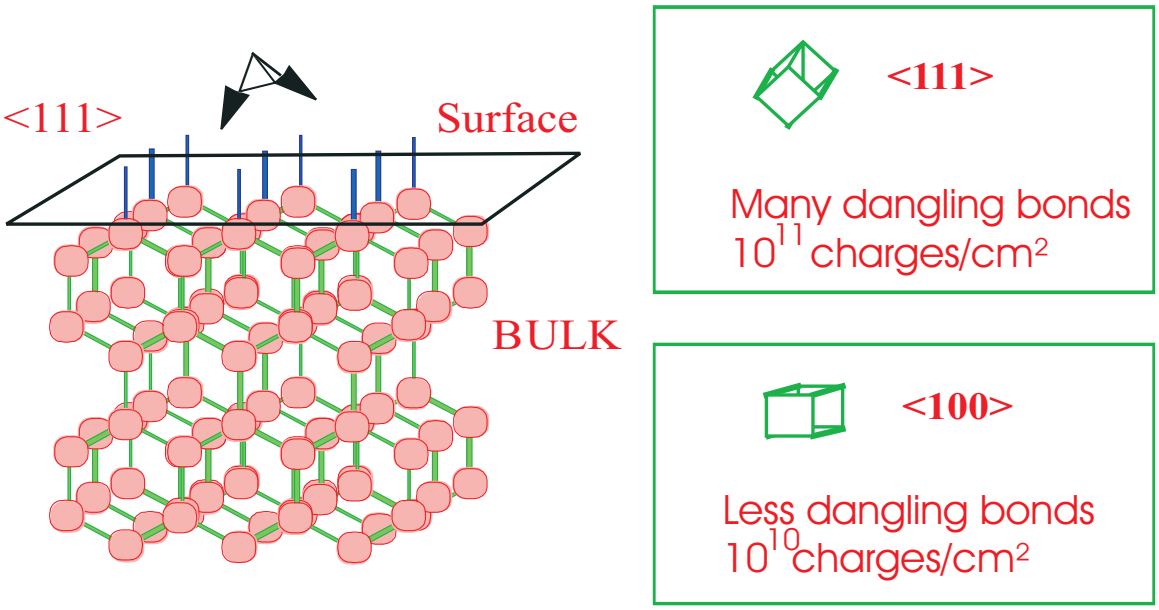

Figure 4.3: **Silicon in $< 111 >$ and $< 100 >$ orientation:** *Standard silicon delivered by industry has $< 111 >$ orientation. For special requirements also $< 100 >$ oriented silicon is available. The advantage is, that $< 100 >$ silicon has less dangling bonds than $< 111 >$ silicon and therefore it has less surface currents. This fact results for $< 100 >$ silicon in a lower increase of interstrip capacitance and lower decrease of interstrip resistance in a sensor with fluence than for $< 111 >$.*

4.5 Signal Readout on Detector Level

The CMS detector modules consist of carbon fibre frames supporting one or two sensors and the read out electronics, hosted on a front end hybrid. Analog readout chips, called APV25, are used. The APV25 readout channels are connected via micro bonds to the aluminium strips of the sensor and apply, with respect to the bias ring potential, $0.75\,V$ to the strips. The APV25 chips are designed for low noise and fast signal readout in high radiation environments. The employed $0.25\,\mu m$ CMOS technology proved to be sufficient radiation hard for the LHC radiation environment. The preamplifiers shape the signal pulse (with a CR-RC filter), which results in well defined voltage pulses with a rise time of $50\,ns$ which are proportional to the accumulated charge. These pulses are sampled every $25\,ns$ and stored in one of 192 pipeline cells for each readout channel. There, the data can be stored for $4.8\,\mu s$ and can be read out e.g. if a signal in the outer calorimeters or muon chambers appears (e.g. two high-energy tracks in the muon chambers) and a trigger signal is sent to the tracker [Sgu04]. Two APV25 modes, peak and deconvolution mode, are selectable for signal processing. In the peak mode, the shaped signals have a rise time of $50ns$ and an adjustable width between $100\,ns$ and $150\,ns$. The CMS bunch crossing time of $25\,ns$ provokes signal overlaps from two consecutive particles traversing the sensor. Latency has to be adjusted for the use of the peak value. In the deconvolution mode, the shaped signal is folded to $25\,ns$. The disadvantage of the deconvolution mode, i.e. a reduced signal height and thus a smaller SNR ratio, is compensated by a unique allocation of consecutive events. Therefore, in CMS only the deconvolution mode will be used for data acquisition [Jon99].

4.6 Design of CMS Test Structures

An extremely important task of the CMS collaboration consists in inspection the quality of the sensors and the compliance with the acceptance criteria. As irradiation tests are destructive and sensor costs are high, a more economic solution was developed. The remaining area of the wafer is filled with different test structures for monitoring different sensor and bulk properties. After cutting the wafer the remaining parts of the wafer, called half moons, are delivered by the suppliers together with the sensors.

In order to compare the behaviour of the wafer material and to control the production process - independently of sensor geometries - each wafer has diodes with an area of 7 x 7 mm^2, a mini sensor with an area of 26.5 x 18.8 mm^2 and identical geometry (except for the two different thicknesses of inner and outer barrel sensors), and MOS structures [CTS00]. A further test structure contains eleven poly crystalline resistors like the bias resistors. The advantage of this test structure is that no connection to an implant below the dielectric is present and no bulk current corrections are required (explained in Section 5.3.4 on Page 65). There are more structures on the wafer which are not used in this thesis. These are used in the Process Quality Control centers of CMS for measurements of surface currents (Gate Controlled Diodes - GCD), for measurements of interstrip resistances or capacitances, and for measurements of aluminium or implant resistivity. A detailed description of the remaining structures can be found at [Spe00][Kra03].

Figure 4.4 shows a standard half moon with the mini sensor, the diode, two MOS structures used for monitoring of surface properties, and two structures with eleven poly crystalline bias resistors. The left MOS structure has a silicon dioxide layer having the thickness of the interstrip region (vendor STM, see end of this chapter) of the sensor or of the region below the aluminium strips (vendor HPK, see end of this chapter). The thickness of the right MOS structure on each half moon is the same as below the aluminium strips of the sensor.

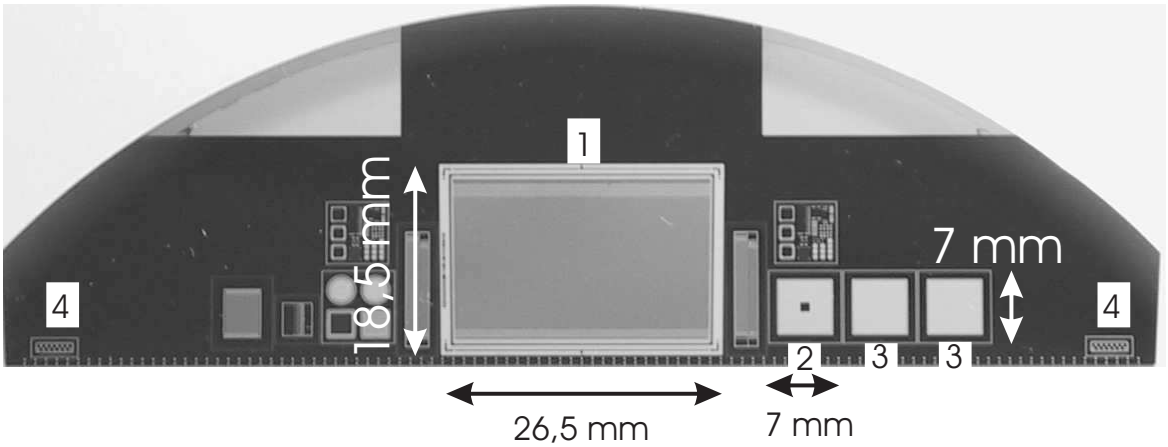

Figure 4.4: **Standard half moon of a CMS wafer:** *The CMS wafer contains in addition to the sensor four half moons. One of these half moons, called standard half moon, contains a mini sensor (1) with the same principle design of the sensor but with fix rectangular strip geometry. The rectangular devices are the standard diode (2) and two MOS (3) structures with oxide thicknesses from the region between the strips and below strip regions of the sensor. Structure (4) contains eleven bias resistors without contact to any implants.*

Parameter	Before irradiation	Tolerance	After irradiation
Resistivity $500\,\mu m$ $320\,\mu m$	 $4,0-8,0\,k\Omega cm$ $1,5-3,0\,k\Omega cm$		
Breakthrough voltage	$>500\,V$		$>500\,V$
Total leakage current slope	$<10\,nA/cm^2$ at $450\,V$ $<100\,nA/V$ between $450\,V$ and $550\,V$		$<30\,\mu A/cm^2$ *at* $500\,V$ and $T=-10^{\circ}C$
Bias resistor Variance from average	$1,5\,M\Omega$	$\pm 0,5\,M\Omega$ $\pm 0,3\,M\Omega$	
Interstrip resistance	$>1\,G\Omega$		$>20\,M\Omega$
Interstrip capacitance	$<1,2\,pF/cm$		$\pm 10\,\%$
Coupling capacitance	$1,2\,pF/cm\mu m$		$\pm 10\,\%$
Strip leakage current	$<100\,nA$ at $400\,V$		
Pinhole (short in coupling capacitance)	$<1\,nA$ at $10\,V$ applied to coupling capacitance		

Table 4.1: **Parameters and limits of the CMS sensors:** *The full depletion voltage, which has to be* $100-300\,V$*, is tested instead of the resistivity. [Spe00]. A sensor is rejected to the supplier if the breakthrough takes place below* $500\,V$ *bias voltage, or the full depletion voltage is out of range, or if more than* $1\,\%$ *of strips have failures.*

4.7 Summary of CMS Sensor Parameters

The CMS sensors are manufactured from n-doped wafers with p^+ strip implants. They contain poly crystalline silicon bias resistors and AC coupling. The strips are enclosed by a bias ring and a guard ring which act as a multiple guard ring structure. The special features of the CMS sensors of which some have never been used in an experiment before are:

- The use of $<100>$ orientated silicon for low surface currents and low increase of interstrip capacitance with irradiation
- The use of a metal overhang design for breakthrough voltages above $500\,V$
- The operating temperature below $-10^{\circ}C$ to avoid annealing effects of irradiated silicon and to keep the total leakage current low in order to reduce the power consumption and to avoid thermal runaway

Table 4.1 summarizes all important parameters of the CMS sensors.

Measurement of parameters will be explained in the next chapter which describes the quality assurance system of the CMS collaboration. Eventually, only two sensor manufactures were accepted to supply sensors for the CMS tracker. Hamamatsu Photonics Company (HPK) in Hamamatsu-City (Japan) supplied all ”thin” inner barrel sensors with a thickness of $320\,\mu m$. The ”thick” outer barrel sensors with a thickness of $500\,\mu m$ were to be supplied by ST Microelectronics (STM) in Sicilia (Italy). The following chapters will discuss problems with the sensors supplied by STM and HPK. As not all problems of the STM sensors have been solved, the CMS collaboration decided to purchase a much larger quantity of sensors from HPK than initially planed.

Chapter 5

Sensor Quality Assurance in CMS

Large scale production of the CMS sensors calls for a reliable quality assurance concept in the participating institutes. For time and cost reasons, the CMS collaboration has to trust in large parts in the vendors quality assurance. Measurement of all sensor parameters for quality control purposes would require too much time because of the large number of parameters involved. The CMS collaboration decided to test the quality of the sensors by taking samples of each batch. The entire batch must have been obtained from a single ingot. Provided that no defects are found in this random sample test, the batch is accepted and the sensors are sent to the gantries, where the first step of detector module production starts. This chapter presents the CMS standard quality assurance program and discusses problems found on some sensors during the production phase [Agr03].

5.1 Standard Quality Assurance in CMS

The sensors are produced by two companies, Hamamatsu Photonics Company (HPK) in Hamamatsu-City (Japan) and ST Microelectronics (STM) in Sicilia (Italy). All sensors are delivered to the Distribution Center at CERN. Here, the sensors are equally distributed to the four Quality Test Centers (QTC) which are located at Pisa, Perugia, Vienna and Karlsruhe. From each Quality Test Center, a small number of approximately 1% of the sensors and 5% of the standard test structures are sent to the two Irradiation Qualification Centers (IQC) at Karlsruhe and Louvain-la-Neuve for radiation hardness inspection. Another 5% of the test structures are sent to Pisa and Strasbourg for bonding tests and a further 5% are sent to the Process Qualification Centers (PQC) at Strasbourg, Vienna and Florence, where the uniformity of the process parameters is tested. In addition, the PQCs inspect a small number of sensors at operating voltage to test the long-term stability of the total leakage current (test duration $72\,h$). A schematic of the logistic system is shown in Figure 5.1.

5.2 Measurements performed in the Quality Test Centers and in the Irradiation Qualification Centers

In the QTCs, the sensor properties are measured directly. The radiation hardness is tested in the IQCs by measuring the sensors and the test structures before and after irradiation with the fluence that is expected in the silicon strip tracker after ten years of service life.

Prior to irradiation, measurements are performed at $20 \pm 1^{\circ}C$ and at a relative humidity below 30% because the leakage currents are low under these conditions. Leakage currents are high after

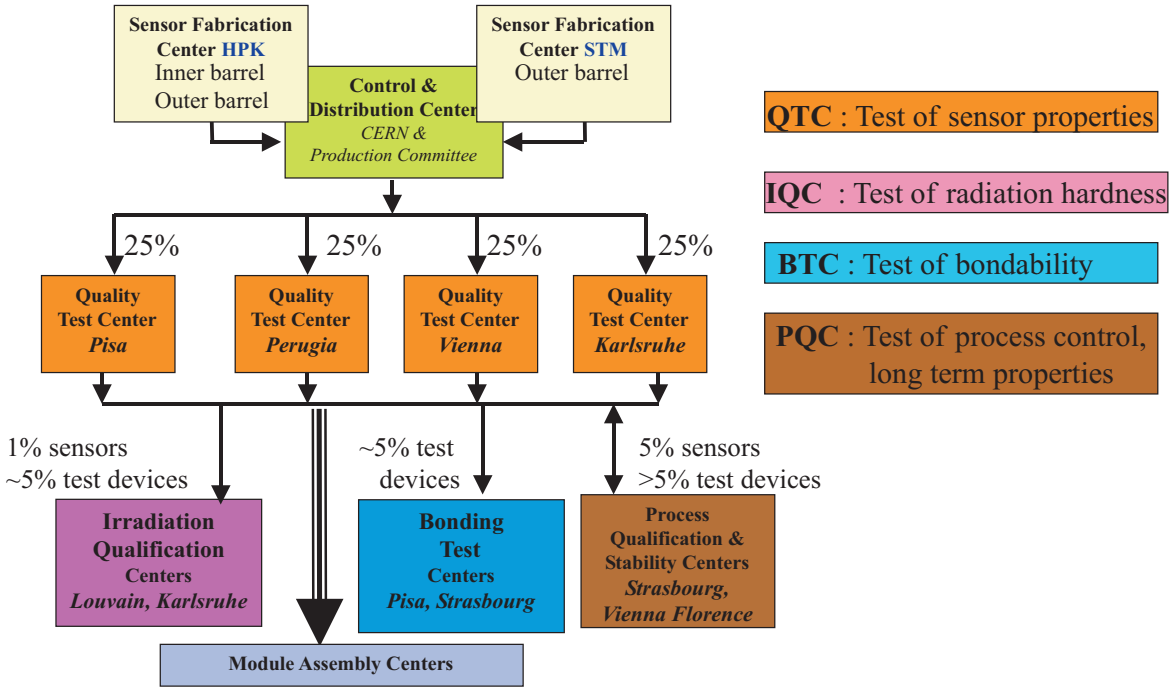

Figure 5.1: **The logistic system of the CMS sensor quality assurance:** *The two suppliers, HPK and STM, deliver the sensors directly to CERN, where the sensors are distributed to the four Quality Test Centers (QTC). There, the sensors are tested for their functionality. An amount of approximately 1% is sent to the two Irradiation Test Centers (IQC) for radiation hardness inspection. Approximately 5% of the test structures are sent to the Process Quality Test Centers (PQC) in order to test various process parameters during the production phase. The Bonding Test Centers (BQC) test the mini sensors for their suitability for bonding. If all Centers declare the delivered sensors as acceptable they are sent to the gantries, where the first detector module production step is performed.*

irradiation, as described in Section 3.1, and undesired annealing effects begin to occur. Therefore, all measurements which take place after irradiation are performed at a low temperature of $-10°C$. A low relative humidity during cold measurements avoids condensation of air humidity and therefore ice on the sensors.

The standard measurements for both QTC and IQC are:

- total leakage current versus bias voltage (IV)
- total capacitance versus bias voltage (CV)
- single strip leakage currents (ILeak)
- bias resistors (Rbias or Rpoly)
- coupling capacitances (CC)
- shorts between strips
- shorts between implants and aluminium strips (Pinhole)
- interstrip resistances (Rint, only done in IQC)

- interstrip capacitances (Cint, only done in IQC)

The names in brackets are abbreviations used by the CMS collaboration. Two abbreviations are in use for the bias resistors. Rbias describes the function of the poly resistor and Rpoly stands for the structure of the resistor (poly crystalline silicon, see Section 2.7 on Page 30).

IV is a ramp versus the bias voltage in increments of $5\,V$ from $0\,V$ to $550\,V$ before irradiation and up to $800\,V$ after irradiation. CV is a ramp versus the bias voltage in increments of $5\,V$ with the upper bias voltage of $350\,V$ before irradiation and $500\,V$ after irradiation. All the strip parameters are measured at $400\,V$ bias voltage. In addition, the IQCs subject a number of random sample strips to a ramp test of strip parameters versus bias voltage (up to $600\,V$) in order to determine e.g. the saturation voltage of single strip parameters like the bias resistor, the leakage current, the coupling capacitance, the interstrip capacitances or the interstrip resistances.

5.3 Measurement Setups in Karlsruhe - The Probe Stations

In Karlsruhe two dedicated probe stations designed and built in the institute are used for the quality assurance of the sensors and the test structures. Figure 5.2 shows one of the two probe stations built and used in Karlsruhe.

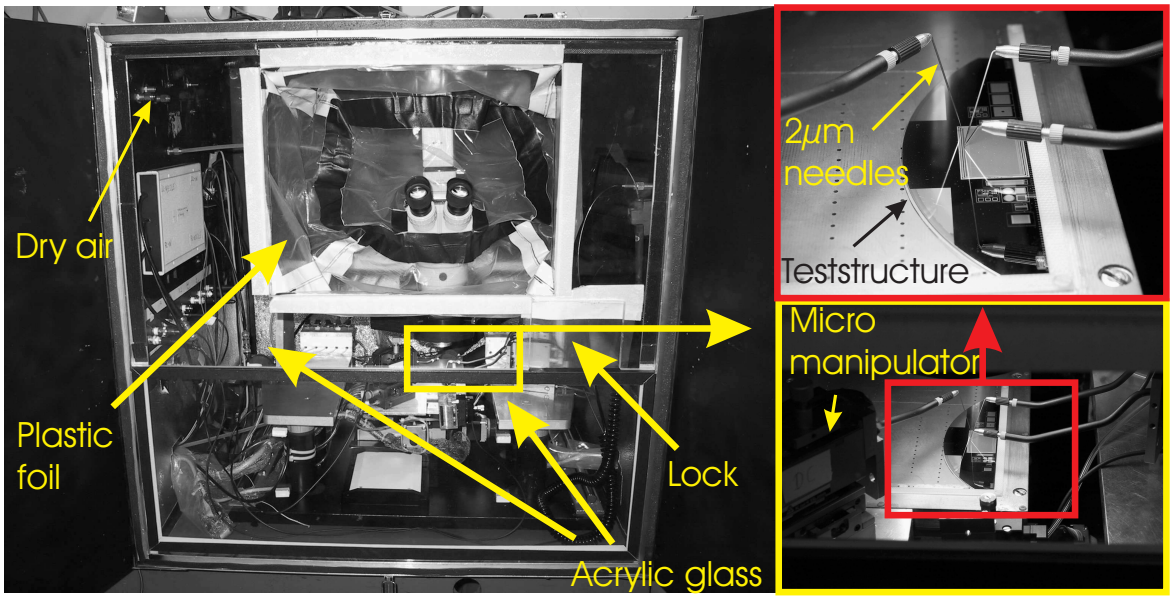

Figure 5.2: **The Karlsruhe probe station:** *The probe station in Karlsruhe enables sensor measurement in dark and cold environments. The JIG secures the sensors by means of vacuum, it has an integral cooling pipe to chill the sensors to $-18°C$, and it provides a high voltage contact on its surface to bias the sensors. The interior of the box is flooded with dry air with a dew point of $-40°C$ to avoid condensation of air humidity on the sensor. An acrylic glass window keeps humid air outside of the aluminium box when the box is opened for inspection. Openings in the acrylic glass (covered with plastic foil) provide access to the interior components of the box.*

During the measurements the sensor lies (with strips upwards) on a JIG which contains integral cooling and vacuum pipes and which provides a high voltage contact by a conducting surface. A

detailed description of the construction of the JIG can be found in [Fre04]. The vacuum necessary for fixing the structures to be tested is applied by pumps. A large reservoir is installed between the pumps and the JIG in order to minimize the operation time of the vacuum pumps and to control the vacuum pressure between an upper and a lower level. The cooling pipes have a good thermal contact with the electrically conducting surface of the JIG and they are able to chill the sensor to $-18°C$ or to heat up the sensor to $+100°C$. A small plate attached to the JIG supports a micro manipulator and moves together with the sensor. The micro manipulator is used to contact the bias ring with a needle having a $7\,\mu m$ tip. With this arrangement it is possible to apply a bias voltage to the sensor while the JIG is moved by three motors in X-, Y-, and Z-direction without loosing the electrical contact. The AC and DC pads are contacted by micro manipulators which have needles with $2\,\mu m$ tips. These micro manipulators are fixed on a plate next to the JIG. Strip scans are performed by bringing these needles into contact with the pads, lowering the JIG, and moving the JIG until the next strip is located below the needles. Finally the JIG travels upwards the same distance as it moved downwards. Probecards are not used in order to maximize flexibility as to the pitch of the structures to be measured.

A large aluminium box enclosing the JIG and the micro manipulators keeps electromagnetic interference away from the sensor and provides a dark environment. The interior of the box is flooded with dry air with a dew point of $-40°C$ to avoid condensation of air humidity on the sensor. An acrylic glass window keeps humid air outside of the aluminium box when the box is opened for inspection. Openings in the acrylic glass (covered with plastic foil) provide access to the interior components of the box.

Outside of the aluminium box a PC controls 27 relays with an I/O card. Via these relays the measurement equipment is connected to the pads and rings of the sensor. The relay wiring diagram can be found in appendix A and the relay settings for the corresponding measurement are given in Table A.1.

The measurement equipment is controlled by the PC via the General Purpose Interface Bus (GPIB). The measurement equipment of the probe station includes:

- **Keithley 6517A (KE6517A)**
  This device has a voltage source with a range of $\pm 1000V$*, a maximum current of* $1\,mA$ *and an additional electro meter which is completely isolated from the voltage source. The electro meter is used for all current measurements.*

- **ISEG**
  This device is a DC-DC converter with a output range of $-6000V$ *to* $0V$ *or* $0V$ *to* $+6000V$ *with a maximum current of* $10\,mA$*. The voltage source of the Keithley 6517A is used as input voltage.*

- **Hewlett Packard 6614C (HP6614C)**
  This device is a voltage source with a range of $0V$ *to* $100V$.

- **Hewlett Packard 4274/4284A (HP4274/4284A)**
  These LCR meters are used for capacitance measurements. They have a test frequency range from $120\,Hz$ *to* $100\,kHz$ *(HP4274) and from* $20\,Hz$ *to* $1\,MHz$ *(HP4284A). The devices have a maximum signal voltage level of* $1V$.

- **ISOBOX**
  This is a circuit board which adds the signal from the HP4274/HP4284A to the high bias voltage. The circuit diagram is shown in appendix B on Page 147

- **Keithley 617 (KE617)**
  This device can be used instead of the HP6614C. It has a voltage source with a range of $\pm 100\,V$ *and has an isolated electro meter like the KE6517A.*

For the connections between each measurement device and the pads and the rings of the sensor only the inner sections of BNC cables are used. The outer sections of the cables are used as shields against electromagnetic interference. In order to eliminate the noise of the mains power network outside of the measurement equipment each device is connected to its power socket via a filter.

The individual measurements and their problems are described below.

5.3.1 Total Leakage Current Measurement (IV)

The measurement circuit of the total leakage current versus voltage (IV) is shown in Figure 5.3. The backplane is on high voltage and the bias ring is connected via the electro meter of the KE6517A to ground. The guard ring is not connected but in floating mode. After irradiation when the leakage current is high, the voltage of the KE6517A is converted with the ISEG module switched between the voltage source of the KE6517A and the sensor. In case of a breakthrough with a rapid current increase above $1\,mA$ the voltage source runs into compliance mode and the KE6517A ramps the bias voltage slowly down to $0\,V$.

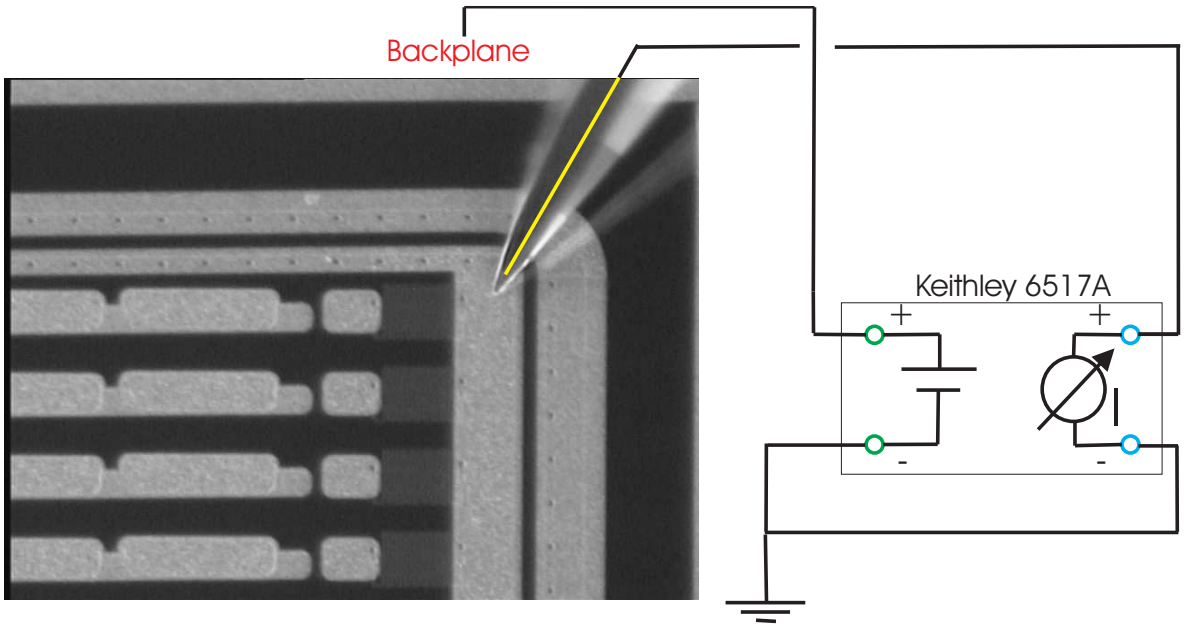

Figure 5.3: **Schematics of IV measurement:** *The total leakage current versus voltage is measured by contacting the bias ring with a micro manipulator needle to the electro meter of the Keithley 6517A, which is switched in series with its voltage source. For currents above* $1\,mA$ *the ISEG module is inserted between the voltage source of the Keithley 6517A and the sensor.*

5.3.2 Total Capacitance Measurement (CV)

The standard frequency in the CMS collaboration for the CV measurement is $1\,kHz$. The measurement of the capacitance voltage characteristics (CV) is not trivial as shown in Figure 5.4. There is an

input voltage to ground limit for the HP4274/HP4284A. For this reason the ISOBOX launches the output signals from the HP4274/HP4284A and decouples the input signals for the HP4274/HP4284A from the high voltage bias circuit. For the decoupling of the temporarily constant high voltage level large capacitances are necessary as shown in the schematics of the ISOBOX in appendix B. These capacitances can discharge on the voltage source during ramping down the voltage and can destroy the voltage source whilst its inner resistance is very low. Therefore, the electrodes of the capacitances of the ISOBOX are shortened with a $220 k\Omega$ resistor. For the CV measurement a relay switches the resistor out of the circuit of the ISOBOX. After the CV measurement is finished the relay is closed and the capacitances are discharged. A few years ago it was decided to run the IV and CV measurements at

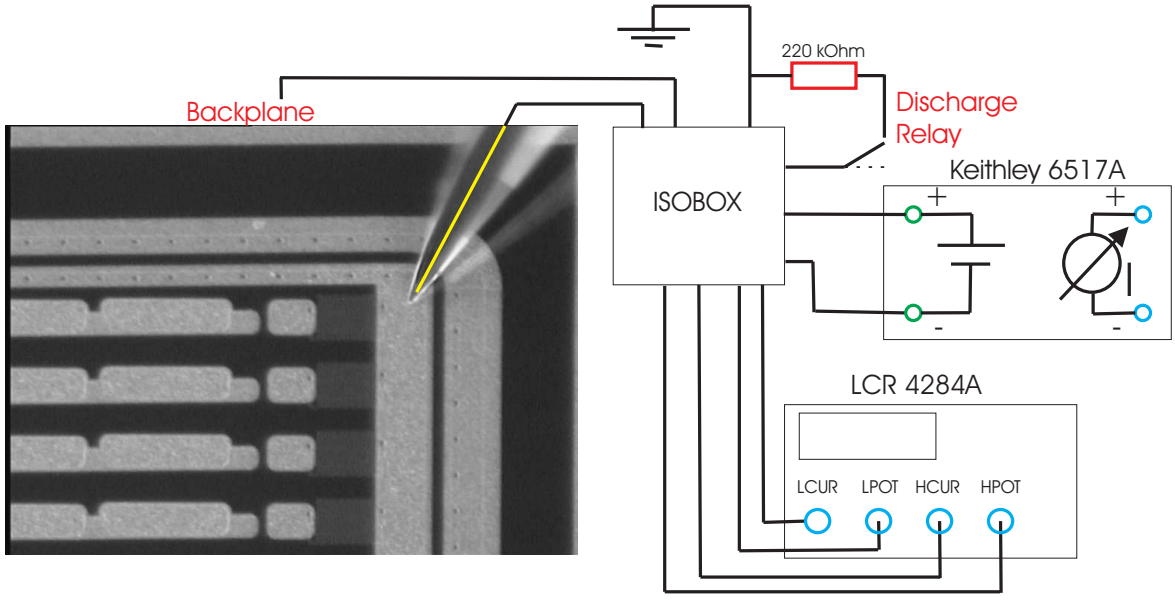

Figure 5.4: **Schematics of CV measurement:** *For the capacitance versus voltage characteristics the LCR 4274/4284 is inserted in the high voltage circuit for biasing the sensor. Since the inputs of the LCR are not high voltage stable an ISOBOX is necessary for adding the signals from the LCR to the high voltage of the voltage source of the Keithley 6517A. The schematics of the ISOBOX is shown in Figure B.1. Due to the large capacitances inside the ISOBOX a further discharge relay is necessary. It shortens the two ends of the large capacitances with an external resistor and discharges them.*

once. The problem not to loose connection of the bias ring to low potential during the switching of the ISOBOX into the high voltage bias circuit is solved by an intermediate state. This intermediate state connects all necessary measurement devices, low and high voltage potential lines into the high bias voltage circuit and afterwards for the IV or CV measurement only the unused lines are disconnected.

5.3.3 Single Strip Leakage Current Measurement (ILeak)

For the strip measurements the sensor has to be biased via the JIG's surface on high voltage and the bias ring connected via a micro manipulator directly to low potential.

Figure 5.5 shows the schematics of the ILeak measurement. For the ILeak measurement the electro meter from the KE6517A is switched between the DC pad and low potential. The falsification of the measurement by potential movements due to bridging the bias resistor is negligible, because the

bias resistor has a magnitude of $M\Omega$ and the bulk material resistance is in the order of $G\Omega$. Therefore the voltage drop at the bias resistor is negligible.

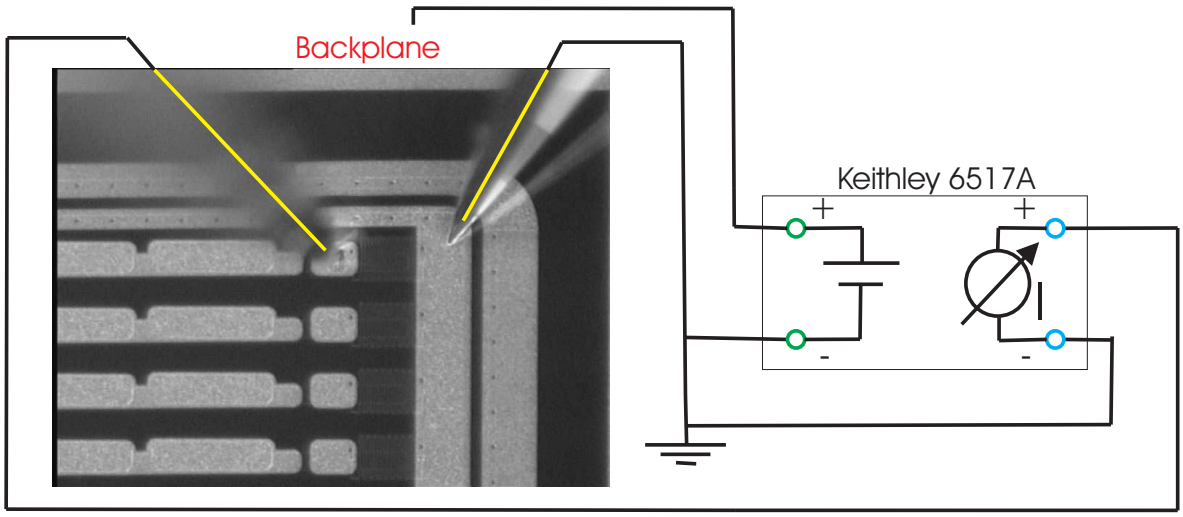

Figure 5.5: **Schematics of single strip leakage current measurement:** *The sensor is biased with high voltage from the Keithley 6517A applied to the JIG's surface and with a needle on the bias ring connected to low potential. The strip leakage currents are measured by connecting the DC pads with the electro meter of the Keithley 6517A to low potential. The voltage drop at the bias resistors can be neglected for small strip currents and high resistances of the sensors bulk.*

5.3.4 Bias Resistor Measurement (Rbias)

The voltage source of the KE617 or HP6614C is switched in series with the electro meter of the Keithley 6517A to the DC pad as shown in Figure 5.6. The measurement voltage of the KE617 is $U_{meas} = 2V$. Contrary to the current flowing through the bias resistor to ground the strip leakage current flows into the electro meter because the inner resistance of the electro meter and the voltage source is lower than the bias resistor. Particularly, high single strip leakage currents require a correction due to the single strip leakage current. This can be easily calculated to:

$$\begin{aligned} R_{Bias} &= \frac{U_{meas}U_{bias}}{(I_{meas}-I_{Leakage})(U_{bias}-U_{meas})} \\ &\approx \frac{U_{meas}}{I_{meas}-I_{Leakage}} \qquad for \quad U_{bias} \gg U_{meas} \end{aligned} \tag{5.1}$$

with the measured current I_{meas} and the single strip leakage current $I_{Leakage}$. This correction is directly done by the probe stations software. Measuring the bias resistor versus bias voltage after irradiation also gives hints for full depletion voltage. In Figure 6.42 bias voltage ramps of the bias resistor measurement before and after irradiation are shown. Before irradiation the depletion zone starts mainly to grow from the surface to the backside and the current introduced by the measurement voltage flows only through the bias resistor to low potential. After irradiation and type inversion the depletion zone starts mainly to grow from the backside. Below full depletion voltage the introduced measurement current flows partially below the dielectric to the bias ring, since the bulk is not fully depleted in this region. The error bars of the full depletion voltage fits of the CV curve are quite large and can be reduced with this method.

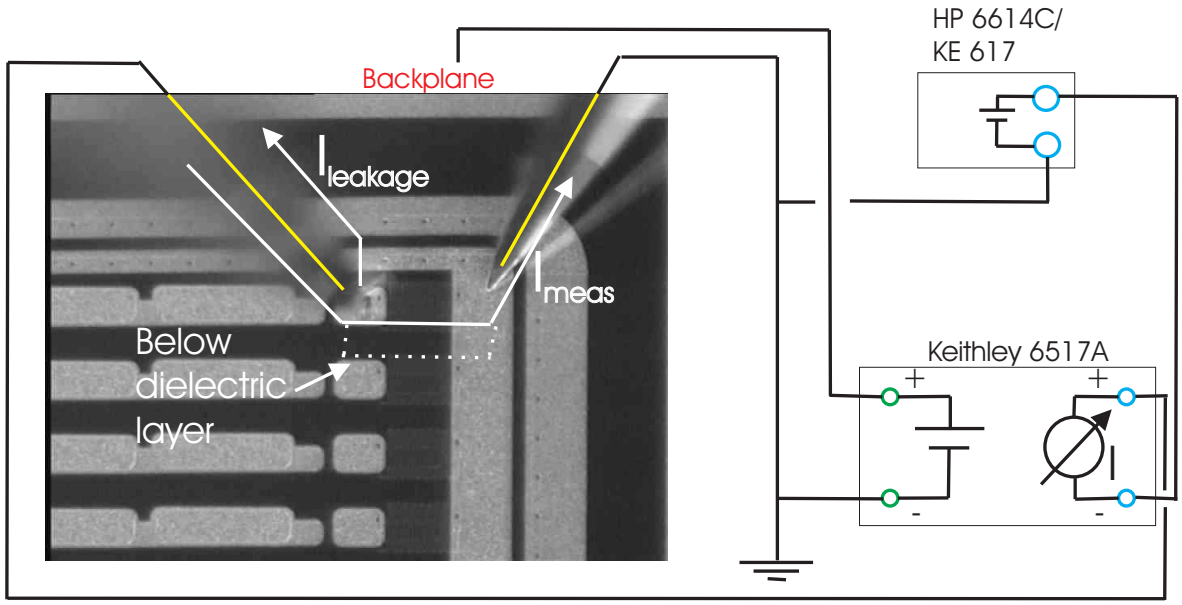

Figure 5.6: **Schematics of bias resistor measurement:** *The sensor is biased with the Keithley 6517A. The voltage source of the Keithley 617 is switched in series with the electro meter of the Keithley 6517A to the DC pad. The measurement voltage of the KE617 is* $U_{meas} = 2V$*. For high single strip leakage currents a correction of the measured current* I_{meas} *due to the the single strip leakage current is necessary.*

5.3.5 Coupling Capacitance Measurement (CC)

In the CMS collaboration the measurement of the coupling capacitance (CC) is done with a measurement frequency of $100\,Hz$. The coupling capacitance is directly measured between the AC and the DC pad as shown in Figure 5.7. The use of the ISOBOX is not necessary because all pads are on low potential. Contacting the AC pad with a micro manipulator affects the potential on the AC pad

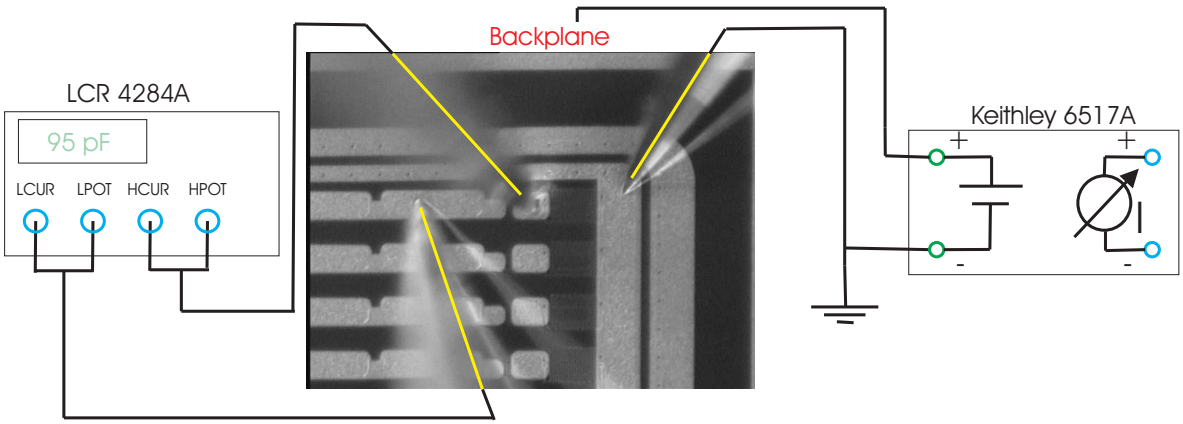

Figure 5.7: **Schematics of coupling capacitance measurement:** *The sensor is biased with the Keithley 6517A. The LCR is connected via two micro manipulators to the AC pad and the DC pad. The measure frequency is* $100\,Hz$*.*

which is floating for other measurements. A clear correlation between single strip leakage current and potential on the AC pad has been observed. Therefore, it is important to do the CC measurement in an own measurement run, i.e. without contacting other pads of the sensor.

5.3.6 Short Measurement (Pinhole)

The resistance of the insulating layer is checked with a voltage of $10\,V$ applied with the KE617/HP6614C between the DC pad and the AC pad as shown in Figure 5.8. In the case that the electro meter of the KE6517A connecting the AC pad to ground sees a current above $1\,nA$ in the probe station's software the coupling capacitance is marked as "leaky" and the corresponding readout channel of the APV25 is not bonded to this AC pad. It is problematical to change the connections of the AC pad and DC pad because on the DC pad the strip current is measured, too.

The problem of affecting other measurements is the same as for the CC measurement. In addition a direct potential movement below the dielectric layer is caused by contacting the voltage source of the KE617/HP6614C to the DC pad. But the pinhole measurement can be done together with the CC measurement in one measurement run and the problem of potential changes is not relevant for the dielectrics voltage stability and its resistance.

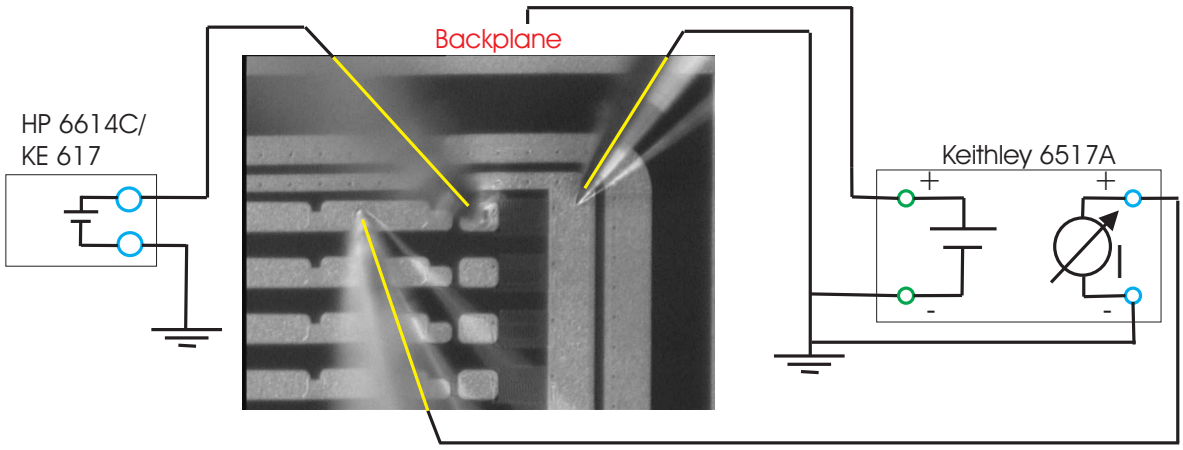

Figure 5.8: **Schematics of pinhole measurement:** *The sensor is biased with the Keithley 6517A. The current through the dielectric is normally tested for an applied voltage of* $10\,V$ *by the Keithley 617 on the DC pad. The AC pad is connected via the electro meter of the Keithley 6517A to ground. In the case that the measured current is above* $1\,nA$ *the capacitance is marked as "leaky" in the probe station's software.*

5.3.7 Interstrip Capacitance Measurement (Cint)

The HP4284A is connected to two neighbored strips. The contacted pads are the AC pads or the DC pads as shown in Figure 5.9. The frequency to measure the small capacitances in the range below $1\,pF$ up to $5\,pF$ is $1\,MHz$ therefore the HP4274 cannot be used for this measurement. The reason to use the highest available measurement frequency of the LCR shows Figure 5.10 which contains the measurement results before and after irradiation of a mini sensor with measurement frequencies of $100\,kHz$ and $1\,MHz$. After irradiation the measurement values with $100\,kHz$ do not saturate for higher bias voltages [Fur02]. The explanation of the different results between the measurement frequencies

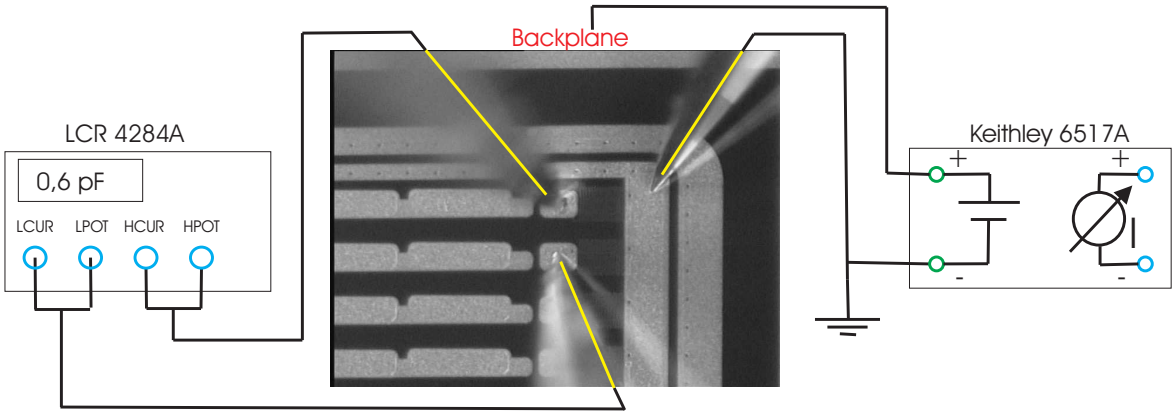

Figure 5.9: **Schematics of interstrip capacitance measurement:** *The sensor is biased with the Keithley 6517A. The HP4824 is connected to two neighbored strips, either on the DC pads or on the AC pads. The measurement frequency is* $1\,MHz$ *because the interstrip capacitances are in the range below* $1\,pF$ *up to* $5\,pF$ *and after irradiation introduced charge carriers get mobile and falsify the measured value of the interstrip capacitance.*

of $100\,kHz$ and $1\,MHz$ is given by the mobility of charge carriers in the dielectric layer. At high frequencies these carriers cannot move and the polarization is inhibited.

An additional capacitance at $1MHz$ given by the small distance between the micro manipulator needles has to be subtracted from the measured interstrip capacitance value. This is done by setting all micro manipulator needles on the pads and then the JIG is moved downwards. While having no contact to the micro manipulator needles, the capacitance is measured and for this needle settings it is subtracted automatically by the probe station's software.

5.3.8 Interstrip Resistor Measurement (Rint)

One DC pad is connected to the voltage source of the HP6614C/KE617 and the neighbored DC pad is connected via the electro meter of the KE6517A to low potential as shown in Figure 5.11. A voltage $U_{meas} = 0.5V$ (or for some applications up to $U_{meas} = 2V$) is applied with the HP6614C/KE617 and a current change is given to the neighbored DC pad if the interstrip resistance is not too large. But this current change can also come from a fluctuation of the single strip leakage current. In order to distinguish between these two cases the measurement is done by stepping the measurement voltage of the HP6614C/KE617. If a linear behavior of the measured current as shown in Figure 5.12(a) is seen the interstrip resistor is measured correctly. The offset of the curve is the single strip leakage current and the slope is the interstrip resistance. In the case of Figure 5.12(b) where the current fluctuations are higher than the introduced measurement current, the lower limit of the interstrip resistance is estimated by

$$R_{int} > \frac{U_{meas}}{I_{max} - I_{min}} \tag{5.2}$$

with the maximum measured current I_{max} and the minimum current I_{min}. The evaluation of the curve is done by the probe stations software with a subroutine calculating the mean square error (MSE). Values below 10^{-4} for the MSE are believed as linear behavior and for values above the lower limit is calculated with Equation 5.2.

One has to take into account that the measurement is disturbed by contacting the DC pads. This

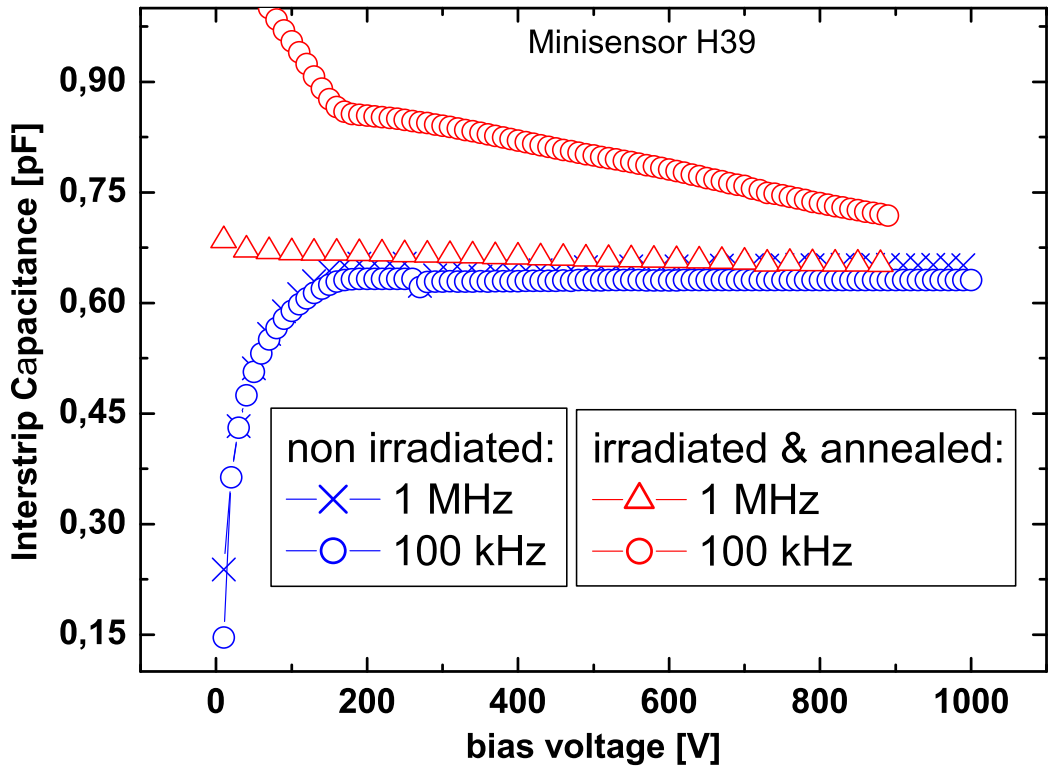

Figure 5.10: **Interstrip capacitance versus bias voltage before and after irradiation:** *After irradiation the measured interstrip capacitance values (here measured between the DC pads) do not saturate for a measurement frequency of* $100\,kHz$ *[Fur02].*

causes a change of the electric field distribution which is responsible for the interstrip resistance. For low single strip leakage currents and high bias resistors this fact can be neglected.

5.3.9 ILeak with Potential on the AC Pad

In addition to the standard ILeak measurement the HP6614C/KE617 voltage source can be contacted to the AC pad as shown in Figure 5.13. This measurement is important for simulating the final sensors condition on the detector module. The readout channel of the APV25 sets the AC pad to a constant potential which is $0.75\,V$ above the potential of the bias ring.

5.3.10 Summary of Measurement Methods

Contacting the pads and rings of a CMS sensor changes the currents and the potentials within the sensor. A correction to the currents is possible if the individual currents can be measured. For the CC and Pinhole measurement it is necessary to connect the AC pad with a micro manipulator needle and therefore the potential on the AC pad changes. This results in a change of the field configuration below the dielectric layer and a change of the single strip leakage current. For this reason the cou-

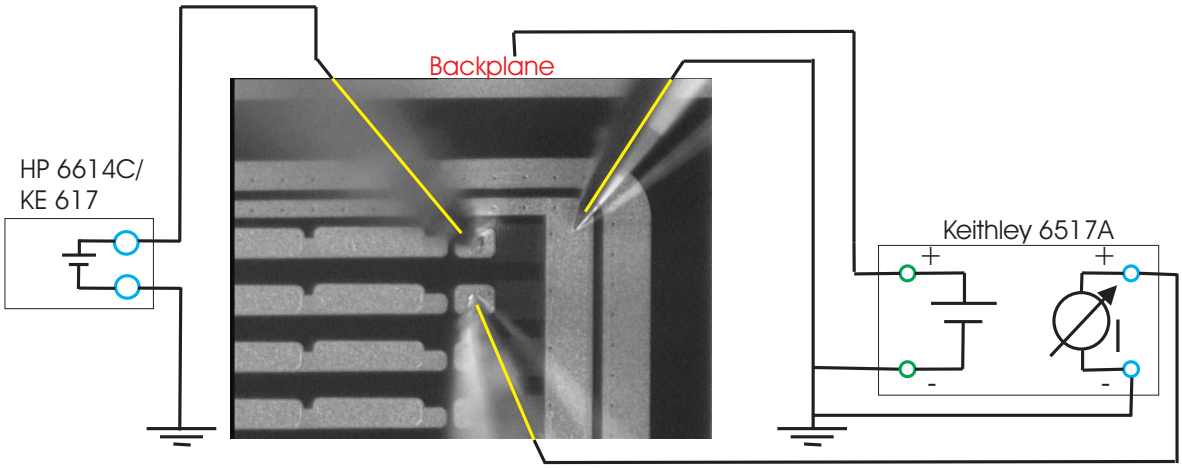

Figure 5.11: **Schematics of interstrip resistance measurement:** *The sensor is biased with the Keithley 6517A. The interstrip resistance is measured by contacting one DC pad with the voltage source of the Keithley 617 and connecting the neighbored DC pad with the electro meter of the Keithley 6517A to low potential. The voltage of the Keithley 617 is ramped in steps from* $0V$ *up to* $0.5V$ *or for some applications up to* $2V$*. This is done to get a linear current behavior of the measured current containing the strip leakage current as constant offset and the interstrip resistance as slope (see Figure 5.12).*

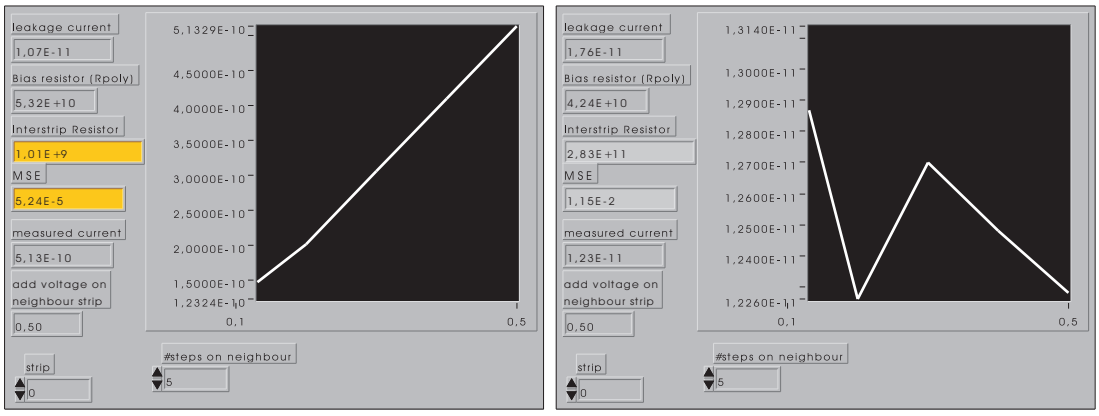

(a) Measured interstrip resistance (b) Too high interstrip resistance

Figure 5.12: **Verification of measured interstrip resistance values:** *The left figure shows an example of a measurable interstrip resistor. The verification of the linear behavior is done with the MSE value. MSE values below* 10^{-4} *are declared as linear behavior. The right figure shows an example of a not measurable interstrip resistor. The fluctuations of the strip leakage current is higher than the current increase caused by the applied voltage on the neighbored DC pad (see Figure 5.11). In this case a lower limit is given for the interstrip resistance calculated by the applied maximum voltage on the neighbored strip and the maximum of the current fluctuations.*

pling capacitance and the pinhole measurement are measured in an own measurement run. The other parameters like ILeak, Rpoly, Cint on DC pads and Rint have to be measured either without contacted AC pad or with a certain voltage on the AC pad like $0.75V$ which corresponds to the voltage offset with readout electronics connected. Cint between the AC pads have to be measured in an own mea-

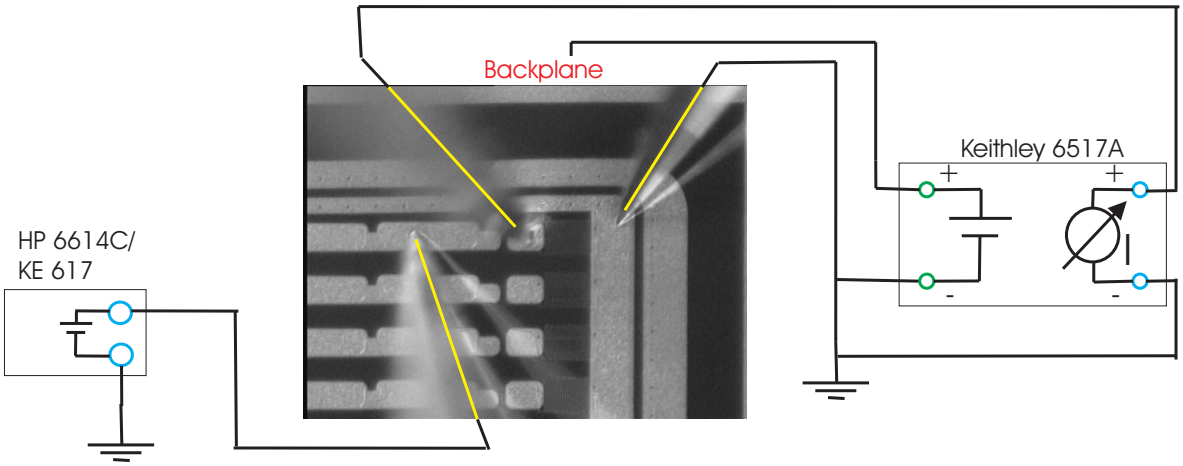

Figure 5.13: **Schematics of single strip leakage current measurement with different potentials on the AC pad:** *In addition to the ILeak measurement in Figure 5.5 the AC pad is connected to the voltage source of the HP6614C/KE617.*

surement run anyway since both needles for the Cint measurement has to set on the AC pads and no other parameter can be measured (Rint between two AC pads is in principle possible, but not used in the CMS collaboration). Table 5.1 gives an overview of the values to be measured in QTC and IQC, the necessary measurement, the determination of the corresponding value, the distortions of the measurement and the solutions of the problems.

5.4 Setup for Measurements during Irradiation

Some problems occurred at STM sensors motivated the development of a setup which allows to measure total and single strip leakage currents during irradiation. The developed setup is shown in Figure 5.14. The voltage of Keithley 6517A is applied to a DC-DC converter due to the high power consumption and the high leakage current above $1\,mA$, which cannot be supported by the Keithley 6517A. The switching unit HP34970A contains a multiplexer unit HP34901A with 20 channels and a switching matrix unit HP34904A with 8×4 channels. For switching reasons, the number of strips, which can be monitored in addition to the total leakage current, are nine without the multiplexer HP34901A and 26 with the multiplexer. The ampere meter from the Keithley 6517A is used for current measurements whilst it is switched between single strips or the bias ring and low potential.

Figure 5.15 shows the copper plate acting as high voltage contact with the sensor glued on it. The strips are connected with via bonds to small copper plates connected via cables to the switching unit HP34970A.

The Keithley 6517A is controlled by a software written in Labview 6.1 and GPIB (**G**eneral **P**urpose **I**nterface **B**us). The cables between the sensor and the switching unit HP34901A are successfully tested up to a maximum length of $10\,m$. This enables to built up the measurement devices outside of the irradiation area and to measure the sensors total and single strip leakage currents during the irradiation. Due to the switching times of the relays and in order to guarantee a stable field configuration within the sensors under test, the currents can be measured with a minimum delay of approximately $1\,s$ between two single current measurements. The temperature is controlled by ex-

Value	Measurement type	Determination	Distortions	Solution
Full depletion voltage U_{FD}	CV ($1kHz$)	Two linear fits $\frac{1}{C^2}$ versus U_{Bias}		
Resistivity ρ	CV	Calculated from U_{FD}		
Flat band voltage U_{FB}	CV ($50kHz$)	Inflection point of CV curve		
Break trough voltage U_{BR}	IV	$\frac{dI}{dU} > 100\frac{nA}{V}$		
Single strip leakage current "ILeak"	ILeak	Direct	Potential changes on strip implants by connecting DC-pad to ground and bridging Rbias	Negligible for ILeak $< 1\mu A$ and Rpoly$> 1M\Omega$
Coupling capacitance "CC"	CC	Direct	Potential changes by contacting the AC and DC pads	CC not affected, own measurement run necessary
Shorts in CC "Pinhole"	Pinhole	"leaky" if $I > 1\,nA$ at $10\,V$	Potential changes by connecting the AC and DC-pad	Current through dielectric layer not affected, but own run necessary
Capacitance between two strips "Cint"	Cint	Direct	Potential changes for DC-DC and AC-AC	Negligible for ILeak $< 1\mu A$ and Rpoly$> 1M\Omega$
Bias resistor "Rbias"	Rbias	Direct see eq. 5.1	ILeak flows into electro meter, measurement voltage disturbs the field below the dielectric, for partially depleted bulk, currents flow below dielectric	Bulk must be fully depleted, and measurement voltage is limited
Resistance between two strips "Rint"	Rint	Slope of current versus voltage or lower limit estimated with eq. 5.2	Potential changes below dielectric layer by measurement voltages	Negligible for low measurement voltages, ILeak $< 1\mu A$, and Rpoly$> 1M\Omega$

Table 5.1: **Overview of measured parameters, corresponding measurements, and problem solutions**

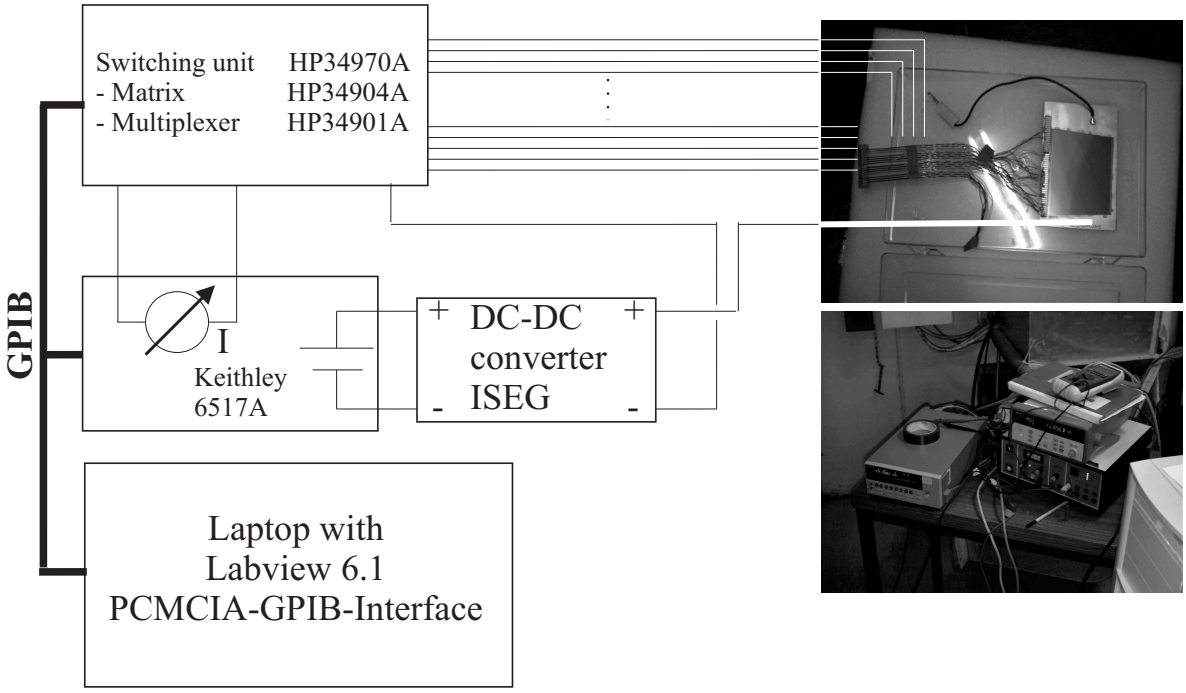

Figure 5.14: **Schematics of setup for current measurements during irradiation:** *The voltage source of the Keithley 6517A is applied to a DC-DC converter. The switching unit HP34970A contains a multiplexer unit with 20 channels and a switching matrix unit with four by eight channels. The ampere meter from the Keithley 6517A is connected via the switching unit to the different strips or the bias ring on one side and the low potential on the other side. The sensor is glued on a plate covered with copper which is connected to high potential.*

ternal devices controlling a cold nitrogen gas flow. Simulating the conditions in the tracker and the expected high currents imply a temperature of $-10°C$ for the measurement during neutron irradiation (see Section 6.3).

5.5 Initial Quality of Supplied CMS Sensors - QTC Results

While HPK has experience from earlier high energy experiments like e.g. Delphi and CDF, STM is a newcomer in the field of high energy particle sensors. This fact results in significant variations in the quality of the supplied sensors. Problems related with the handling and the protected transport of the sensors which lead to sensor damage on the sensors have been solved completely during the production phase and just the intrinsic quality differences of the sensors remain. The majority of the sensors supplied by HPK have an excellent quality with low leakage currents, uniform strip parameters within one sensor, and uniform parameters within a supplied batch of sensors. With the exception of a single delivery which contained sensors with an excessive initial resistivity, almost none of the sensors had to be rejected (except for the reason mentioned above). Unlike HPK, STM sensors tend to have higher leakage currents, less uniformity of strip parameters within one sensor, and high variances of the parameters within one batch of sensors. Since one batch of sensors supplied by HPK contains at least 20 sensors, many batches of STM sensors contain only one sensor. Whilst just one delivery of HPK sensors is rejected, a large number of sensors and whole batches are rejected and returned to

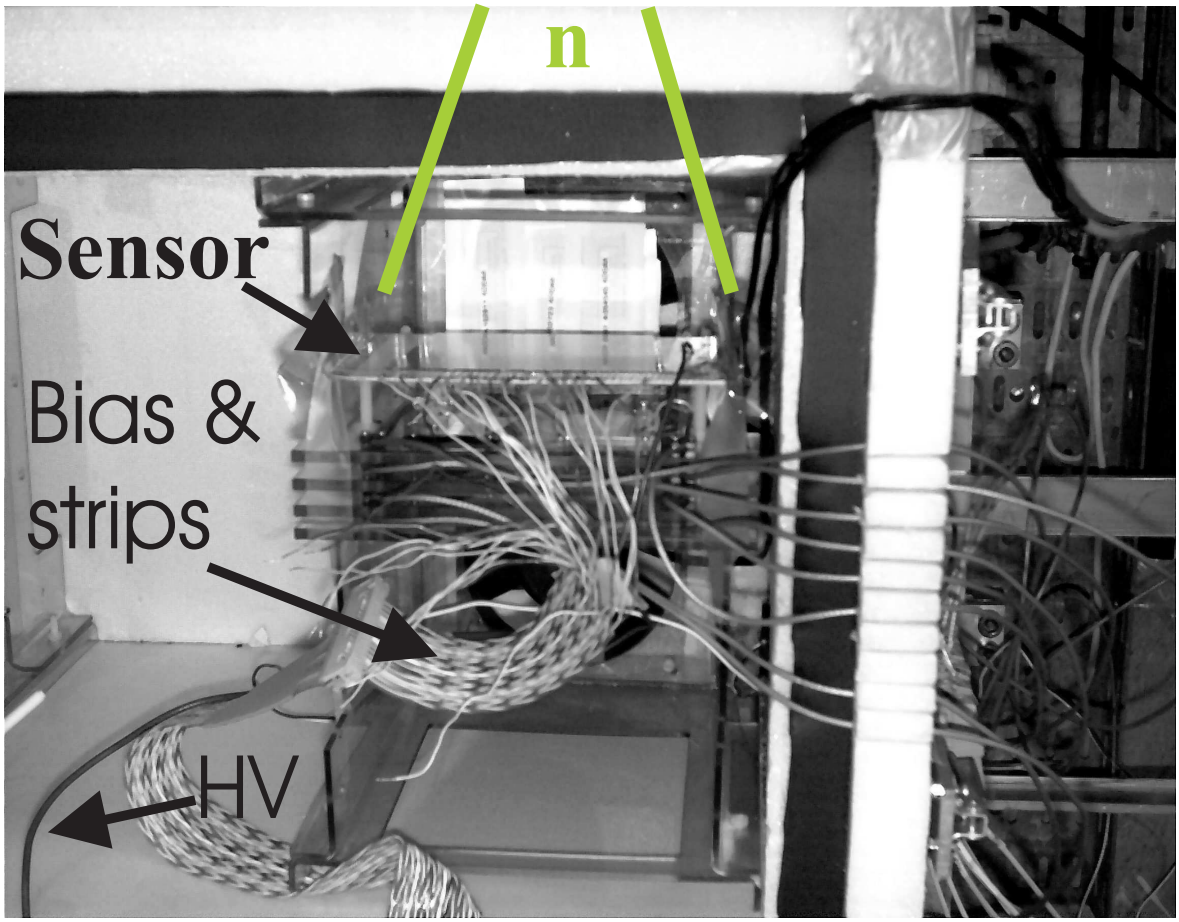

Figure 5.15: **Picture of a sensor for current measurements in the irradiation box for neutron irradiation in Louvain-la-Neuve:** *The copper plate containing the glued sensor is put in front of the standard stacks (below the sensor) for neutron (n) irradiation. The cables connect the sensor to the DC-DC converter and the switching unit HP34970A.*

STM due to too high leakage currents, too many faulty strip parameters, or parameters found to be out of range in PQC measurements. The quality of two representative and accepted sensors supplied by HPK and STM is shown in the following graphs which contain the results of measurements performed by QTC using the Karlsruhe probe stations. Both sensors have the W5A sensor geometry and they were measured at a temperature of $20°C$ and at a relative humidity below 20%. The differences in the CV curves in Figure 5.16(a) are related to different initial wafer resistivity. Therefore, the sensors have different full depletion voltages (see Equation 2.26 on Page 24). The differences in the IV curves in Figure 5.16(b) indicate excessive quality variations as the leakage currents do not depend on initial resistivity for sensors with same geometry and the same production masks. Strip parameters are measured at an applied bias voltage of $400V$. Both suppliers are able to produce coupling capacitances at a reliable quality level as shown in Figure 5.17(a). The pinhole test in Figure 5.17(b) shows that the HPK sensor has coupling capacitances with a higher current through the dielectric layer than sensors supplied by STM. This results from the marginally lower thickness of the dielectric layer in HPK sensors.

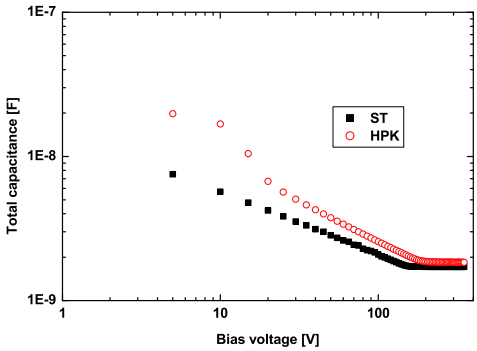

(a) The double logarithmic scaling emphasizes the kink in the graph at full depletion voltage. The behavior of the curves is as expected (see Section 2.4.2 on Page 24). The full depletion voltage is $U_{FD} = 144\,V$ for the STM sensor and $U_{FD} = 184\,V$ for the HPK sensor.

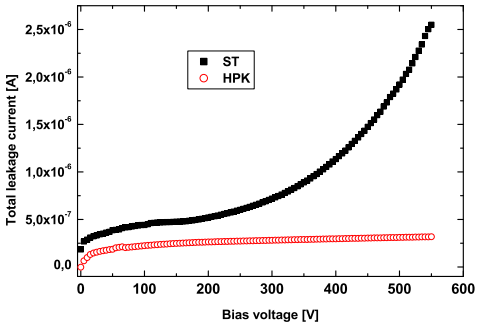

(b) The total leakage current curves are measured at $20°C$. Most of the STM sensors show a kink in the IV curve shortly above full depletion voltage.

Figure 5.16: **IV and CV of HPK and STM sensors measured at QTC:** *These diagrams have been obtained from typical samples of the sensors supplied by STM and HPK. Both sensors have the W5A geometry. The differences observed in the CV curves are caused by differences in resistivity, whereas the differences observed in the IV curves are due to variations in the quality of the sensors.*

Figure 5.17(c) shows the bias resistor values of these two sensors. The occasional measurement above the trend of the curve of the HPK sensor is due to minute residues on the DC pads which sometimes cause bad electrical contact. The real values lie in the trend of the curves and are always found by repeat measurements. This problem is not observed on STM sensors. The single strip leakage currents in Figure 5.17(d) indicate to excessive variations in sensor quality. Many sensors supplied by STM have sporadic strips or even strip regions with significantly higher leakage currents in comparison with the other strips of the same sensor. This intrinsic sensor problem will be dealt with in Section 5.7, 6.7.4, and 6.7.5.

In principle, both suppliers are able to produce sensors with a reliable initial quality. The issue of radiation hardness which is the second important point for the evaluation of the sensors will be investigated in sections 6.5-6.11.3.

5.6 Long-term Stability and Chemical Reactions of STM Sensors

The reason to perform a close visual inspection of STM sensors is a problem with the long-term stability of these sensors in terms of total leakage currents which are measured at PQC for $72\,h$. Some sensors show an increase of total leakage current up to a few μA with time. Because no electrical measurement showed a hint of the origin of these increases, a look through a high resolution microscope shows that a number of dark colored stains developed on the aluminium structures of the bias ring and the guard ring. In a visual inspection campaign it was found that on most of the sensors supplied by STM a suspect formation of stains had occurred on the bias ring and the guard ring. The following analysis is intended to find out the origin of the stains and to answer the question of resulting problems concerning the functionality of these sensors during their service life at LHC.

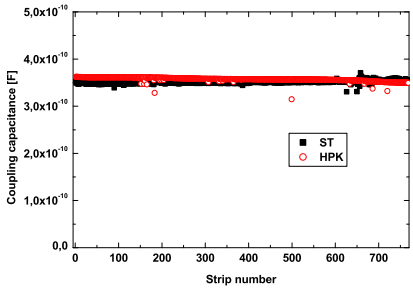

(a) The coupling capacitances of both suppliers have equal quality.

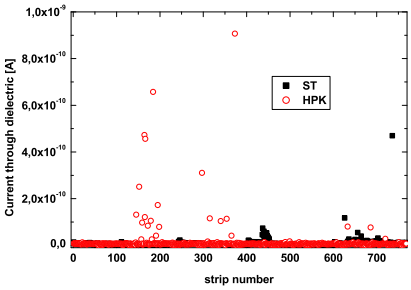

(b) The current through the dielectric layer of the coupling capacitances is below the limit of $1\,nA$.

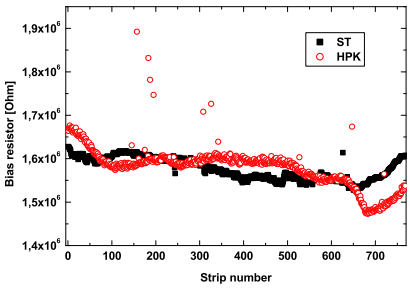

(c) Both companies produce bias resistors of a comparable quality. The single bias resistors with higher values are not measured correctly because sometimes residues on the DC pad cause bad electrical contact. This problem is not observed on STM sensors.

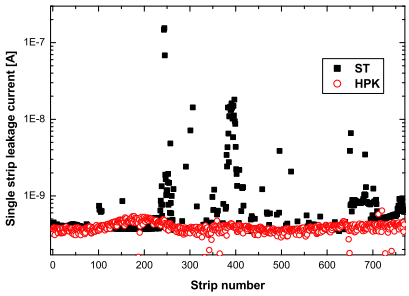

(d) The single strip leakage currents show significant variations in sensor quality. Most STM sensors have single strip leakage currents which are mostly times within the limits of the specifications, but they are sometimes significantly higher than the average values of the other strips.

Figure 5.17: **Strip parameters of HPK and STM sensors measured in QTC:** *Strip parameters are measured at the same conditions as in the IV and CV measurements in Figure 5.16. For single strip leakage currents, significant variations in quality are observed between sensors from STM and HPK.*

5.6.1 Visual Inspection of Stains

Figure 5.18 shows a stain found on the guard ring of an STM sensor.

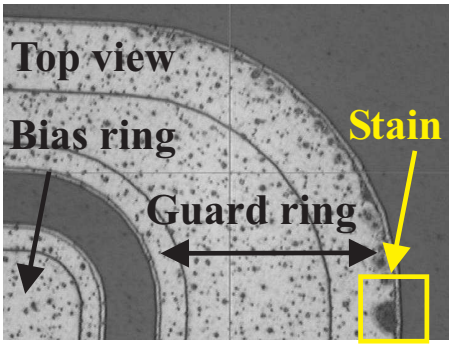

Figure 5.18: **Stain on guard ring of STM sensor:** *The picture shows a top view of a guard ring. After a few hours of operation, dark stains appear on STM sensors.*

On some sensors even structural damage after formation of stains was found as illustrated in Figure 5.19.

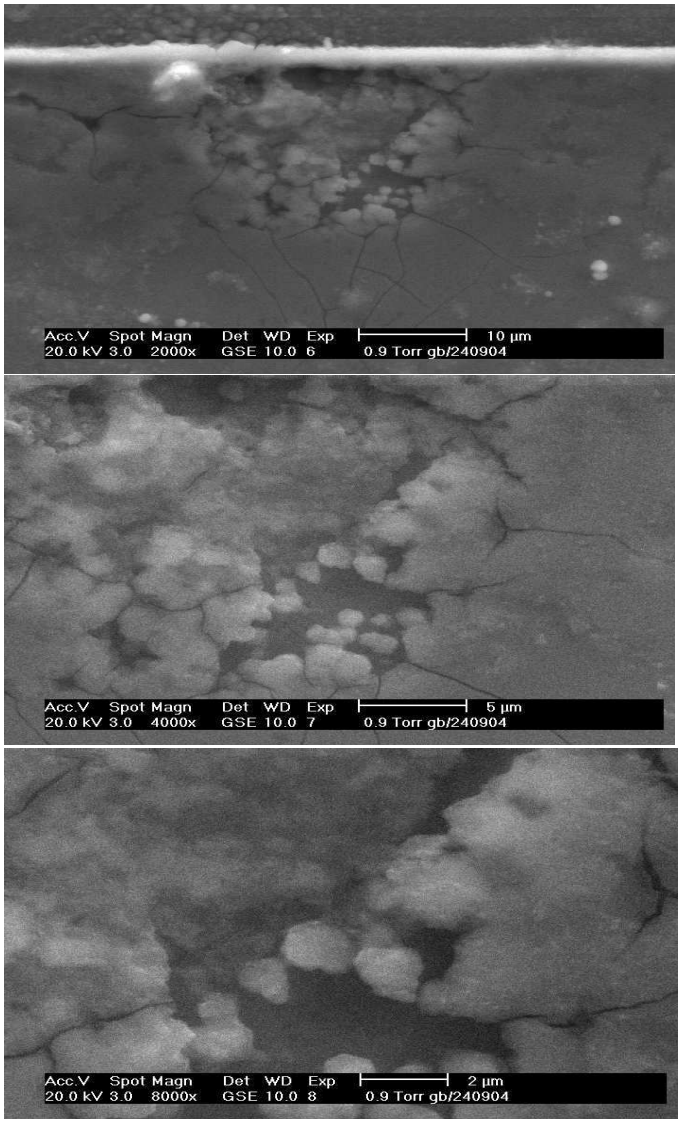

Figure 5.19: **Pictures of a crack on STM sensor:** *These pictures, taken with an electron microscope, show top views of a stain. The magnification of the electron microscope is increased from the upper picture to the lower one. Cracks have formed in the aluminium around the stain.*

Further visual inspection was performed to find out weather the formation of stains saturates with time. Figure 5.20 shows the formation of a stain over time on a sensor biased to $450V$. The relative humidity of the air is monitored and maintained at approximately 50% during the long-term test. It can be observed that the growth of the stains does not stop. On the contrary, initially unaffected parts of the aluminium structures start to develop stains over a longer time scale. It has to be pointed out that conditions such as higher temperature and higher air humidity during these tests accelerate the growth of the stains. In the CMS tracker, stain formation is expected to start on a time scale of weeks or even months.

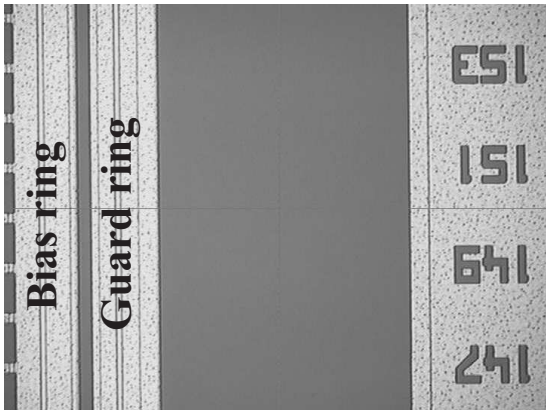

(a) Bias & guard ring before long-term test

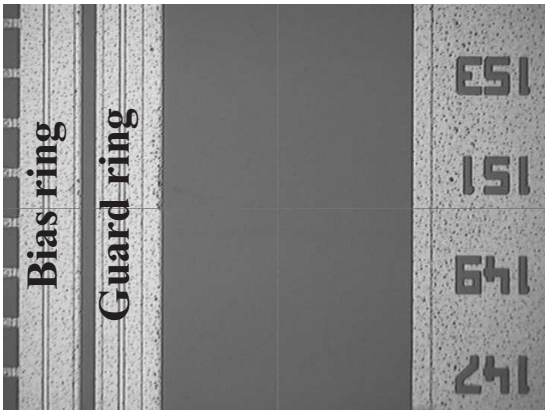

(b) Bias & guard ring after 17 *h* long-term test

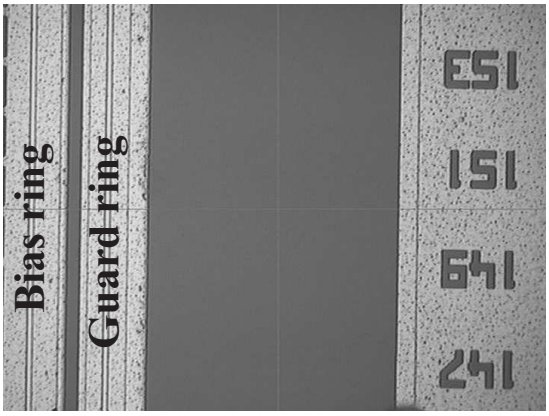

(c) Bias & guard ring after 42.5 *h* long-term test

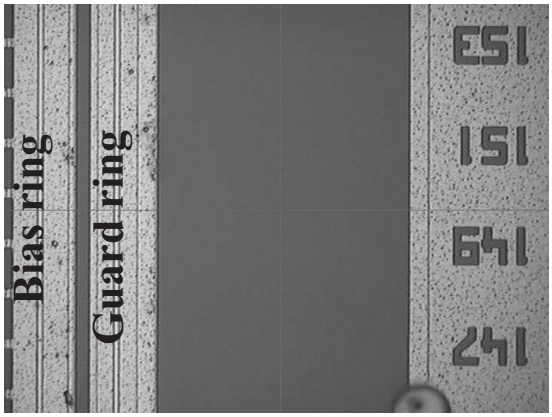

(d) Bias & guard ring after 96 *h* long-term test

Figure 5.20: **Formation of stains on guard ring of STM sensor over time:** *The pictures are top views on a guard ring and a bias ring of an STM sensor. The stains appear first on the guard ring and later on the bias ring, too.*

The visual inspections necessitated a detailed chemical analysis to find out the origin of the stains because the long-term tests require too much time and the limited number of long-term test stations prohibits to perform tests on a reliable sampling base to assure the quality of the sensors.

5.6.2 Chemical Analysis of Stains with Electron Microscopes

At the Fraunhofer Institut in Berghausen (near Karlsruhe) the first chemical analysis of a stain with a special electron microscope (ESEM[1]) was performed in order to find out weather the stains still consist of elementary aluminium or weather a chemical reaction like an oxidation of the aluminium has occurred. Figure 5.21 shows photographs of a stain analyzed as follows using different methods.

Figure 5.21(b) demonstrates that the stain is not homogeneous but clearly structured. Figure 5.22 shows element distribution of the same region as in Figure 5.21. This is measured by exciting the electrons of the different elements and by measuring the energies of the resulting photon emission [Fre04].

[1] **E**nvironmental **S**canning **E**lectron **M**icroscopy

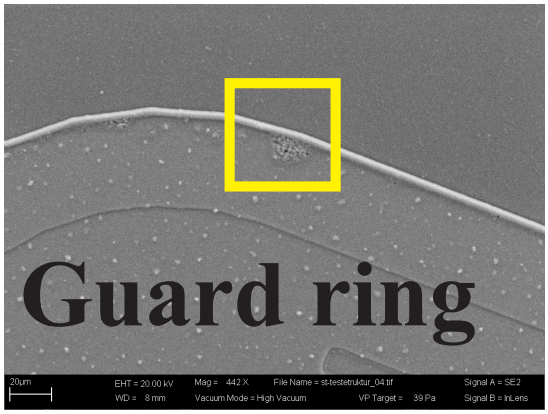

(a) ESEM picture of a guard ring

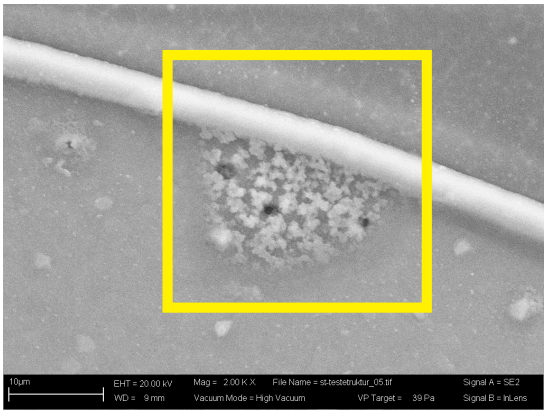

(b) ESEM picture of a Stain

Figure 5.21: **Electron microscope pictures of stain on guard ring of STM sensor:** *The stain on the guard ring (top view) is not homogeneous but clearly structured.*

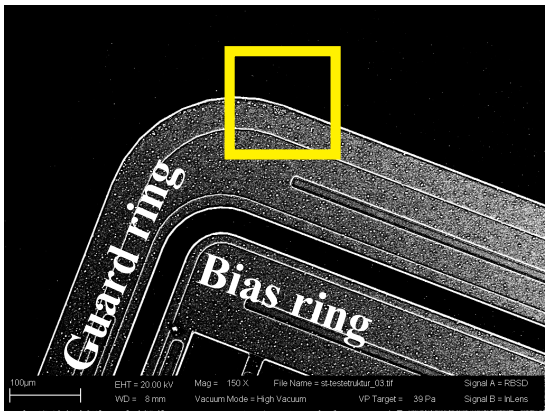

(a) Element distribution on a guard ring

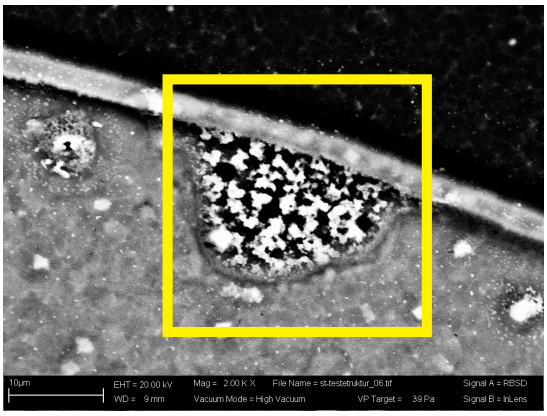

(b) Element distribution within a stain

Figure 5.22: **Element distribution on guard ring of STM sensor:** *The varying darkness levels of individual regions (top view) stand for different chemical elements. The structures in Figure 5.21 are formed by different chemical elements.*

The element distribution in Figure 5.22(b) implies a conglomerate of different chemical substances. Therefore, a detailed element analysis is carried out to obtain hints as to the kind of chemical reaction and to find out weather the reaction is caused by the sensors' own substances or wether external factors (e.g. air humidity) cause the development of stains. Figure 5.23 illustrates the analysis of different regions within the stain in Figure 5.22. The peaks in Figure 5.23(a)-5.23(f) represent the element contents of Al, Si, O, P, S, and K. The other unnamed peaks are secondary photon emission peaks of these elements. It is obvious that the chemical reactions took place between these elements because further elements are not observed.

Figures 5.23(a) and 5.23(b) show the element distributions in the homogeneous parts of the aluminium and the silicon dioxide in the passivation layer which match expectations well. A large concentration of phosphorous is found in the silicon dioxide and a small one within the stain but nothing is found in the part of the guard ring not affected by the stain. At the border between the guard ring

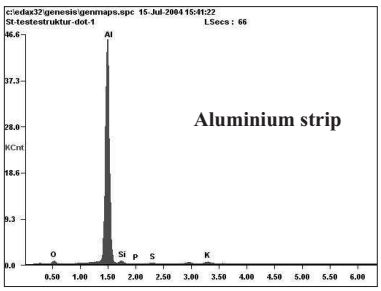

(a) Element analysis on uniform aluminium part of a guard ring of a STM sensor

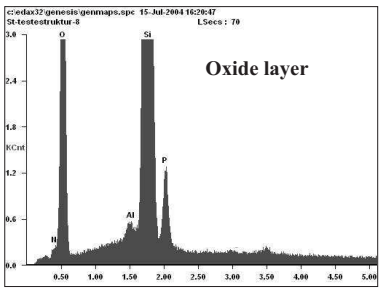

(b) Element analysis on the passivation layer of a STM sensor

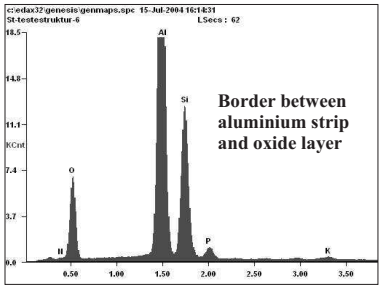

(c) Element analysis at the border between guard ring and passivation layer of a STM sensor

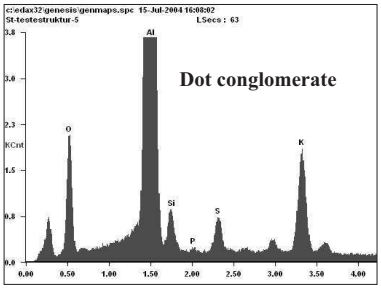

(d) Element analysis of a stain on a guard ring of a STM sensor

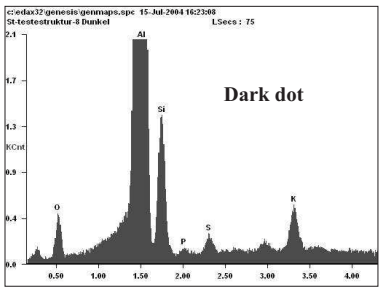

(e) Element analysis of a dark part of a stain on a guard ring of a STM sensor

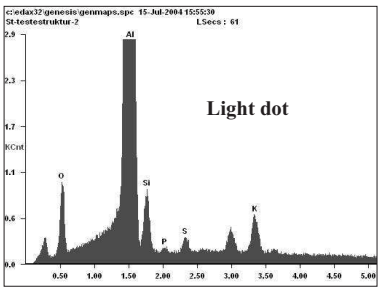

(f) Element analysis of a light part of a stain on a guard ring of a STM sensor

Figure 5.23: **Element analysis on STM sensor with electron microscope:** *The graphs show electron counts versus photon energies for different STM sensor regions. The aluminium, the passivation layer far away from the stain, and the border between aluminium and passivation layer (5.23(a) - 5.23(c)) show the expected distribution of Al, Si, and O. P is found everywhere on the sensor with higher concentrations in the passivation layer. The entire dot conglomerate (5.23(d)) of Figure 5.22, the dark (5.23(e)) and the light parts (5.23(f)) of this stain, contain high additional concentrations of potassium and sulphur.*

and the silicon dioxide (Figure 5.23(c)) the phosphorous concentration decreases. In addition to *Al*, *O*, and *Si* also *S* and *K* are found in the whole stain area (Figure 5.23(d)).

A more detailed element analysis performed for a dark portion of the stain (Figure 5.23(e)) and for a light portion (Figure 5.23(f)) shows a large peak of potassium and a non-negligible one for sulphur. Further analysis on other stains shows the same impurities of potassium but no sulphur is found in

these stains.

The element distribution maps of two further structures shown in Figure 5.24 and 5.25 have been taken by an ESEM at the Forschungszentrum in Karlsruhe. The colored dots are maximum peaks of the photon counts of the corresponding elements.

The area surrounding the stain is contaminated with potassium and the oxygen concentration is higher than expected. The chemical structure of a stain is not detectable by ESEM but the element ratio of Al to O matches with $2/3$ to Al_2O_3. This fact hints to an oxidation process within the aluminium structures. As Al_2O_3 is not electrically conductive, the metal overhang design is not effective any more in this region of the guard ring (Figure 5.24) and the bias ring (Figure 5.25).

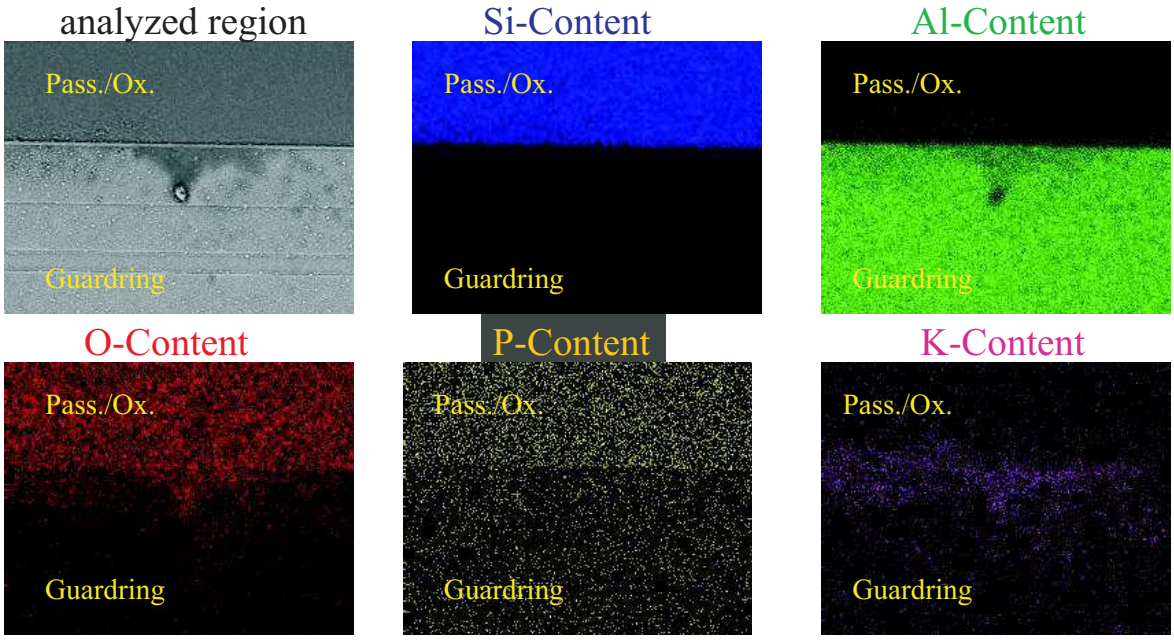

Figure 5.24: **Element map of guard ring on STM sensor:** *The pictures (top view) show the element distribution maps found on a guard ring. The colored dots represent the maximum peaks of the counted photons of the corresponding elements. The fact that no Si signal is seen on the guard ring leads to the conclusion that the aluminium within the stain is not etched away down to the silicon dioxide layer as it would be expected from the aluminium distribution in the upper right map. For oxygen and potassium, a clear local correlation with the stain is found. The concentration of phosphorous is higher in the silicon dioxide than in the aluminium but there is no evidence as to connect the phosphorous concentration with the stain evolution.*

Figure 5.26 shows a further potassium distribution on a guard ring of an STM sensor. The contamination of potassium can be found at the edge regions of the aluminium structures but also within the aluminium structure without any connection to the edge regions.

Obviously, the origin of the stain formation seems to be potassium contamination. The presence of phosphorous and potassium can be explained by residues of acids or lyes used during the sensor production process. Potassium hydroxide in particular is a standard chemical used in semiconductor manufacturing [KOH01].

The question as to which kind of chemical reaction takes place cannot be answered by an analysis of the elements. A further hint to the origin of the oxidation process comes from a comparison of a

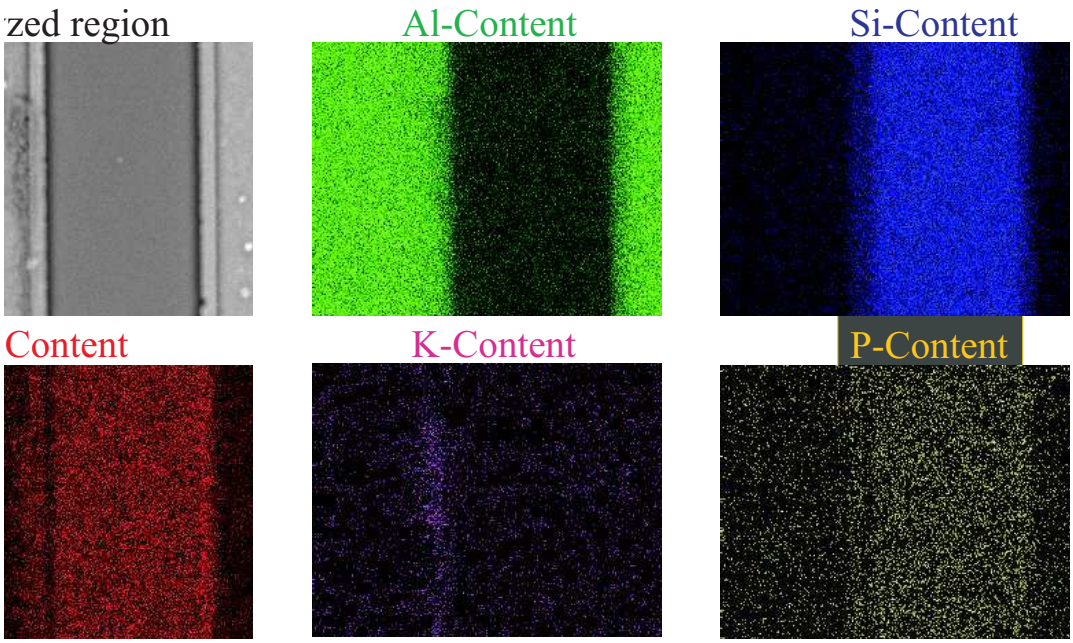

Figure 5.25: **Element map of bias ring on STM sensor:** *The correlation between potassium and oxygen and the stain on the bias ring is the same as for the guard ring in Figure 5.24.*

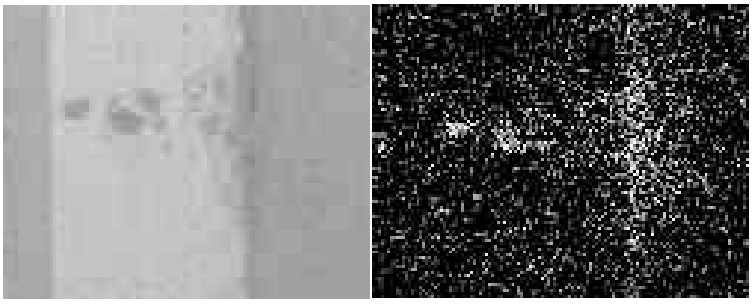

Figure 5.26: **Potassium distribution on guard ring of STM sensor:** *The plot on the right hand side shows the potassium distribution within the guard ring region on the plot on the left hand side. The potassium is not only found at the edge regions of the aluminium structures but also in the middle without connection to the edge regions.*

bias ring region with and without coverage by the passivation layer. Figure 5.27 shows that there are no differences for the passivated and non passivated regions. This corresponds to other observations of stains observed underneath passivated areas of bias rings. Many of these stains developed around the channel like via connecting the bias ring implant to its aluminium structure and many stains developed in regions of the bias ring far away from the vias. In the CMS collaboration various experiments have been carried out at different air humidities. After several hours of operation at a very low relative air humidity, a visual inspection showed no formation of stains. After increasing the air humidity, the stains developed after $30\,min$. This implies that the air humidity acquires through small cracks within the passivation layer to the aluminium structures of the bias ring and the guard ring and enables the formation of stains.

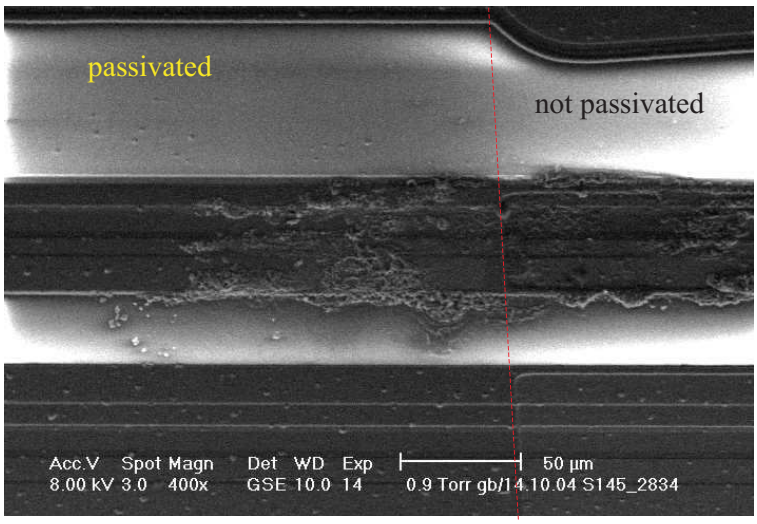

Figure 5.27: **Picture of partially passivated bias ring on STM sensor:** *The picture shows a top view of a bias ring which is passivated on the left hand side and where the passivation layer is removed on the right hand side. The chemical reaction underneath the passivation layer is not connected with the chemical reaction in the non passivated area.*

5.6.3 Relationship of Sensor Operation and Stain Formation

Figure 5.28 shows stains on DC pads which have been observed after a long-term test of 1169 h at 450 V and a relative air humidity of 50%. No formation of stains on AC pads is observed for even 2000 h of operation. Due to the low statistics, the formation of stains on AC pads at much higher operation times cannot for sure be neglected.

With an applied bias voltage the formation of stains always starts on the guard ring and then continuous on the bias ring and finally on the DC pads.

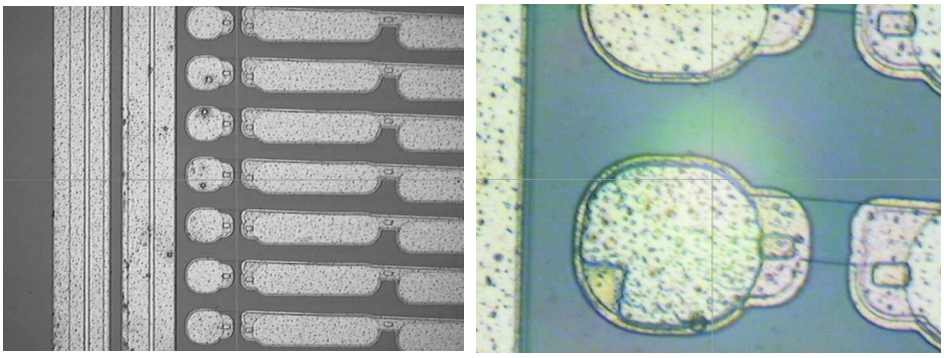

(a) (b)

Figure 5.28: **Picture of stains on DC pads of STM sensor:** *After* 1169 h *at a bias voltage of* 450 V *and a relative air humidity of* 50%*, the stains are also observed on the DC pads. On AC pads no stains have been seen until* 2000 h *of operation.*

5.6.4 Conclusions from Stain Analysis

Visual inspections hint to an operation related effect of stain formation. This finding is supported by the accelerated stain formation with high air humidity and under applied bias voltage. Without applied bias voltage, a stain formation is not observed but cannot for sure be neglected.

The appearance of stains underneath passivated areas of the sensors imply the existence of small cracks within the passivation layer which cannot be detected by visual inspection. These are probably caused by formation of small hillocks developed during high temperature processes of sensor production.

Analysis with the electron microscope endorse the assumption that stains are caused by chemical reactions with potassium (probably as catalyst for the oxidation process as no end of the expansion of the stains is observed) and oxygen with the aluminium structures of a sensor. The fact that stain formation initially occurs at the edges between the passivation layer and the aluminium structures can be explained by an insufficient cleaning (washing) process after which residues of potassium compounds remain at the edges. These stains are most probably Al_2O_3 and are not electrically conductive, which affects the functionality of the sensors because the metal overhang is reduced at the bias ring, the guard ring, and the strips.

The stain issue is accompanied by other problems like low interstrip resistances for some batches or the stress dependencies shown in Section 5.7. The stains endanger due to their non electrical conductive behavior the functionality of the STM sensors' metal overhang design what suggested to purchase more sensors from HPK because the STM sensors are unreliable.

5.7 Stress Dependencies of STM Sensors

Most sensors delivered by STM are in addition to the evolution of stains affected by mechanical stress dependencies. These sensors show a kink in the IV characteristics above full depletion voltage after which the total leakage currents get much higher than expected. The standard current level at full depletion voltage is for non affected sensors between $500\,nA$ and $2\,\mu A$ and for affected sensors it can be several $10\,\mu A$. The slope of the current after the kink depends strongly on the mechanical stress which is applied by the vacuum at the JIG. The stronger the vacuum, the higher the total leakage current results. In order to guarantee the functionality of the affected sensors and to predict their behavior during the service life of CMS a further test is performed. Some of these sensors are qualified during irradiation. This section describes the observations on these stress affected sensors done in the QTC's and the results of the leakage current measurements during irradiation will be described in Section 6.7.5.

5.7.1 Observation of Kinks in IV and ILeak

In the Karlsruhe probe stations the vacuum level applied to the sensors is buffered with a large reservoir between the JIG and the vacuum pumps and the pressure inside the reservoir is controlled automatically between two levels (see Section 5.3). Figure 5.29 shows the total leakage current dependency of a STM sensor on the vacuum pressure.

The highest current level is caused by a strong vacuum level. The lowest current levels are observed at nearly no pressure and the middle current values, which are reproduced here, are caused by a medium pressure value. The very high sensitivity of the leakage current to mechanical stress accents Figure 5.30. Here, the pump of the vacuum reservoir is switched on and off between two vacuum pressure levels and the total leakage current follows strictly the pressure in the vacuum reservoir.

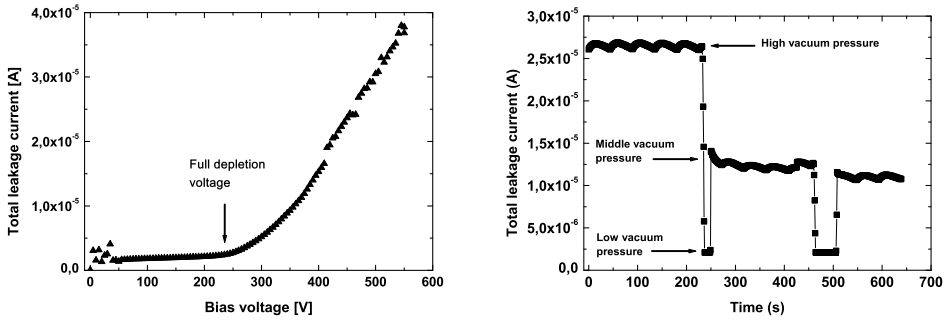

(a) (b)

Figure 5.29: **Total leakage current dependence on large vacuum changes of an STM sensor:** *The vacuum of the JIG is buffered with a large vacuum reservoir. The pressure in the reservoir is controlled automatically. The plot on the left hand side shows the IV characteristics of an STM sensor with applied vacuum at the JIG. The kink is always shortly above full depletion voltage of the sensor. The plot on the right hand side shows the total leakage current at* $450V$ *applied bias voltage. If the vacuum is significantly reduced the total leakage current goes down to* $2\mu A$*. The middle current level is reproducible by switching between no vacuum and the same vacuum pressure in the reservoir as before.*

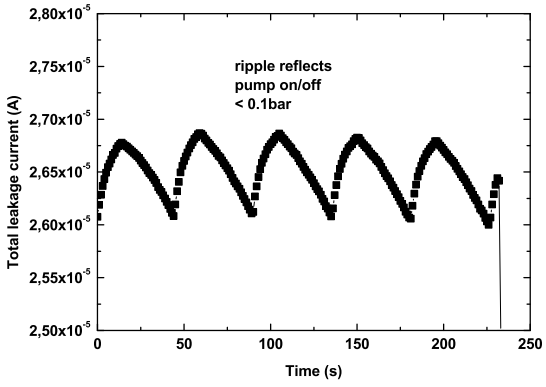

Figure 5.30: **Total leakage current dependence on small changes in vacuum for a STM sensor:** *Even the low pressure changes in the vacuum reservoir and therefore low changes of the mechanical stress cause measurable effects in the sensors total leakage current.*

Figure 5.31 shows single strip leakage currents versus bias voltage. The single strip leakage current of strip 238 rises up after full depletion voltage which is $200V$ for this sensor.

It is obviously that the total leakage current, which is the sum of all single strip leakage currents and edge currents, is driven by some high single strip leakage currents. For this reason, the problem of the high total leakage current has to be investigated on strip level.

A clear specification for the mechanical stress dependence is not possible because the real stress conditions in the tracker and the mechanical stress distribution on the JIG are unknown.

A parametrization of the vacuum strength and the level of the total leakage current is not possible since each sensor has an individually dependence on mechanical stress. The only common observation for all affected STM sensors is that the kink in the single strip leakage current is $20-30V$ above the full depletion voltage of the sensor. For HPK sensors even for highest vacuum levels at the JIG no dependence on mechanical stress is observed.

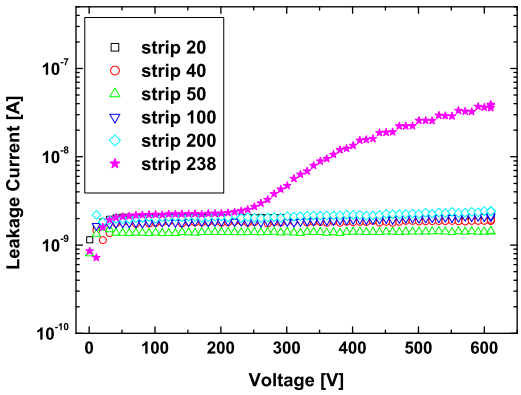

Figure 5.31: **Single strip leakage current of a STM sensor under mechanical stress:** *The high total leakage current under mechanical stress is driven by high single strip leakage currents. The full depletion voltage of this sensor is around* $200V$ *and the kink of the current is observed* $20-30V$ *above full depletion voltage.*

5.7.2 Summary of Stress Dependence in QTC

Most of the sensors are within the specifications of CMS, but the kink in the IV characteristic is present for almost all of the STM sensors. For all of these sensors, the total leakage current is driven by a few leaky strips. Many of these strips are out of specifications (max. $100nA$ per strip). For this reason, many sensors of STM have a too high number of faulty strips. For HPK sensors never a stress dependency on any sensor parameter was observed. Optical inspections exclude visible damage of the aluminium overhang and etching the aluminium and passivation layer to have a look on the p^+-implants gives no information to the problem, too. In order to find out the origin of the high leakage currents, the radiation hardness is under deep investigation in Section 6.7.5 with the aim to get further hints to the problem written above. The question to be answered is weather the leakage currents of the strips observed to be leaky (above $100nA$) under mechanical stress get worse or improve with irradiation. The individuality of the sensors leakage currents makes a direct comparison of the evolution of sensor parameters with fluence impossible and each sensor would have to be checked at all fluences. The first problem of irradiating sensors many times and to measure them afterwards is the activity after each irradiation step which has to cool down on a few days time scale requiring long time for these irradiations and measurements. The second main problem are costs and time reasons which prohibit to do the scenario with many irradiations with a reliable number of sensors. These problems provoke a monitoring of total and single strip leakage currents during irradiation. If a suspect effect is observed at a certain fluence it is possible to stop the irradiation and to make a detailed analysis on the sensor. The results of these leakage current measurements during irradiation are shown in Section 6.7.5.

Chapter 6

Irradiations for CMS

By far, not all mechanisms and factors of influences on radiation hardness of silicon sensors are known. It is a large active field of research. In order to guarantee the radiation hardness of the CMS sensors a small amount of the sensors supplied by the companies STM and HPK is irradiated with $26 MeV$-protons in Karlsruhe and with a spectrum of fast neutrons in Louvain-la-Neuve. The main reason to irradiate sensors is to guarantee their radiation hardness and to develop strategies to overcome emerging problems. Section 6.1 describes how to simulate with available radiation sources the expected radiation environment after service life of CMS. Afterwards, an overview of the used irradiation facilities is given in Sections 6.2 and 6.3. Section 6.4 explains the standard procedure of irradiation and following annealing of sensors used in IQC (see Sections 5.1 and 5.2). This is followed by the results concerning the full depletion voltage in Section 6.5, the total and single strip leakage currents in Section 6.7 and the strip parameters like the bias resistors in Section 6.8, the coupling capacitances in Section 6.9, the interstrip resistances, and the interstrip capacitances in Section 6.10. The functionality of the sensors is also tested on detector module level. The signal-to-noise ratio is investigated in Section 6.11.

In order to get the results from the Sections 6.5-6.11 the following structures were irradiated:

- 35 sensors in frame work of the IQC
- 60 mini sensors in frame work of the IQC (see Section 4.6 on Page 56)
- 80 diodes in frame work of the IQC
- 27 detector modules in frame work of the IQC
- 2 HPK sensors (special annealing study)
- 2 STM sensors (leakage current measurement during neutron irradiation)
- 10 special bias resistor structures (see Section 4.6 on Page 56)

All measurement results from Section 6.5 are used to calculate scenarios of the sensors' full depletion voltage development. The sensors, mini sensors, and diodes irradiated in Louvain for IQC are taken into account for the itemize above.

6.1 Scaling of Fluences with NIEL

The harsh radiation environment contains different particles and fluences depending on the position inside CMS and the luminosity of the LHC. Charged hadrons and back scattered neutrons from the ECAL dominate this fluence as shown in Table 1.4 on Page 11 and Figure 1.11 on Page 10. Those particle spectra cannot be simulated by a single irradiation facility, as different types of particles are required. Therefore, it was decided by the CMS collaboration to use the irradiation sources which are available inside the CMS collaboration. These are the Kompakt-Zyklotron (KAZ) in Karlsruhe accelerating protons to $26\,MeV$ and the isochronous cyclotron in Louvain-la-Neuve accelerating deuterons from which a fast neutron spectrum is generated by shooting the deuterons onto a fixed *Be* target. In order to find beam conditions leading to similar irradiation damage expected in the tracker the NIEL hypothesis, which is explained in Chapter 3, is used. From the particles damage function, shown in Figure 6.1, the hardness factors κ for the irradiation facilities particles are determined.

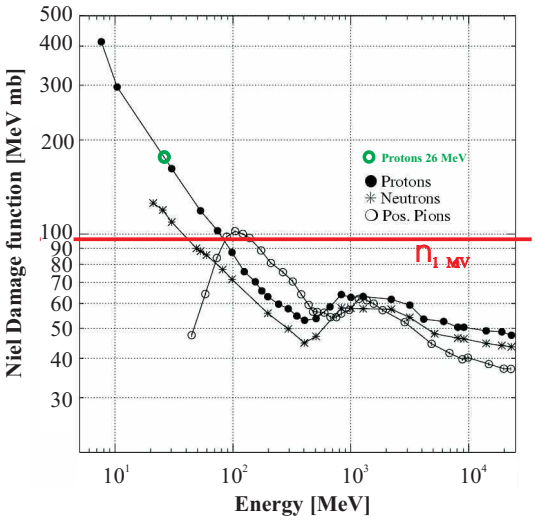

Figure 6.1: **NIEL damage functions for positive pions, protons, and neutrons:** *The damage functions are decreasing with increasing energy. The damage function of neutrons with an energy of* $1\,MeV$ *and a damage function value of* $95\,MeV\,mb$ *is used as reference for scaling of particle fluences. Damage function ratios of other particles and energies to the reference value is called "hardness factor" (see Equation 3.4). For protons with an energy of* $26\,MeV$ *used in the Kompakt-Zyklotron in Karlsruhe the hardness factor is* 1.85. *The averaged hardness factor of the neutron spectrum used for the spectrum of neutrons in Louvain-la-Neuve is* 1.95.

6.2 The Kompakt Zyklotron at Karlsruhe

The Kompakt-Zyklotron (KAZ) in Karlsruhe accelerates protons up to an adjustable energy between $18\,MeV$ and $40\,MeV$. The maximum available beam current is around $100\,\mu A$ [Fur04a][Sch84][Sch04]. The advantage of the KAZ, contrary to other accelerator types, is the H^--source. The H^- ions are accelerated inside the KAZ and a magnetic field bends them to a circular track. When the H^- ions achieved the required energy, they are shot through a stripping foil which removes the electrons. Since the H^+ ions circular track in the magnetic field is of the opposite direction to the H^- ions, the same magnetic field can be used to move the H^+ ions out of the KAZ to the beam lines in which the H^+ ions gets to the beam target. The current produced by the electrons collected in the stripping foil is proportional to the H^+ fluence. This enables an measurement of the beam current during the irradiation. In the IQC a proton energy of $26\,MeV$ is used. The hardness factor (see Equation 3.4) of the protons at this energy is 1.85 as extracted from the Figure 6.1. Figure 6.2 shows the beam line and the irradiation setup used for scans perpendicular to the proton beam (explained in Section 6.2.1). The aluminium box supporting the structures to be irradiated is thermally isolated with Styrodur© plates and has a $3\,cm$ thick layer of carbide at the back to stop the protons passing the double mylar foil windows and

the structures to be irradiated. The aluminium box is flooded with cold nitrogen gas to avoid local overheating and annealing effects. The temperature is monitored with temperature dependent resistors (Pt100) and is regulated with the cold nitrogen gas flow with a mass flow controller. Cooling pipes with liquid cooling fluid inside would be activated by the protons and therefore they are not suitable for the beam setup. Only 15 minutes are necessary to irradiate an area of $100\,cm^2$ to a fluence of $1 \cdot 10^{14}\,n_{1MeV}/cm^2$ using a beam current of $2\,\mu A$ and scanning the area two times with a box velocity of $\sim 110\,mm/s$. Higher beam currents can overheat the mylar foil and the frames inside the aluminium box fixing the sensors. The maximum used current is $16\,\mu A$ for irradiations of silicon. Higher currents could inflame the graphite used as beam absorber behind the structures to be irradiated.

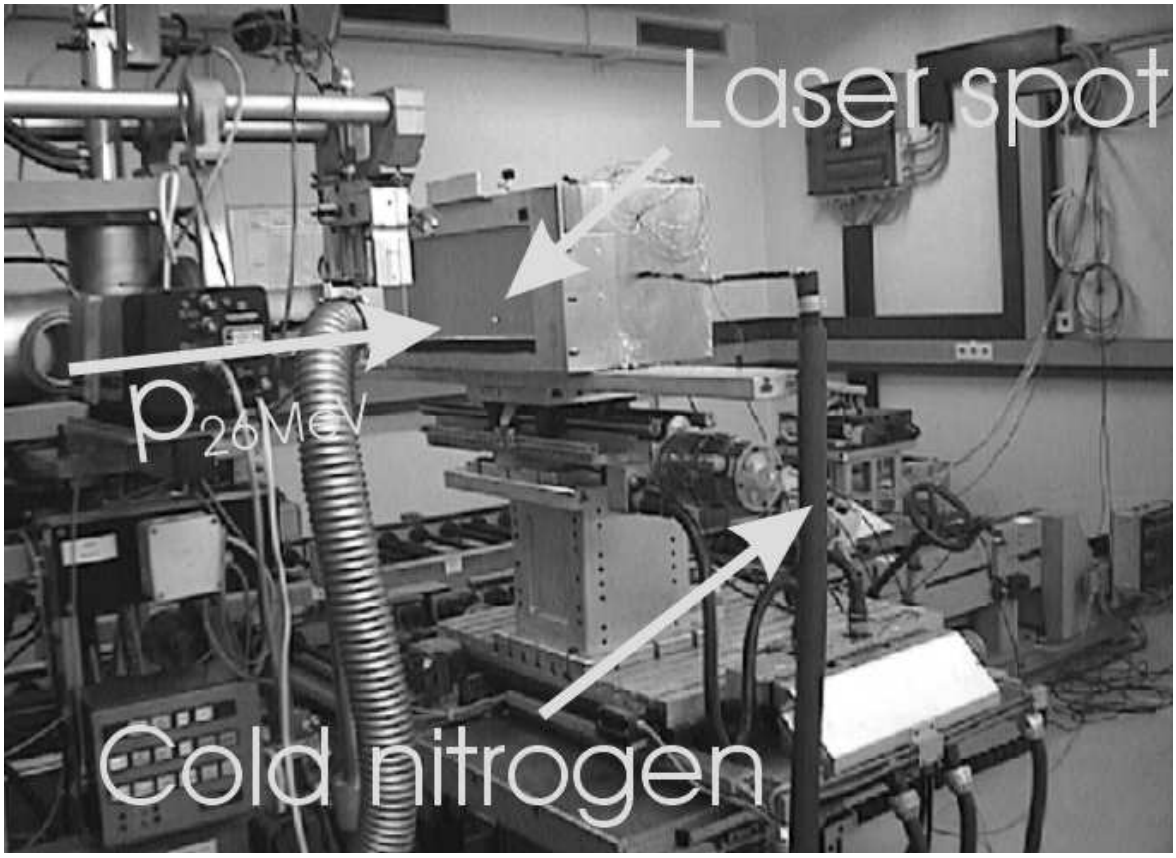

Figure 6.2: **The Kompakt-Zyklotron in Karlsruhe:** *At the Kompakt Zyklotron at the Forschungszentrum in Karlsruhe protons with an energy of* $18\,MeV$ *up to* $40\,MeV$ *are available for irradiation. The box supporting the structures to be irradiated can move in two directions. During irradiation, scans in front of the proton beam are performed. With a proton current of* $2\,\mu A$ *only* $15\,min$ *are necessary to irradiate an area of* $100\,cm^2$ *to a fluence of* $1 \cdot 10^{14}\,n_{1MeV}/cm^2$*. The box is flooded with cold nitrogen gas to keep the temperature during and after irradiation as cold as necessary to avoid local overheating or annealing effects. A red laser is used for aligning the scan areas.*

In earlier irradiations some sensors were biased during irradiation to test the oxides stability [Fur02]. The frames used for fixing the sensors and test structures and to apply a bias voltage are shown in Figure 6.3.

In order to be more efficient new frames made of aluminium are used as shown in Figure 6.4. The

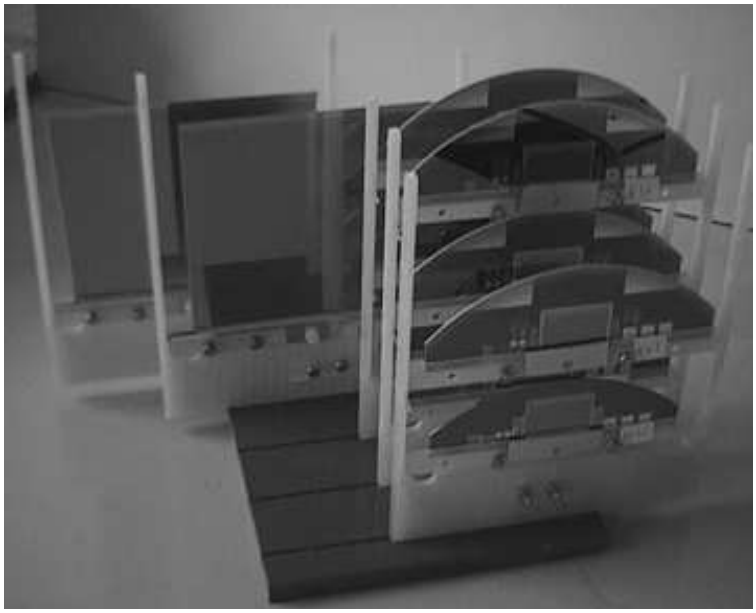

Figure 6.3: **Picture of CMS sensors in stacks ready for irradiation:** *The sensors and test structures to be irradiated are stacked in frames of glass fiber or teflon. The clamps fixing the structures contain electrical contacts, which allow to apply a certain voltage to the structures.*

structures which have to be irradiated are fixed with capton tape and the whole area of the irradiation box $(20\,cm \times 40\,cm)$ can be used for irradiation.

6.2.1 Calculation of Proton Fluence

The scans are performed in X- (left-right) and Z- (up-down) direction. In order to avoid an inhomogeneous fluence profile, the Z-movements are performed outside of the area to be irradiated. For this reason, only the velocity in X-direction of the scans is important for the achieved proton fluence. The proton fluence Φ_p of a scanned area A is given by [Die03]:

$$\Phi_p = \frac{It}{eA} \tag{6.1}$$

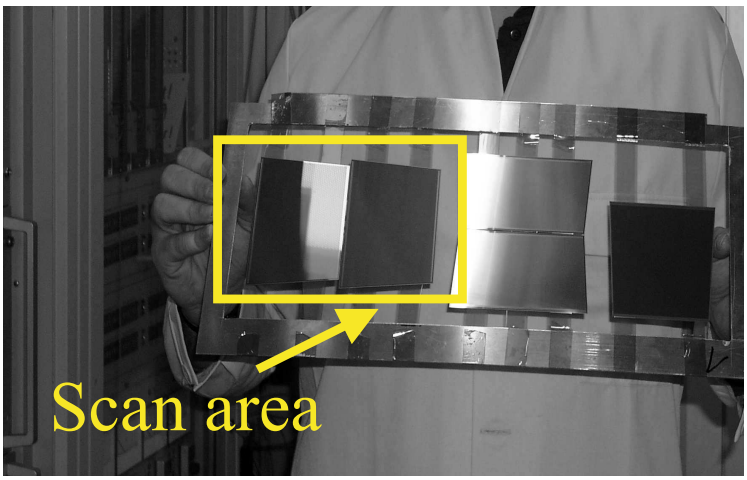

Figure 6.4: **Aluminium frame for proton irradiation:** *The sensors are fixed with capton tape and the whole scan area of the irradiation setup* $(20\,cm \times 40\,cm)$ *can be used for irradiation.*

with the proton beam current I, the irradiation time t, and the area to be irradiated A. The beam current is an integral over the current density

$$I = \int\int j(x,z)dxdz = \int\int j(v_x \cdot t, z)v_x dtdz \tag{6.2}$$

with the scan velocity in X-direction v_x. Moving in Z-direction on the area to be irradiated would give an inhomogeneous profile on the structures. Therefore, a larger area ($1-2$ beam radius on each side) is scanned and only the inner homogeneous area is used. The integral can be approximated with a scan height Δz:

$$I = \int e\Phi_p(z)v_x dz \approx \sum_i e\Phi_p(z)v_x \Delta z_i \tag{6.3}$$

with the distance Δz_i between two movements in X-direction. For homogenous scans these distances are equal and the final equivalent fluence Φ_{eq} is then given to

$$\Phi_{eq} \approx \frac{I}{ev_x \Delta z} \cdot \kappa \tag{6.4}$$

with the hardness factor κ from Equation 3.4 on Page 38.

6.2.2 Measurement of Proton Fluence

After irradiation the fluence is checked by activation of Ni-foils placed behind the irradiated structures. Natural Ni has a fraction of 63% of the $^{58}_{28}Ni$ isotope. The protons with an energy of $26\,MeV$ activate the $^{58}_{28}Ni$ isotope via a $(p,2n)$ reaction.

$$\begin{aligned} p + {}^{58}_{28}Ni &\rightarrow {}^{57}_{29}Cu + 2n \\ {}^{57}_{29}Cu &\rightarrow {}^{57}_{28}Ni + \beta^+ + \nu_e \end{aligned} \tag{6.5}$$

The following β^+ decay of the produced $^{57}_{29}Cu$ ($\tau_{1/2} = 199\,ms$) gives the $^{57}_{28}Ni$ isotope with a half life time of $35.6\,h$ [PKS98]. This isotope decays via electron capture and the emission of the characteristic γ at $1377.6\,keV$ which is measured with a germanium detector. The current activity $a(t_{measurement})$ is used to determine the activity at $3.77\,d$ after end of the irradiation because the method with the Ni-foil is calibrated with this procedure. The reference activity $a(3.77d)$ is calculated to [Die03]:

$$a(3.77d) = a(t_{measurement}) \exp\left(-\frac{(3.77d - t_{measurement})\ln(2)}{\tau_{1/2}}\right) \tag{6.6}$$

with $\tau_{1/2} = 35.6\,h$. For other proton energies, the calibration factor from the Ni-foil has to be corrected to the proton energy with the corresponding cross section shown in Figure 6.5 [LB91], which leads to the following calibration factor:

$$f_{cal}(\sigma_E) = \frac{\sigma_E}{\sigma_{26MeV}} \cdot 19.28 \frac{kBq \cdot cm^2}{mg \cdot \mu Ah} = \frac{\sigma_E}{\sigma_{26MeV}} \cdot 8.57 \cdot 10^{-13} \frac{kBq \cdot cm^2}{mg \cdot p} \tag{6.7}$$

with the interaction cross section σ_E of the protons with energy E and the NI-foil, and with the reference interaction cross section σ_{26MeV} of $26\,MeV$ protons. Finally the equivalent fluence is given by:

$$\Phi_{eq} = \frac{a(3.77d)}{f_{cal}(\sigma_E)} \cdot \kappa \tag{6.8}$$

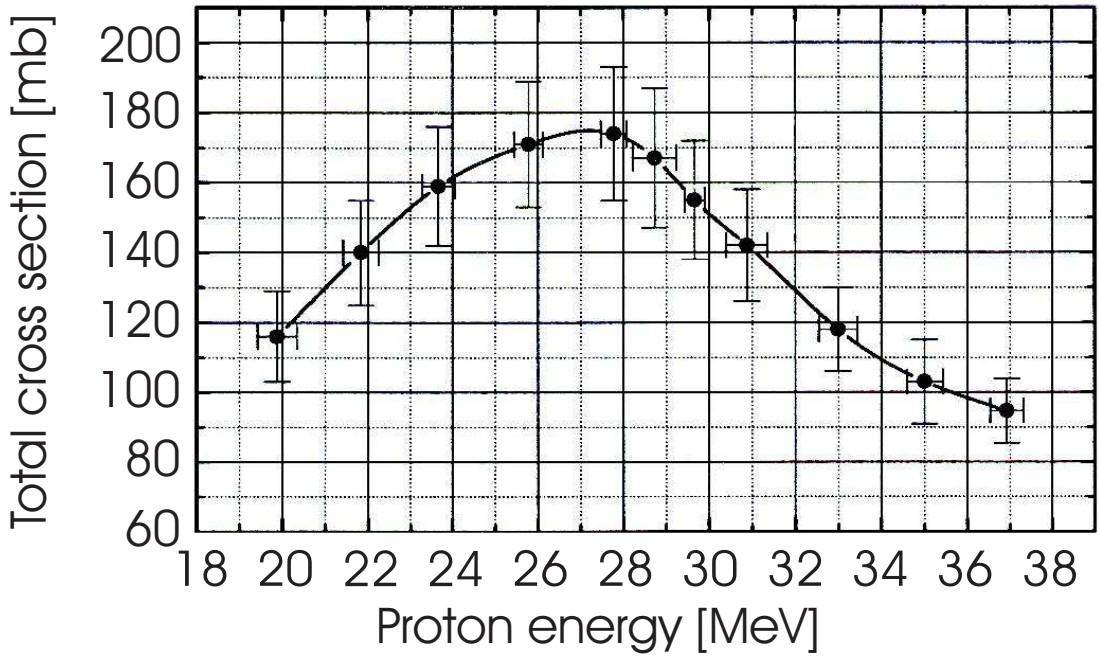

Figure 6.5: **Cross sections for protons with Ni:** *Protons with an energy of* $26\,MeV$ *and a cross section for Ni of* $172\,mb$ *are used for the irradiations in Karlsruhe [LB91].*

One has to take care that the *Ni*-foil is irradiated homogenously, otherwise it has to be cut and each piece has to be weighted and measured individually. For a fluence of $2.4 \cdot 10^{14}\, n_{1MeV}/cm^2$ 4 scans with a beam current of $2\,\mu A$, a Δz-step of $1\,mm$, and a velocity $v_x = 110\,mm/s$ are performed.

For some applications the dose D is more interesting than the fluence. In order to calculate the dose, first the stopping power $P_{Stopping}(E)$ has to be calculated. The parametrization is given by NIST [NIS]:

$$\begin{array}{lcl} P_{Stopping}(E) & = & 8.1\,\frac{MeV\cdot cm^2}{g} + 8.8\,\frac{MeV\cdot cm^2}{g}\exp\left(-\frac{E-25.1\,MeV}{17.1\,MeV}\right) \\ P_{Stopping}(\frac{E}{d}) & = & \frac{P_{Stopping}(E)}{4.3083}\left[\frac{MeV}{mm}\right] \end{array} \tag{6.9}$$

Finally the dose is calculated to:

$$D = \Phi_p P_{Stopping} \cdot 1.6022 \cdot 10^{-13}\,\frac{J}{MeV} \tag{6.10}$$

A $26\,MeV$-proton fluence of $2.4 \cdot 10^{14}\, n_{1MeV}/cm^2$ corresponds to a dose of $340\,kGy$, which is five times higher than predicted in the CMS Technical Design Report [CTDRA00] with $67\,kGy$ (see Figure 1.11 on Page 10). Since at $50\,kGy$ the charge concentration of the oxide layers saturates [Wue01], it can be assumed that higher doses do not change the properties of the sensors oxide layers anymore.

6.3 The Neutron Facility at Louvain-la-Neuve

The irradiation facility in Louvain-la-Neuve is an isochronous cyclotron accelerating deuterons which are shot onto a fix *Be* target as shown in Figure 6.6. The deuterons interact with the *Be* as follows:

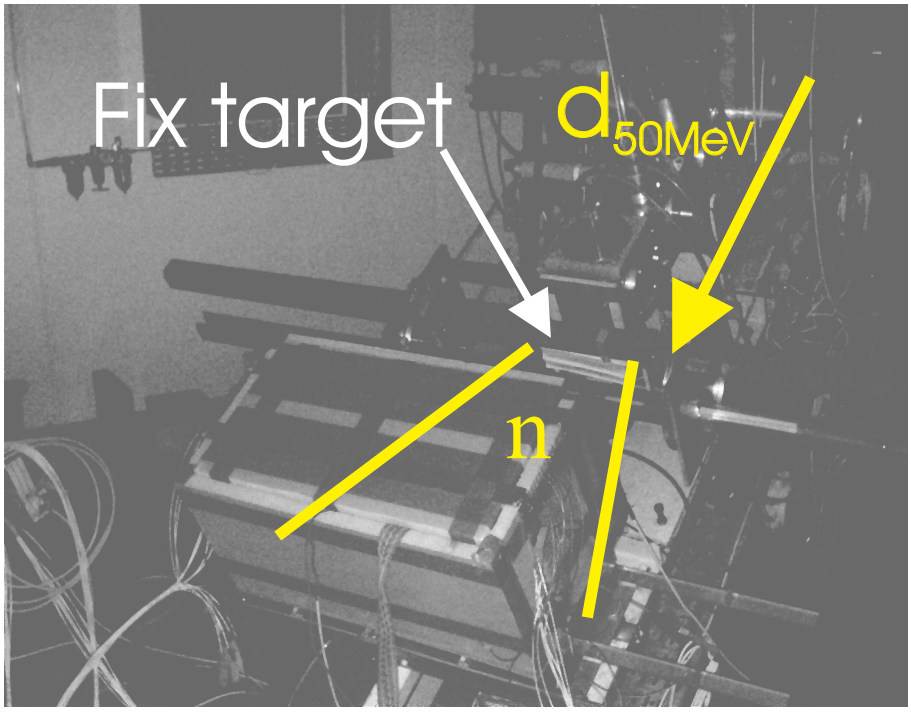

Figure 6.6: **The irradiation facility in Louvain-la-Neuve:** *The Cyclotron in Louvain-la-Neuve accelerates deuterons to an energy of* $50\,MeV$. *These are directly shot onto a fix Be-target which is described in Figure 6.7. In order to avoid annealing effects, the box containing the structures to be irradiated, is flooded by cold nitrogen gas. Up to 16 hours of irradiation are necessary for a fluence of* $2.4 \cdot 10^{14}\, n_{1MeV}/cm^2$.

$$^{9}_{4}Be + d \rightarrow n + X \tag{6.11}$$

The *Be*-target has a thickness of $1\,cm$ and the deuteron beam used for the irradiations presented in the next sections is $11\,\mu A$. The beam time structure is made of $4\,ns$ bunches with a repetition period of $80\,ns$ reflected in the secondary neutron beam. The schematics of the fix *Be*-target, the collimator and absorber are shown in Figure 6.7. The absorber is made of a $1\,mm$ thick polystyrene layer, a $1\,mm$ thick *Cd* layer, and a $1\,mm$ thick *Pb* layer to reduce the contamination by charged particles inside the neutron beam. The spectrum of neutrons after the absorber shows Figure 6.8. The average neutron energy is $20.4\,MeV$. The remaining beam impurities are summarized in Table 6.1 [Gre02]. A hardness factor of $\kappa = 1.95$ is given for the full neutron beam with all its impurities. The dose after irradiation is checked by an alanine dosimeter measuring the γ-dose as constant fraction of approximately 2.4% of the total beam.

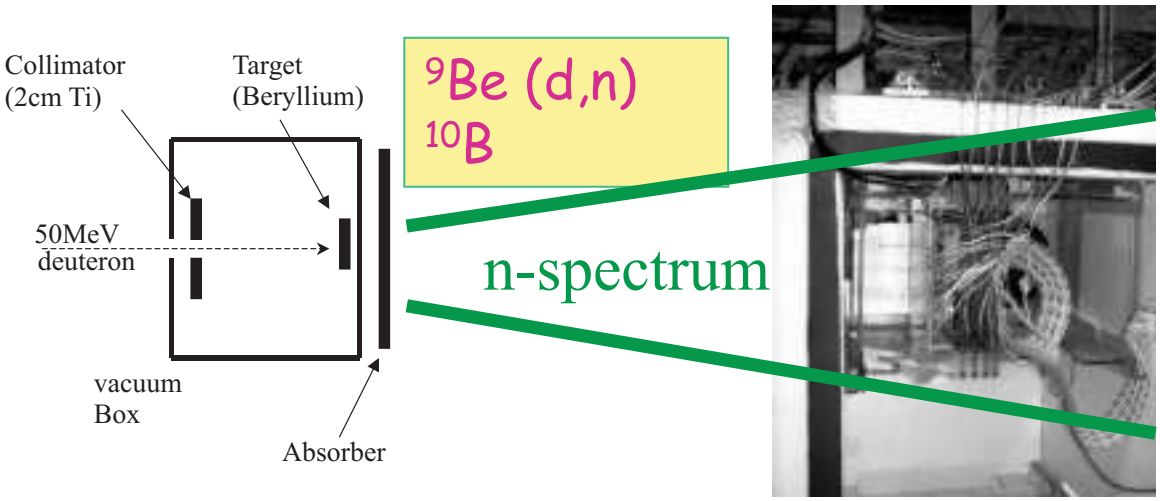

Figure 6.7: **Fix target of the irradiation facility in Louvain-la-Neuve:** *The deuterons are shoot onto a fix* 1 *cm thick Be target. The secondary beam is filtered by an absorber built of a* 1 *mm layer polystyrene, a* 1 *mm layer of Cd, and a* 1 *mm layer of Pb.*

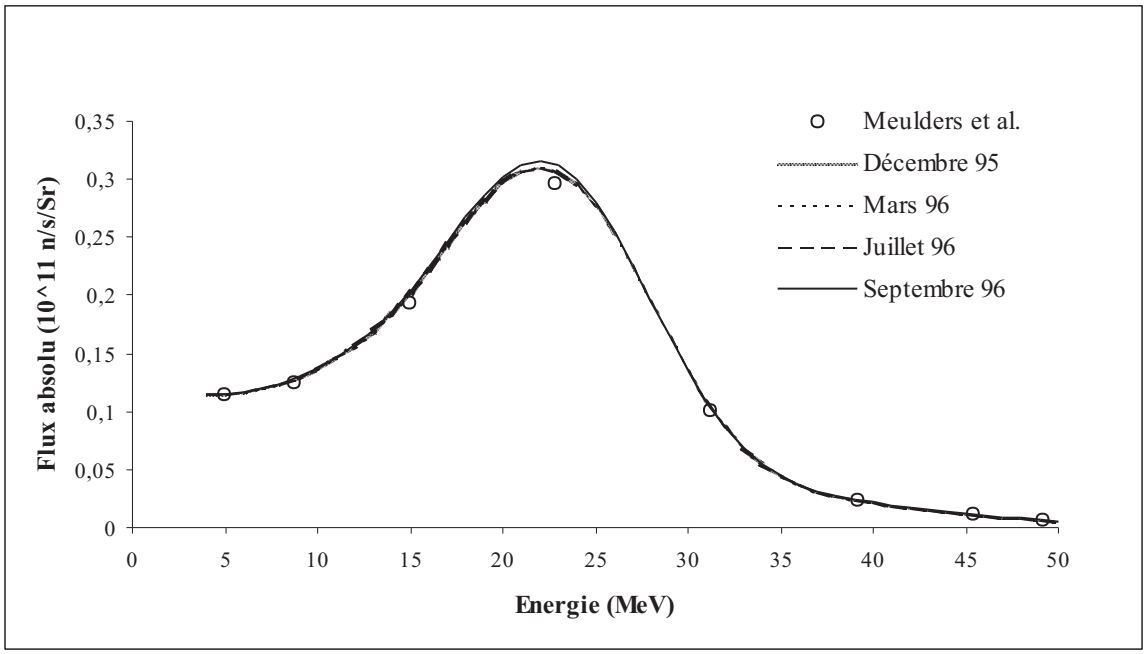

Figure 6.8: **Energy spectrum of neutrons at the irradiation facility in Louvain-la-Neuve:** *The neutron spectrum has an average energy of* 20.4 *MeV after the fix target and after the absorber filtering the impurities of the neutron beam. The remaining beam contains in addition to the neutrons around* 2.4% *of gammas and around* 0.03% *of charged particles. The final hardness factor of the beam spectrum is* $\kappa = 1.95$ *[Gre02] .*

Particle type	Fraction	$< E > [MeV]$	$E_{max}\ [MeV]$
n	≈ 1	20	50
p	$1.5 \cdot 10^{-4}$	12.61	25
e^-	$1.6 \cdot 10^{-4}$	1.57	6
γ	$2.4 \cdot 10^{-2}$	1.93	10

Table 6.1: **Neutron beam impurities in Louvain-la-Neuve:** *The fraction of charged particles is approximately* 0.03% *[Gre02].*

6.4 Standard Irradiation and Annealing Procedure

The maximum expected fluences in the tracker are $0.5 \cdot 10^{14}\, n_{1MeV}/cm^2$ for sensors with a thickness of $500\,\mu m$ and $1.6 \cdot 10^{14}\, n_{1MeV}/cm^2$ for sensors with a thickness of $320\,\mu m$. Due to the high uncertainties of the expected fluences (see Section 1.4.3 on Page 8) a safety margin of 50% is added to the fluences above. Before irradiation, the sensors are qualified on strip level at a bias voltage of $400\,V$ and a temperature of $20 \pm 1^{\circ}C$. In addition for five strips the values are measured versus bias voltage, in the following called ramps. Afterwards the sensors are irradiated. After irradiation, a annealing of $80\,min$ at $60^{\circ}C$ is performed. This corresponds to the expected minimum in the full depletion voltage after beneficial annealing. At annealing temperatures above room temperature, the minimum of the full depletion voltage is higher than predicted by the Hamburg model. For this reason, the sensors are kept after the high temperature annealing for $24\,h$ at room temperature. After this in the following called "standard annealing" procedure, the full depletion voltage behaves like predicted with the Hamburg model. After the standard annealing, the same measurements as before irradiation are performed at $-10^{\circ}C$.

The following sections describe the results of the standard irradiation procedure on many sensors,mini sensors, and diodes in IQC and the results of an annealing study done on two HPK sensors. For some parameters special irradiation campaigns took place and the results are included in the investigations of the corresponding parameters.

6.5 Results of Full Depletion Voltage Measurements

For CMS the full depletion voltage is the most important parameter of a sensor. Particularly after type inversion, the sensors cannot be operated below full depletion voltage due to the partially depleted bulk which grows from the backside of the sensor to the strip implant side. An overdepletion of approximately 50% is necessary to reach the maximum of the signal to noise ratio. Due to this fact, for a full depletion voltage of $400\,V$ a bias voltage of $600\,V$ is necessary. In the following the observations of full depletion voltage measured with the standard IQC procedure (see previous Section), with annealing at $20^{\circ}C$ and $60^{\circ}C$, and for special batches supplied by HPK are presented.

6.5.1 Full Depletion Voltage after Service Life at LHC

Figure 6.9 shows the full depletion voltages of proton irradiated $320\,\mu m$ mini sensors supplied by HPK and of $500\,\mu m$ mini sensors supplied by STM after standard IQC annealing procedure of $80\,min$

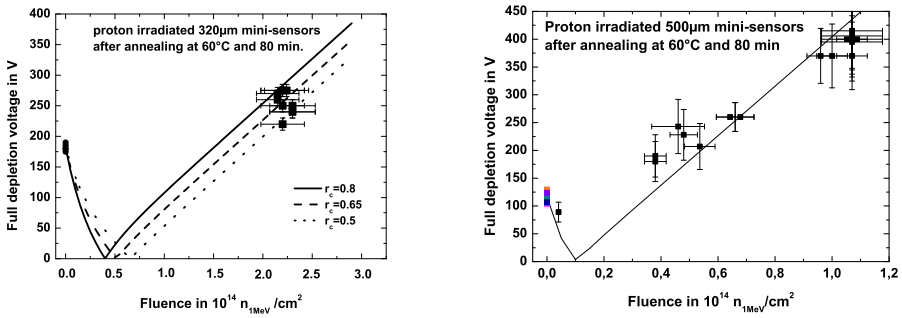

(a) HPK mini sensors (b) STM mini sensors

Figure 6.9: **Full depletion voltages of HPK and STM mini sensors before and after proton irradiation:** *The development of the full depletion voltage follows the prediction of the Hamburg model [Mol99]. The incomplete donor removal parameter r_C is 0.65 ± 0.15 (see Equation 3.17 on Page 44).*

at $60°C$ and subsequent $24\,h$ at room temperature. The full depletion voltages of all structures supplied by both companies observed in IQC correspond most times well to the expectations of the Hamburg model in Section 3.4 on Page 44.

6.5.2 Annealing of Full Depletion Voltage

The annealing of the total capacitance and the full depletion voltage with time is measured for two W1TID sensors supplied by HPK. Figure 6.10 shows the CV characteristics of these two sensors after proton irradiation with a fluence of $2.4 \cdot 10^{14}\, n_{1MeV}/cm^2$ for different annealing steps at $20°C$ and $60°C$. The plot $1/C^2$ versus bias voltage accentuates the kink of the curves at full depletion voltage.

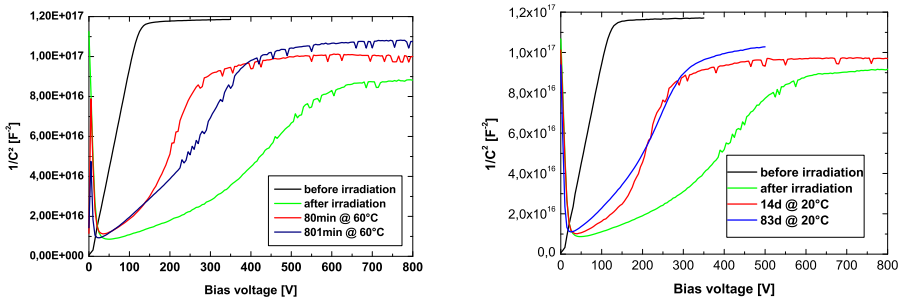

(a) Annealing at $60°C$ (b) Annealing at $20°C$

Figure 6.10: **CV curves of HPK sensors versus annealing time:** *The plot $1/C^2$ versus bias voltage accentuates the kink of the curves at full depletion voltage. The kinks shift to lower voltages with beneficial annealing (below $80\,min$ / $14\,d$) and to higher voltages with the reverse annealing (beyond $80\,min$ / $14\,d$). The increase of total capacitance values for the full depleted sensors after irradiation results from the dielectric constant (ε_R) changes of the sensor's bulk. This total capacitance value of a fully depleted sensor shows only a decreasing behavior with time and is not connected to the annealing of the full depletion voltage.*

The kink of the curve at full depletion voltage shifts to lower voltages with beneficial annealing (below $80\,min$ at $60°C$ or $14\,d$ at $20°C$) and to higher voltages with the reverse annealing (beyond $80\,min$ or $14\,d$). The higher total capacitance values beyond full depletion voltage after irradiation result from the dielectric constant (ε_R) changes of the sensor's bulk. The total capacitance of a fully depleted sensor only decreases with time and does not show a similar annealing behavior as the annealing of the full depletion voltage. This fact leads to the conclusion that the radiation damage which is responsible for the changes of the effective doping concentration and for the changes of ε_R is not necessarily the same.

Figure 6.11 shows the beneficial annealing of the full depletion voltage of the two sensors. The

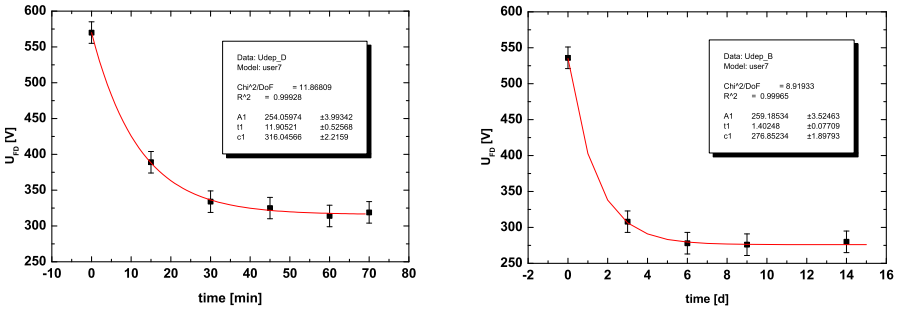

(a) Annealing at $60°C$ (b) Annealing at $20°C$

Figure 6.11: **Beneficial annealing of full depletion voltage on HPK sensors:** *The time constants for the beneficial annealing are* $\tau_A = 11.9 \pm 0.5\,min$ *for* $60°C$ *and* $\tau_A = 1.4 \pm 0.07\,d$ *for* $20°C$. *This is around* $2/3$ *of the values summarized in Table 3.6 on Page 46. The full depletion voltage after beneficial annealing at* $60°C$ *is with* $316 \pm 2\,V$ *approximately* $40\,V$ *higher than for annealing at* $20°C$.

time constants are approximately $2/3$ of the values expected after [Mol99]. After beneficial annealing at $60°C$ the full depletion voltage is approximately $40\,V$ higher than for beneficial annealing at $20°C$. This mystery can be explained with the observations done for the reverse annealing. Figure 6.12 contains the beneficial and the reverse annealing of the full depletion voltage of the sensor annealed at $60°C$. For each annealing step above $70\,min$ an additional annealing steps of $24\,h$ at room temperature took place. With this procedure, the offset of $40\,V$ disappears completely and the same minimum of full depletion voltage is measured as for annealing at $20°C$. The explanation for this fact are either excited states of some radiation damage due to the higher temperature or the appearance of further damage which decays at room temperature. It has to be pointed out that this offset is normally only observed during reverse annealing and there is no comparable effect observed for the total capacitance [CDMR03].

Figure 6.13 shows the reverse annealing of full depletion voltage for a proton irradiated mini sensor supplied by HPK. The annealing is done at $60°C$ with subsequent annealing phases of $24\,h$ at room temperature after each annealing step. The higher time constant of $\tau_y \approx 2,000\,min$ (in comparison to $1,260\,min$ in Table 3.6 on Page 46) is within the range of the errors given for Equation 3.22 on Page 45.

Since the CMS tracker will not be annealed at temperatures above room temperature, the offset in full depletion voltage observed in Figure 6.12 will not be present during the service life of the CMS tracker and for this reason it is not under deep investigation. The following two sections show cases for which the parametrization of the Hamburg model is not valid.

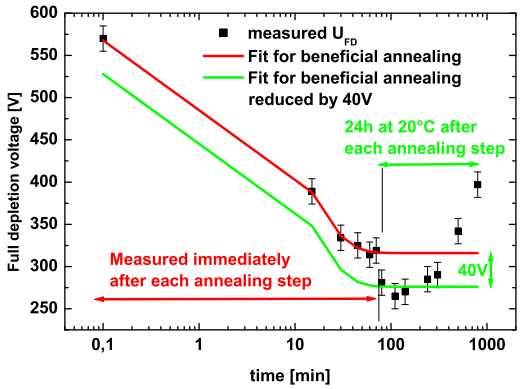

Figure 6.12: **Beneficial and reverse annealing of full depletion voltage on HPK sensor:** *This plot shows the annealing at* $60°C$ *including reverse annealing. For annealing steps above* $70\,min$ *at each annealing step the sensor has been annealed at room temperature for* $24\,h$*. This causes a drop of the full depletion voltage of* $40\,V$ *and the sensors full depletion voltage follows the valid parametrization of the Hamburg model. With this procedure the mystery of the* $40\,V$ *difference in figures 6.11(a) and 6.11(b) can be explained with either excited states of radiation damage or with appearance of further damage which decays at room temperature. This fact cannot be observed for the total capacitance.*

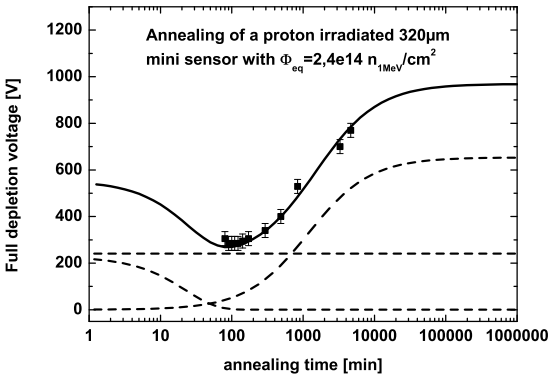

Figure 6.13: **Reverse annealing of a HPK mini sensor after proton irradiation:** *The reverse annealing time constant* τ_y *of the mini sensors full depletion voltage is approximately* $2,000\,min$ *instead of the expected* $1,260\,min$ *in Table 3.6 on Page 46. The deviation can be explained with the large uncertainties of the reverse annealing time constant [Fur03].*

6.5.3 Full Depletion Voltages of Final STM Pre-series Sensors

The sensors supplied by STM have a different initial quality than sensors supplied by HPK (see Section 5.5). Further differences in quality are found for various sensor parameters after irradiation. After many problems reported to STM, a final pre-series of sensors had to be evaluated before and after proton irradiation. Table 6.2 gives a short overview about the final STM pre-series sensors which were irradiated with protons in Karlsruhe. Figure 6.14 shows the full depletion voltage after standard

Sensor ID	Geometry	Thickness $[\mu m]$	Fluence 10^{14} $\left[\frac{n_{1MeV}}{cm^2}\right]$
30211034572227	W5B	500	0.1
30211034572312	W5B	500	0.2
30211034572304	W5B	500	0.2
30210934442308	W5A	500	0.3
30210934442343	W5A	500	0.3
30211434890233	W7B	500	0.65
30211434603447	W7B	500	0.65

Table 6.2: **Sensors from final STM pre-series:** *The seven sensors come from a final STM pre-series.*

annealing procedure of seven STM sensors at four different fluences.

For the five sensors at the lowest fluences, the full depletion voltages are in range of expectations whereas the two W7B sensors with the highest fluence have full depletion voltages which are approximately 100% above the expectations of the Hamburg model. A further worrying fact is the large difference between the two sensors full depletion voltage although the sensors had the same initial full depletion voltage and have been irradiated and annealed at the same time under the same conditions. The total capacitances of the sensors versus applied bias voltage is shown in Figure 6.15. The total capacitance of the fully depleted W7B sensors are equal but the kinks at full depletion voltage reflect the difference in full depletion voltages in Figure 6.14.

After irradiation of 20 STM sensors no large deviation has been found between measured and expected full depletion voltages except of the two case written above. These two outliers from the STM sensors' final pre-series which show this new and completely unknown problem, are a further hint that there are still intrinsic problems in the STM sensors' quality and their radiation hardness. In particular, the schedule of the CMS tracker did not allow further investigations for this problem what results in further orders of HPK sensors.

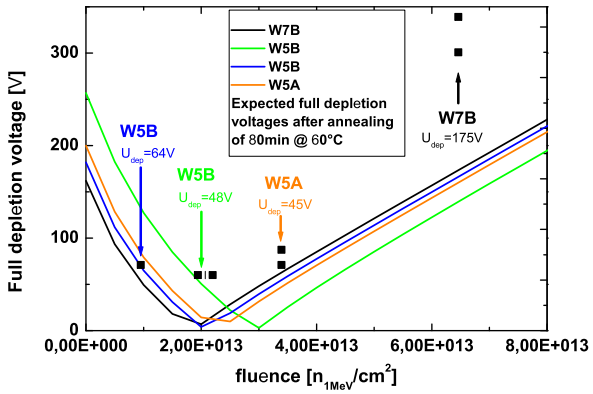

Figure 6.14: **Full depletion voltages of final STM pre-series sensors:** *The expected development of U_{FD} is shown for the different initial U_{FD}. The square dots present the measured U_{FD} after standard annealing procedure and the values below the sensors geometries are the expectations after the Hamburg model. The W7B sensors have a* 100% *higher U_{FD} than expected and have also a difference to each other while they had the same initial full depletion voltage.*

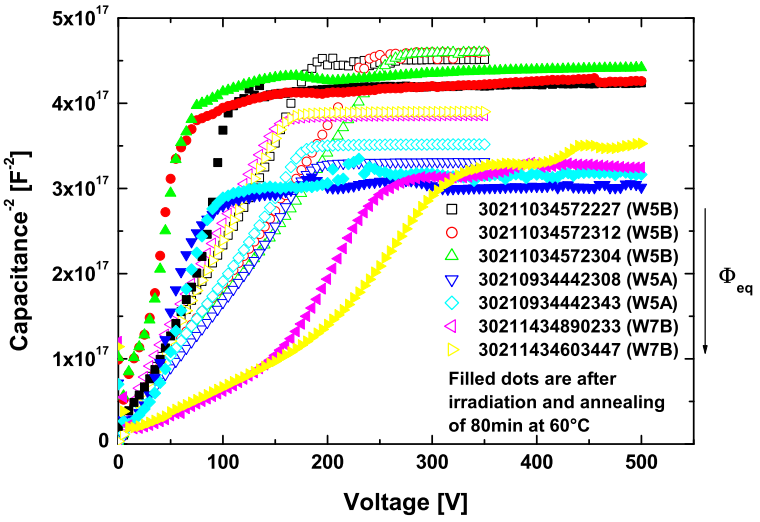

Figure 6.15: **Total capacitance from final STM pre-series sensors:** *After irradiation and standard annealing of* $80\,min$ *at* $60°C$ *(filled dots) a large difference has been observed for the W7B sensors full depletion voltage (kink in curves). They had the same initial* U_{FD} *and exact the same fluence and annealing procedure.*

6.5.4 Parametrization for High Resistivity Sensors from HPK

Another problem found in the QTC is that HPK delivered a few batches of sensors with too high initial resistivity. HPK orders ingots of defined resistivity which is - instead of the important value of full depletion voltage which depends also on geometry (see Section 2.4.1) - the requested value in the contract between HPK and the CMS collaboration.

The full depletion voltage results low with high resistivity (see Equation 2.26 on Page 24). The full depletion voltage after irradiation in Equation 3.17 on Page 44 also depends on the initial resistivity. The lower donor concentration of these sensors bulk is at lower fluences compensated by the introduction of acceptors. After same fluence and same annealing conditions, for these sensors a higher final full depletion voltage is expected than for sensors built of standard material. Unfortunately, the sensor geometries IB1, W1TID, and W3 are affected by this problem. Large safety margins of the expected fluence to the design fluence are given for W3 sensors as shown in Table 1.4 on Page 11. For IB1 and W1TID sensors the situation is worst. They will be irradiated to the maximum design fluence and their radiation environments are near to the limits set for sensor operation within the CMS tracker. HPK explained the problem of the too high initial resistivity with the resistivity profile and sent a measurement plot, which is shown in Figure 6.16(a), to the CMS collaboration.

The edge regions of the wafers have a significant higher resistivity than the middle region of the wafer. Figure 6.16(b) shows schematically the position of a W1TID sensor and its four half moons and the diodes and MOS structures. Measurements of the full depletion voltages of the diodes, mini sensors, and sensors - taking the geometry factors into account - make the explanation from HPK reliable because the full depletion voltages varies from the inner region to the outer regions of the wafers. The average full depletion voltage value is approximately $60\,V$ for the diodes and $100\,V$ for the sensors. Many of these sensors' full depletion voltages are below the limits given in Table 4.1

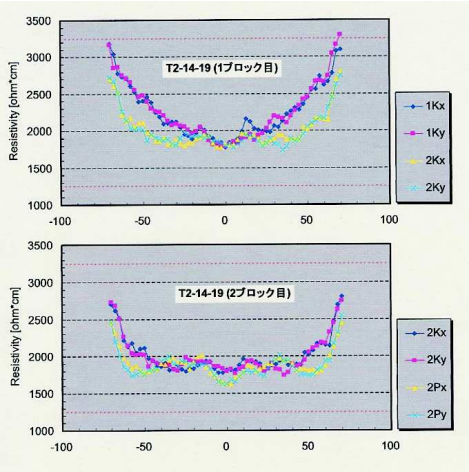

(a) The edges regions from the origin wafers have a significant higher resistivity than in the middle of the wafer.

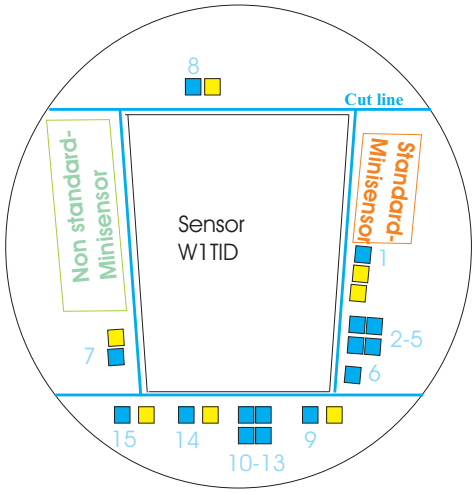

(b) The wafer contains the W1TID sensor and four half moons. The light squares are positions of the MOS structures and the dark ones the positions of the diodes.

Figure 6.16: **Resistivity distribution of HPK wafers with too high resistivity:** *HPK explained with the left plot the question of the origin of the too high resistivity problem. The right plot is a schematic picture of a W1TID wafer with its cut lines.*

on Page 57.

The construction schedule from the CMS tracker community forced the CMS collaboration to check these sensors on their radiation hardness properties in order to guarantee that they will be fully functional during service life of CMS. Therefore, it was decided to irradiate one W1TID, one IB1, one W3 sensor and addition 15 standard half moons from these wafers with the neutron beam in Louvain-la-Neuve. The half moons are irradiated with three different fluences and they were beneficial annealed to get the parameters for the stable damage of the Hamburg model (see Section 3.4). After irradiation, all sensors and half moons are annealed for 80 min at 60°C and following annealing of 24 h at room temperature.

Figure 6.17 shows the full depletion voltages before and after irradiation for the diodes of the 15 standard half moons. The final full depletion voltage is found to be much lower than expected by the Hamburg model and the parameters given in Section 3.4. Table 6.3 shows the parameters fitted to the full depletion voltages of the diodes.

Parameter	literature value	values found for HPK
g_C $\left[10^{-2}\,cm^{-1}\right]$	1.49 ± 0.04	1.218 ± 0.09
r_C	0.65 ± 0.05	0.32 ± 0.11

Table 6.3: **Parameters of the Hamburg model fitted for high resistivity HPK diodes after neutron irradiation:** *The values of the acceptor introduction rate g_C is for the high resistivity diodes after neutron irradiation* 20% *lower than expected. Even* 50% *lower values are fitted for the incomplete donor removal r_C.*

The values found for diodes are also valid for the mini sensors as shown in Figure 6.18. The geometry correction factor of 1.25 is taken into account by dividing the measured full depletion voltage of

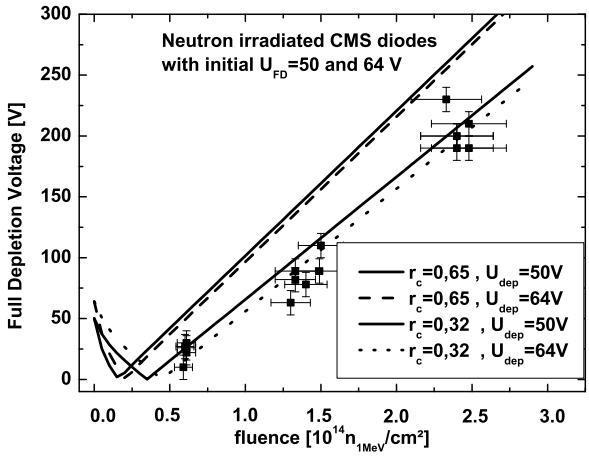

Figure 6.17: **Full depletion voltages of HPK high resistivity diodes before and after neutron irradiation:** *The upper curves present the expectation from the Hamburg model after annealing of* 80 *min at* 60°*C. The two lower curves are the fits to the measured values. The stable damage slope* g_C *is found to be* 20% *lower than expected and even only half of the expected value is found for the incomplete donor removal* r_C *(see Section 3.4)[Fur03].*

the mini sensors by this factor (see Table 2.2 on Page 25).

Finally, the same parametrization found for the diodes and mini sensors seems to be valid for the three sensors shown in Figure 6.19. The measured full depletion voltage is divided by the corresponding correction factors from Table 2.2 on Page 25.

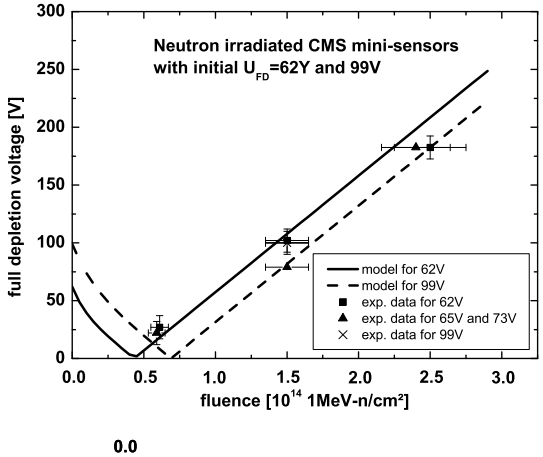

Figure 6.18: **Full depletion voltages of HPK high resistivity mini sensors before and after neutron irradiation:** *The values found on diodes are also valid for the mini sensors. The measured full depletion voltage is divided by the geometry factor of* 1.25 *(see Table 2.2 on Page 25) [Fur03].*

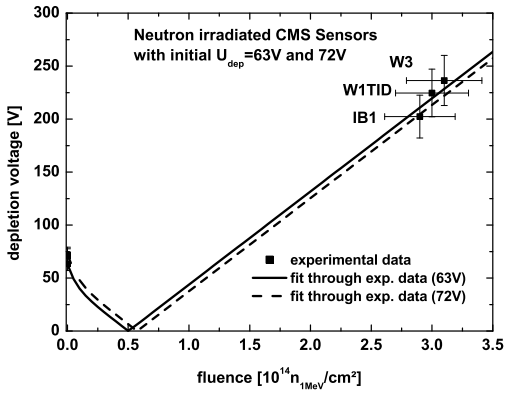

Figure 6.19: **Full depletion voltages of HPK high resistivity sensors before and after neutron irradiation:** *The measured full depletion voltages are divided by the corresponding geometry correction factor from Table 2.2 on Page 25. The stable damage parameters from the diodes in Figure 6.17 are also valid for the sensors.*

Figure 6.20 shows the full depletion voltage of two W1TID sensors of the high resistivity deliveries after proton irradiation. The sensors are annealed for $80\,min$ at $60°C$ and subsequent annealing of $24\,h$ at room temperature. The full depletion voltage is compared with the expectations from Equation 3.16 for literature values and for values given in Table 6.3 observed for these sensors under neutron irradiation. The full depletion voltage minimum is $70\,V$ smaller than expected for literature values and $35\,V$ higher than expected for the values observed for neutron irradiation.

The interesting point of the comparison of the full depletion voltage after neutron irradiation

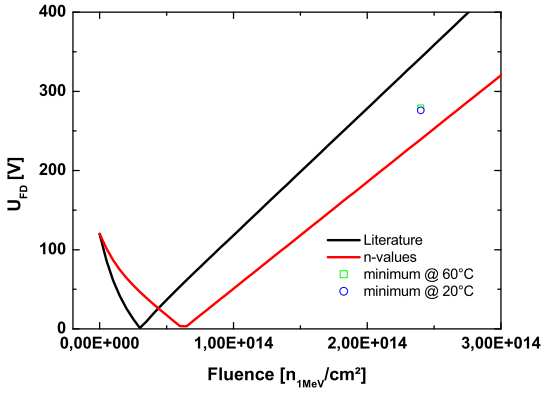

Figure 6.20: **Full depletion voltage of proton irradiated high resistivity sensors in comparison with the Hamburg model:** *The minimum values of full depletion voltage for annealing at* $60°C$ *and* $20°C$ *are between the literature values and values from neutron irradiation in Table 6.3. The full depletion voltage minimum is* $70\,V$ *smaller than expected from the literature and* $35\,V$ *above the values observed from neutron irradiation.*

and after proton irradiation of the high resistivity material is that the high resistivity bulk material is radiation harder for neutron irradiation than for proton irradiation. Up to now only a better situation for charged particle irradiation is found by increasing the oxygen content of the bulk material [Luu04][DW02]. In order to find out the origin of this fact a C-DLTS measurement (see Section 3.1) has been done in Hamburg. A precise description of the setup and the quantitative evaluation can be found in [Sta04]. A diode of the high resistivity material is irradiated with protons to a fluence of $10^{11}\, n_{1MeV}/cm^2$. Unfortunately, the defect concentration is not small compared to the initial doping concentration. Due to this fact, only a qualitative interpretation of the plots in Figure 6.21 is possible.

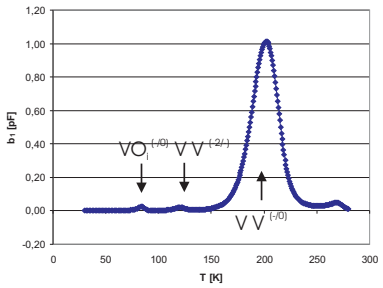

(a) Acceptors before annealing

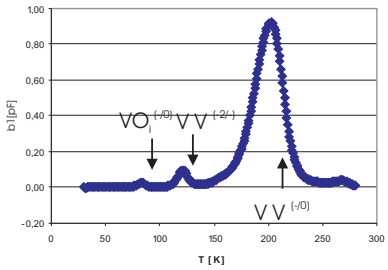

(b) Acceptors after annealing of $81\,min$ at $80°C$

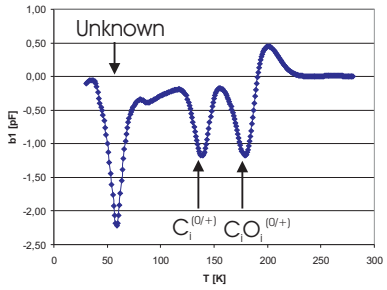

(c) Donors before annealing

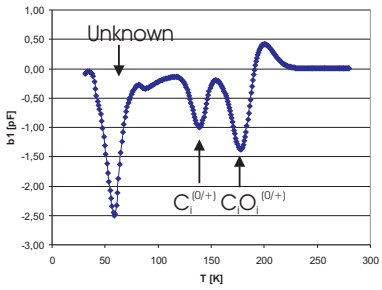

(d) Donors after annealing of $81\,min$ at $80°C$

Figure 6.21: **DLTS spectra of high resistivity HPK material after proton irradiation:** *The identification of the defects is done with a table from [Mol99]. The acceptors $V_2^{(2-/-)}$ and $V_2^{(-/0)}$ are divacancy defects and $VO_I^{(-/0)}$ is a vacancy defect with an interstitial oxygen atom (see Figure 3.1 on Page 37). The interstitial carbon atoms $C_i^{(0/+)}$ and the carbon atoms paired with interstitial oxygen atoms $C_iO_i^{(0/+)}$ behave like donors. The donor like defects responsible for the peak at $58\,K$ are completely unknown and hint to a new kind of radiation damage. This radiation damage do not decrease with annealing time and seem to be the most probable explanation for the lower stable damage parameters observed after irradiation.*

The identification of the defect levels is done according to a table from [Mol99]. The defects $VV^{(2-/-)}$, $VV^{(-/0)}$, and $VO_I^{(-/0)}$ (see Figure 3.1 on Page 37 and Table 3.3 on Page 40) behave like acceptors and their existence is reliable if one takes into account that oxygen is also present in pure silicon. The defects $C_i^{(0/+)}$ and $C_iO_i^{(0/+)}$ behave like donors and their existence is reliable because

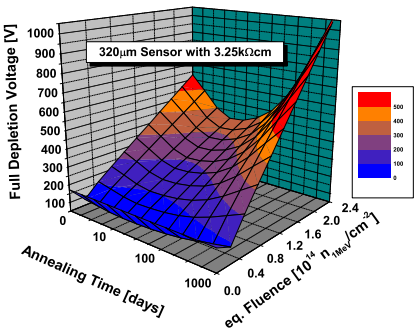

(a) Full depletion voltage of IB1 sensors with literature values [Mol99]

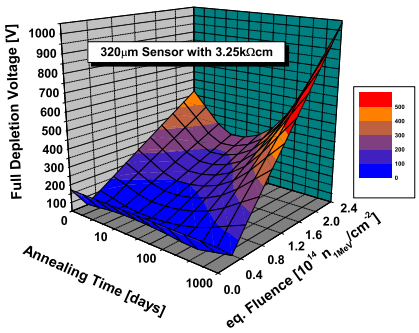

(b) Full depletion voltage of IB1 sensors calculated for measured values from Table 6.3

Figure 6.22: **Full depletion voltage of IB1 sensors calculated for literature values and currently measured values of high resistivity sensors:** *The parameters from literature lead to higher full depletion voltages with irradiation and annealing (left hand side) than the current parameters (see Table 6.3) observed for high resistivity sensors supplied by HPK which are used for plot on the right hand side.*

also carbide impurities are present in pure silicon. The peak level at $58\,K$ is completely unknown. It is for sure that it is not built of carbide or oxygen containing defects what can be concluded from the results of the defect investigations of two collaborations at CERN (RD48/RD50). This donor peak is a stable damage component as it shows no annealing behavior. It is the most probable explanation for the parameters found in Table 6.3.

Figure 6.22 compares the full depletion voltage of sensors with parameters from Table 6.3 and literature values versus fluence and annealing time at $20^{\circ}C$. The time constant for the reverse annealing is taken from Figure 6.13.

From this and the scenario calculations in Section 6.6 and Appendix C, it was concluded that it is possible to operate detector modules containing these sensors during the whole service life of CMS. In addition, the radiation environment of the IB1 sensors in the second layer is less critical than for the first layer (see Table 1.4 on Page 11).

6.5.5 Summary of Full Depletion Voltage Measurements

For most of the mini sensors and sensors supplied by STM and HPK, the development of full depletion voltage follows the predictions of the Hamburg model. The development of the full depletion voltage with irradiation and annealing time shows in all cases a type inversion of the structures bulk, and in all cases a beneficial annealing and a reverse annealing is observed. The end of beneficial annealing is observed in all cases at $80\,min$ at $60^{\circ}C$ or $14\,d$ at $20^{\circ}C$. The total capacitance of the sensors shows in all cases a decrease with irradiation and an increase with annealing time both independent on the full depletion voltage changes with irradiation or annealing. A reverse annealing is not observed in case of the total capacitance. For these reasons, it can be concluded that the radiation damage responsible for the changes of full depletion voltage and total capacitance of a fully depleted structure are not of the same kind.

Cases for which the Hamburg model does not predict correctly the development of full depletion

voltage are rare and can be explained by a new kind of radiation damage - found by a C-DLTS measurement - which is stable in time. The level of the unknown defects is found at $58\,K$ and cannot be correlated to oxygen or carbon containing defects. This unknown damage behaves like donors and compensates partially (approximately 20%) the introduction rate of acceptor levels (g_C) with irradiation. The two sensors from STM which full depletion voltage changes in an unpredictable way are an exception of the standard observations. The reason for this has not been found.

6.6 Full Depletion Voltage Scenarios for CMS Sensors at LHC

In this section, the development of the full depletion voltage of each sensor design is calculated for each fluence value in Table 1.4 on Page 11 using the literature values for the changes of full depletion voltage with fluence and the annealing parameters from Section 3.4. In addition, scenarios are calculated for IB1, W1TID, and W3 sensors which are partially built of the high resistivity material discussed in Section 6.5.4. For these sensors own irradiation parameters have been found for neutron irradiation which are shown in Table 6.3. Since the statistic for changes of full depletion voltage with proton irradiation of this material is low, the worst case, i.e. literature values for the Hamburg model, are used for the calculation of the changes with charged hadron fluence.

Table 6.4 shows the assumptions for irradiation times, break times, shutdown times, intervention times and for the corresponding temperature of the sensors with which the full depletion voltage scenarios in Figure 6.26 and in Appendix C are calculated. The source code of the program can be found in Appendix D on Page 155.

	time $[d]$	temperature $[^\circ C]$
Irradiation	60	-20
Break	14	-20
Irradiation	60	-20
Break	14	-20
Irradiation	60	-20
Shut down	129	-20
Service and repair	28	$+10$

Table 6.4: **Assumptions for the trackers' operation times and operation temperatures during one year:** *The annealing during the service and repair period has to chosen in order to keep the full depletion voltage as low as possible. The time of* $28\,d$ *and the temperature of* $+10^\circ C$ *for annealing is motivated in the following.*

The scenario for the development of the full depletion voltage during operation with time is schematically explained in Figure 6.23. Until the service and repair intervals at higher temperature, in which the tracker anneals, the temperature is kept as low as possible to avoid reverse annealing. During the irradiation runs acceptors are created which decrease (increase) the full depletion voltage before (after) type inversion (see Equation 2.25 on Page 24). With beneficial annealing the acceptors decay and the full depletion voltage increases (decreases) before (after) type inversion. The reverse annealing delivers a contribution in the other direction than the beneficial annealing.

The design luminosity of $L = 500\,fb^{-1}$ is expected to be reached approximately after eight years of operation and one of the three irradiation runs of $60\,d$ [CTDRA00]. Due to the high uncertainties in the simulated fluences it is expected to run the CMS tracker for ten years. Thus, all scenarios are calculated for ten years whereas the design fluence is reached after eight years and $60\,d$.

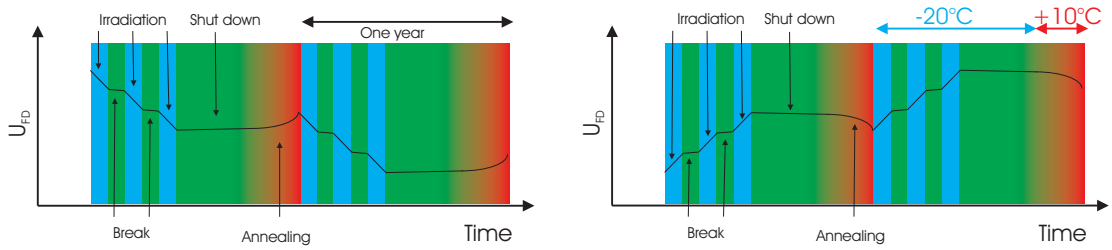

(a) Before type inversion

(b) After type inversion

Figure 6.23: **Schematics of a CMS full depletion voltage scenario:** *Three irradiation runs of approximately* $60\,d$ *with breaks of* $14\,d$ *in between are performed per year. Until the service and repair intervals at higher temperature, where the tracker anneals, the temperature is kept as low as possible in order to avoid reverse annealing. During the irradiation runs acceptors are created which decrease (increase) the full depletion voltage before (after) type inversion (see Equation 2.25 on Page 24). With beneficial annealing a part of the acceptors decay and the full depletion voltage increases (decreases) before (after) type inversion. The reverse annealing delivers a contribution in the other direction than the beneficial annealing.*

Figure 6.24 shows the full depletion voltage scenario for IB1 sensors of the most inner barrel layer for $28\,d$ at different annealing temperatures per year. The initial resistivity is $1.5\,k\Omega cm$. The small extractions of the annealing contributions during the service and repair periods before and after type inversion show that the beneficial annealing requires at least an annealing temperature of $+10°C$ in order to reach the maximum beneficial annealing effect. The extraction of the annealing period after type inversion shows in addition that the reverse annealing gives non negligible contributions above $+10°C$ which accumulate significantly. This leads to the large spread of the shown curves.

The annealing time of $28\,d$ at an annealing temperature of $+10°C$ in Table 6.4 is a proposal which is taken from numerous full depletion voltage scenario calculation results as of the kind shown in Figure 6.24. These results for different annealing temperatures and annealing times of IB1 sensors' final full depletion voltage of the most inner tracker layer are summarized in Figure 6.25. The initial resistivity is $\rho = 3\,k\Omega cm$ and the fluences are taken from Table 1.4 on Page 11.

Figure 6.26 shows the calculated full depletion voltage scenarios for IB1 sensors of the most inner layer of the CMS tracker for the annealing assumptions of Table 6.4 on Page 106 and for the full expected initial resistivity spectrum.

The differences in radiation hardness observed on the high resistivity material in Section 6.5.4 would result in approximately $32\,V$ lower full depletion voltage after the service life of ten years than expected for the standard material. With this result, which is the worst case expectation, these sensors can be used within the CMS tracker.

Appendix C summarizes the worst case scenarios of all sensor geometries. Table C.1 includes the maximum full depletion voltages of all sensor geometries after ten years of operation and after the physical goal of a luminosity of $L = 500\,fb^{-1}$.

New simulations of the radiation environment in the CMS tracker yield higher fluences than previously expected for ring 5 detector modules of disc 7 to disc 9 (see Table 1.4 on Page 11). In this case, the final full depletion voltage is approximately $676\,V$ for ring 5 detector modules on disc 9 as shown in Figure C.7 on Page 152. With a sensors thickness of $400\,\mu m$ the final full depletion voltage would be approximately $433\,V$ as shown in Figure C.8 on Page 153. In order to have a sufficient safety margin in the signal-to-noise-ratio, it is not recommended to get lower in sensor thickness. Unfortu-

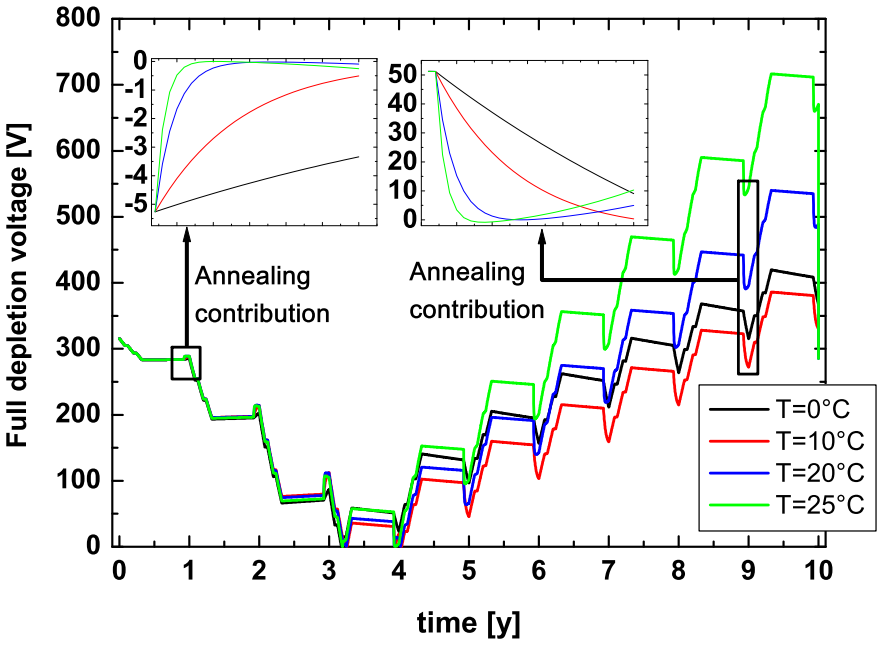

Figure 6.24: **Full depletion voltage scenario for IB1 sensors at different annealing temperatures:** *The scenario of the full depletion voltage strongly depends on the annealing procedure which is* $28\,d$ *for the shown scenarios. The small extractions of the annealing contributions during the service and repair periods before and after type inversion show that the beneficial annealing requires at least an annealing temperature of* $+10°C$ *in order to reach the maximum beneficial annealing effect. The extraction of the annealing period after type inversion shows in addition that the reverse annealing gives non negligible contributions above* $+10°C$ *which accumulate significantly. This leads to the large spread of the shown curves.*

nately, the results from the new radiation environment simulations come too late and a further order of sensors with other bulk thickness was not possible anymore.

6.7 Results of Leakage Current Measurements

6.7.1 Total Leakage Current after Service Life at LHC

The temperature of the sensors depends on their position in the tracker and their heat flow. The tracker is designed to operate sensors at a maximum temperature of $-10°C$. For this reason, the current related damage rate α has to be scaled down to this temperature and is at this temperature after annealing of $80\,min$ at $60°C$ approximately $\alpha(-10°C) \approx 1.86 \cdot 10^{-18}\,A/cm$. The fluence dependence of the total leakage current density has been investigated on sensors, mini sensors, and diodes. Figure 6.27 shows the results measured on 14 mini sensors. The fluctuations can be explained by the large ratio of edge to active volume of the sensor because the guard ring is left floating and by the fluctuations of temperature during the measurements. Studies of current measurements on sensors implemented in

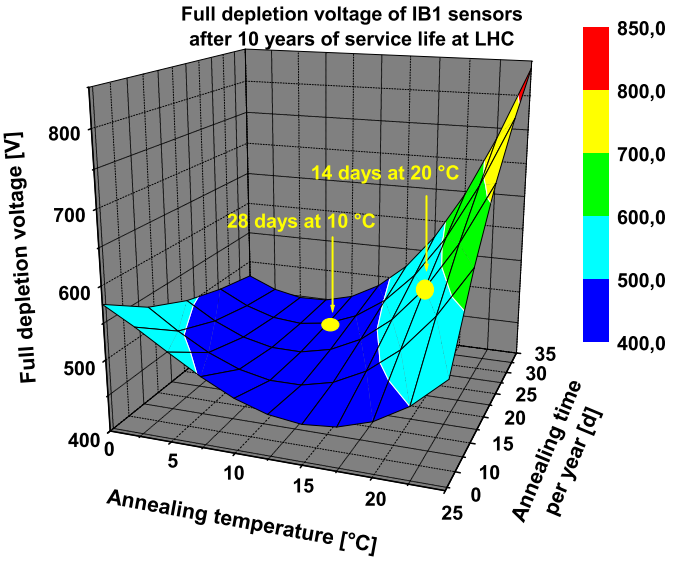

(a) Full depletion voltage versus annealing time and temperature

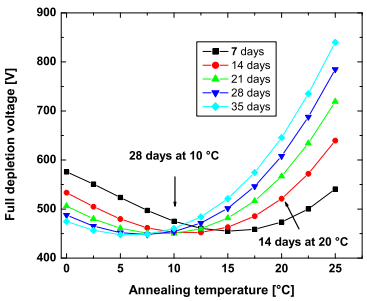

(b) Full depletion voltage versus annealing temperature

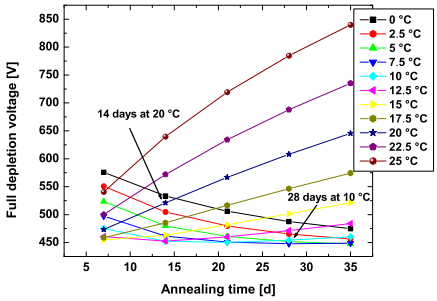

(c) Full depletion voltage versus annealing time per year

Figure 6.25: **Full depletion voltage of IB1 sensors after service life at LHC versus annealing time and annealing temperature:** *The scenarios are calculated for IB1 sensors of the most inner tracker layer and with the break times, irradiation times and remaining shut down times from Table 6.4. The initial resistivity is* $\rho = 3\,k\Omega cm$ *and the fluences are taken from Table 1.4 on Page 11. Since the annealing behavior does not depend on initial resistivity, the minimum of full depletion voltage is for all sensor geometries and fluences at an annealing time of* $28\,d$ *and at an annealing temperature of* $+10°C$.

detector modules can be found in [Wei04]. Due to the lower edge to active volume ratio of the sensor in comparison to the mini sensors, the sensors currents follow well the expectations. In all cases Equation 3.12 on Page 41 seems to be valid for the CMS sensors and the scaling of proton fluence to equivalent fluence via the NIEL-hypothesis (see Section 3.1) works correctly.

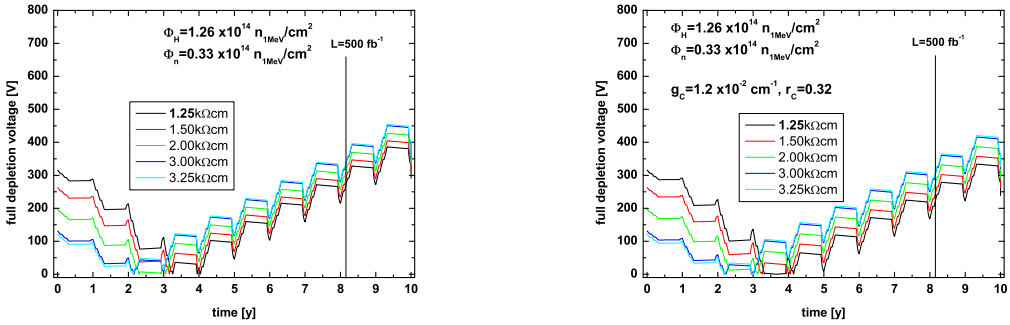

(a) Literature values

(b) Values from Table 6.3

Figure 6.26: **Full depletion voltage scenarios for IB1 sensors:** *The final full depletion voltage after ten years is approximately* $32V$ *higher for the standard material (left hand side) than for the high resistivity material (right hand side) because the stable damage slope* g_C *and the incomplete donor removal* r_C *of the high resistivity material are much lower than the literature values.*

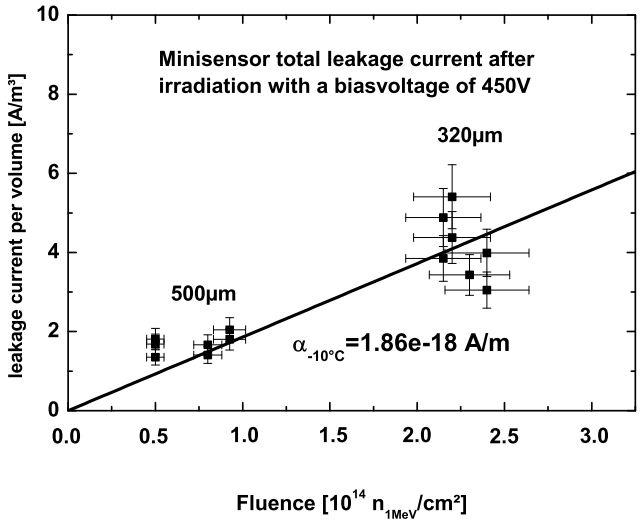

Figure 6.27: **Increase of leakage current of CMS mini sensors after proton irradiation:** *The figure shows the total leakage current density of 14 mini sensors at* $450V$ *after proton irradiation and annealing of 80 minutes at* $60°C$ *versus fluence. The value of the current related damage rate at* $-10°C$ *is* $\alpha = 1.8610^{-18} A/cm$ *[Fur03].*

6.7.2 Annealing of Total Leakage Current

Up to now, never a reverse annealing behavior, i.e. an increase of leakage current with annealing time, has been observed for the total leakage current. This results from the different annealing behavior of the damage in the band gap of the irradiated silicon. Since the radiation damage with energy levels around the middle of the band gap increases the thermally generated current, the damage which energy levels are located at the edges of the band gap contributes to the changes of the effective doping

concentration which results in changes of the full depletion voltage.

Figure 6.28 shows the total leakage current of two W1TID sensors versus bias voltage at different annealing times and for two different annealing temperatures. The total leakage current does not saturate for even high annealing times but is still decreasing.

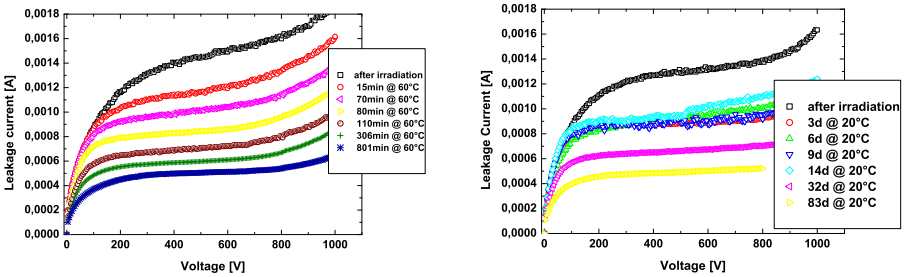

(a) Annealing at $60°C$ (b) Annealing at $20°C$

Figure 6.28: **Annealing of total leakage current of HPK sensors:** *The total leakage current - here measured at $-10°C$ and $600V$ bias voltage - decreases with annealing time and does not saturate at even high annealing times at which the reverse annealing of the full depletion voltage is far proceeded (see Figure 6.13).*

Figure 6.29 shows the annealing of the total leakage current density of the two sensors versus annealing time at a measurement temperature of $T_{measure} = -10°C$ and an applied bias voltage of $600V$. The fluctuations of the measurement temperature of $T_{measure} = -10 \pm 1.5°C$ causes due to the

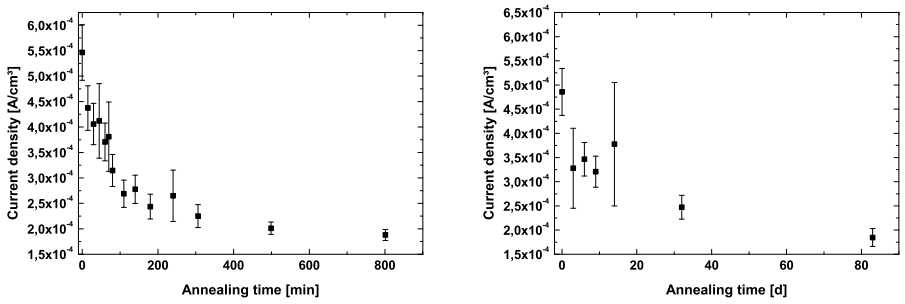

(a) Annealing at $60°C$ (b) Annealing at $20°C$

Figure 6.29: **Annealing of total leakage current density:** *The total leakage current density measured at $-10°C$ and $600V$ decreases with annealing time. Small fluctuations in temperature cause larger changes of the current density than the annealing. For this reason, the error bars are larger for annealing steps with temperature fluctuations during the measurements.*

exponential dependence of the current on temperature (see Equation 2.34 on Page 26) higher effects in the current density than the annealing itself. For this reason some error bars in Figure 6.29(a) and 6.29(b) are larger than the other ones due to the larger temperature fluctuations observed during the measurement.

The current annealing also takes place at low temperatures, contrary to the full depletion voltage annealing which can be assumed to be completely frozen below $-10°C$. For this reason, the total

leakage current of a single sensor is expected to be below $600\,\mu A$ for the whole service life at LHC (see the recommendations to the annealing scenarios and the planned beam time intervals in Section 6.6).

6.7.3 Characterization of Single Strip Leakage Currents

As like the total leakage current, the single strip leakage currents also anneal with time as shown in Figure 6.30.

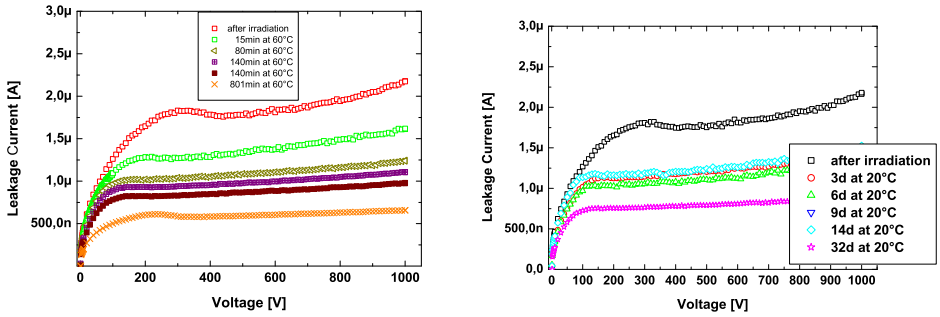

(a) Annealing at $60°C$ (b) Annealing at $20°C$

Figure 6.30: **Annealing of single strip leakage current after proton irradiation:** *As like the total leakage current, the single strip leakage current of the two HPK sensors from the previous section anneals with time and temperature. Small fluctuations in $T_{measure}$ of around $1.5°C$ have larger influences to the observed leakage current than the current annealing.*

The annealing of the leakage current density of the sensors is also measured on strip level as shown in Figure 6.31. The current density of the strips is calculated by:

$$i_{strip} = \frac{I_{leakage,strip} N_{strip}}{V_{sensor}} \tag{6.12}$$

with the single strip leakage current $I_{leakage,strip}$, the sensor volume $V_{sensor} = 2.73\,cm^3$, and the number of strips $N_{strip} = 768$. The ratio of the total leakage current - which is the sum of all single strip leakage currents and partially edge currents - to the single strip leakage current is the same at all annealing steps. For this reason, a significant change in the guard rings field configuration and therefore also in its efficiency with annealing can be excluded. Taking leakage current annealing effects at low temperatures with respect to the total leakage current into account, the single strip leakage current is expected to be below $1\,\mu A$ during the whole service life at LHC.

6.7.4 Evaluation of Final STM Pre-series Sensors

The final STM pre-series to be evaluated still have leakage currents which are variable under mechanical stress (see Section 5.7). Figure 6.32 shows the total leakage current versus bias voltage of seven irradiated sensors (see Table 6.2 on Page 99) before and after proton irradiation. The sensors were annealed using the standard procedure and were subjected to identical mechanical stress conditions before and after irradiation.

The current linearly increases with fluence after irradiation and the subsequent standard annealing procedure as expected from Equation 3.11 on Page 41. The kink in the IV characteristics ob-

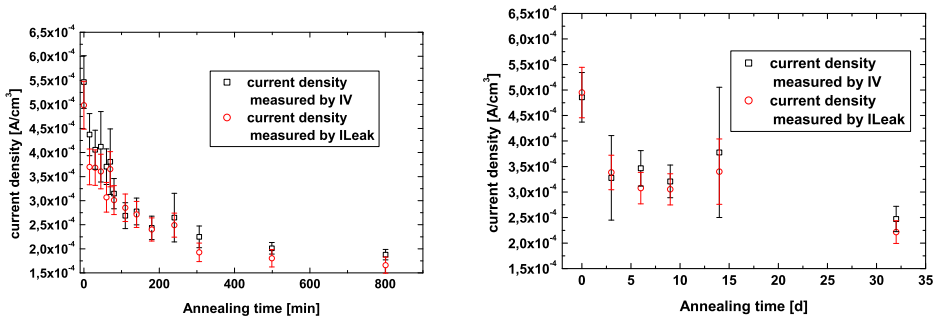

(a) Annealing at 60°C (b) Annealing at 20°C

Figure 6.31: **Annealing of single strip leakage current density after proton irradiation:** *The single strip leakage current density measured at* $-10°C$ *and* $600V$ *decreases with annealing time. Small fluctuations in temperature cause larger changes of the current density than the annealing. For this reason, the error bars are larger for annealing steps with temperature fluctuations during the measurements. Finally, there are no differences observed in the annealing of the total and the single strip leakage currents.*

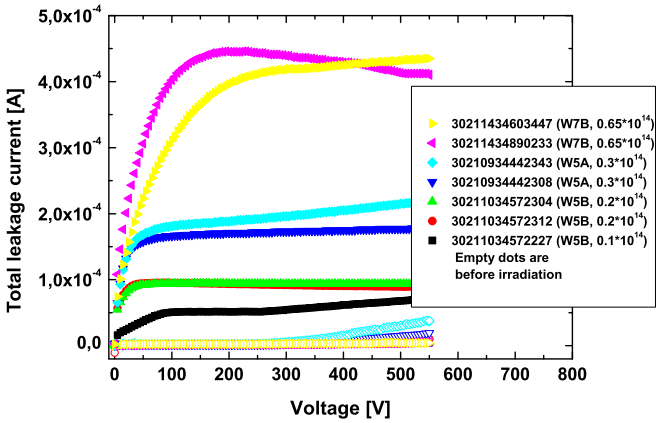

Figure 6.32: **Total leakage currents from final STM pre-series sensors before and after proton irradiation:** *The current increases linearly with fluence after proton irradiation and the subsequent standard annealing procedure (filled dots) (see Table 6.2 on Page 99) as expected (see Equation 3.11 on Page 41). The kink in the IV characteristics observed prior to irradiation is still present after irradiation on the two sensors 30211034572227 and 30210934442343 whereas the other sensors seem to have no kink in their IV characteristics anymore. Figure 6.33 shows that these kinks still come from too high single strip leakage currents.*

served prior to irradiation is still present after irradiation on the two sensors 30211034572227 and 30210934442343 whereas the other sensors seem to have no kink in their IV characteristics anymore.

The question wether the kink is too small after irradiation or wether it has actually disappeared on some sensors can be answered by the measurement results for the single strip leakage currents in

Figure 6.33.

Some single strip leakage currents are still higher than the average values of the other strips after irradiation and the subsequent standard annealing procedure. This leads to the conclusion that the mechanical stress problem does not really improve with irradiation, i.e. only the proportion of the higher single strip leakage current with respect to the total leakage currents becomes smaller and the kink is too small to be visible in the IV characteristics after irradiation. Significant is the observation that the high single strip leakage currents can appear and/or disappear with irradiation.

These measurements performed after a specified fluence and a specified annealing procedure give no conclusive results about the behavior of the single strip leakage currents during the whole service life of CMS. It cannot be guaranteed that these sensors' single strip leakage currents are most times within the range of the limits given in Table 4.1 on Page 57. In addition, it has to be taken into account that the stress conditions are within the CMS tracker are completely unknown.

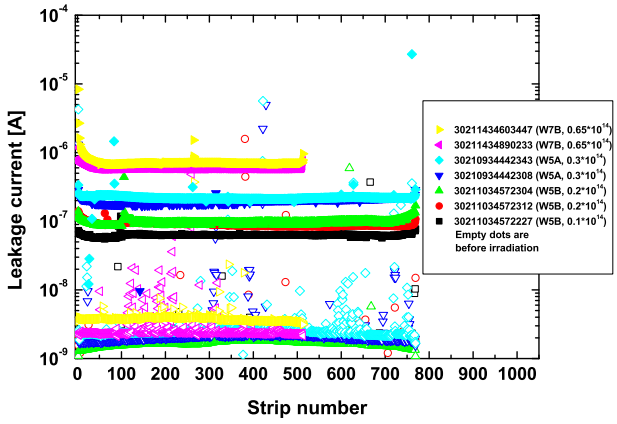

Figure 6.33: **Single strip leakage currents of final STM pre-series sensors before and after proton irradiation:** *The applied bias voltage is* $400\,V$. *Some single strip leakage currents are still higher than the average values of the other strips after irradiation and the subsequent standard annealing procedure (filled dots). The average single strip leakage current increases linearly with fluence as expected (see Equation 3.11 on Page 41). Significant is the observation that the high single strip leakage currents can appear and/or disappear with irradiation. These "hot strips" endanger the functionality of the detector module because "fake hits" can be observed.*

6.7.5 Leakage Current Measurements on STM Sensors during Irradiation

The reason why STM sensors are sensitive against mechanical stress, exclusively presented before irradiation in Section 5.7, cannot be found and explained in QTC. The effect is still present after irradiation and the subsequent standard annealing procedure as shown in the previous section. The changes in the single strip leakage currents during IQC are unpredictable and it cannot be excluded that some single strip leakage currents exceed the specified limits and decrease afterwards during service life at LHC. In order to guarantee the functionality of these sensors during their whole service life at LHC and to find such "hot strips", a special irradiation test is performed. Two sensors are irradiated and their total leakage current and a number of single strip leakage current values are measured during irradiation. Strips whose leakage currents exceed the specified limit of $100\,nA$ before irradiation

(with mechanical stress applied) are expected to become suspect during irradiation and no mechanical stress applied. In particular, a break through in the current voltage characteristic is expected for the overdepletion maximum $U_{applied} - U_{FD}$ at the sensor's bulk type inversion. A new setup, described in Section 5.4, has been developed for this measurement. The neutron beam setup in Louvain-la-Neuve is used for the two irradiation tests below. The neutrons do not cause any ionization in the sensors' bulk. Nevertheless, the total leakage current measured during irradiation is caused by the effects explained in Section 2.3.1, 2.3.4 and the irradiation damage in Chapter 3. The impurities of the neutron beam (see Table 6.1 on Page 95) cause a constant offset in the measured leakage current by ionization which is expected to disappear immediately after switching off the neutron beam. The functionality of the sensors is not expected to suffer from these ionization effects during the measurements discussed below. In order to avoid self annealing and local overheating and to simulate operating conditions similar to the environment in the CMS tracker, the sensors are kept at $-10°C$ during irradiation.

An STM sensor containing three leaky strips (above $100\,nA$) and 20 strips with single strip leakage currents above the average value, but still within the limits, is used for the first irradiation test. From a total of 512 strips, three leaky strips (strip numbers 158, 367, 479), three with a higher current level still within specifications (strip numbers 11, 192, 225), and three strips without any suspect behavior under mechanical stress (strip numbers 275, 350, 500) were monitored during irradiation.

Figure 6.34 shows the total and single strip leakage currents of this sensor during irradiation.

Once the beam has been adjusted (not shown in this figure), all single strip leakage currents are

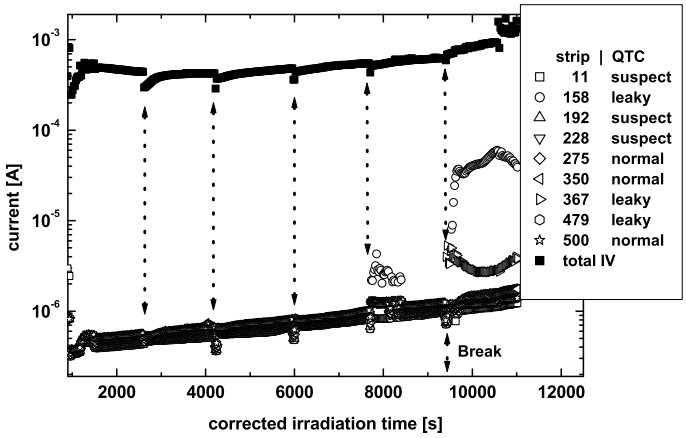

Figure 6.34: **Total and single strip leakage currents of an STM sensor during the first neutron irradiation test:** *The "corrected time" is the duration of the irradiation without the break times. The upper curve presents the total leakage current at* $450\,V$ *bias voltage. The lower curves are nine single strip leakage currents. Strips 275, 350 and 500 had a normal current level in QTC, whilst strips 11, 192 and 225 had current levels above the average current values but not out of specification, and strips 158, 367 and 479 were above the acceptable limit of* $100\,nA$*. The vertical dotted lines show the times of measurement interruptions during which the beam had been switched off. After the interruptions (which are not shown here), a large leakage current increase beyond the expected range of type inversion (*$5000 - 7500\,s$*) is observed on two strips (strips 158 and 367) - leaky before irradiation - under and without mechanical stress applied.*

on the same leakage current level. This leakage current level is mainly caused by ionization due to beam impurities (see Table 6.1 on Page 95) and radiation damage, which increases the thermal current generation (see Chapter 3). The expected range of type inversion - at which the overdepletion has its maximum - is somewhere between $5,000 - 7,500\,s$, which corresponds to a fluence of approximately $0.22 \cdot 10^{14}\, n_{1MeV}/cm^2$ up to $0.33 \cdot 10^{14}\, n_{1MeV}/cm^2$. The high range of the expected point of type inversion is caused by the uncertainty of very short-lived damage not considered in the parametrization of the current related damage rate α which is described in Chapter 3.

In two out of the three leaky strips, leakage currents increase significantly after the two interruptions following type inversion. Figure 6.35 presents the IV characteristics and single strip leakage current ramps measured during the interruptions of the irradiation.

Prior to irradiation (Figure 6.35(a)), slightly above full depletion voltage, the total leakage current rises sharply (without mechanical stress applied). During an interruption before type inversion (Figure 6.35(b)), the kink cannot be observed due to the high total leakage current. In the first interruption after type inversion (Figure 6.35(c)), at a bias voltage of $430\,V$, one of the three leaky strips jumps to a

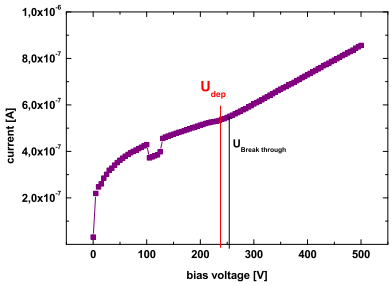

(a) Total leakage current before irradiation

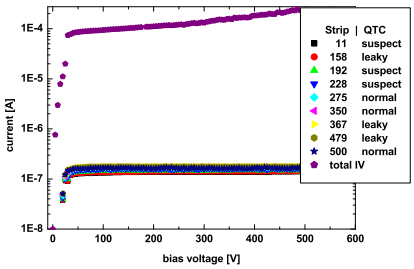

(b) IV and single strip leakage currents before type inversion

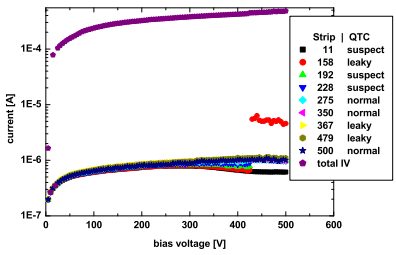

(c) IV and single strip leakage currents at first interruption after type inversion

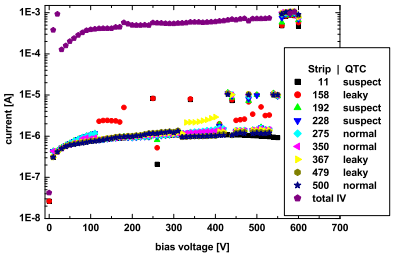

(d) IV and single strip leakage currents at second interruption after type inversion

Figure 6.35: **Total and single strip leakage currents of a STM sensor during interruptions at the first neutron irradiation:** *The upper curves in the diagrams present the total leakage currents measured at $-10°C$, and the lower ones show the single strip leakage currents at the same temperature. The IV curve prior to irradiation 6.35(a) shows the standard kink shortly above full depletion voltage. During the second interruption 6.35(b) the kink is hidden due to the high total leakage current. Immediately after type inversion 6.35(c), once a bias voltage of $430\,V$ has been reached, one of the leaky strips jumps to a higher level and during the final qualification after type inversion 6.35(d) all strips jump between different leakage current levels and the sensor does not work reliably anymore.*

much higher leakage current level. This effect is reproducible. After the second interruption, the same effect is also observed on a second leaky strip. Finally (Figure 6.35(d)), the sensor does not work anymore because the single strip leakage currents jump between different leakage current levels.

The conclusion of this irradiation test is that strips which shown higher currents under mechanical stress, endangers the sensors' functionality after type inversion and it is expected that the higher leakage currents can increase the noise on detector module level (see Section 2.10 on Page 32). After this test and its worrying results, a second irradiation test with another sensor was done. Whilst for the first irradiation only the multiplexer in the setup was available, for the second irradiation also a switching matrix is used and therefore a higher statistic of 26 single strip leakage currents is available.

Figure 6.36 shows the total leakage current of the second sensor during neutron irradiation.

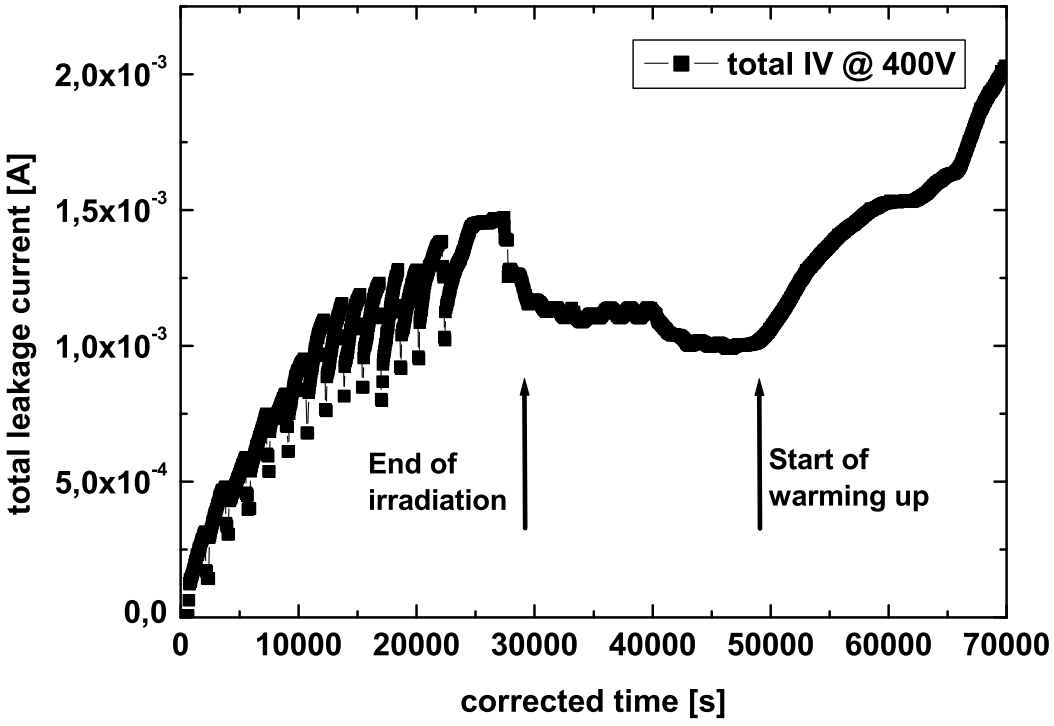

Figure 6.36: **Total leakage current of a STM sensor during second neutron irradiation and following long term test:** *The "corrected time" is the time of irradiation without the times during the breaks. The temperature is* $-10°C$*. The total leakage current is increasing with fluence. The down going peaks represent the interruptions done for current ramp measurements. After the end of irradiation, many very short-lived damage decay and the current increase after* $50,000s$ *corresponds to an increase in temperature [Fur04b].*

Figure 6.37 shows in detail the first part of Figure 6.36. During irradiation the current increases with fluence. At each interruption when the beam is switched off the current decreases significantly. This is obviously the offset by ionization caused by the charged beam impurities and the photons. After the interruptions of approximately $20 min$ each, the current starts from an even lower level. This comes from decays (annealing) of very short-lived damage in the sensor's bulk or surface which is not

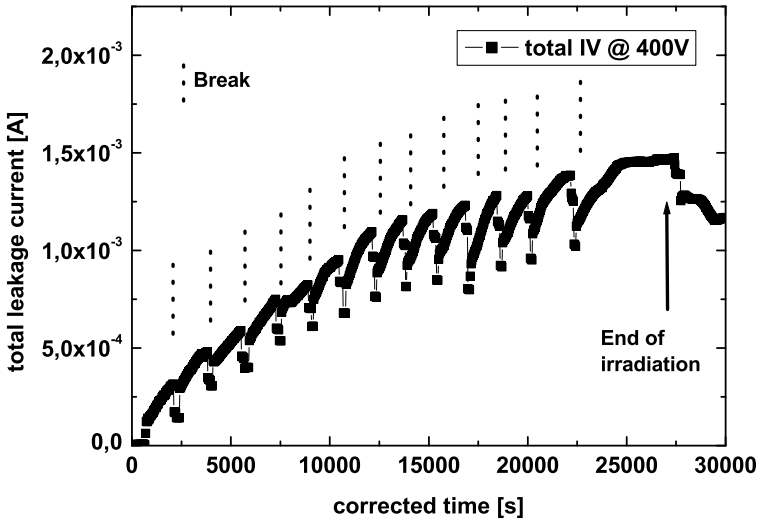

Figure 6.37: **Total leakage current of a STM sensor during second neutron irradiation:** *The plot shows in detail the first part of Figure 6.36. After switching off the beam, a sharp decrease in current is observed. The decrease is assumed to be the ionization offset caused by the charged beam impurities and the photons. After the interruptions, the current starts from a significant lower level. This corresponds to decays of very short-lived damage which decay (annealing) is not suppressed at* $-10°C$.

suppressed by the low temperature. This damage can cause either an increase of bulk current or an increase of surface current.

The total leakage current after end of irradiation is shown in Figure 6.38.

The missing part in this figure of approximately $1200\,s$ is used for current ramp measurements on the sensor. The curve is fitted with an exponential decay and the current during the short time scale decay $I_{short}(t)$ is found to be:

$$I_{short}(t) = (2.578 \pm 0.385) \exp\left(-\frac{t}{3084 \pm 47 s}\right) mA + (1.07 \pm 0.01)\, mA \tag{6.13}$$

An increase of the trapping probability is expected for the electrons and holes (see Section 2.3.4 on Page 22) with fluence. Thus, the current produced by ionization is expected to decrease with fluence. Figure 6.39 shows the current produced by ionization versus fluence.

A linear fit for the ionization current per sensor's volume J_{offset} is given by:

$$J_{offset}(\phi_{eq}) = (-2.55 \pm 0.21) \cdot 10^{-13} \phi_{eq} \frac{\mu A}{n_{1MeV}\, cm} + (42.19 \pm 2.34) \frac{\mu A}{n_{1MeV}\, cm} \tag{6.14}$$

Up to this point, the principle behavior of the total leakage current of the sensor is well understood. Kinks in the IV curves cannot be observed any more because the fraction of a single strip leakage current does hardly influence the high total leakage current. Figure 6.40 presents the single strip leakage currents of three strips from the sensor used for the second neutron irradiation.

The general behavior of the strips is the same as for the total leakage current of the sensor. But interesting is the fact that the leakage current of two strips leaky in QTC jump between a higher leakage

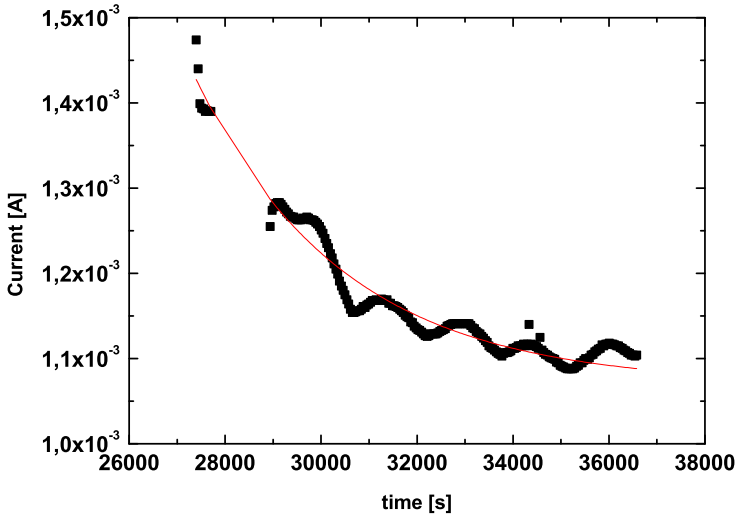

Figure 6.38: **Decay of very short-lived damage after neutron irradiation:** *After switching off the beam current, some damage in the sensor's bulk decay and the total leakage current decreases. The time constant of the decay is fitted to* $\tau = 3084 \pm 47\,s$.

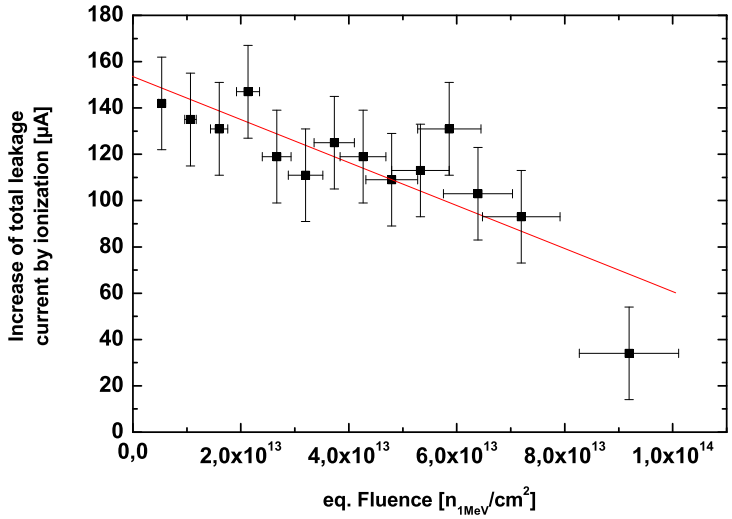

Figure 6.39: **Ionization current versus fluence:** *The current produced by ionization decreases with fluence due to the higher trapping probability. The slope is fitted to* $(-9.29 \pm 1.78) \cdot 10^{-13}\,\mu A cm^2/n_{1MeV}$.

current level and the average leakage current level from the other strips (not shown in Figure 6.40). These jumps are expected to be reflected in detector modules noise. They appear after type inversion assumed to be reached at approximately $6000 \pm (1000)\,s$ of irradiation and disappear after end of ir-

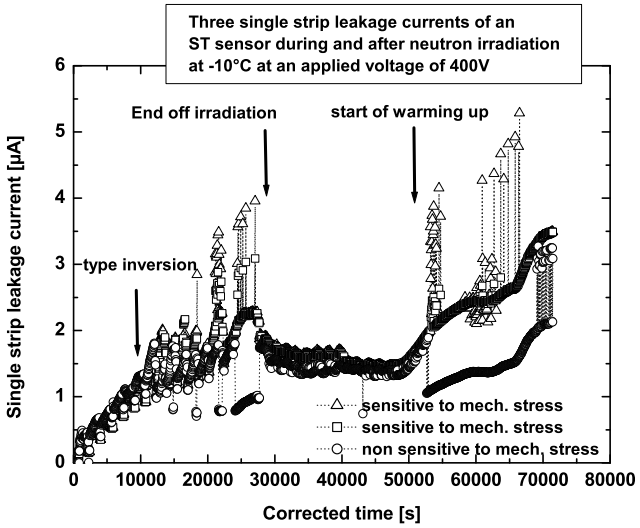

Figure 6.40: **Single strip leakage currents of a STM sensor during second neutron irradiation and following long term test:** *The principal behavior of the 26 monitored strip currents (only three are shown in this figure) follows the behavior of the total leakage current in Figure 6.36. The leakage currents of the two leaky strips start to jump up and down beyond type inversion which is assumed to be at* $5000 - 7000\,s$*. One strip current with average current level before irradiation starts to jump between a lower level and the average level of the other strips [Fur04b].*

radiation but they appear again during the warming up phase. Another strip with average current level before irradiation and no dependence on mechanical stress starts at the same time to jump between the average current level and a lower one.

The jumping of the leakage currents of the three strips is not understood. A possible explanation would be an additional generation of electrons or holes, e.g. caused by micro discharges which can be connected with the stress dependence. The decrease of a leakage current level implies that the leakage current flows to other strips or directly to the bias ring and not through the DC pad and the bias resistor to the bias ring. These surface currents should flow below the dielectric layer and can be caused by a localized high charge impurity concentration of the dielectric layer. Together with the high increase of interstrip capacitance shown in Section 6.10.3, which also implies this fact, this is the most probable explanation for the leakage current changes. These ”hot strips” endanger the functionality of a detector module because ”fake hits” will be observed.

6.7.6 Summary of Leakage Current Measurements

The behaviour of the total leakage current is for all cases shown above correlated to the behaviour of the single strip leakage currents because the total leakage current is the sum of all single strip leakage currents and currents from edge effects. No deviation with respect to expectations from literature has been found for all leakage currents of HPK structures (diodes, mini sensors and sensors). The stress dependence problem of the STM sensors does neither improve nor worsen after standard IQC procedure (see Section 6.4). Without mechanical stress applied, the parameters of the sensors are most times within specifications of Table 4.1 on Page 57.

On the other side, the measurement of the STM sensors' total and single strip leakage currents during neutron irradiation causes doubts concerning the radiation hardness of these sensors. The impurities of the neutron beam in Louvain-la-Neuve of charged hadrons and photons cause an increase in the leakage currents by generation of electron-hole pairs. The size of this ionization current is found to decrease with fluence due to the increasing trapping probability. The parametrization given in Equation 6.14 is only valid for the deuteron beam current of $11\,\mu A$ (see Section 6.3). The decay of very short-lived damage and charge ups has been measured after switching off the neutron beam and its time constant is $\tau = 3084 \pm 47\,s$ which is only valid for the beam setup in Louvain-la-Neuve. Other defects are expected to be created for other radiation types like protons or pions and therefore other time constants are possible. The principal behaviour of the sensors' leakage currents is well understood except of the jumping leakage current levels of the strips observed during both irradiations of STM sensors in the previous section. The reason for the increase of the current levels is not found. Possible explanations can be either a creation of further electron-hole pairs due to local break through mechanisms or a significant change of electric field configuration due to charge ups. These changes can force single strip leakage currents to sink in different regions of the sensor. The second possibility seems to be most probable because one strip under investigation has a significant lower leakage current level than the average value of the other strips which were observed. This possibility is underlined by the changes of the interstrip capacitance of STM sensors which is found to change significantly with irradiation (see Section 6.10.3) what implies high surface currents (see Section 2.6).

These "hot strips" whose leakage currents changes more or less randomly with time, irradiation, and maybe annealing endanger the functionality of the detector module because "fake hits" can be observed during operation of CMS.

6.8 Results of Bias Resistor Measurements

A certain potential is applied at the p^+ strip implant of the sensor via the bias resistor. The resistance of the bias resistor contributes to the resulting noise on a detector module (see Section 2.10). For this reason, it is important to investigate the behaviour of the resistance with fluence and annealing. The bias resistors are made of heavily doped poly crystalline silicon. The initial doping concentration is expected to change in the same way with irradiation like the bulk material of the sensor. Thus, for p-doped poly crystalline silicon an increase of its acceptor concentration and a resulting decrease of its resistance is expected and for n-doped poly crystalline silicon a compensation of its donor concentration with resulting increase of its resistance should be observed, respectively. A type inversion of the poly crystalline silicon is expected for n-type poly crystalline silicon after a certain fluence .

In the following, the observations concerning the resistance of the poly crystalline silicon resistors done in IQC in Karlsruhe are described followed by extended studies to fluences above expectations in the CMS tracker in order to enhance the effects observed in IQC. An important question to be answered is wether the functionality of the principle design of the CMS sensor can be assured at future high energy experiments like SLHC at which maximum fluences up to approximately $10^{16} n_{1MeV}/cm^2$ are expected.

6.8.1 Bias resistors after Service Life at LHC

The measured resistances of the poly crystalline silicon resistors before and after proton irradiation and following standard annealing procedure are shown in Figure 6.41.

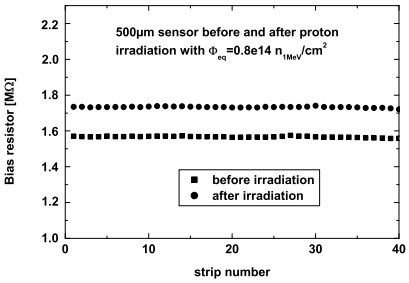

(a) *The bias resistors have an average increase of* $0.15 M\Omega$ *for fluences of* $0.8 \cdot 10^{14} n_{1MeV}/cm^2$ *and after standard annealing procedure [Fur03].*

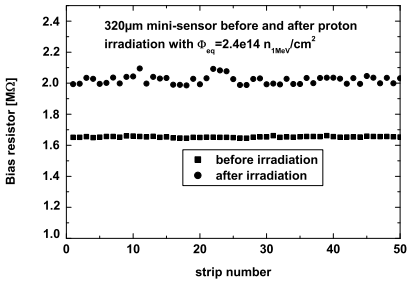

(b) *The bias resistors have an average increase of* $0.35 M\Omega$ *for fluences up to* $2.4 \cdot 10^{14} n_{1MeV}/cm^2$ *and after standard annealing procedure [Fur03].*

Figure 6.41: **Bias resistors after proton irradiation with outer and inner barrel fluence:** *The bias resistors of both suppliers increase with fluence. The increase seems to be correlated with the fluence because the increase of* $0.15 M\Omega$ *at* $0.8 \cdot 10^{14} n_{1MeV}/cm^2$ *(left hand side) is much lower than the increase of* $0.35 M\Omega$ *at* $2.4 \cdot 10^{14} n_{1MeV}/cm^2$ *(right hand side). After the design fluence of inner and outer barrel sensors, the sensors' bias resistors are still in specifications of Table 4.1 on Page 57.*

An increase of the resistance of the poly crystalline silicon resistors is observed after irradiation with the corresponding design fluence and following standard annealing procedure. For STM sensors - irradiated with protons up to $0.8 \cdot 10^{14} n_{1MeV}/cm^2$ - an average increase of $0.15 M\Omega$ is measured, and for HPK sensors - irradiated with $2.4 \cdot 10^{14} n_{1MeV}/cm^2$ - the average increase is found to be $0.35 M\Omega$. An increase of the bias resistors resistances is observed after irradiations done for all STM and HPK sensors and mini sensors. A parametrization of the resistance versus the fluence, which is valid for all bias resistors, is not given in this work due to the fact that the bias resistors have different diameters, lengths, resistivity, grain size, or different doping concentrations and doping types (see Section 2.7 on Page 30). In summary, no increase above $0.35 M\Omega$ at $2.4 \cdot 10^{14} n_{1MeV}/cm^2$ has been observed in IQC. The reason why this increase has not been observed in [Fur02] is the use of clamps (see Figure 6.3 on Page 90) during irradiation supporting electrical contacts which were necessary for that irradiation campaign. These clamps covered partially the structures to be irradiated in the region of the bias resistors and stopped the proton beam before reaching the structures to be irradiated.

An interesting question is wether the change of the resistance of the poly crystalline silicon saturates at a certain fluence. Figure 6.42 shows the measurement results of the bias resistors versus applied bias voltage on the seven sensors from the final STM pre-series (see Table 6.2 on Page 99) after proton irradiation and standard annealing procedure.

After irradiation, the depletion zone grows with increasing bias voltage from the backside of the sensor to the strip implant side. The voltages at which the measured bias resistors saturate due to the fact that no measurement current flows below the dielectric layer to the bias ring (see Section 5.3.4) correlates well with the full depletion voltages in Figure 6.14. On all STM sensors the observed increase of the bias resistors' resistance with irradiation is with $0.15 M\Omega$ still in specifications of Table 4.1 and independent on the fluence and the initial resistance. The change of the resistance varies therefore between approximately 7.5 % and 15 % depending on the initial value.

The increase of the bias resistors resistance at design fluence is for HPK sensors in all cases approximately $0.35 M\Omega$. Due to the fact that the contract with STM has been canceled, no further investigations such as annealing behavior or fluence dependencies have been done on the bias resistors

of STM sensors, but only on those of HPK. The following section will answer the question wether the increase of the resistance of the poly crystalline silicon resistors of HPK sensors saturates at a certain fluence and wether annealing takes place.

6.8.2 Annealing of Poly Crystalline Silicon Resistors

Figure 6.43 shows the resistance versus bias voltage of the poly crystalline silicon resistors after inner barrel design fluence at different annealing steps on two HPK sensors.

The measured value of the resistance saturates above full depletion voltage for the reasons given in Figure 6.42. The bias voltages at which the bias resistors saturate reflect the behavior of full depletion voltage in Figure 6.10. The increase of the resistance of the bias resistors after irradiation is caused by the fluence and a slight increase with annealing time is observed for annealing at $60°C$. This annealing effect is expected also to take place at $20°C$ with a much lower rate. Up to annealing times of one year at $20°C$ no annealing of the resistance has been observed. For this reason, an annealing effect of the resistance will not be observed during service life of CMS. The increase of the saturation plateau from $1.55\,M\Omega$ before irradiation to $1.82\,M\Omega$ by $0.27\,M\Omega$ after irradiation has the same order of magnitude as shown in Figure 6.41(b).

One open question is the dependence of the resistance of the poly crystalline bias resistors on fluence and annealing. A further reason for the changes observed above can be the difference in temperature between QTC ($20°C$) and IQC ($-10°C$) measurements which can cause an increase of the resistance of the poly crystalline silicon. The poly crystalline silicon is either heavily p-doped or n-doped (see Section 2.7 on Page 30) and - in comparison to silicon - an increase of acceptors is expected by irradiation. Thus, a temperature dependence of the resistance is expected before and after irradiation. In order to answer wether the resistance depends on temperature, measurements on

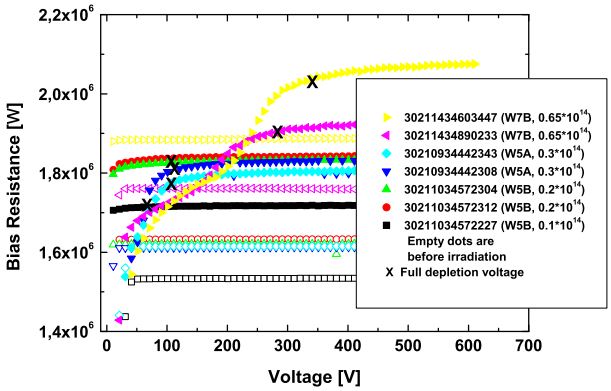

Figure 6.42: **Measurements of bias resistors versus bias voltage of the final STM pre-series sensors before and after proton irradiation:** *After irradiation, the depletion zone grows with increasing bias voltage from the backside of the sensor to the strip implant side. The voltages at which the measured bias resistors saturate due to the fact that no measurement current flows below the dielectric layer to the bias ring (see Section 5.3.4) correlates well to the full depletion voltages in Figure 6.14. The observed increase of the bias resistors' resistance on all STM sensors with irradiation is with* $0.15\,M\Omega$ *still in specifications of Table 4.1 and independent on the fluence. The change of the resistance varies therefore between approximately* $7.5\,\%$ *and* $15\,\%$ *depending on the initial value.*

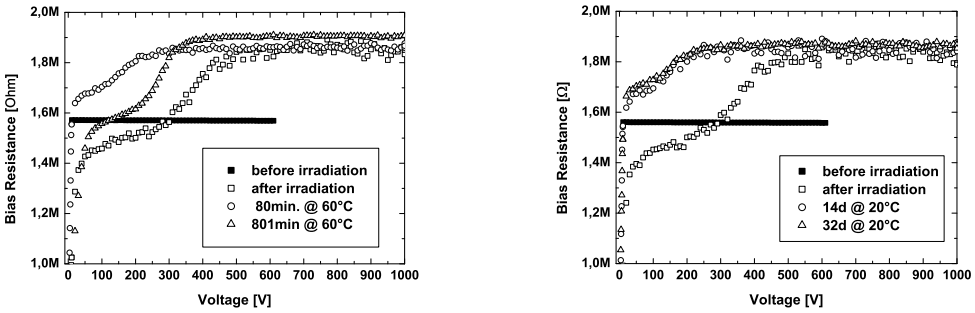

(a) Annealing at $60°C$

(b) Annealing at $20°C$

Figure 6.43: **Annealing of bias resistors after proton irradiation:** *The measured value of the bias resistors at $-10°C$ saturates above full depletion voltage for the reasons given in Section 5.3.4. The bias voltages at which the bias resistors saturate reflect the behavior of the full depletion voltage in Figure 6.10. The increase of the resistance after irradiation is caused by the fluence and a slight increase with annealing time is observed for annealing at $60°C$ [Fur05]. After the increase which is for all cases approximately $0.35 M\Omega$, the bias resistors are still in specifications of Table 4.1. The change is - depending on the initial value - between $16\,\%$ and $23\,\%$.*

special test structures on the standard half moons (see Section 4.6 on Page 56) are performed. At least two test structures containing eleven bias resistors without contact to a strip implant are on these half moons. In the following, the applied voltage to the resistors is $2V$. This voltage is the worst expected voltage drop at the bias resistors after irradiation of the sensors. The current through such a poly crystalline silicon resistor before and after irradiation and after $2h$ annealing time at $60°C$ versus measurement temperature shows Figure 6.44.

The current versus temperature behavior of a poly crystalline silicon resistor at an applied voltage of $2V$ is given by a straight line:

$$\begin{aligned} I_{Rpoly} &= m_I \cdot T + c \\ I_{Rpoly,non\,irrad} &= (3.32 \pm 0.014) \cdot 10^{-3}\, T - (0.1459 \pm 0.0033) \quad \mu A \\ I_{Rpoly,irrad\,annealed} &= (3.21 \pm 0.011) \cdot 10^{-3}\, T - (0.1576 \pm 0.0026) \quad \mu A \end{aligned} \tag{6.15}$$

with the current's slope m_I and a constant offset c. The resistance of the poly crystalline silicon resistor is calculated by the ohmic law. Figure 6.45 shows the resistance versus temperature of the poly crystalline silicon resistor in Figure 6.44. It shows the expected hyperbolic behavior for a linear current versus temperature dependence.

The dependence of the resistance of poly crystalline silicon on temperature, fluence, and annealing has not been taken into account during the design phase of the CMS sensors. In order to enhance the effects of irradiation and annealing and to test the functionality of the poly crystalline silicon resistors at SLHC conditions, studies with higher fluences are presented in the following section.

6.8.3 Bias Resistors after Service Life at SLHC

Figure 6.46 shows the behavior of poly crystalline silicon resistors for fluences of $10^{15}\, n_{1MeV}/cm^2$ and $10^{16}\, n_{1MeV}/cm^2$ measured on the special test structures which were investigated in the previous section.

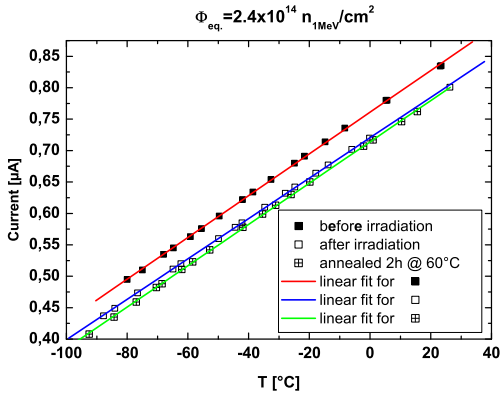

Figure 6.44: **Current through a poly crystalline silicon resistor versus temperature before and after proton irradiation:** *The current through the poly crystalline silicon resistor behaves linearly with temperature. The applied measurement voltage is* $2V$*. After irradiation, the current is lower than before irradiation what results in a higher resistance of the bias resistor. After an annealing of* $2h$ *at* $60°C$*, a further decrease of the current is observed. These observations lead to the conclusion that the observed differences of the bias resistors of the HPK sensors depend on temperature, fluence, and annealing.*

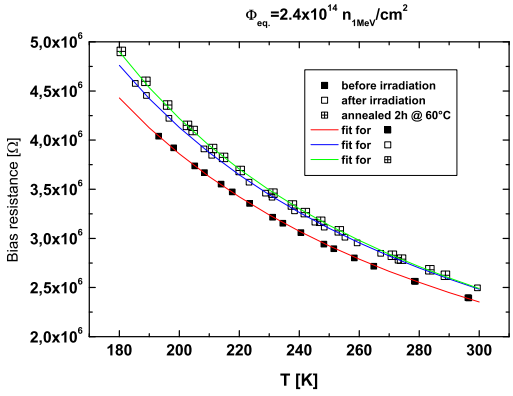

Figure 6.45: **Resistance of a poly crystalline silicon resistor versus temperature before and after irradiation:** *The resistance of the poly crystalline silicon resistor shows the expected hyperbolic function of temperature. It increases with irradiation and in addition an annealing effect of the same direction has to be taken into account (see Figure 6.44).*

For fluences up to $10^{15}\,n_{1MeV}/cm^2$ the resistance of the poly crystalline silicon resistors increases with irradiation. The increase is approximately $0.5\,M\Omega$ at room temperature and it is approximately $0.7\,M\Omega$ at $-10°C$. The resistance at room temperature decreases approximately $0.3\,M\Omega$ for fluences up to $10^{16}\,n_{1MeV}/cm^2$. In both cases, an annealing effect is observed at $60°C$ which gives a slight increase of approximately 1%. Figure 6.47 shows the current of a poly crystalline silicon resistor at $2V$ and its resistance after a fluence of $5 \cdot 10^{16}\,n_{1MeV}/cm^2$.

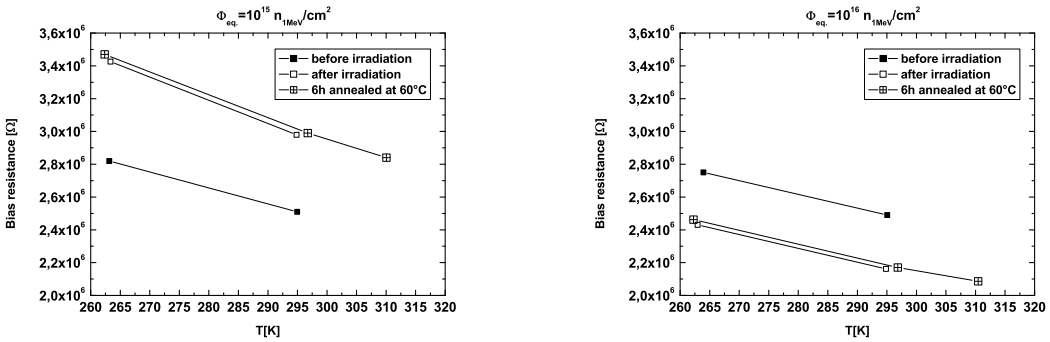

(a) (b)

Figure 6.46: **Resistance of poly crystalline silicon resistors before and after proton irradiation and annealing with fluences up to** $10^{16} n_{1MeV}/cm^2$**:** *The poly crystalline silicon resistors show before and after irradiation and after annealing a similar temperature dependence as shown in Figure 6.45. The resistance increases with a fluence of* $10^{15} n_{1MeV}/cm^2$ *(left hand side) up to* $0.7 M\Omega$*. For the higher fluence of* $10^{16} n_{1MeV}/cm^2$ *(right hand side) the resistance decreases. With an annealing time of* $6h$ *at* $60°C$ *in both figures a slight increase of approximately* 1% *is observed.*

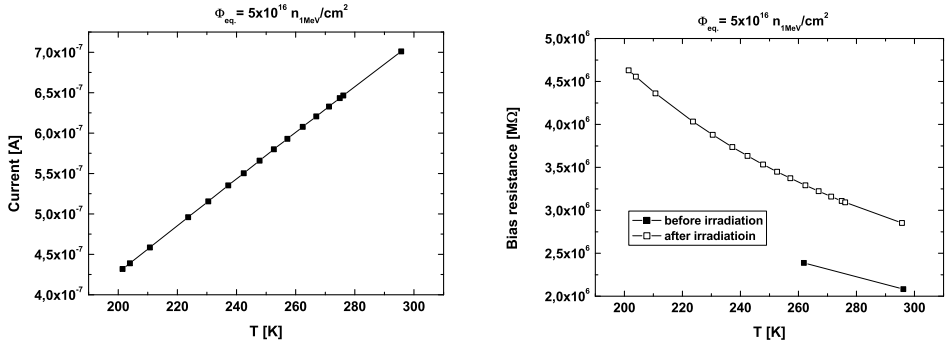

(a) (b)

Figure 6.47: **Current and resistance of poly crystalline silicon resistor irradiated to** $5 \cdot 10^{16} n_{1MeV}/cm^2$**:** *The current through the poly crystalline silicon resistor at* $2V$ *(left hand side) is still linear with temperature but has a higher slope than in Figure 6.44. The resistance (right hand side) shows an increase with fluence of* $0.8 M\Omega$ *at room temperature.*

The current through the poly crystalline silicon resistor after a fluences of $5 \cdot 10^{16} n_{1MeV}/cm^2$ is still linear versus temperature what results in a hyperbolic resistance behavior versus temperature.

6.8.4 Summary of Bias Resistor Measurements

A parametrization of the resistance versus fluence and annealing is not possible due to the unknown geometry (length & diameter), the unknown doping concentration, and the unknown grain size of the poly crystalline silicon resistors. The surface to active volume ratio of the grains within these resistors is assumed to be large, i.e. surface currents can become important. For these reasons, only a

qualitative description of the changes can be given in the following.

Only a decrease of its resistance with fluence is expected for p-doped poly crystalline silicon because the initial acceptor doping concentration is expected to increase with fluence. The increase of the resistance of the bias resistors observed in IQC hints therefore to n-doped poly crystalline silicon within the bias resistors.

For fluences up to $10^{15} n_{1MeV}/cm^2$ the resistance of all bias resistors increases with irradiation. For the higher fluences beyond $10^{15} n_{1MeV}/cm^2$ - depending on the initial resistance - type inversion can be observed. This is the case for the poly crystalline silicon resistors irradiated to $10^{16} n_{1MeV}/cm^2$. The resistance started at a comparatively high initial value before irradiation - probable near to the point of type inversion - and end at a significant lower one after end of irradiation. In the case of the bias resistors irradiated to $5 \cdot 10^{16} n_{1MeV}/cm^2$ which started with a very low initial value, one cannot distinguish if the poly crystalline silicon is type inverted or not because only an increase of the resistance is observed and the turning point which corresponds to the point of type inversion is unknown.

In n-type poly crystalline silicon an annealing after irradiation should consequently reduce the resistance before type inversion and increase it afterwards, respectively. In all cases shown above independent if before or after type inversion, the annealing gives a slight increase of the resistance of approximately 1%. This change is too small and its direction is opposite to the expectations before type inversion. It cannot be excluded that other effects like e.g. increase of surface currents overlap the annealing effects.

Finally, for fluences after service life of CMS, an average increase of $\approx 0.35 M\Omega$ ($\approx 0.15 M\Omega$) is expected for the resistance of the bias resistors on inner (outer) barrel sensors. After the increase of the resistance, the bias resistors are within the specifications of Table 4.1 on Page 57. A further important conclusion is the fact that even at high fluences up to $5 \cdot 10^{16} n_{1MeV}/cm^2$ the poly crystalline silicon acts as ohmic resistor with a still hyperbolic dependence on temperature. With this observation, it seems to be possible to operate sensors with strip or pixel design with bias resistors and AC-coupling also at radiation environments like SLHC. This reduces the problem of functional sensor designs for SLHC to the investigation on radiation harder bulk material which can be fully depleted after these fluences.

6.9 Results of Coupling Capacitance Measurements

The AC connection between the sensor's strip and the readout channel is realized by coupling capacitances. A decrease of the capacitance values by irradiation or annealing reduces the signals at the amplifiers. For this reason, it is important to know the dependence of the capacitance values on fluence and annealing. The observations concerning the changes of the coupling capacitances done in IQC in Karlsruhe are described below followed by an annealing study carried out on two HPK sensors.

6.9.1 Coupling Capacitances after Service Life at LHC

Figure 6.48 shows coupling capacitance values of a STM outer barrel sensor before and after proton irradiation and standard annealing procedure.

The decrease by irradiation (up to $15\,pF$ on STM sensors) cannot be measured on the mini sensors due to the shorter strip length and therefore lower coupling capacitance values as the fluctuations of the measured values with a measurement frequency of $100\,Hz$ are approximately $1\,pF$ which is comparable to the expected change of the coupling capacitance value.

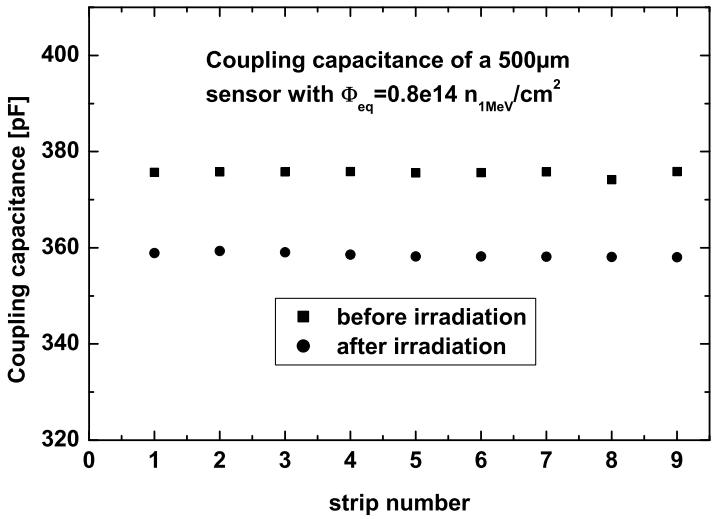

Figure 6.48: **Coupling capacitances of a STM sensor before and after proton irradiation:** *The value of the coupling capacitance of this sensor decreased* $15\,pF$ *by irradiation [Fur03]. A possible explanation for this is the change of* ε_R *of the* $Si0_2/Si_3N_4$ *layers and the changes in the field configuration after irradiation.*

There are two possible reasons for the change of the coupling capacitance values. One is that the dielectric constant ε_R of the $Si0_2/Si_3N_4$ layers changes because charge carriers are induced. The second possible reason are changes in the field configuration after type inversion of the sensors' bulk. A detailed study of coupling capacitances and their dependence on the electric field configuration before irradiation can be found in [Fur02]. The single contributions to the changes of the coupling capacitance values cannot be measured individually.

6.9.2 Annealing of Coupling Capacitances

An important question is wether annealing takes place at coupling capacitance values. This question is answered by an annealing study done on the two W1TID sensors from HPK which were already presented in the previous sections. The results of this annealing study are shown in Figure 6.49.

The measurement of the coupling capacitance values requires a good electrical contact to both the DC and the AC pad. The residuals of the passivation layer on the DC and AC pads of the HPK sensors are comparatively thick and robust. The many values below the average ones in Figure 6.49 are related to bad contacts to the AC pads. The upper dots at $368\,pF$ give the coupling capacitance values before irradiation. After irradiation, a decrease of the coupling capacitances is observed. The middle values at $364\,pF$ in Figure 6.49(b) could be caused by some dust particles on the micro manipulator needle or bad electrical contact wether it is before any annealing and it is not observed in Figure 6.49(a). An annealing behavior is not observed for the coupling capacitance because the charges in the dielectric layer are expected to be stable in time and not moveable.

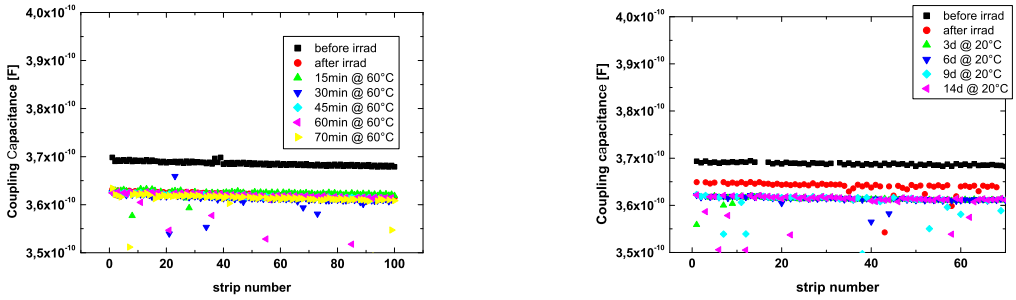

(a) Annealing at $60°C$

(b) Annealing at $20°C$

Figure 6.49: **Annealing of coupling capacitances after proton irradiation:** *Since no changes in time are observed, the changes in the coupling capacitance values are coming from the fluence changing the properties of the dielectric layers. The middle values on the right hand side are caused by bad electrical contact and dust on the tip of the needle used for the measurement [Fur05].*

6.9.3 Summary of Coupling Capacitance Measurements

All values of the coupling capacitances are still within specifications of Table 4.1 on Page 57 after irradiation and annealing but the decrease of the coupling capacitance values observed on HPK and STM are not the same. Since the STM sensors show a decrease of their coupling capacitance values of approximately 4% at $0.8 \cdot 10^{14} n_{1MeV}/cm^2$, on HPK sensors the decrease is found to be lower with approximately 2% at $2.4 \cdot 10^{14} n_{1MeV}/cm^2$. This fact is a further - non critical - difference of the sensors' quality. A possible explanation for this fact is the lower thickness of the dielectric layer of the HPK sensors. Due to this, the changes of ε_R yield to a lower change in the coupling capacitances on HPK sensors than on STM sensors.

6.10 Results of Interstrip Capacitance and Interstrip Resistance Measurements

The interstrip resistance value strongly depends on the electric field configuration and therefore also on bias voltage. If no suspect behavior for the interstrip resistance is observed before irradiation, i.e. too low initial values before irradiation, the interstrip resistances are also after irradiation - even at low bias voltages - too high to see a measurement current in the fluctuations of the single strip leakage current (see Section 5.3.8 on Page 68). Therefore, a change of the interstrip resistance value is not detectable neither with fluence nor with annealing but a lower limit can be given by Equation 5.2 on Page 68.

Large noise is expected for a too high increase of the interstrip capacitance (see Equation 2.58 on Page 33) after irradiation. The interstrip capacitance strongly depends on surface currents (see Section 2.6 and 4.4). The initial quality of the sensors has to be excellent, i.e. nearly no charge impurities in the interface between sensors bulk and dielectric layer, in order to have no dependence of the interstrip capacitance on applied bias voltage. If the initial quality of the interface is not excellent, the advantage of the $< 100 >$ gets lost and the interstrip capacitance value significantly increases.

The changes of interstrip resistances and interstrip capacitances are correlated with each other. The LCR meter used for the measurements of the interstrip capacitances (see Section 5.3.7 on Page 67)

measures the total impedance between two strips and afterwards it calculates the capacitance via the phase shift of the measurement signal. This procedure requires a high interstrip resistance value or the error bars of the interstrip capacitance values are too large to see an effect caused by irradiation or annealing. For this reason, the lower measured limit of the interstrip resistance value is used to reduce the error bars of the measured interstrip capacitance values because the interstrip resistance limit is measured independently on the interstrip capacitance value (see Section 5.3.8).

In the following, the observations concerning the interstrip capacitances done in the IQC in Karlsruhe are summarized followed by a study done in order to find out a limit for the initial flat band voltage before irradiation followed by the annealing of the interstrip capacitance shown at two W1TID sensors supplied by HPK. Finally, it is shown on sample base of final STM pre-series sensors that not all influences on the radiation hardness of the interstrip capacitances are known.

6.10.1 Interstrip Capacitances after Service Life at LHC

The significant different quality of the sensors supplied by STM and HPK is the main problem of the following observations. The flat band voltage was during the whole production phase below $2V$ for HPK sensors and varied for STM sensors from approximately $2V$ up to more than $40V$. The high initial flat band voltages ($> 5V$) can be explained with high charge carrier impurities in the interface of the sensors bulk and the dielectric layer (see Section 2.6 and 4.4). These differences in quality result in complete different observations concerning the interstrip capacitance before and after irradiation and subsequent standard annealing procedure. For this reason, no examples of standard observations are given but it is referred to the following sections in which the two companies' sensors are dealt individually.

6.10.2 Interstrip Capacitance versus Flat Band Voltage

The PQCs found MOS structures on STM half moons with high flat band voltages (see Section 2.6) from $5V$ up to $40V$. HPK MOS structures never showed a value which is significantly above $2V$ what suggests a low charged impurity concentration in the interface between the dielectric layer and the sensor's bulk. As explained in Section 2.6, charge carriers in this interface can cause energy band bending below the dielectric layer affecting the interstrip capacitances and interstrip resistances. The advantage of the $< 100 >$ orientated silicon for radiation hardness is expected to get lost by high initial impurity concentration and therefore high flat band voltage. Figure 6.50 shows the variety of flat band voltages before irradiation. The measurement frequency is $50kHz$.

Since charged particles' coulomb field causes ionization in insulating materials (see Chapter 3), more damage in the dielectric layer is expected by them than by neutral particle irradiation. Some STM mini sensors are irradiated with protons in Karlsruhe for this worst case expectation of the radiation environment in the CMS tracker. One irradiation is performed with five half moons with flat band voltages of $5V$, $7V$, $14V$, $20V$, and $38V$. A high initial flat band voltage results in a high initial interstrip capacitance before irradiation as shown in Figure 6.51(a).

Figure 6.51(b) shows the interstrip capacitance values of these mini sensors after a fluence of $2.4 \cdot 10^{14} n_{1MeV}/cm^2$ and standard annealing procedure. This irradiation was performed with inner barrel design fluence to enhance the influence of the irradiation. A high initial flat band voltage results in a high increase of the interstrip capacitance values after irradiation and standard annealing procedure.

Since the increase of the interstrip capacitance values is larger than originally expected, a second irradiation is performed in order to set a limit to the flat band voltage which limits the increase of

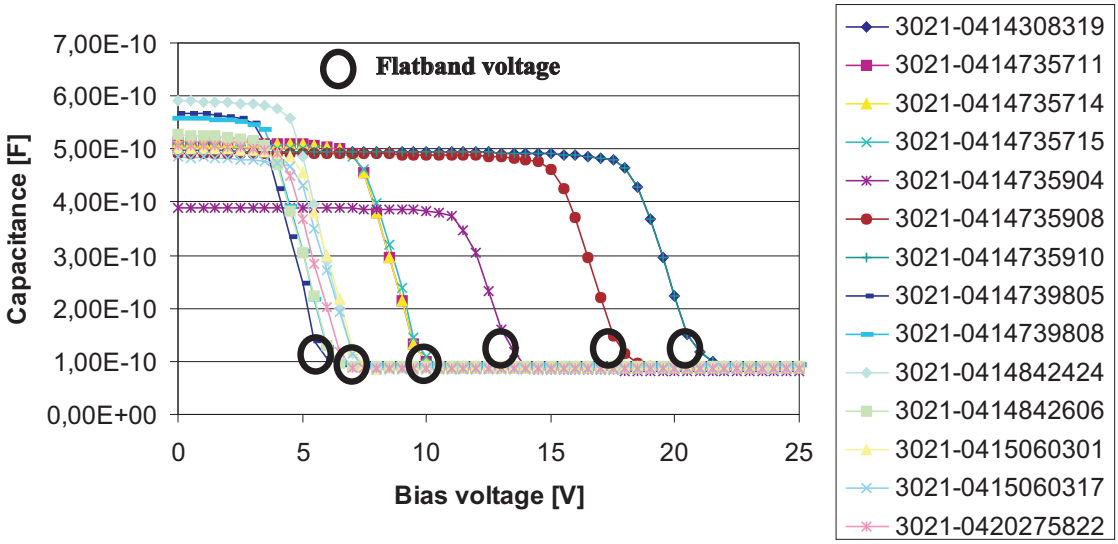

Figure 6.50: **Flatband voltage of STM outer barrel mini sensors:** *The flat band voltages, which are the reflection points of the presented CV characteristics, vary from* $5V$ *up to* $40V$ *(only up to* $20V$ *shown here). They are measured with a frequency of* $50kHz$ *on the MOS structures located on the same half moons as the mini sensors.*

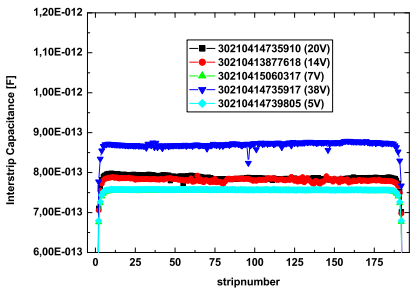

(a) Interstrip capacitances before irradiation

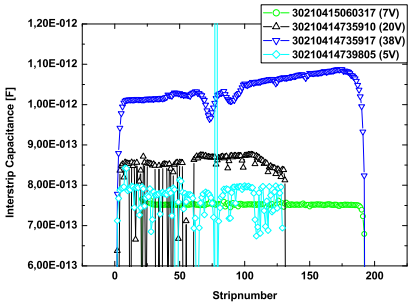

(b) Interstrip capacitances after proton irradiation with inner barrel fluence and standard annealing of $80min$ and $60°C$

Figure 6.51: **Interstrip capacitances of STM mini sensors before and after proton irradiation with inner barrel design fluence:** *The increase of the interstrip capacitance with irradiation scales with the initial full depletion voltage. The down going peaks are caused by bad electrical contacts. No interstrip capacitance increase is observed for the lowest flat band voltages of* $5V$ *and* $7V$.

interstrip capacitance value below 10% (see Table 4.1 on Page 57). For this reason, the structures are irradiated with a fluence of $0.5 \cdot 10^{14} n_{1MeV}/cm^2$ which corresponds to the expected radiation environment in the CMS tracker. After irradiation, the structures are annealed following the IQC standard procedure. The results of this irradiation campaign are given in Figure 6.52.

Figure 6.52(a) shows the initial interstrip capacitances of half moons with flat band voltages of $5V$, $9.5V$, $13.5V$, $20V$ and $36V$. As shown in Figure 6.51(a) the initial interstrip capacitance scales

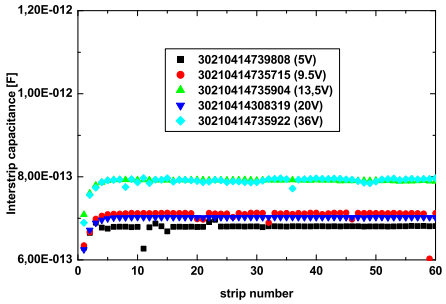

(a) Interstrip capacitances before second irradiation

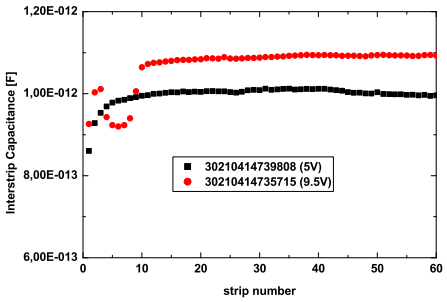

(b) Interstrip capacitances after second proton irradiation (18 years service life at LHC)

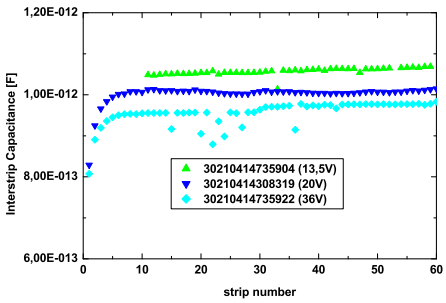

(c) Interstrip capacitances after second proton irradiation (10 years service life at LHC)

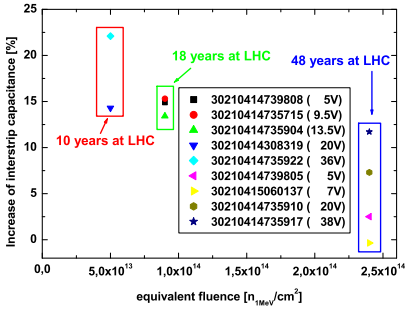

(d) Increase of interstrip capacitance values after proton irradiation

Figure 6.52: **Interstrip capacitances of STM mini sensors with too high flat band voltages before and after proton irradiation with outer barrel design fluence:** *The mini sensors are irradiated with the outer barrel design fluence and are annealed after standard IQC procedure afterwards. The low flat band voltage samples in 6.52(b) are irradiated to a fluence corresponding to 18 years of outer barrel service life at LHC. Therefore, the increase is higher than for the samples in 6.52(c) which are irradiated to a fluence corresponding to ten years of service life at LHC. The percentage of the interstrip capacitance values' increase in the graph at the right hand bottom side is suspect. The fact that higher fluences cause lower increase of interstrip capacitances hints to a further unknown parameter which is responsible for the observed increase of the interstrip capacitance values with fluence.*

with initial flat band voltage. The half moons with the low initial flat band voltages are irradiated to a fluence of 18 years service life at LHC. For this reason, the increase of their interstrip capacitance values is higher than expected after the service life within the CMS tracker.

The increase (in percentage) of the two irradiation campaigns' samples' interstrip capacitance values is shown in 6.52(d). The suspect fact that the increases of interstrip capacitance values does not scale with fluence hints to a further unknown parameter which is responsible for the observed increase after irradiation.

After these two irradiation campaigns, a limit of maximum $10\,V$ for the flat band voltage is given to STM as acceptance criterium with the hope to keep the increase of the interstrip capacitance value below 10%. The next sensors supplied by STM show a significant lower flat band voltage of approx-

imately $2V$. This is achieved by STM by reducing the positive charge carriers in the silicon dioxide [STM04]. Unfortunately, the irradiation facility in Karlsruhe was not available for a long period of more than one year and therefore the first irradiation tests with the new dielectric quality was done much later. The results of these tests are summarized in Section 6.10.3 where a final pre-series of STM sensors is evaluated for their interstrip capacitance values before and after proton irradiation.

6.10.3 Undetectable Parameters - Evaluation of Final STM Pre-series

The next problem which appeared after the problem of too high initial flat band voltages is that very low interstrip resistances out of specifications have been found on STM sensors. This problem has been solved in a study by the CMS collaboration. The removing of the passivation layer which probably contained impurities with negative charge carriers significantly improved the interstrip resistance. It is most probable that the negative charge carriers in the passivation layer partially reduced the Coulomb field of the positive charge carriers in the dielectric layer. STM reduced after this study also the negative charge carrier concentration in the passivation layer. Finally, all flat band voltages in the final STM pre-series sensors are with approximately $2V$ below the limit given to STM which is $10V$. Together with the observations from the studies in the previous section it is expected that no problems concerning the radiation hardness of the interstrip capacitances of these STM sensors occur anymore because their initial quality improved significantly.

Figure 6.53(a) shows the interstrip capacitance ramps of the final STM pre-series sensors from Table 6.2 on Page 99 before and after proton irradiation with subsequent standard IQC annealing procedure. Their increase in percentage with irradiation is shown in Figure 6.53(b).

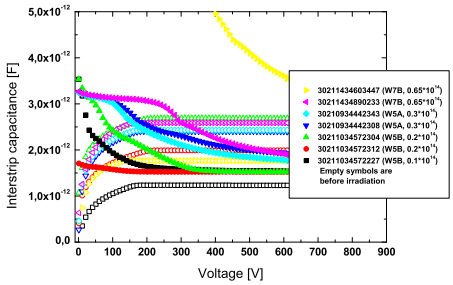

(a) Bias voltage ramps of interstrip capacitances from final STM pre-series sensors

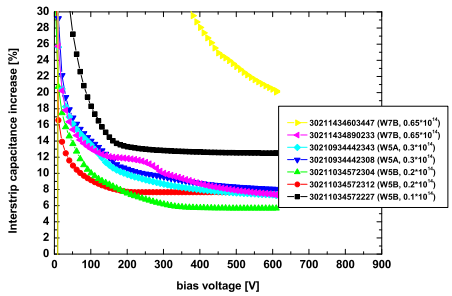

(b) Increase of interstrip capacitances from final STM pre-series sensors after irradiation

Figure 6.53: **Bias voltage ramps of interstrip capacitances from final STM pre-series sensors:** *The interstrip capacitances versus bias voltage after proton irradiation (filled dots) on the left hand side show the expected decreasing behavior with increasing bias voltage (see Section 5.3.7 on Page 67). Their increase (in percentage) is shown on the right hand side. The limit by specifications of* 10% *for increase of interstrip capacitance with irradiation is not fulfilled. The late saturation of the interstrip capacitance value far beyond full depletion voltage is a further problem with unknown origin. This behavior is not observed on HPK sensors (see next Section).*

A low flat band voltage does not necessarily prohibit the increase of the interstrip capacitance values with irradiation. A parametrization of the increase with fluence is not possible and the origin of the increase seems to come from further not detected quality problems of the final STM pre-series sensors.

6.10.4 Annealing of Interstrip Capacitance

The initial flat band voltage observed on all HPK structures is approximately $2\,V$. This low value and the experience from the previous Sections anticipate the increase of the interstrip capacitance values to be low after proton irradiation. Figure 6.54 shows the interstrip capacitance values versus bias voltage measured between the DC pads of two W1TID sensors before and after proton irradiation with a fluence of $2.4 \cdot 10^{14}\, n_{1MeV}/cm^2$ and at different annealing steps.

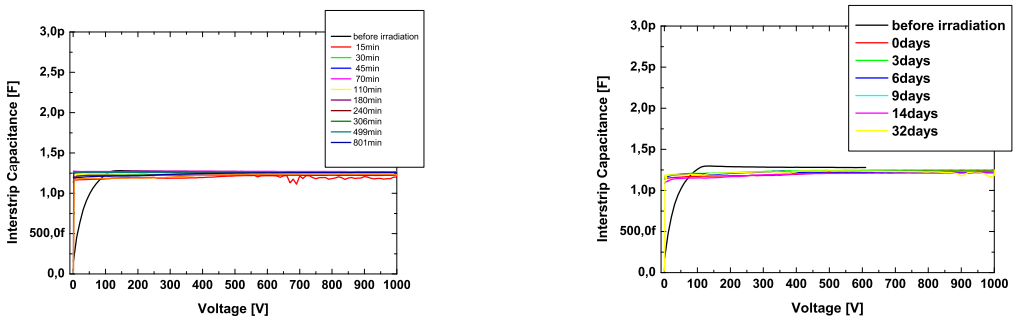

(a) Annealing at $60°C$

(b) Annealing at $20°C$

Figure 6.54: **Annealing of interstrip capacitance of HPK sensors measured between DC pads:** *The interstrip capacitance does neither change with fluence (here proton irradiated to* $2.4 \cdot 10^{14}\, n_{1MeV}/cm^2$*) nor with annealing. The annealing of the capacitance of the strips to the backside contact (see Figure 6.10 on Page 96) does hardly influence the interstrip capacitance values.*

The measured capacitance results from the capacitance network of the sensor (see Section 2.10 on Page 32). The contributions of the strips capacitances to the backside contact does hardly influence the measured interstrip capacitance. The fact that no changes are observed neither with fluence nor with annealing reflects the low concentration of charge carrier impurities within the interface of the sensors bulk and its dielectric layer.

Figure 6.55 shows the interstrip capacitance ramps of these two sensors measured between the AC pads.

The decrease of the coupling capacitance with irradiation (see Section 6.9.1) does not influence the interstrip capacitance between the AC pads. This observation can be explained with the high measurement frequency of $1\,MHz$ from the LCR meter. The charge carriers inside the dielectric layer are not able to move at this frequency (see Section 5.3.7).

6.10.5 Summary of Interstrip Capacitance Measurements

The interstrip capacitance is the most important contribution to the noise of a readout channel on a detector module (see Equation 2.58 on Page 33). On HPK sensors, the changes observed after irradiation with design fluence expected after service life of CMS are quite low and no annealing behavior is observed. In some cases, after irradiation a very small increase of the interstrip capacitance value is observed with the LCR meter. This increase can be traced back to a change of the parallel interstrip resistance which can be estimated by the changes of the phase shift of the LCR meter and the measured lower limit (see Section 5.3.8 on Page 68). Since the interstrip resistance values and the interstrip capacitance values are still within specifications of Table 4.1 of Page 57, no problems during service life of CMS are expected for detector modules built from HPK sensors.

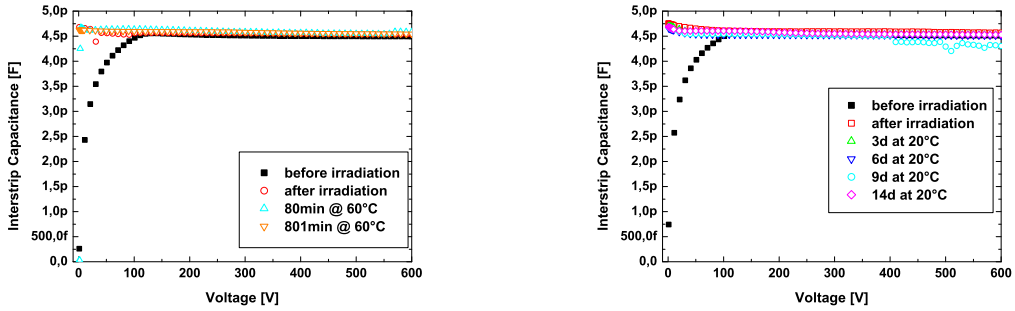

(a) Annealing at $60°C$

(b) Annealing at $20°C$

Figure 6.55: **Annealing of interstrip capacitance of HPK sensors measured between AC pads:** *The interstrip capacitance between the AC pads shows neither changes with fluence (here proton irradiated to* $2.4 \cdot 10^{14} n_{1MeV}/cm^2$*) nor with annealing. The decrease of the coupling capacitance value with irradiation (see Section 6.9.1) does not influence the interstrip capacitance between the AC pads. This observation can be explained with the high measurement frequency of* $1\,MHz$ *from the LCR meter. The charge carriers inside the dielectric layer are not able to move at this frequency (see Section 5.3.7) [Fur05].*

For STM sensors, the situation is completely different. Larger changes of the interstrip capacitance values of the initial values are observed after irradiation and subsequent standard annealing procedure. One outlier even showed more than 50% increase of its interstrip capacitance with irradiation. All studies performed to find out the origin of this fact lead to no conclusive results. Finally, it can be concluded that there are further unknown parameters responsible for the changes of the interstrip capacitance (and interstrip resistance) values which could not be detected in PQC, in QTC, or in IQC. This is the best example why the quality assurance concept of CMS has to contain irradiation tests in order to assure the functionality of the sensors.

6.11 Results of Signal-to-Noise-Ratio Measurements

The most important parameter of a detector module for particle detection is the signal to noise ratio (SNR). The signal is reduced after irradiation by trapping effects which swallow charge carriers from the produced signal. Contrary, the noise increases due to changes observed for strip parameters and due to changes of the properties of the readout electronics of the detector modules. All changes together decrease the signal to noise ratio of the detector modules. The measurements of signal to noise ratio of irradiated detector modules is presented below.

6.11.1 Signal-to-Noise-Ratio after Service Life at LHC

In addition to the irradiation tests on sensor level also irradiation tests on detector module level have been carried out. In these cases also the readout electronics is irradiated with the same fluence as the sensors. Figure 6.56 shows the signal to noise ratio of two detector modules - built with STM sensors - before and after irradiation.

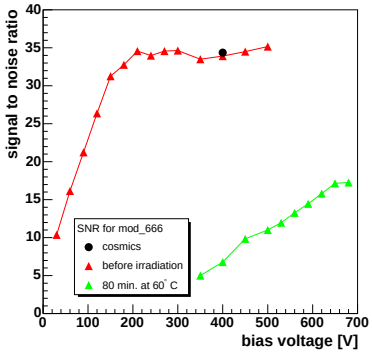

(a) peak mode

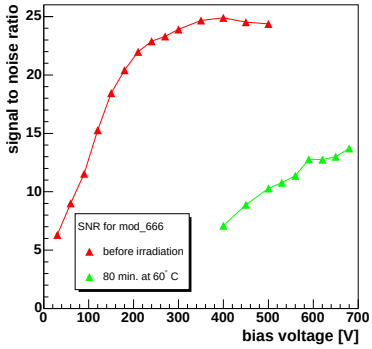

(b) deconvolution mode

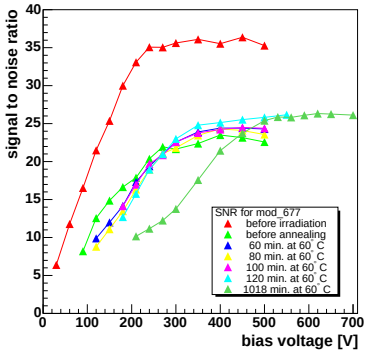

(c) peak mode

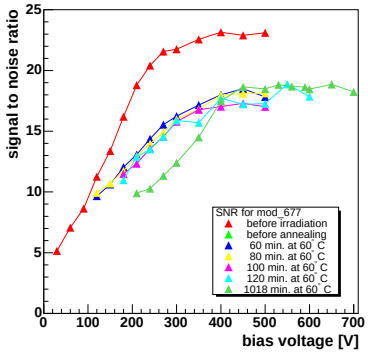

(d) deconvolution mode

Figure 6.56: **Signal to noise ratios of CMS detector modules with STM sensors before and after irradiation:** *The upper detector module is irradiated with neutrons in Louvain-la-Neuve to a fluence of* $1.2 \cdot 10^{14} n_{1MeV}/cm^2$ *and the lower one is proton irradiated in Karlsruhe to a fluence of* $0.7 \cdot 10^{14} n_{1MeV}/cm^2$*. After irradiation, the SNR is observed for electrons from a* ^{90}Sr *source which are MIPs in silicon (see Section 2.3.3 on Page 21). The SNR saturation level - measured at* $-10°C$ *- is above the limit of ten for peak mode as shown in the plots on the left hand side and the same behavior is observed in deconvolution mode as shown in the plots on the right hand side. At higher annealing time and therefore higher full depletion voltage (i.e. advanced reverse annealing, see Section 3.4), the saturation of the SNR shifts to higher bias voltages with slight increase of the maximum plateau of the SNR [Wei04]. This slight increase can be explained with the annealing of the single strip leakage current which results in decrease of noise.*

A ^{90}Sr source provides electrons which are MIPs in silicon (see Section 2.3.3 on Page 21). The applied bias voltage at which the SNR saturates depends on the full depletion voltage which follows the parametrization given in Section 3.4 on Page 44. The maximum plateau of the SNR only decreases with fluence because the fluence increases the trapping probability and increases the noise. Annealing slightly increases the saturation of the SNR due to the decrease of single strip leakage current with annealing. The figures 6.56(a) and 6.56(c) show the SNR for peak mode and Figure 6.56(b) and 6.56(d) show the SNR for deconvolution mode (see Section 4.5 on Page 55) [Wei04a]. The SNR is because of the signal shaping lower in deconvolution mode than for peak mode. However, it is above the limit of ten what is necessary for CMS requirements. These observations are the same for detector modules containing STM or HPK sensors. The problems shown in the next section are only observed

on detector modules containing STM sensors.

6.11.2 Evaluation of Final STM Pre-series Sensors on Detector module Level

Eight detector modules containing sensors from the final STM pre-series are tested for radiation hardness. They have been irradiated with four different fluences, one before sensors' bulk type inversion, one at type inversion, one direct after type inversion and one with the design fluence of outer barrel sensors. Figure 6.57 shows the fluences and the expectations for full depletion voltages which are not verified here by measurements on sensor level.

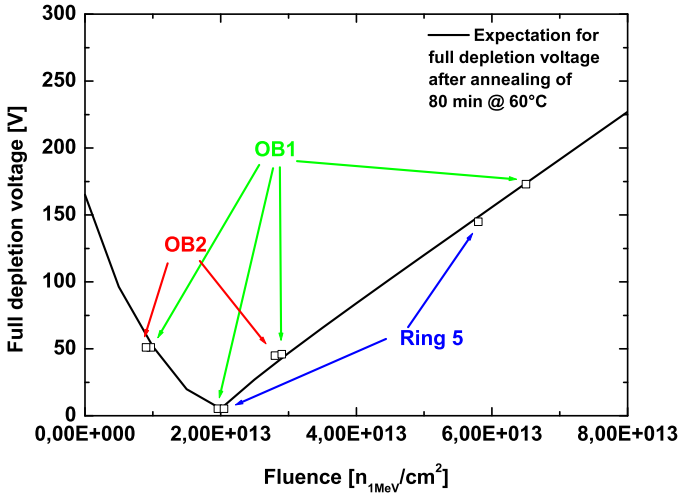

Figure 6.57: **Full depletion voltages of detector modules with sensors from final STM pre-series:** *Eight different detector modules with same initial full depletion voltages (approximately* $168\,V$*) are irradiated with four different fluences. The dots presents the expected full depletion voltages at the fluences which are measured with NI-foils (see Section 6.2.2 on Page 91). The full depletion voltage is not verified by measurements on sensor level.*

Figure 6.58 shows the noise of six of these detector modules before and after proton irradiation and subsequent standard annealing procedure [Wei04a].

The readout chip APV25 has readout channels at its edge regions with noise levels above the average noise levels of the other readout channels. Therefore, strips with number $n \cdot 128$ are not taken into account for the following evaluation because it cannot be detected wether the noise is a sensor or a readout channel feature. The number of noisy channels changed on the seven measured detector modules. The number of noisy strips on a detector module either increases or decreases or the noise values just changed. A correlation with fluence, applied bias voltage, full depletion voltage, overdepletion and noise cannot be observed and the fluctuations seem to be completely random. This is a critical fact because neither the location nor the level of the noise can be anticipated. The problem of a noisy strip level before irradiation can be solved by removing the wire bond between the strip and the readout channel. Since the number and the levels of noisy and non noisy strips change in all directions, this procedure is not sufficient because further noisy strips can develop at each time during

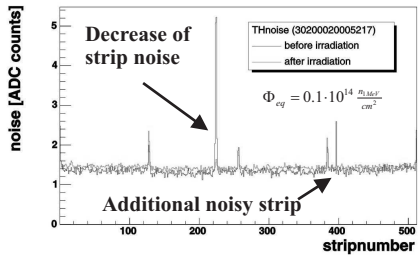

(a) OB2 detector module with fluence before type inversion

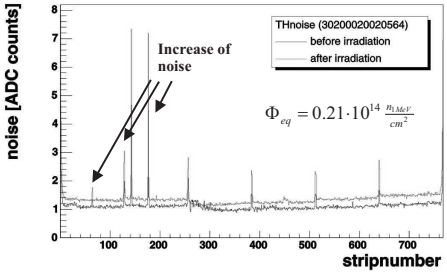

(b) Ring 5 detector module with fluence at type inversion

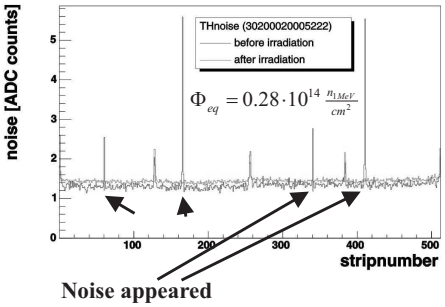

(c) OB2 detector module with fluence shortly beyond type inversion

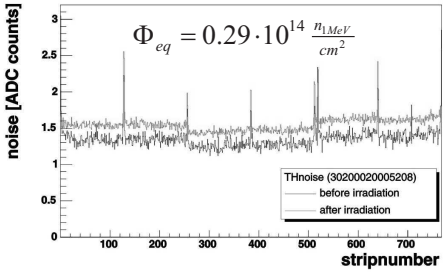

(d) OB1 detector module with fluence shortly beyond type inversion

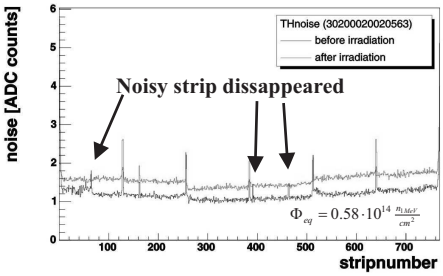

(e) Ring 5 detector module with design fluence

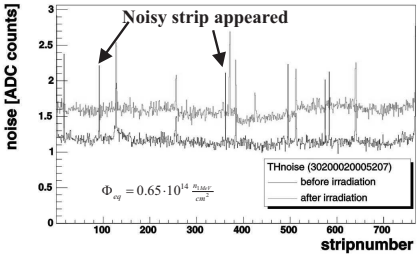

(f) OB1 detector module with design fluence

Figure 6.58: **Noise before and after irradiation and standard annealing for detector modules with STM final pre-series sensors:** *The plots show the noise at* $400V$ *bias voltage before and after proton irradiation with subsequent standard annealing procedure. At the edges from the APV25 the intrinsic noise is high and therefore for all* $n \cdot 128$ *channels the noise is not taken into account for any study because it cannot be detected wether it is a sensor or a readout channel feature. After irradiation, the too high noise level of some strips decreases significantly or even goes down to the average value of the other strips within the same detector module. On the other side, the noise level of the strips increases significantly on some detector modules after irradiation - even on strips which were not suspect in any parameter before irradiation [Wei04a]. The changes of the noise happens randomly because a correlation between overdepletion, applied bias voltage, full depletion voltage, fluence and noise cannot be detected.*

the service life of the CMS tracker.

A further critical problem has been found on the OB1 detector module which has been irradiated with a fluence corresponding to type inversion of the sensor's bulk. The noise before and after proton irradiation is shown in Figure 6.59. A group of 32 neighbored channels has a significant too high noise level. This case is termed common mode noise (CMN).

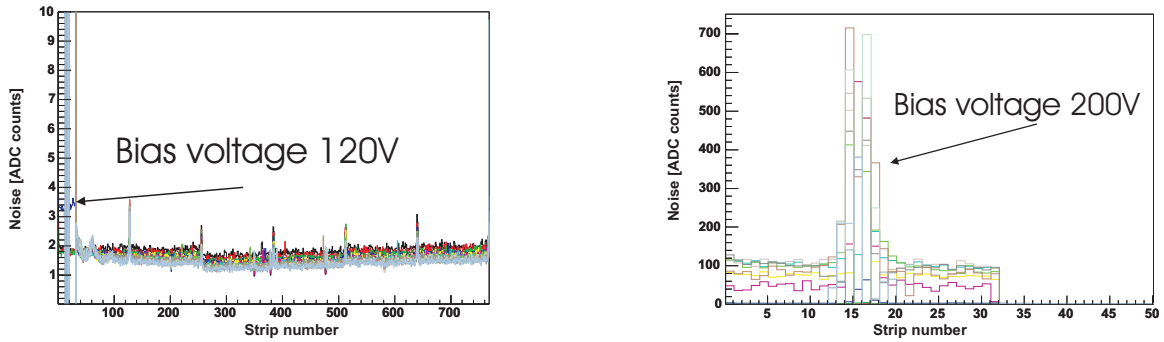

(a) (b)

Figure 6.59: **Common mode noise versus bias voltage of a detector module with STM sensors:** *The plot on the left hand side shows the noise of all readout channels up to an applied bias voltage of* $120V$*. The plot on the right hand side shows the noise values of the group of 32 channels for applied bias voltages up to* $450V$*. The high noise level still increases for voltages above* $200V$ *on two channels but it saturates on the other affected channels on a 50 times higher level than the average level of the other channels of the detector module. The fact that the common mode noise appears at even low bias voltages can be explained with the overdepletion which starts at very low bias voltages because the full depletion voltage is approximately zero for this detector module.*

The noise level of these 32 channels is saturating above a bias voltage of $200V$ except for two channels on which the noise level still increases with bias voltage. The fact that the common mode noise appears at even low bias voltages can be explained with the overdepletion which starts at very low bias voltages because the full depletion voltage is approximately zero for this detector module. Furthermore, a correlation of the 32 channels and the internal circuits of the APV25 is not found. Since the voltages of the readout electronics have not been changed but only the bias voltage applied to the sensors, the origin of the noise is within the sensor. It is possible to reproduce the effects of the noise on this detector module. The same problem was observed once on a further detector module but it was not reproducible and disappeared completely. This observation seems to be caused by charge carrier concentrations within the sensors which are removed by the applied high electrical field.

Finally, the signal to noise ratio after irradiation is the most important parameter on which a detector module is declared as suitable. The SNR, measured on non noisy strips of the seven detector modules, is shown in Figure 6.60.

The SNR is for the peak mode and the deconvolution on all detector modules above the limit of ten but not all of the detector modules are irradiated to the full design fluence. On some detector modules a higher over depletion than 50% is necessary to reach the saturation of maximum SNR. This can be caused by too high full depletion voltages above expectation as it was observed in Section 6.5.3 on Page 98.

Taking all observations concerning the SNR and the noise of the detector modules into account to the observations of the tests on sensor level, the sensors from the final STM pre-series have to be

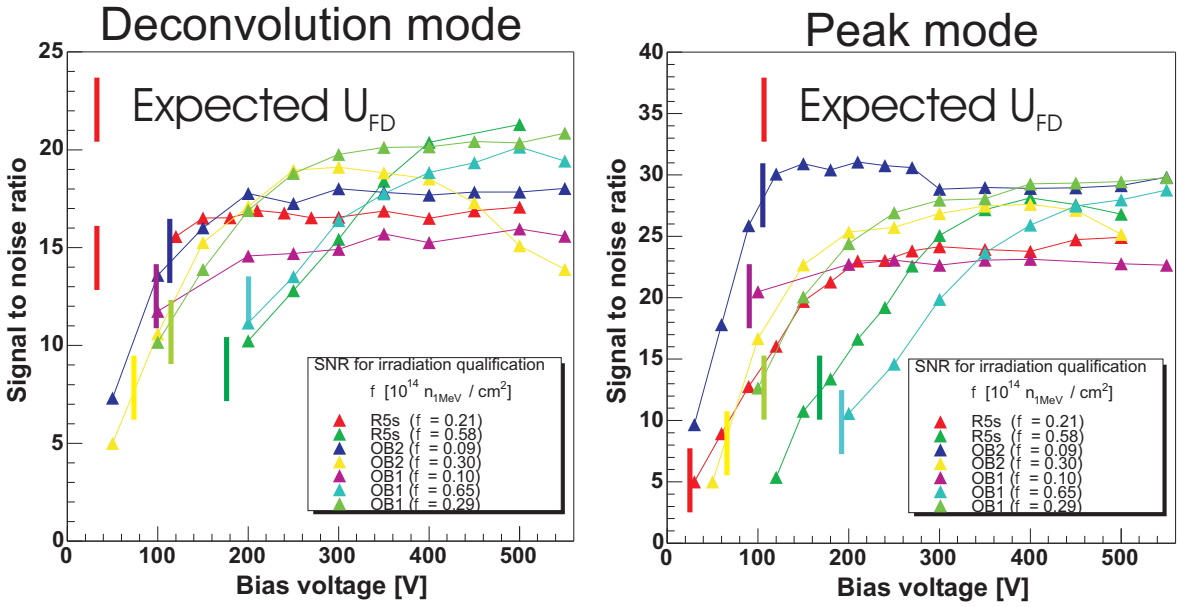

Figure 6.60: **Signal to noise ratio of CMS detector modules with final STM pre-series sensors after proton irradiation:** *The signal to noise ratios are above ten for all detector modules in deconvolution mode (left hand side) and peak mode (right hand side) but not all of them are irradiated with the full expected design fluence. For some sensors a higher overdepletion than* 50% *is necessary to reach the saturation of maximum SNR.*

declared as suspect. The origin of the failures is not traced back to a single feature but it is most probable that the sum of all problems shown in this thesis can cause all the failures observed on these detector modules.

6.11.3 Summary of Signal-to-Noise Measurements

The SNR in deconvolution mode of detector modules built of HPK sensors and STM sensors is still high enough to detect MIPs (see Section 2.3.3 on Page 21) after irradiation and annealing and therefore they fulfill the requirements for operation at CMS. The bias voltage at which the SNR value saturates is typically 50% above the full depletion voltage of the sensors. The decrease of the SNR is caused by two effects. The first one is the decrease of the charge collection efficiency due to production of trapping centers which swallow produced charge carriers. The second reason is the increase of the noise. Before irradiation, the main contribution to the noise of the detector modules comes from the interstrip capacitance of the strip sensors as shown in Table 2.3 on Page 34. The shot noise contribution given by Equation 2.52 on Page 32 is proportional to leakage current and dominates finally the noise of a CMS detector module after irradiation.

On detector modules built of STM final pre-series sensors, the noise values of some readout channels change randomly with irradiation. Since more than 2% of the readout channels changed in an unpredictable way with irradiation, these detector modules are not within the specifications. The changes of the noise levels with time and irradiation significantly endanger the functionality of the tracker because these ”hot strips” can cause fake events during operation of the tracker.

6.12 Summary of all Measurements after Irradiation

The behavior of full depletion voltage and total leakage current of silicon before and after irradiation has been investigated e.g. by collaborations like RD39, RD48, and RD50 at CERN. Whereas RD39 reduces trapping with cryogen techniques, RD48 was looking especially for the annealing of silicon, and RD50 investigates in other bulk materials in order to keep the full depletion voltage after irradiation as low as possible and to reach a sufficient charge collection efficiency [DKN99][Ada00]. The parameterizations given by these collaborations for the development of full depletion voltage and for the development of total leakage current have been checked during the large scale production of the CMS sensors. The results from the full depletion voltage measurements in Section 6.5 and from the total and single strip leakage current measurements in Section 6.7 correspond well to the predictions of these collaborations except of a small number of sensors on which some surprising observations have been done. Most of these outliers already have been suspect in the quality assurance before irradiation. The valid parametrization of the full depletion voltage has been used to calculate the best annealing scenario for the CMS sensors. The final result of these calculations is that the tracker has to be annealed for $28\,d$ at $+10^{\circ}C$ per year in order to get the maximum beneficial annealing effect and to reduce the reverse annealing to an acceptable limit.

The Sections 6.5-6.11 give a further important contribution to the investigations done by the collaborations mentioned above. The large scale production of the CMS sensors showed that there are still unknown parameters responsible for the sometimes non predictable changes of full depletion voltage and for total and single strip leakage currents.

In addition to the observations mentioned above, the changes with fluence and the annealing of the bias resistors, the coupling capacitances, the interstrip capacitances, the interstrip resistances, and the SNR after proton irradiation have been measured.

The effects observed in the previous sections can be summarized as follows:

- A new kind of a stable stable damage component of the full depletion voltage is observed for all sensors with too high resistivity supplied by HPK as shown in Figure 6.21. This stable damage component partially compensates the increase of acceptor concentration and makes the sensors approximately 25% radiation harder under neutron irradiation. Interesting is the fact that these sensors are radiation harder under irradiation with neutral particles than with charged particles because up to now only the opposite is observed under enrichment of the sensors bulk with oxygen.

- The lowest final full depletion voltage of the CMS sensors can be achieved by an annealing scenario with yearly annealing of $28\,d$ at $+10^{\circ}C$.

- The resistance of the bias resistors increases approximately 20% after service life at CMS. The current through these poly crystalline silicon resistors behaves linearly versus temperature whose slope and offset changes with fluence. A hyperbolic curve results for the resistance value versus temperature after all fluences up to $5 \cdot 10^{16}\, n_{1MeV}/cm^2$.

- The resistance of the n-doped bias resistors of the CMS sensors increase with irradiation and after type inversion of the poly crystalline silicon a decrease of their resistance is observed. The order of magnitude at which the type inversion is observed is $10^{16}\, n_{1MeV}/cm^2$.

- The resistance of the bias resistors shows an slight annealing behavior of approximately 1% independent on fluences up to $5 \cdot 10^{16}\, n_{1MeV}/cm^2$.

- The coupling capacitance values decrease with fluence expected after service life at CMS approximately 4% for STM sensors and 2% for HPK sensors.
- In no case an annealing behavior of coupling capacitances is observed.
- The interstrip capacitances of the HPK sensors do not change with fluence.
- The interstrip capacitances of the HPK sensors show no annealing behavior.

The observed unpredictable changes of the STM sensors' parameters - particularly single strip leakage current and single noisy "hot strips" - endanger the functionality of the whole CMS tracker. The partially jumping of strip parameters can cause fake events which can disturb the reconstruction of the whole event of interest.

Summary

The main topic of this thesis is the verification of the radiation hardness of the CMS sensor design. In order to guarantee the functionality of the CMS sensors during the service life of the CMS tracker, 39 sensors, 60 mini sensors, 80 diodes, 27 detector modules, and 10 special test structures were irradiated with the fast neutron spectrum in Louvain-la-Neuve or with the $26\,MeV$-protons in Karlsruhe. All sensors and test structures have been measured before and after irradiation at two dedicated probe stations in Karlsruhe which have been designed and built for this purposes. These probe stations are able to measure all sensor parameters in a wide temperature range from $-18°C$ to $+100°C$ and at high bias voltages up to $1000\,V$. Furthermore, a new dedicated measurement setup has been developed in order to measure total and single strip leakage currents during neutron irradiation.

The fact that ST-Microelectronics (STM) in Catania (Sicily) is a newcomer in high voltage stable sensor production is reflected by a number of problems found during the Quality Assurance of these sensors. The number of problems that occurred during the production phase of the CMS sensors emphasizes the importance of the quality assurance concept for the CMS collaboration. Many of these problems have been detected in the Quality Test Centers and the Process Qualification Centers. Nevertheless, the impact of these problems on radiation hardness has been determined.

The cause of the electrolytically formation of electrically non conductive stains on the aluminium structures of the STM sensors is found to be contamination with potassium. The process steps at STM which cause this contamination of the sensors is unknown within the CMS collaboration. Therefore, it is only possible to provide STM with a feedback and not with a suggestion for the solution of the problem. Another problem withe the STM sensors is the relevance of the leakage current dependence on mechanical stress with regard to radiation hardness was found by measuring the total and single strip leakage currents during neutron irradiation. Strip leakage currents with mechanical stress dependence prior to irradiation have been found to increase or decrease - independently from mechanical stress - unpredictably with irradiation.

Finally, the evaluation of a final STM pre-series of sensors (in which all problems mentioned above should have been eliminated) which was performed in the Irradiation Qualification Test Center in Karlsruhe, showed that the cuts for certain sensor parameters observed by STM were not suitable for the CMS collaboration because STM is not able to find all sensors with a suspect behavior. The main problems which are still observed in the final pre-series are the inhomogeneity of the sensors' parameters within entire batches and the unpredictable development of sensor parameters with time, irradiation, and annealing.

The experience of the Hamamatsu-Photonics-Company (HPK) at Hamamatsu-City (near Tokyo) in the high voltage stable sensor business is reflected in the homogeneity of the sensor parameters within an entire batch. This results in a detailed and reliable analysis of sensor parameter changes with both fluence and annealing. The development of leakage currents and full depletion voltage with irradiation and annealing has been predicted accurately by earlier studies and has been verified again in the Irradiation Qualification Centers. For some HPK sensors, the full depletion voltage

proves to be approximately 20% more radiation hard than expected with literature values given in the Hamburg model. A new unidentified stable donor level after irradiation, partially compensating the increase in the number of acceptors, has been found by means of deep level transient spectroscopy and seems to be responsible for this higher radiation hardness. The coupling capacitance values decrease by approximately 2% on HPK sensors (4% on STM sensors) with irradiation and show no annealing behavior. The interstrip capacitances of HPK sensors do neither change with irradiation nor with annealing. The resistance of the poly-crystalline silicon of the bias resistors increases with irradiation by approximately $15\% - 20\%$ for a fluence of $2.4 \cdot 10^{14} n_{1MeV}/cm^2$. The resistance of the poly crystalline silicon increases slightly (1%) with annealing, independently from fluence. All these effects and the generation of trapping centers within the silicon of the sensor reduce the signal-to-noise ratio (SNR) of the detector modules. However, the SNR after irradiation is still above 10 what is high enough to detect Minimum Ionizing Particles (MIPs).

Proposals for annealing and operation temperatures have been made and corresponding full depletion voltage scenarios have been calculated with the "Hamburg model" and the measured parameters. The lowest final full depletion voltage can be achieved by an annealing scenario with 28 days of annealing at $+10^{\circ}C$ each year of operation at LHC. With these proposals and the experience from the measurements performed, it will be possible to operate the CMS tracker during the entire service life of the LHC. The full depletion voltage scenarios of the sensors in ring 5 on disc 9 show that even in this region of the tracker, where the radiation environment is harsher than previously expected, detector modules can be operated.

Recapitulating it can be said that the CMS sensors are not "off-the-shelf" diodes. Their radiation hardness requirements relies on special know-how regarding resistivity and break through voltage. This know-how can be found at manufacturers which specialize in semiconductor sensors but not at manufacturers which specialize in electronic chips. For such manufacturers, a long learning phase has to be anticipated as the experience with STM has shown. The main problem seems to consist in electrically charged impurities and in the special quality requirements which are stricter for low ohmic and high voltage stable sensors than for comparatively high ohmic circuits in electronic chips. Therefore, it was decided that practically the whole tracker will be build with HPK sensors.

Finally, it has been demonstrated that the sensors supplied by HPK have more than sufficient radiation hardness. From the sensors point of view it is possible to overcome all obstacles in the way of constructing a $206 m^2$ "all-silicon" tracker which will remain fully operational for ten years.

Appendix A

Relay Schematics of the Karlsruhe Probe Station

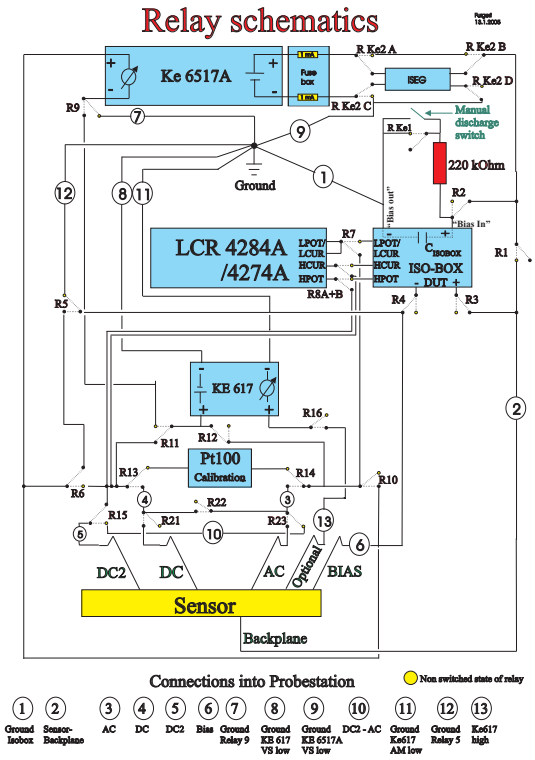

Figure A.1: **Relay schematics of the Karlsruhe probe station:** *The relays 17-20 are on the calibration board with the Pt100. The light dots present the switched off (default) state of the relays. The circles with numbers inside are the locations of the cables lead-through from outside of the aluminium box to the inner side. The ground is defined by a large block of copper inside the aluminium box. The fuses in front of the voltage source of the KE6517A prohibit a destructively discharging of the ISOBOX on the device.*

Measurement	Relays set
IV	5,6
Intermediate IV-CV	2-6
CV	1-5
Leakage current on DC	13,21
Leakage current on AC	6,10,14,23
Leakage current on DC2	15
Bias resistor on DC	9,13,21
Bias resistor on DC2	9,15
Coupling capacitance on DC-AC	6,7,8A+B,13,14,21,23
Coupling capacitance on DC-DC2	6,7,8A+B,13-15,21,23
Pinhole on AC	6,10,11,13,14,21,23
Pinhole on DC	12-14,21,23
Interstrip resistance on DC	12-14,21
Interstrip resistance on DC2	12,14,15,21,22
Interstrip capacitance	6,7,8A+B,14,15,21,22
Leakage current on DC with applied voltage on AC	12-14,21,23
Calibration capacitance 2.4 pF	6,7,8A+B
Calibration capacitance 335 pF	6,7,8A+B,20
Calibration capacitance 10.8 nF	6,7,8A+B,19,20
Calibration capacitance 4.7 nF	6,7,8A+B,17-20

Table A.1: **Relay settings for measurements with the probe station in Karlsruhe:** *The relays 17-20 are on the circuit board with the calibration capacitances and the Pt100 readout.*

Appendix B

The ISOBOX

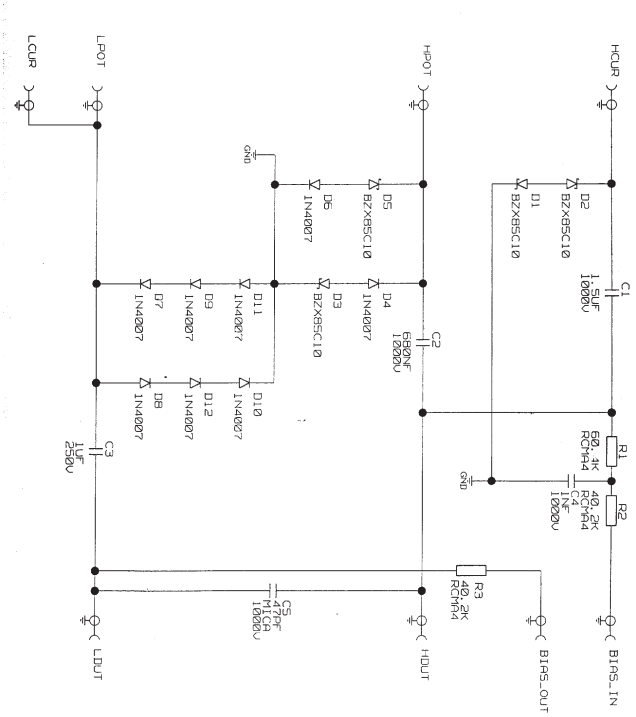

Figure B.1: **Circuit diagram of the ISOBOX:** *The ISOBOX couples the signal voltage from the HP4274/HP4284 into high voltage circuits and filters the signal voltage afterwards out of these circuits. The original design comes from Hewlett Packard. The large capacitances are exchanged with higher voltage stable ones. These high capacitances charged up to* $1000\,V$ *are able to discharge on voltage sources and to destroy them. The capacitance of* $47\,pF$ *between LDUT and HDUT is inserted to the original design and forces the measurement device into a defined measurement range. This is necessary for non defined capacitances in semiconductors, where the HP4274/HP4284 switches between all ranges needing much time [Gla02]. The offset of* $47\,pF$ *is not relevant for CV curves since only the form of the curve is relevant for full depletion or flat band voltage.*

Appendix C

Full Depletion Voltage Scenarios

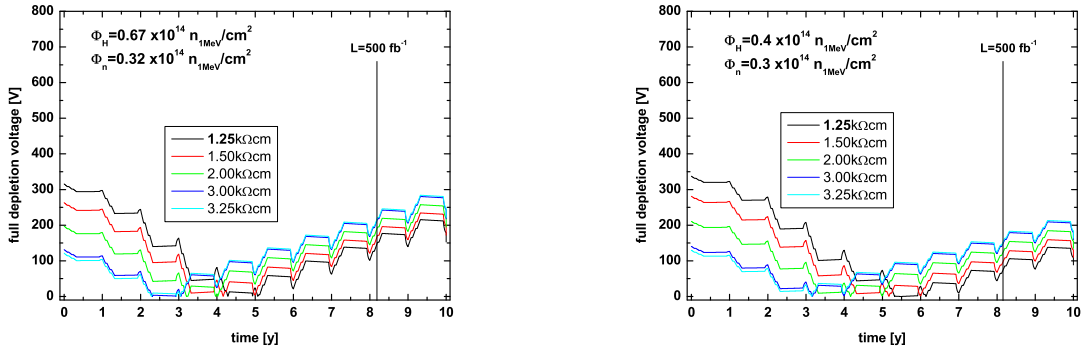

(a) IB1 outer layer

(b) IB2 inner layer

Figure C.1: **Full depletion voltage scenarios for IB1 outer layer and IB2 inner layer sensors:** *The final full depletion voltage is around* $169V$ *lower for the outer layer of IB1 (left) than for the inner layer (Figure 6.26). In principle it is acceptable to put the high resistivity IB1 sensors to the outer layer. For IB2 sensors in the inner tracker layer the final full depletion voltage is around* $213V$ *and below each limit of the sensor performance.*

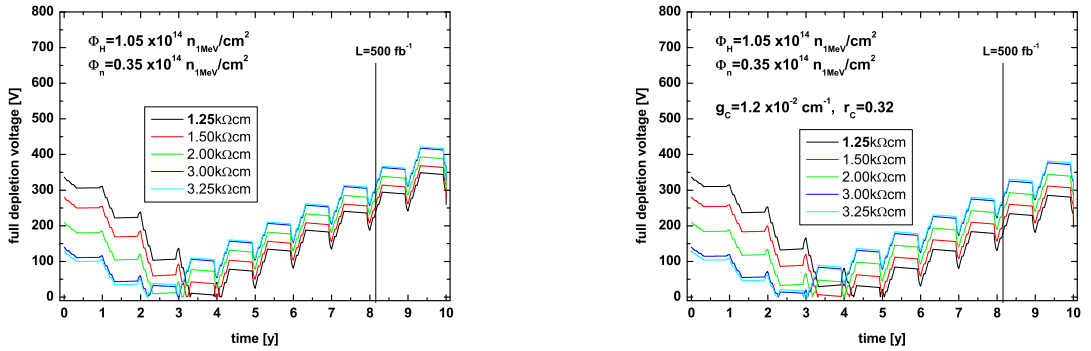

(a) Literature values

(b) Values from Table 6.3

Figure C.2: **Full depletion voltage scenarios for W1TID sensors:** *The final full depletion voltage of the high resistivity sensors (right) is for the same reasons as in Figure 6.26 around* $29V$ *lower than for the expectations from literature (left).*

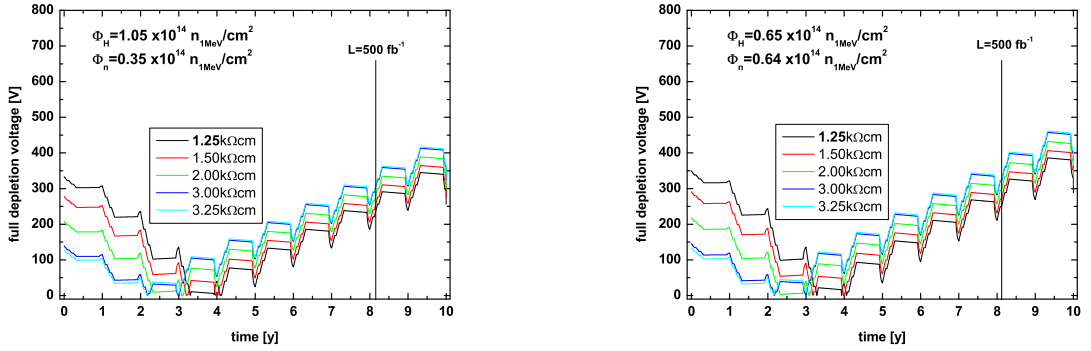

(a) W1TEC

(b) W2

Figure C.3: **Full depletion voltage scenarios for W1TEC and W2 sensors:** *The final full depletion voltages will be below* $400V$ *at the design luminosity of* $500\,fb^{-1}$*. It will be* $417V$ *after* $10y$ *for W1TEC and* $467V$ *for W2. The large difference in full depletion voltage between these two sensor types comes from the geometry factors in Table 2.2.*

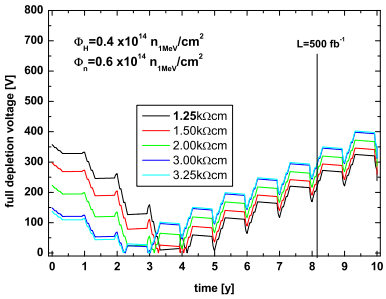

(a) High hadron fluence and literature values

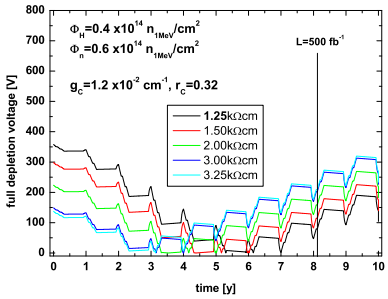

(b) High hadron fluence and values from Table 6.3

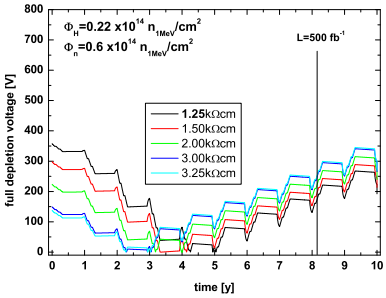

(c) Low hadron fluence and literature values

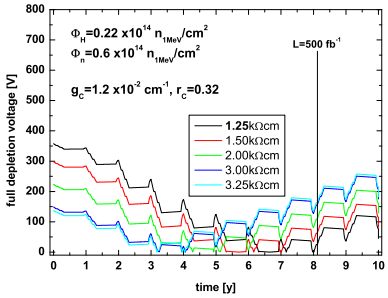

(d) Low hadron fluence and values from Table 6.3

Figure C.4: **Full depletion voltage scenarios for W3 sensors:** *The variety of W3 sensors fluences is quite large. Therefore the scenarios C.4(a) and C.4(b) for are calculated for the highest charged hadron fluence near to the barrel. Figure C.4(c) and C.4(d) present the sensors near to the ECAL, where the charged hadron fluence has its minimum. All final full depletion voltages are below* $400V$*. The final full depletion voltages are up to* $87V$ *lower for the high resistivity sensors.*

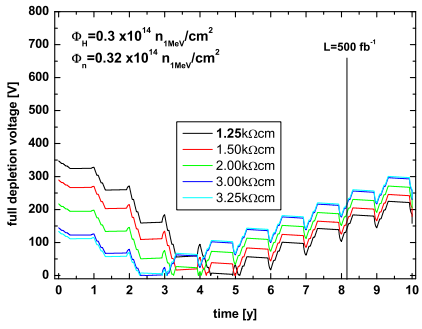

(a) Low neutron fluence

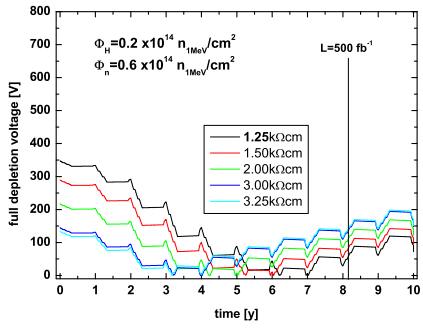

(b) High neutron fluence

Figure C.5: **Full depletion voltage scenarios for W4 sensors:** *The distribution of the neutron fluence is quite large for W4 sensors. The difference in final full depletion voltage* $102V$ *between the highest and the lowest fluence.*

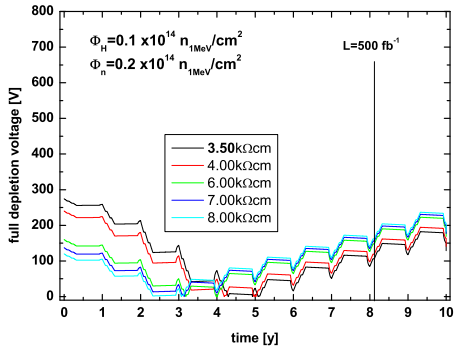

(a) OB1 inner layer

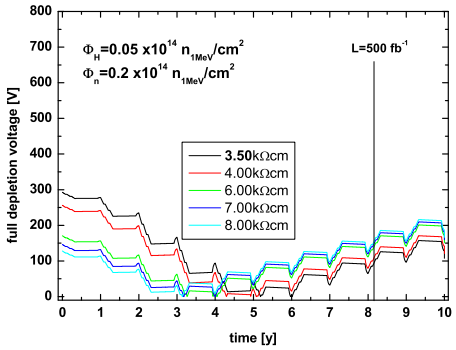

(b) OB2 inner layer

Figure C.6: **Full depletion voltage scenarios for OB1 and OB2 sensors:** *The final full depletion voltages are below* $400V$ *for OB1 and OB2 sensors and depend hardly on the position in the tracker, which is neutron dominated in the outer barrel region.*

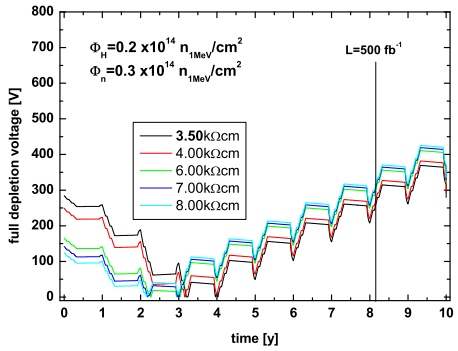

(a) Disc 7 ring 5 modules

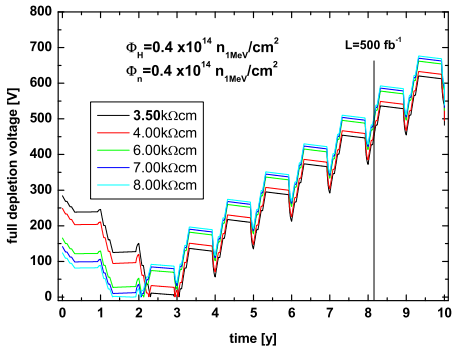

(b) Disc 9 ring 5 modules

Figure C.7: **Full depletion voltage scenarios for ring 5 modules in disc 7 and 9:** *The charged hadron fluence and the neutron fluence are much higher in the forward direction of the tracker (disc 9, right) as for the modules in disc 7 (left). The final full depletion voltage for disc 9 modules will be* $676V$ *after ten years and will be* $251V$ *higher than for disc 7 modules.*

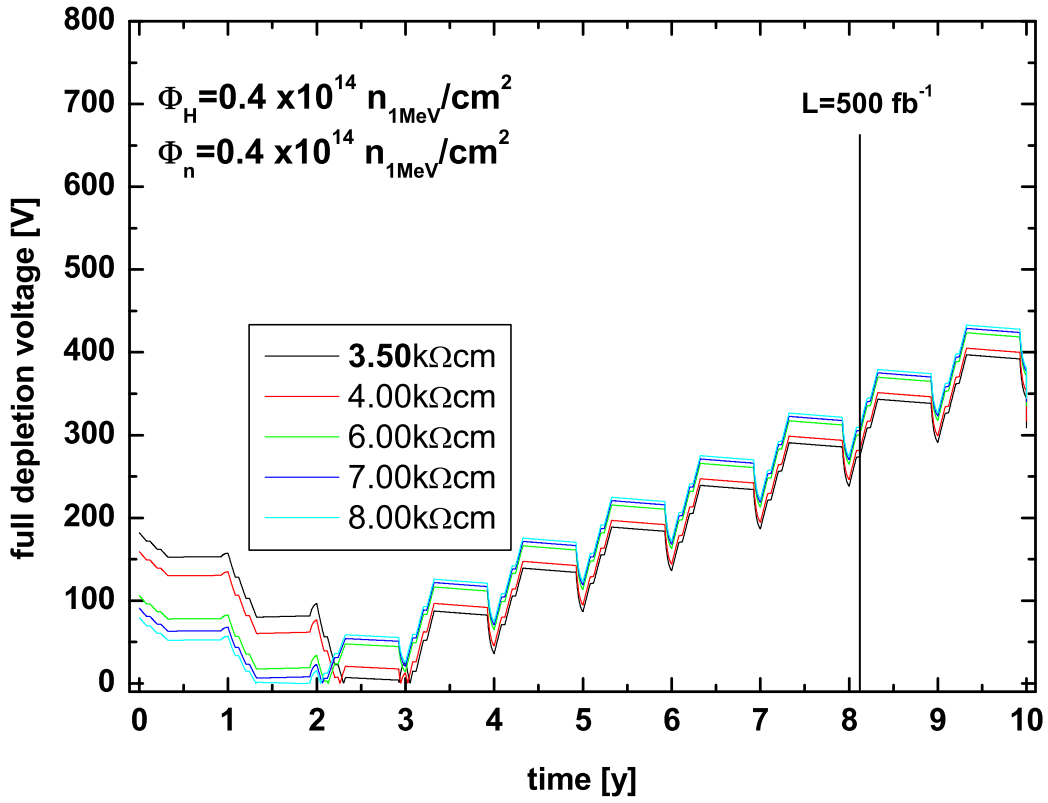

Figure C.8: **Full depletion voltage scenario for ring 5 disc 9 modules with a sensor thickness of** $400\,\mu m$**:** *The thickness of ring 9 modules has to be reduced, due to the higher fluences as the original design fluence. The proposal of* $400\,\mu m$ *thickness is the best compromise between maximum full depletion voltage and signal to noise ratio.*

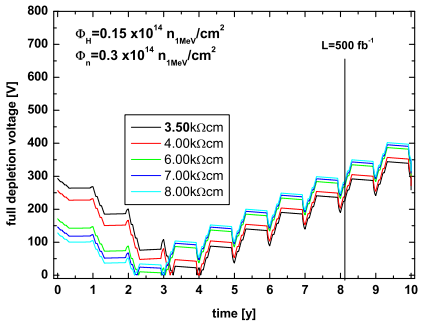

(a) Ring 6 modules

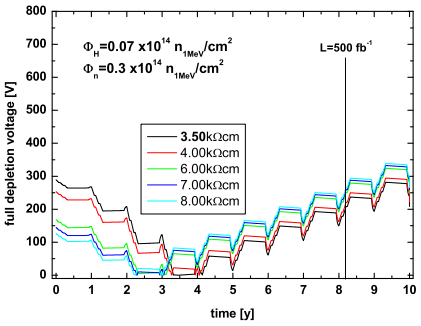

(b) Ring 7 modules

Figure C.9: **Full depletion voltage scenarios for ring 6 and ring 7 modules:** *The final full depletion voltages are below* $400\,V$ *for ring 6 and ring 7 modules.*

	U_{FD} after $500\,fb^{-1}$	U_{FD} after $10\,y$	thickness	Φ_n $10^{14}\,\frac{n_{1MeV}}{cm^2}$	Φ_H $10^{14}\,\frac{n_{1MeV}}{cm^2}$
IB1 inner layer	$350\,V$	$453\,V$	$320\,\mu m$	0.33	1.26
IB1 inner layer with high ρ	$292\,V$	$420\,V$	$320\,\mu m$	0.33	1.26
IB1 outer layer	$196\,V$	$284\,V$	$320\,\mu m$	0.32	0.67
IB2 inner layer	$144\,V$	$213\,V$	$320\,\mu m$	0.3	0.4
OB1 inner layer	$162\,V$	$237\,V$	$500\,\mu m$	0.2	0.1
OB2 inner layer	$146\,V$	$216\,V$	$500\,\mu m$	0.2	0.05
W1TID	$290\,V$	$412\,V$	$320\,\mu m$	0.35	1.05
W1TID with high ρ	$262\,V$	$383\,V$	$320\,\mu m$	0.35	1.05
W1TEC	$293\,V$	$417\,V$	$320\,\mu m$	0.35	1.05
W2	$325\,V$	$462\,V$	$320\,\mu m$	0.64	0.65
W3 for high proton fluence	$281\,V$	$402\,V$	$320\,\mu m$	0.6	0.4
W3 with high ρ for high proton fluence	$209\,V$	$320\,V$	$320\,\mu m$	0.6	0.4
W3 for low proton fluence	$239\,V$	$345\,V$	$320\,\mu m$	0.22	0.6
W3 with high ρ for low proton fluence	$162\,V$	$258\,V$	$320\,\mu m$	0.22	0.6
W4 for high neutron fluence	$207\,V$	$300\,V$	$320\,\mu m$	0.6	0.2
W4 for low neutron fluence	$132\,V$	$198\,V$	$320\,\mu m$	0.32	0.3
Ring 5 disc 7	$299\,V$	$425\,V$	$500\,\mu m$	0.3	0.2
Ring 5 disc 9	$483\,V$	$676\,V$	$500\,\mu m$	0.4	0.4
Ring 5 disc 9 with $d = 400\,\mu m$	$309\,V$	$433\,V$	$500\,\mu m$	0.4	0.4
W6	$281\,V$	$402\,V$	$500\,\mu m$	0.3	0.15
W7	$236\,V$	$339\,V$	$500\,\mu m$	0.3	0.07

Table C.1: **Final sensor full depletion voltages in the CMS tracker:** *The final full depletion voltages are calculated with literature values and for the high resistivity (ρ) material with values from Table 6.3 on Page 101. The neutron fluences Φ_n and the hadron fluences Φ_H are taken from Table 1.4 on Page 11. For ring 5 modules on disc 9 it is recommended to order sensors with a maximum thickness of* $400\,\mu m$.

Appendix D

Source Code for Full Depletion Voltage Scenario Calculation

The code below is written in LabTalk which is a programming language for Origin 6.1 [Ori]. The program calculates the sensors' full depletion voltages under certain fluences and annealing scenarios with 5 different initial resistivity values. The assumptions for the annealing, irradiation, and shut down times can be found in Table 6.4 on Page 106. The design fluence is expected to be reached after 8 years and one of 3 irradiation runs. This fluence is stretched to ten years of LHC operation. The stable damage produced by proton (charged hadrons) irradiation and by neutron irradiation is calculated via an average irradiation. This is necessary because the radiation hardness of some sensor supplied by HPK are more radiation hard under neutron irradiation than under proton irradiation (see Section 6.5.4). Since the beneficial annealing is an exponential decay of acceptors, the current amount of beneficial annealing defects is the sum of previous damage and the new damage. The reverse annealing damage - which is found to be a second order process - produced per day by irradiation is assumed to grow individually, i.e. it is not added to previous reverse annealing but its annealing progress is calculated individually for its remaining time within the CMS tracker. In order to calculate the ongoing of the reverse annealing, the reverse annealing time in the tracker is calculated to a corresponding annealing at a reference temperature $Tref2$. This temperature has to be chosen below all other operation temperatures during service life of CMS.

res1=3000; //initital resistivity in Ωcm
res2=4000;
res3=6000;
res4=8000;
res5=10000;
ds=0.5; // Sensor thickness in mm
corr=1; //correction factor for full depletion voltage (see Equation 2.27 on Page 24)
sf=1; //security factor for fluences
*pFdesign=sf*1.3e14; //total p-fluence in* n_{1MeV}/cm^2 *for 500* fb^{-1}
*nFdesign=sf*0.33e14; //total n-fluence in* n_{1MeV}/cm^2 *for 500* fb^{-1}
Tref=21+273.15; // reference temperature
Tcold=-20+273.15; // temperature during run time
Tinterv=10+273.15; // Annealing temperature during intervention
Tshut=-20+273.15; // temperature during shutdown

```
tintervention=28; // Annealing time per intervention per year
tbreak=14; // Time without run (breaks between irradiation times)
trun=30; // Run time per slot
tshutdown=365-3*trun-2*tbreak-tintervention; // shutdown time
// Parameter for Hamburg Model (see Section 3.4):
N0a=1/(1.602e-19*1450); // results after division by resistivity in initial Neff
pgc=1.49e-2; // stable damage introduction rate for protons
ngc=1.49e-2; // stable damage introduction rate for neutrons
prc=0.65; //incomplete donor removal for protons
nrc=0.65; //incomplete donor removal for neutrons
c1=10.9e-2*res1/N0a;
c2=10.9e-2*res2/N0a;
c3=10.9e-2*res3/N0a;
c4=10.9e-2*res4/N0a;
c5=10.9e-2*res5/N0a;
ga=1.81e-2; gY=5.16e-2;
kA0=2.4e13; kY0=1.5e15; EaA=1.09*1.602e-19; EaY=1.33*1.602e-19;
// stretch Fluence from design-luminosity (500 fb^-1) to 10 years
pF=pFdesign/642*810; nF=nFdesign/642*810;
// calculate average irradiation damage
rc=(prc*pF+nrc*nF)/(pF+nF); gc=(pgc*pF+ngc*nF)/(pF+nF);
// calculate beneficial and reverse annealing time constants in days
tYcold=1/(kY0*exp(-EaY/(kB*Tcold))*60*60*24);
tAcold=1/(kA0*exp(-EaA/(kB*Tcold))*60*60*24);
tYshutdown=1/(kY0*exp(-EaY/(kB*Tshut))*60*60*24);
tAshutdown=1/(kA0*exp(-EaA/(kB*Tshut))*60*60*24);
tYinterv=1/(kY0*exp(-EaY/(kB*Tinterv))*60*60*24);
tAinterv=1/(kA0*exp(-EaA/(kB*Tinterv))*60*60*24);
// distribute total fluence over years
F4=(pF+nF)/(8.1*3*trun); // daily fluence from 4. to 10. year (see Table 1.3 on Page 10)
F1=0.1*F4; //daily fluence in 1. year
F2=0.33*F4; //daily fluence in 2. year
F3=0.66*F4; //daily fluence in 3. year
// Reading column names
%K = %H!wks.col1.name$; // time [d]
%I = %H!wks.col2.name$; // fluence
%L = %H!wks.col3.name$; // stable damage for res1
%M = %H!wks.col4.name$; // beneficial all
%N = %H!wks.col5.name$; // reverse all
%O = %H!wks.col6.name$; // Full depletion voltage for res1
%P = %H!wks.col7.name$; // stable damage for res2
%Q = %H!wks.col8.name$; // Full depletion voltage for res2
%R = %H!wks.col9.name$; // stable damage for res3
%S = %H!wks.col10.name$; // Full depletion voltage for res3
%T = %H!wks.col11.name$; // stable damage for res4
%U = %H!wks.col12.name$; // Full depletion voltage for res4
%V = %H!wks.col13.name$; // stable damage for res5
```

```
%W = %H!wks.col14.name$; // Full depletion voltage for res5
%A = %H!wks.col15.name$; // time=0, for full depletion voltage prior to irradiation
%B = %H!wks.col16.name$; // Full depletion voltage prior to irradiation
// Initialize columns for 10 years
for(i=1;i<10*365+1;i=i+1){
%H_%K[i]=i;
%H_%I[i]=0;
%H_%L[i]=0;
%H_%M[i]=0;
%H_%N[i]=0;
%H_%O[i]=0;
%H_%P[i]=0;
%H_%Q[i]=0;
%H_%R[i]=0;
%H_%S[i]=0;
%H_%T[i]=0;
%H_%U[i]=0;
%H_%V[i]=0;
%H_%W[i]=0;
%H_%A[i]=0;
%H_%B[i]=0;
};
// fill array with current fluences
for (y=0;y<10;y=y+1){ for (d=1;d<366;d=d+1){
//first irradiation run of year
If (d<trun+1 && y==0){F=d*F1};
If (d<trun+1 && y==1){F=3*trun*F1+d*F2};
If (d<trun+1 && y==2){F=3*trun*F1+3*trun*F2+d*F3};
If (d<trun+1 && y>2){F=3*trun*F1+3*trun*F2+3*trun*F3+3*trun*(y-3)*F4+d*F4};
//first break of year
If (d>trun && d<trun+tbreak+1 && y==0){F=trun*F1};
If (d>trun && d<trun+tbreak+1 && y==1){F=3*trun*F1+trun*F2};
If (d>trun && d<trun+tbreak+1 && y==2){F=3*trun*F1+3*trun*F2+trun*F3};
If (d>trun && d<trun+tbreak+1 && y>2){F=3*trun*F1+3*trun*F2+3*trun*F3+3*trun*(y-3)*F4+trun*F4};
//second irradiation run of year
If (d>trun+tbreak && d<2*trun+tbreak+1 && y==0){F=trun*F1+(d-trun-tbreak)*F1};
If (d>trun+tbreak && d<2*trun+tbreak+1 && y==1){F=3*trun*F1+trun*F2+(d-trun-tbreak)*F2};
If (d>trun+tbreak && d<2*trun+tbreak+1 && y==2){F=3*trun*F1+3*trun*F2+trun*F3+(d-trun-
tbreak)*F3};
If (d>trun+tbreak && d<2*trun+tbreak+1 && y>2){F=3*trun*F1+3*trun*F2+3*trun*F3+3*trun*(y-
3)*F4+
trun*F4+(d-trun-tbreak)*F4};
//second break of year
If (d>2*trun+tbreak && d<2*trun+2*tbreak+1 && y==0){F=2*trun*F1};
If (d>2*trun+tbreak && d<2*trun+2*tbreak+1 && y==1){F=3*trun*F1+2*trun*F2};
If (d>2*trun+tbreak && d<2*trun+2*tbreak+1 && y==2){F=3*trun*F1+3*trun*F2+2*trun*F3};
If (d>2*trun+tbreak && d<2*trun+2*tbreak+1 && y>2)
```

```
{F=3*trun*F1+3*trun*F2+3*trun*F3+3*trun*(y-3)*F4+2*trun*F4};
//third irradiation run of year
If (d>2*trun+2*tbreak && d<3*trun+2*tbreak+1 && y==0){F=2*trun*F1+(d-2*trun-2*tbreak)*F1};
If (d>2*trun+2*tbreak && d<3*trun+2*tbreak+1 && y==1){F=3*trun*F1+2*trun*F2+(d-2*trun-
2*tbreak)*F2};
If (d>2*trun+2*tbreak && d<3*trun+2*tbreak+1 && y==2){F=3*trun*F1+3*trun*F2+2*trun*F3+
(d-2*trun-2*tbreak)*F3};
If (d>2*trun+2*tbreak && d<3*trun+2*tbreak+1 && y>2){F=3*trun*F1+3*trun*F2+3*trun*F3+
3*trun*(y-3)*F4+2*trun*F4+(d-2*trun-2*tbreak)*F4};
//shutdown period of year
If (d>3*trun+2*tbreak && y==0){F=3*trun*F1};
If (d>3*trun+2*tbreak && y==1){F=3*trun*F1+3*trun*F2};
If (d>3*trun+2*tbreak && y==2){F=3*trun*F1+3*trun*F2+3*trun*F3};
If (d>3*trun+2*tbreak && y>2){F=3*trun*F1+3*trun*F2+3*trun*F3+3*trun*(y-2)*F4};
//write calculated fluence into cell
%H_%I[y*365+d]=F;
}; // end loop days
}; // end loop years
// Annealing
F=0; // current daily fluence
for (y=0;y<10;y=y+1){
IF (y==0){F=F1};
IF (y==1){F=F2};
IF (y==2){F=F3};
IF (y>2){F=F4};
for (d=1;d<366;d=d+1){
// Beneficial annealing Udep
IF (d==1 && y==0){%H_%M[y*365+d]=ga*F};
IF (d>1 && d<trun+1 && y==0)
{%H_%M[y*365+d]=%H_%M[y*365+d-1]*exp(-1/tAcold)+ga*F};
IF (d<trun+1 && y!=0)
{%H_%M[y*365+d]=%H_%M[y*365+d-1]*exp(-1/tAcold)+ga*F};
IF (d>trun && d<trun+tbreak+1)
{%H_%M[y*365+d]=%H_%M[y*365+d-1]*exp(-1/tAcold)};
IF (d>trun+tbreak && d<2*trun+tbreak+1)
{%H_%M[y*365+d]=%H_%M[y*365+d-1]*exp(-1/tAcold)+ga*F};
IF (d>2*trun+tbreak && d<2*trun+2*tbreak+1)
{%H_%M[y*365+d]=%H_%M[y*365+d-1]*exp(-1/tAcold)};
IF (d>2*trun+2*tbreak && d<3*trun+2*tbreak+1)
{%H_%M[y*365+d]=%H_%M[y*365+d-1]*exp(-1/tAcold)+ga*F};
IF (d>3*trun+2*tbreak && d<3*trun+2*tbreak+tshutdown+1)
{%H_%M[y*365+d]=%H_%M[y*365+d-1]*exp(-1/tAshutdown)};
IF (d>3*trun+2*tbreak+tshutdown)
{%H_%M[y*365+d]=%H_%M[y*365+d-1]*exp(-1/tAinterv)};
}; //end loop over days
}; //end loop over years
// reverse Annealing
```

```
Tref2=Tcold; // Tref2 is used for virtual scenario of reverse annealing, i.e. in the
//following the corresponding daily reverse annealing at temperatures higher than
//Tref2 is calculated to a corresponding annealing time at Tref2. For this reason,
//Tref2 has to be below all other operation temperatures.
// annealing time constant for Tref2
tYref2=1/(kY0*exp(-EaY/(kB*Tref2))*60*60*24);
//ratio of reverse annealing time constants from Tref2 to operation temperatures
tvirtualcold=tYref2/tYcold;
tvirtualshutdown=tYref2/tYshutdown;
tvirtualinterv=tYref2/tYinterv;
// fill column %H_%L with virtual days at Tref2
for (y=0;y<10;y=y+1){ for (d=1;d<366;d=d+1){
If(d<3*trun+2*tbreak+1){%H_%L[y*365+d]=tvirtualcold};
If(d>3*trun+2*tbreak && d<3*trun+2*tbreak+tshutdown+1){%H_%L[y*365+d]=tvirtualshutdown};
If(d>3*trun+2*tbreak+tshutdown){%H_%L[y*365+d]=tvirtualinterv};
}; //end loop over days
}; //end loop over years
// accumulate reverse annealing at Tref2
F=0; // initialize fluence
for (y=0;y<10;y=y+1){
IF (y==0){F=F1};
IF (y==1){F=F2};
IF (y==2){F=F3};
IF (y>2){F=F4};
for (d=1;d<366;d=d+1){
zws=0; //sum for remaining annealing days
If(d<trun+1){
for(i=1;i<365*10-(y*365+d);i=i+1)
{zws=zws+%H_%L[i];
%H_%N[y*365+d+i]=%H_%N[y*365+d+i]+gY*F*(1-1/(1+zws/tYref2))
}; //end for
}; //end If
If(d>trun+tbreak && d<2*trun+tbreak+1){
for(i=1;i<365*10-(y*365+d);i=i+1)
{zws=zws+%H_%L[i];
%H_%N[y*365+d+i]=%H_%N[y*365+d+i]+gY*F*(1-1/(1+zws/tYref2))
}; //end for
}; //end If
If(d>2*trun+2*tbreak && d<3*trun+2*tbreak+1){
for(i=1;i<365*10-(y*365+d);i=i+1)
{zws=zws+%H_%L[i];
%H_%N[y*365+d+i]=%H_%N[y*365+d+i]+gY*F*(1-1/(1+zws/tYref2))
}; //end for
}; //end If
}; //end loop over days
}; //end loop over years
// stable damage
```

```
for(d=1;d<10*365+1;d=d+1){
%H_%K[d] = d; // Time
%H_%L[d] = rc*N0a/res1*(1-exp(-c1*%H_%I[d] )) + gc*%H_%I[d]; // Stable damage res1
%H_%P[d] = rc*N0a/res2*(1-exp(-c2*%H_%I[d] )) + gc*%H_%I[d]; // Stable damage res2
%H_%R[d] = rc*N0a/res3*(1-exp(-c3*%H_%I[d] )) + gc*%H_%I[d]; // Stable damage res3
%H_%T[d] = rc*N0a/res4*(1-exp(-c4*%H_%I[d] )) + gc*%H_%I[d]; // Stable damage res4
%H_%V[d] = rc*N0a/res5*(1-exp(-c5*%H_%I[d] )) + gc*%H_%I[d]; // Stable damage res5
};
// Calculate full depletion voltage
for(d=1;d<10*365+1;d=d+1){
%H_%O[d] = corr*773.4e-12 * sqr(ds) * abs(N0a/res1-%H_%L[d]-%H_%M[d]-%H_%N[d]);
%H_%Q[d] = corr*773.4e-12 * sqr(ds) * abs(N0a/res2-%H_%P[d]-%H_%M[d]-%H_%N[d]);
%H_%S[d] = corr*773.4e-12 * sqr(ds) * abs(N0a/res3-%H_%R[d]-%H_%M[d]-%H_%N[d]);
%H_%U[d] = corr*773.4e-12 * sqr(ds) * abs(N0a/res4-%H_%T[d]-%H_%M[d]-%H_%N[d]);
%H_%W[d] = corr*773.4e-12 * sqr(ds) * abs(N0a/res5-%H_%V[d]-%H_%M[d]-%H_%N[d]);
};
// Calculate initial full depletion voltage
%H_%B[1] = corr*773.4e-12 * sqr(ds) * N0a/res1;
%H_%B[2] = corr*773.4e-12 * sqr(ds) * N0a/res2;
%H_%B[3] = corr*773.4e-12 * sqr(ds) * N0a/res3;
%H_%B[4] = corr*773.4e-12 * sqr(ds) * N0a/res4;
%H_%B[5] = corr*773.4e-12 * sqr(ds) * N0a/res5;
// Write maximum of full depletion voltage into following cells
%H_%B[6] = max(%H_%O[1],%H_%O[10*365]);
%H_%B[7] = max(%H_%Q[1],%H_%Q[10*365]);
%H_%B[8] = max(%H_%S[1],%H_%S[10*365]);
%H_%B[9] = max(%H_%U[1],%H_%U[10*365]);
%H_%B[10] = max(%H_%W[1],%H_%W[10*365]);
```

List of Figures

1.1 LHC and experiments at CERN . . . 2
1.2 Higgs production at LHC . . . 3
1.3 Production cross sections of the Higgs boson in the standard model . . . 3
1.4 Branching ratio of the Higgs boson versus mass . . . 4
1.5 Production of SUSY particles at LHC . . . 5
1.6 The CMS detector . . . 5
1.7 Pictures of a CMS rod and a CMS outer barrel detector module . . . 7
1.8 Pictures of a CMS petal and a CMS wedge shaped detector module . . . 8
1.9 Picture of a CMS inner barrel shell . . . 8
1.10 The schematics of the CMS tracker . . . 9
1.11 Fluences and doses in the CMS tracker . . . 10

2.1 The element silicon . . . 14
2.2 Energy bands in silicon lattice . . . 14
2.3 Simplified band model of metal, semiconductor and insulator . . . 15
2.4 Energy levels of p- and n-doped silicon . . . 17
2.5 Fermi Levels, state density, and free charge density in silicon . . . 18
2.6 Band structure of silicon . . . 20
2.7 Absorption coefficients of Si, GaAs and Ge . . . 20
2.8 Energy loss of electrons in silicon after Bethe-Bloch formula . . . 22
2.9 The p-n-junction . . . 23
2.10 Energy band structure of a Schottky contact . . . 27
2.11 Energy band structures of a MOS structure . . . 28
2.12 Schematics of a semiconductor sensor . . . 30
2.13 Schematics of noise sources in a CMS detector . . . 33

3.1 Examples of different lattice damage in silicon . . . 37
3.2 Damage simulation in silicon . . . 38
3.3 Displacement damage of several particles versus energy . . . 39
3.4 Increase of leakage current density with fluence . . . 42
3.5 Current annealing of irradiated silicon . . . 43
3.6 Changes in the effective doping concentration with fluence . . . 45
3.7 Annealing of the effective doping concentration after irradiation . . . 46
3.8 Full depletion voltage versus fluence and annealing time . . . 47

4.1 Principle design of a CMS sensor . . . 52
4.2 Principle of the metal overhang design . . . 54

4.3 Silicon in $< 111 >$ and $< 100 >$ orientation 55
4.4 Standard half moon of a CMS wafer 56

5.1 The logistic system of the CMS sensor quality assurance 60
5.2 The Karlsruhe probe station 61
5.3 Schematics of IV measurement 63
5.4 Schematics of CV measurement 64
5.5 Schematics of single strip leakage current measurement 65
5.6 Schematics of bias resistor measurement 66
5.7 Schematics of coupling capacitance measurement 66
5.8 Schematics of pinhole measurement 67
5.9 Schematics of interstrip capacitance measurement 68
5.10 Interstrip capacitance versus bias voltage before and after irradiation 69
5.11 Schematics of interstrip resistance measurement 70
5.12 Verification of measured interstrip resistance values 70
5.13 Schematics of single strip leakage current measurement with different potentials on the AC pad 71
5.14 Schematics of setup for current measurements during irradiation 73
5.15 Picture of a sensor for current measurements in the irradiation box for neutron irradiation in Louvain-la-Neuve 74
5.16 IV and CV of HPK and STM sensors measured at QTC 75
5.17 Strip parameters of HPK and STM sensors measured in QTC 76
5.18 Stain on guard ring of STM sensor 76
5.19 Pictures of a crack on STM sensor 77
5.20 Formation of stains on guard ring of STM sensor over time 78
5.21 Electron microscope pictures of stain on guard ring of STM sensor 79
5.22 Element distribution on guard ring of STM sensor 79
5.23 Element analysis on STM sensor with electron microscope 80
5.24 Element map of guard ring on STM sensor 81
5.25 Element map of bias ring on STM sensor 82
5.26 Potassium distribution on guard ring of STM sensor 82
5.27 Picture of partially passivated bias ring on STM sensor 83
5.28 Picture of stains on DC pads of STM sensor 83
5.29 Total leakage current dependence on large vacuum changes of an STM sensor 85
5.30 Total leakage current dependence on small changes in vacuum for a STM sensor . . . 85
5.31 Single strip leakage current of a STM sensor under mechanical stress 86

6.1 NIEL damage functions for positive pions, protons, and neutrons 88
6.2 The Kompakt-Zyklotron in Karlsruhe 89
6.3 Picture of CMS sensors in stacks ready for irradiation 90
6.4 Aluminium frame for proton irradiation 90
6.5 Cross sections for protons with Ni 92
6.6 The irradiation facility in Louvain-la-Neuve 93
6.7 Fix target of the irradiation facility in Louvain-la-Neuve 94
6.8 Energy spectrum of neutrons at the irradiation facility in Louvain-la-Neuve 94
6.9 Full depletion voltages of HPK and STM mini sensors before and after proton irradiation 96
6.10 CV curves of HPK sensors versus annealing time 96

6.11 Beneficial annealing of full depletion voltage on HPK sensors 97
6.12 Beneficial and reverse annealing of full depletion voltage on HPK sensor 98
6.13 Reverse annealing of a HPK mini sensor after proton irradiation 98
6.14 Full depletion voltages of final STM pre-series sensors 99
6.15 Total capacitance from final STM pre-series sensors 100
6.16 Resistivity distribution of HPK wafers with too high resistivity 101
6.17 Full depletion voltages of HPK high resistivity diodes before and after neutron irradiation 102
6.18 Full depletion voltages of HPK high resistivity mini sensors before and after neutron irradiation 102
6.19 Full depletion voltages of HPK high resistivity sensors before and after neutron irradiation 103
6.20 Full depletion voltage of proton irradiated high resistivity sensors in comparison with the Hamburg model 103
6.21 DLTS spectra of high resistivity HPK material after proton irradiation 104
6.22 Full depletion voltage of IB1 sensors calculated for literature values and currently measured values of high resistivity sensors 105
6.23 Schematics of a CMS full depletion voltage scenario 107
6.24 Full depletion voltage scenario for IB1 sensors at different annealing temperatures . . 108
6.25 Full depletion voltage of IB1 sensors after service life at LHC versus annealing time and annealing temperature 109
6.26 Full depletion voltage scenarios for IB1 sensors 110
6.27 Increase of leakage current of CMS mini sensors after proton irradiation 110
6.28 Annealing of total leakage current of HPK sensors 111
6.29 Annealing of total leakage current density 111
6.30 Annealing of single strip leakage current after proton irradiation 112
6.31 Annealing of single strip leakage current density after proton irradiation 113
6.32 Total leakage currents from final STM pre-series sensors before and after proton irradiation 113
6.33 Single strip leakage currents of final STM pre-series sensors before and after proton irradiation 114
6.34 Total and single strip leakage currents of an STM sensor during the first neutron irradiation test 115
6.35 Total and single strip leakage currents of a STM sensor during interruptions at the first neutron irradiation 116
6.36 Total leakage current of a STM sensor during second neutron irradiation and following long term test 117
6.37 Total leakage current of a STM sensor during second neutron irradiation 118
6.38 Decay of very short-lived damage after neutron irradiation 119
6.39 Ionization current versus fluence 119
6.40 Single strip leakage currents of a STM sensor during second neutron irradiation and following long term test 120
6.41 Bias resistors after proton irradiation with outer and inner barrel fluence 122
6.42 Measurements of bias resistors versus bias voltage of the final STM pre-series sensors before and after proton irradiation 123
6.43 Annealing of bias resistors after proton irradiation 124

6.44 Current through a poly crystalline silicon resistor versus temperature before and after proton irradiation . . . 125
6.45 Resistance of a poly crystalline silicon resistor versus temperature before and after irradiation . . . 125
6.46 Resistance of poly crystalline silicon resistors before and after proton irradiation and annealing with fluences up to $10^{16} n_{1MeV}/cm^2$ . . . 126
6.47 Current and resistance of poly crystalline silicon resistor irradiated to $5 \cdot 10^{16} n_{1MeV}/cm^2$ 126
6.48 Coupling capacitances of a STM sensor before and after proton irradiation . . . 128
6.49 Annealing of coupling capacitances after proton irradiation . . . 129
6.50 Flatband voltage of STM outer barrel mini sensors . . . 131
6.51 Interstrip capacitances of STM mini sensors before and after proton irradiation with inner barrel design fluence . . . 131
6.52 Interstrip capacitances of STM mini sensors with too high flat band voltages before and after proton irradiation with outer barrel design fluence . . . 132
6.53 Bias voltage ramps of interstrip capacitances from final STM pre-series sensors . . . 133
6.54 Annealing of interstrip capacitance of HPK sensors measured between DC pads . . . 134
6.55 Annealing of interstrip capacitance of HPK sensors measured between AC pads . . . 135
6.56 Signal to noise ratios of CMS detector modules with STM sensors before and after irradiation . . . 136
6.57 Full depletion voltages of detector modules with sensors from final STM pre-series . 137
6.58 Noise before and after irradiation and standard annealing for detector modules with STM final pre-series sensors . . . 138
6.59 Common mode noise versus bias voltage of a detector module with STM sensors . . 139
6.60 Signal to noise ratio of CMS detector modules with last STM pre-series sensors after proton irradiation . . . 140

A.1 Relay schematics of the Karlsruhe probe station . . . 145

B.1 Circuit diagram of the ISOBOX . . . 147

C.1 Full depletion voltage scenarios for IB1 outer layer and IB2 inner layer sensors . . . 149
C.2 Full depletion voltage scenarios for W1TID sensors . . . 150
C.3 Full depletion voltage scenarios for W1TEC and W2 sensors . . . 150
C.4 Full depletion voltage scenarios for W3 sensors . . . 151
C.5 Full depletion voltage scenarios for W4 sensors . . . 151
C.6 Full depletion voltage scenarios for OB1 and OB2 sensors . . . 152
C.7 Full depletion voltage scenarios for ring 5 modules in disc 7 and 9 . . . 152
C.8 Full depletion voltage scenario for ring 5 disc 9 modules with a sensor thickness of $400\mu m$ . . . 153
C.9 Full depletion voltage scenarios for ring 6 and ring 7 modules . . . 153

List of Tables

1.1 Specifications of wedge shaped CMS sensors 9
1.2 Specifications of rectangular CMS sensors 10
1.3 LHC luminosity and CMS fluence distribution with time 10
1.4 Maximum fluences expected in the CMS tracker 11

2.1 Properties of silicon 15
2.2 Correction factors for full depletion voltage of CMS sensors 25
2.3 Noise sources of the CMS readout system 34

3.1 Characteristics of typical irradiation interactions in silicon 36
3.2 Lindhardt Partition function values for several particles 38
3.3 Energy levels of important defects in silicon 40
3.4 Parameters for leakage current annealing at room temperature 41
3.5 Time constants for long-term current annealing 43
3.6 Time constants of beneficial and long-term reverse annealing of full depletion voltage 46

4.1 Parameters and limits of the CMS sensors 57

5.1 Overview of measured parameters, corresponding measurements, and problem solutions 72

6.1 Neutron beam impurities in Louvain-la-Neuve 95
6.2 Sensors from final STM pre-series 99
6.3 Parameters of the Hamburg model fitted for high resistivity HPK diodes after neutron irradiation 101
6.4 Assumptions for the trackers run time and annealing temperatures during one year . . 106

A.1 Relay settings for measurements with the probe station in Karlsruhe 146

C.1 Final sensor full depletion voltages in the CMS tracker 154

Bibliography

[Ada00] W. Adam et al. *Micro-strip sensors based on CVD diamond*. Nucl. Instr., Methods in Physics Research, A 453:141-148, 2000.

[Agr03] J.-L. Agram et al. *The silicon sensors for the compact muon solenoid tracker - design and qualification procedure*. CMS Note 2003/015, Nucl. Instrum. Methods A 517 (2004):77-93, 2003.

[BBB94] U. Biggeri, E. Borchi, M. Bruzzi Z. Li and S. Lazanu. *Studies of Deep Levels in High Resistivity Silicon Detectors Irradiated by High Fluence Fast Neutrons Using a Thermally Stimulated Current Spectrometer*. IEEE Transactions on Nuclear Science, 41(4):964-970, 1994.

[BL83] J. Bourgin and M. Lannoo. *Point defects in Semiconductors II, volume 35 of Springer Series in Solid-State Sciences*. Springer Verlag, ISBN 0-387-11515-3, 1983.

[Bla68] Frank J. Blatt. *Physics of Electronic Conduction in Solids*. McGraw-Hill, Hamburg, New York, London, Paris, Tokio, 1968.

[Bra00] S. Braibant et al. *Investigation of design parameters and choise of substrate resistivity and crystal orientation for the CMS silicon strip detector*. CMS Note 2000/011, CERN, 2000.

[Bra79] P. Bräunlich. *Thermally Stimulated Relaxation in Solids*. Volume 37 of Topics in Applied physics, Springer-Verlag, 1979.

[CDMR03] D. Creanza, M. Depalma, N. Manna and V. Radicci. *Reverse annealing studies on standard diodes irradiated with 34MeV proton beam.* 2nd RD50 Workshop at CERN, Geneva, 2003.

[Chi95] Alexander Chilingarov. *Radiation studies and operational projections for silicon in the ATLAS inner detector*. Nucl. Instr., Methods in Physics Research, A 360:432, 1995.

[CTDRA00] *CMS Technical Design Report Adendum*. LHCC 2000-016, 2000.

[CTS00] *Technical Specifications*. IT-2777/EP/CMS.

[Die03] Alexander Dierlamm. *Untersuchungen zur Strahlenhärte von Siliziumsensoren*. PhD thesis, Institut für Experimentelle Kernphysik der Universität Karlsruhe (TH), IEKP-KA/2003-23, 2003.

[Die04] Alexander Dierlamm. *Private communication - the pictures are extracted from a simulation result with ISE-TCAD*, 2004.

[DKN99] T. Dubbs, W. Kroeger, T. Nissen, T. Pulliam, D. Roberts, W.A. Rowe, H.F.W. Sadronizki, A. Seiden, B. Thomas, A. Webster and G. Alers. *Development of radiation-hard materials for microstrip detectors*. IEEE Transactions on Nuclear Science, 46:839-843, 1999.

[DKS97] A. Djouadi, J. Kalinowski and M. Spira, HDECAY. *A program for Higgs boson decays in the standard model and its supersymmetric extension*. hep-ph/9704448, 1997.

[DW02] C. DaVia and S.J. Watts. Nucl. Instr., Methods in Physics Research, B 186:111, 2002.

[Fei97] H. Feick. *Radiation Tolerance of Silicon Particle Detectors for High-Energy Physics Experiments*. Ph.D Thesis, University of Hamburg, 1997.

[FFG94] E. Fretwurst, H. Feick, M. Glaser, C. Gössling, E.H.M. Heijne, A. Hess, F. Lemeilleur, G. Lindström, K.H. Mählmann, A. Rolf, T. Schulz, C. Soave. *Reverse annealing of the effective impurity concentration and long term operational scenario for silicon detectors in future collider experiments*. Nucl. Instr., Methods in Physics Research, A 342:119-125, 1994.

[Fre04] S. Freudenstein. *Materialanalyse und Fehlerstudien an hochspannungsfesten Silizium-Mikrostreifendetektoren für das CMS-Experiment*. Institut für Experimentelle Kernphysik der Universität Karlsruhe (TH), Diploma thesis, IEKP-KA/2004-13, 2004.

[Fur02] A. Furgeri. *Studien zu Strahlenschäden an Siliziumstreifensensoren für CMS*. Diploma thesis, Institut für Experimentelle Kernphysik der Universität Karlsruhe (TH), Diploma thesis, IEKP-KA/2002-14, 2002.

[Fur03] Alexander Furgeri et al. *Radiation Damage Effects on CMS Sensors - Quality Assurance and Irradiation Tests*. IEEE- Nuclear Science Symposium, Portland Oregon, TNS.2004.839091, 2003.

[Fur04a] A. Furgeri. *Irradiation Facilities in Karlsruhe*. www-ekp.physik.uni-karlsruhe.de/∼furgeri/irradiation_center/, 2004.

[Fur04b] A. Furgeri et al.. *Leakage current of CMS single-sided strip sensors under neutron irradiation*. Vertex Conference, Menaggio 2004, Nucl. Instr., Methods in Physics Research, A 560:108-111, 2006.

[Fur05] A. Furgeri et al.. *Results of Irradiation Quality Assurance of CMS Silicon Microstrip detector*. Position Sensitive Detectors Conference 2005, Liverpool, accepted by Nucl. Instr., Methods in Physics Research, A, 2005.

[GKS84] Reinhard Glang, San-Mei Ku and Alfred Schmitt. *Process for fabricating polycrystalline silicon film resistors*. United States Patent 4467519, http://www.freepatentsonline.com/4467519.html, 1984.

[Gla02] Maurice Glaser. private communication with Maurice Glaser, technician at CERN, 2002.

[Gre02] Gh. Gregoire et al. *An intense fast neutron beam in Louvain-la-Neuve*. http://www.fynu.ucl.ac.be/themes/he/cms/neutron_beam.

[Gri96] P. Griffin et al. *Neutron cross sections taken from ENDF/B-VI, ORNL*. 1996.

[Hag02] K. Hagiwara et al. *Review of particle physics*. Phys. Rev., D66:010001, 2002.

[Har02] F. Hartmann. *The CMS All-Silicon Tracker - Strategies to ensure a high quality and radiation hard Silicon Detector*. Nucl. Instr., Methods in Physics Research, A 478, 2002.

[Hof97] H. Hofer et al. *CMS - electromagnetic calorimeter*. CERN/LHCC 1997/033, Geneva, 1997.

[HuA93a] M. Huhtinen and P. Aarino. *Estimation of pion induced displacement damage in silicon*. 1993.

[HuA93b] M. Huhtinen and P. Aarino. *Pion induced displacement damage in Silicon devices*. 1993.

[huh01] M. Huhtinen. *Simulation of non-ionising energy loss and defect formation in silicon*. 2001.

[IL95] H. Ibach und H. Lüth. *Festkörperphysik*. Springer Verlag, 1995.

[Jon99] L.L. Jones et al. *The APV25 deep submicron readout chip for CMS detectors*. 5th Workshop on Electronics for the LHC Experiments (LEB99), Snowmass, Colorado, 1999.

[Kit02] Ch. Kittel. *Einführung in die Festkörperphysik*. ISBN 3-486-27219-5, 2002.

[KOH01] *Materials Used in Semiconductor Manufacturing (Page 2)*. http://www.semiconfareast.com/semicon_matls2.htm, 2001.

[Kon92] A. Yu. Konobeyev et al. *Neutron displacement damage cross sections for structural materials below 800MeV*. 1992.

[Kra03] M. Kramer et al. *The Silicon Sensors for the Compact Muon Solenoid Tracker - Design and Quality Procedure*. CMSNOTE 2003/015, 2003.

[Kra04] M. Krammer. *The silicon sensors for the Inner Tracker of the Compact Muon Solenoid experiment*. Nucl. Instr., Methods in Physics Research, A 531:238-245, 2004.

[KS01] Danek Kotlinski and Andrey Staromudow. *High level tracker triggers for CMS*. Nucl. Instr., Methods in Physics Research,, A 501:222-228, 2001.

[LB91] Hans Landolt and Richard Boernstein. *Numerical data and functional relationships in science and technology : new series - Radionuklidproduktion bei mittleren Energien.*. Springer Verlag, ISBN 3-540-54711-8, 1991.

[LFL80] V.A.J. van Lint T.M. Flanagan R.E. Leadon J.A. Naber and V.C. Rogers. *Mechanisms of radiation effects in electronic materials, Volume 1*. John Wiley and Sons, New York, Chichester, Brisbane, Toronto, 1980.

[LN62] J. Lindhard and V. Nielson. *Nuclear collisions and ionisations fluctuations in charged particle detectors*. Physical Letters, 2(5):209-211, 1962.

[Lut99] Gerhard Lutz. *Semiconductor Radiation Detectors*. Springer Verlag Berlin, 1999.

[Luu04] Panja Luukka et al. *Results of proton irradiations of large area strip detectors made of high-resistivity Czochralski silicon*. Nucl. Instr., Methods in Physics Research, Accelerator Spectrometers Detectors and Associated Equipment, Volume 530 Issues 1-2 September 2004 A:117-121, 2004.

[LWM86] M.S. Lazo, D.M. Woodall und P.J. McDaniel. *Silicon and silicon dioxide neutron damage functions*. Sandia National Laboratories, 1986.

[MG92] E. Meijer, H.G. Grimmeiss. *Transient current measurements for the characterization of deep defects in semiconductors*. Semicond. Sci. Technol. 7:188-197, 1992.

[Mig01] Ernesto Migliore. *'Investigations of operating scenarios for the sensors of the CMS silicon Tracker*. CMS NOTE 2001/023, 2001.

[MLK77] G.L. Miller, D.V. Lang, L.C. Kimerling. *Capacitance Transient Spectroscopy*. Ann. Rev. Mater. Sci. 377-448, 1977.

[Mol99] Michael Moll. *Radiation Damage in Silicon Particle Detectors*. Universität Hamburg, DESY-THESIS-1999-040, 1999.

[Mov55] J.E. Moval. *Theory of ionization fluctuations*. Phil. Mag. 46:263, 1955.

[Mue98] Th. Müller. *The CMS Tracker and its performance*. Nucl. Instr., Methods in Physics Research, A 408:119-127, 1998.

[NIS] *National Institute of Standards and Technology*. http://physics.nist.gov/.

[Ori] *Origin 6.1, Scientific software combining presentation and calculation*. http://www.originlab.com/.

[PKS98] G. Pfennig, H. Klewe-Nebenius and W. Seelmann-Eggebert. *Karlsruher Nuklidkarte*. 6th edition 1995, revised reprint 1998, ISBN 3-921879-18-3, 1998.

[Pro98] *The Tracker Project, Technical design report*. CERN/LHCC 1998/006, Geneva, 1998.

[Ram39] S. Ramo.*Currents Induced by Electron Motion*. Proceedings of the IRE, vol. 27, pp. 584-5, 1939

[SAND04] C. Sander, W. de Boer, M. Herold, V. Zhukov, A. V. Gladyshev and D. I. Kazakov. *Excess of EGRET Galactic Gamma Ray Data interpreted as Dark Matter Annihilation*. arXiv:astro-ph/0408272 v2, 2004.

[Sch04] H. Schweickert. *private communication about current properties of the KAZ*. 2004.

[Sch84] H. Schweickert. *Das Karlsruher Kompaktzyklotron*. KfK-Nachrichten, 16.4.1984.

[Sch96] T. Schulz. *Investigations on the Long Term Behavior of Damage Effects and Corresponding Defects in Detector Grade Silicon after Neutron Irradiation*. PhD Thesis, University of Hamburg, 1996.

[SFF94] T. Schulz, H. Feick, E. Fretwurst, G. Lindström, M. Moll, K.H. Mählmann. *Long term reverse annealing in silicon detectors*. IEEE Transactions on Nuclear Science, 41(4), 1994.

[Sgu04] S. Sguazzoni. *The CMS Si-Tracker*. in procedings, 2004.

[SH95] B. Sapoval and C. Hermann. *Physics of Semiconductors*. 1995.

[Spe00] C. NOTE. *Invention to Tender: IT-2777/EP/CMS, Technical Specification*. 11/2000.

[SSZ00] H. Spiesberger, M. Spira and P. M. Zerwas. *The standard model Higgs: Physical basics and scattering experiments*. hep-ph/0011255, 2000.

[Sta04] J. Stahl. *Defect Characterization in High-Purity Silicon after γ- and Hadron Irradiation*. PhD Thesis 2004/028, University of Hamburg, ISSN 1435-8085, 2004.

[STM04] Statement of STM given in Catania to the CMS collaboration, 2004.

[Sum93] G. P. Summers et al. *Damage correlations in semiconductors exposed to gamma, electron and proton radiations*. 1993.

[Sze85] S.M. Sze. *physics of semiconductor devices*. John Wiley and Sons, 1985.

[Ves04] A. Vest. *SUSY/Higgs analysis at Karlsruhe*. Status report, DCMS Meeting, Aachen, 2004.

[Wei04] Thomas Weiler. *Studies on Silicon Strip Detectors for the CMS Experiment*. PhD thesis, Institut für Experimentelle Kernphysik der Universität Karlsruhe (TH), IEKP-KA/2004-22, 2004.

[Wei04a] Thomas Weiler. *Measured after irradiation and annealing*.

[Wue01] J. Wüstenfeld et al. *Surface effects before and after ionisation-induced surface defects*. 6th ROSE Workshop on Radiation Hardening of Silicon Detectors, 2001.

[Wun92] R. Wunsdorf. *Systematische Untersuchungen zur Strahlenresistenz von Siliziumdetektoren für die Verwendung in Hochenergiephysik-Experimenten*. Universität Hamburg, 1992.

[Zac95] Chiara Zaccherini. *Process for forming implanted regions with lowered channeling risk on semiconductors*. United States Patent 5436177, http://www.patentstorm.us/patents/5436177.html, 1995.

[Zio94] H.-J. Ziock et al. *Temperature dependence of the radiation induced change of depletion voltage in silicon PIN detectors*. Nucl. Instr., Methods in Physics Research, A 342:96-104, 1994.

[ZLi95] Zheng Li. *Experimental comparison among various models for the reverse annealing of the effective concentration of ionized space charge (n_{eff}) of neutron irradiated silicon detectors*. IEEE Transactions on Nuclear Science, 42(4):224-234, 1995.

Acknowledgements

A project like this thesis cannot be done by a single person without any help. Generally I thank to all people who assists me during my PhD and in particular the following persons and groups enabled this thesis.

- I thank Prof. Dr. Wim de Boer for giving me the opportunity to do this work on silicon sensors and for the confidence he had to give me the freedom in organizing the tasks connected to the irradiation tests and sensor measurements. In particular, I enjoyed the long discussions with him about the results from this work.
- I thank the Co-referent Prof. Dr. Thomas Müller
- Dr. Peter Blüm gave me many useful contributions to my script
- Dr. Alexander Dierlamm introduced me well into the irradiation procedure at the cyclotrons in Karlsruhe
- Without the excellent team work of whole CMS sensor group the large amount of qualifications and special measurement campaigns could not have been carried out
- The good work done by my diploma students Stefanie Freudenstein, Andreas Sabelleck and Michael Krause enabled many results from this thesis
- A large fraction of the the standard sensor measurements is the work of the students Marcel Spurny, Thomas Punz, Johannes Junge, Johannes Hagmann and Cedric Menge
- Dr. Eric Forton organized and carried out the neutron irradiations in Louvain-la-Neuve
- The assistance of the technicians Tobias Barvich, Pia Steck and Norman Seith was a great help without which many studies could not have been carried out
- The good management of the bureaucratic affairs by Mrs. Haas and Mr. Fuchs enabled me many purchases and business travels with a minimum effort
- The employee attitude with my colleagues Dr. Hans-Jürgen Simonis, Dr. Guido Dirkes, Dr. Florian Hauler, Dr. Levin Jungermann, Martin Frey, Stefan Heier, Johannes Bol, Thomas Weiler, Christian Piasecki and Manuel Fahrer was terrific
- The cyclotron crew from the ZAG-AG enabled with their excellent work irradiations with a high precision
- The jobs given to the mechanical work shop have excellent be done in a very short time
- The electronic work shop enriched me with many funny experiences
- My colleagues at RD39 at CERN gave me many useful hints for the understanding of semiconductors
- Certified Translator Thorsten Jess gave me many useful language contributions to my thesis